Universidade do Minho
Escola de Ciências

Weronika Wojtak

A novel dynamic field model supporting a continuum of bump amplitudes: Analysis and Applications

July, 2021

A novel dynamic field model supporting a continuum of bump amplitudes: Analysis and Applications
Weronika Wojtak
UMinho | 2021

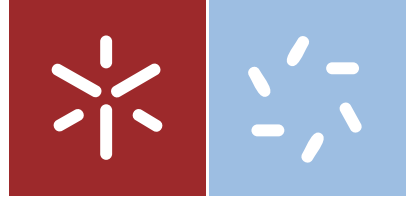

Universidade do Minho
Escola de Ciências

Weronika Wojtak

A novel dynamic field model supporting a continuum of bump amplitudes: Analysis and Applications

PhD Thesis in Applied Mathematics

Work supervised by
Professor Wolfram Erlhagen
Professor Estela Bicho

July, 2021

Acknowledgements

Many people have supported me throughout my Ph.D. journey, and I shall attempt to name a few of them here. First, I feel truly fortunate for the opportunity to have worked under the guidance of my supervisors, Estela Bicho and Wolfram Erlhagen, to whom I am most grateful. I thank Wolfram for the endless patience he showed when supervising my work and allowing me the freedom to pursue my own ideas. I remain indebted to Estela for her support and encouragement and having my back during all those moments of need. I cannot imagine two supervisors who cared more for their students, both as scientists and human beings.

I would like to express my gratitude to Stephen Coombes for the opportunity to work on a project that motivated me to study mathematics and eventually inspired the work described in this thesis. I also thank Daniele Avitabile for his help with the numerical continuation method.

I thank my colleagues from the MAR Laboratory at the University of Minho, all of whom I met over the last few years. While I cannot list all their names here, every single person there contributed to my work in one way or another, and for that, I am beyond grateful. I also extend special thanks to Flora Ferreira for all her help with my work on the neural field models and with many other things.

Most of the people whom I would like to acknowledge contributed to my work in less direct ways. A huge thank you to my friends Karolina, Sara, Ana Luisa, César, and Hélder for making good times great and bad times less horrible. I thank Patrícia and Liliana for making me feel like part of their family and never ceasing to entertain me. I am grateful to Soraya for her friendship, to Jelle for the beers, and to Ben for good (and bad) jokes. I thank Paweł for his encouragement to start this Ph.D. and his moral support to finish it. Finally, I thank my mother and sister for putting up with me and standing behind me every step of the way during my academic journey.

The work received financial support from FCT through the Ph.D. fellowship PD/BD/128183/2016.

STATEMENT OF INTEGRITY

I hereby declare having conducted this academic work with integrity. I confirm that I have not used plagiarism or any form of undue use of information or falsification of results along the process leading to its elaboration.

I further declare that I have fully acknowledged the Code of Ethical Conduct of the Universidade do Minho.

Resumo

Um novo modelo de campos dinâmicos neuronais que suporta padrões de atividade estáveis com um contínuo de valores de amplitude: Análise e Aplicações

Esta tese introduz um novo modelo de campos dinâmicos neuronais (DNFs) capaz de representar e memorizar integralmente todas as entradas externas de uma forma robusta. DNFs, expressas como equações integro-diferenciais, têm sido utilizados desde 1950 para descrever a atividade de populações neuronais de grande escala no córtex, sendo o modelo introduzido por Amari na década de 1970 o mais utilizado. Ao acoplar dois campos do tipo Amari, construímos um modelo que permite a integração temporal contínua das entradas externas. O novo modelo supera a insuficiência das equações clássicas de DNFs, cujas soluções, inicialmente desencadeadas por entradas externas, não preservam quaisquer características das entradas. Primeiramente, foram analisadas rigorosamente as soluções de uma e de múltiplas regiões localmente excitadas tanto do modelo de Amari como do novo modelo em uma e duas dimensões espaciais, utilizando análise de estabilidade linear e técnicas de continuação numérica. Em aplicações de neurociência cognitiva, comparamos a formação de soluções orientadas por entrada externa em ambos os modelos, utilizando simulações numéricas de tarefas de memória de múltiplos itens. Um foco específico é a aprendizagem neuro-plausível e a reprodução de intervalos de tempo utilizando o integrador neuronal. DNFs têm sido amplamente aplicados na robótica com o objectivo de dotar os robôs com capacidades cognitivas. Os dois últimos capítulos são dedicados a aplicações da robótica industrial. A primeira experiência envolve uma tarefa cooperativa em que o robô aprende a ordem de entrega de diferentes objetos a um operador. O segundo exemplo é uma tarefa de pesquisa de objetos em que o robô tem de tomar decisões sob incerteza, com base em provas acumuladas de ensaios anteriores.

Palavras-chave: campos dinâmicos neuronais, continuação numérica, integrador neuronal, memória de trabalho, robótica cognitiva

Abstract

A novel dynamic field model supporting a continuum of bump amplitudes: Analysis and Applications

This thesis introduces a novel dynamic neural field model capable of representing and memorizing the integral of previous inputs in a robust way. Neural field models have been used since the 1950s to describe the activity of large-scale neuronal populations in the cortex. They are typically cast as integro-differential equations, with one of the most commonly used formulation being the model introduced by Amari in the 1970s. By coupling two fields of Amari type, we construct a model that provides a continuous attractor to perform temporal integration of inputs. The new model overcomes the shortcoming of classical neural field equations, whose solutions, initially triggered by external inputs, do not preserve input characteristics like for example intensity or duration. In the first part of this thesis, we rigorously analyze single and multi-bump solutions of both the Amari model and the new two-field model in one and two spatial dimensions, using linear stability analysis and numerical continuation techniques. In cognitive neuroscience applications, we systematically compare the formation of input-driven solutions in both models using numerical simulations of multi-item memory tasks. A specific focus is on the neuro-plausible learning and reproduction of time intervals using the neural integrator. Dynamic neural field models have been also extensively applied in the domain of robotics, with the goal to endow autonomous robots with cognitive abilities. The last two chapters are devoted to real-world robotics applications in modern manufacturing environments. The first experiment is a human-robot cooperation in an assembly task in which the robot learns the serial order of handing over different objects to a human operator. The second example is an object search task in which the autonomous robot has to make trial-by-trial decisions under uncertainty based on accumulated evidence from previous trials.

Keywords: cognitive robotics, dynamic neural field, neural integrator, numerical continuation, working memory

Contents

List of Figures

List of Tables

1 Introduction and outline

Dynamic neural fields models describe the mean firing activity in large neuronal populations within the cortex. They are formalized as nonlinear integro-differential equations, describing the evolution of neuronal activity in terms of time, and one or two spatial dimensions. Developed already in the 1970s to study pattern formation in neural tissue, the model family is still very popular in theoretical neuroscience since the mathematical formulations are simple enough to support analytical treatment. At the same time, neural field models have been used in the past to explain key aspects of neural population dynamics as observed in various neurophysiological studies.

A particularly successful formulation of a neural field was provided by Amari in 1977. He studied the existence and stability of spatially localized activity patterns, or bumps, that emerge in response to sufficiently strong external input applied to the neurons in the field. A bump persists after the transient input is no longer present due to strong recurrent excitation and inhibition within the neural network. Since bumps are input specific, they have been frequently used to model the neural mechanisms supporting a working memory function.

A known shortcoming of classical neural field models, like for instance Amari's formulation, is their inability to represent input features such as strength and duration in the self-sustained activity pattern. The unique bump shape is exclusively determined by the parameters of the spatial interactions within the neural population.

The focus of this thesis is to address this issue by developing, analyzing and applying a novel neural field model supporting the existence of bumps with a continuum of amplitudes and shapes. These attractor states can be used for instance to explain the neural integration of external inputs of any strength and duration.

The remainder of this thesis is structured as follows.

Chapter 2 provides a general introduction to the neural field models. We begin with a short historical overview of the neuronal modeling describing the activity of the brain on different spatial scales, from single cells to the whole cortex. We then discuss two of the most commonly used neural field models, namely the Wilson and Cowan model and the Amari model. We introduce the reader to the concept of working memory and explain how the neural activity that is believed to underpin this process is modeled using so-called bump attractors. The chapter ends with some general remarks on neural field models.

Chapter 3 introduces the Dynamic Field Theory (DFT), a biologically inspired theoretical framework used for modeling neuronal processes that account for a large number of behaviors and cognitive capacities. We discuss some differences between this framework and the neural field models presented in the previous chapter. DFT has been extensively used in the domain of cognitive robotics, since it provide means for endowing autonomous robots with high-level cognitive functions. We review the DFT approach to robotics and explain how neural fields are used to build complex control architectures. Finally, we discuss some of the shortcomings of the classical models that motivated the need for a new type of neural field model introduced in this thesis.

Chapter 4 Motivated by the shortcomings of the classical neural field models, we introduce our new model that is constructed by coupling together two equations of Amari type. We explain in detail the derivation of the novel model and analyze solutions of a space-clamed version of the model.

Chapter 5 We analyze the existence and stability of stationary bump solutions of the Amari model. To this end we employ three different approaches: Amari's linear stability analysis, a Lyapunov method for the one-dimensional model, and Pinto's and Ermentrout's stability analysis for one and two spatial dimensions.

Chapter 6 We apply the three stability analysis methods to the new two-field model introduced in Chapter 4. We conclude that all three approaches yield qualitatively similar results for both model classes.

Chapter 7 The focus is on the numerical analysis of single- and multi-bump solutions of both the Amari model and the two-field model. In particular, we employ numerical continuation techniques to find localized solutions in both models, determine their stability and follow them as the model parameters vary.

We begin with an overview of the pseudo-arclength continuation method and present the problem setting. Using a classical Mexican hat connectivity function, we find some interesting differences between the two models and explain how the initial conditions affect the pattern formation process. We then investigate the bifurcation structure in the models when an oscillatory interaction kernel is used, and find that in this case both models support the existence of multi-bump solutions. It is further shown that the so-called snaking phenomenon occurs in both models. We also discuss how the obtained results relate to those described in the previous chapter.

Chapter 8 is concerned with input-induced multi-bump solutions and their application to working memory modeling. The necessary conditions for the existence and stability of multi-bump solutions of the two-field model are given in the beginning of the chapter. We then systematically compare the pattern formation process in the Amari model and the two-field model in tasks with multiple memory items. We investigate how input-induced variations of the memory strength affect the inference of nearby memory traces and their spatial drift in response to random activity fluctuations.

Chapter 9 introduces an application of the two-field model for measuring and reproducing time intervals. We begin with introducing an interval reproduction task in which monkeys learn to measure and subsequently reproduce temporal intervals. Inspired by this experiment, we test in a series of numerical simulations the ability of the new model to accumulate external input over time during the measurement phase of the task. During the interval production phase, the stored information is used to reproduce the time interval either by adjusting input strength or initial condition of the neural integrator. Finally, we discuss the impact of the result on our goal to endow robots with advanced temporal cognition capacities.

Chapter 10 presents a dynamic neural field (DNF) model for sequence learning and planning of a robotics assistant. We test the DNF architecture in an assembly task in which a robot learns rapidly by observation the sequential order of object transfers between an assistant and an operator to subsequently substitute the assistant in the joint task. The results show that the robot is able to proactively plan the series of handovers in the correct order.

Chapter 11 introduces a DNF model of value-based decision making of an autonomous robot in a simulated factory environment. We test the model in the scenario in which a mobile robot searches at two different workbenches a specific object to deliver it to an operator. We show that the robot achieves a high

search efficiency in stationary as well as dynamic environments based on the accumulated evidence from previous trials.

Chapter 12 The final chapter summarizes the contribution of the work presented in this thesis and discusses possible directions for future research.

Appendix A discusses the methods used for numerical simulations and provides some examples of source codes implemented in MATLAB and Julia.

Appendix B gives initial conditions and parameters used in Chapters 10 and 11.

2 Neural field modeling

2.1 From models of a single neuron to population modeling

Ever since the pioneering work of the neuroanatomist Santiago Ramón y Cajal in the late nineteenth century it is known that the fundamental units comprising the human brain are neurons [122]. His observations resulted in hundreds of drawings illustrating neuronal cells in cortical tissue, one of which we show in Figure 1. This drawing gives only a glimpse of the enormous number of neurons in the cortex and complexity of connections between them. The human brain is estimated to contain 86 billion neurons and a similar

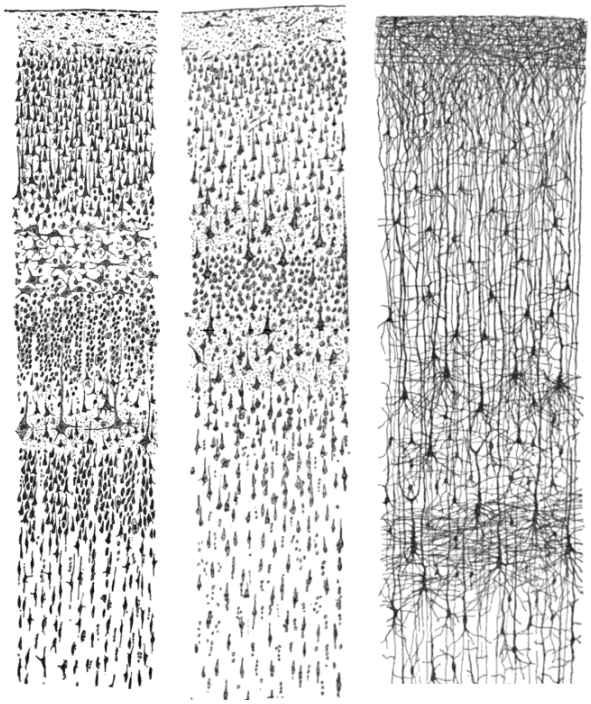

Figure 1: The reproduction of a drawing by Santiago Ramón y Cajal from *Comparative study of the sensory areas of the human cortex* (1899) showing neurons in the human cortex that he observed under the microscope.

number of non-neuronal glia cells [10]. Neurons consist of three functionally distinct parts: the cell body, or soma, the dendrites and the axon. Dendrites collect input signals from other neurons and pass them to the cell body. The collected signals are integrated in the cell body, and if the total arriving input exceeds a certain threshold, then neuron generates an output signal. This output signal, referred to as an action potential, or a spike, is a short burst of electrical activity that is transmitted through the axon to other neurons. The junction between the axon of one neuron and the dendrite of another neuron is called the *synapse*. The neuron sending the signal is referred to as the *presynaptic* cell and the receiving neuron as the *postsynaptic* cell. A schematic of a neuron is shown in Figure 2a.

Mathematical modeling of neural processes is one of the approaches toward advancing our understanding of how the brain works. The first model of neuronal activity was perhaps the model of frog nerve stimulation proposed by Lapicque in 1907 [102]. The model was phenomenological in nature, i.e. it did not aim to capture the details of neuron's electrophysiology. It has been a starting point for developing a class of integrate-and-fire models, that are still widely used today (see [26] for a recent review).

For modeling the behavior of a single neuron perhaps the most iconic work is due to Hodgkin and Huxley in the early 1950's. They performed a series of experiments on the giant axon of the squid, and used the results to develop a model describing the generation and propagation of action potentials [77]. Action potentials are the result of currents passing through the ion channels, that Hodgkin and Huxley measured and described their dynamics in terms of differential equations. This work paved the way to the formulation of more detailed biophysical neuron models (see [128]) and led to the Nobel Prize for Hodgkin and Huxley in 1963. Some other canonical models of a single neuron include the FitzHugh-Nagumo model [59, 117], the Morris-Lecar model [116], and the quadratic integrate-and-fire model [103], to name only a few examples.

Models of neuronal activity may concern structures on different spatial scales (see Figure 2b). Examples that we briefly described above concern the *microscopic* scale, that includes modeling single cells or subcellular structures. When the population comprising large number of neurons with similar properties is considered, we speak of *mesoscopic* spatial scale. At this scale it is assumed that the behavior of each individual cell is irrelevant and the focus is on the collective dynamics of entire population. This approach is known as *neural mass modeling*, i.e., describing large number of cells by low-dimensional models, usually using systems of ordinary differential equations (ODEs). The neural mass models considered in the literature are typically variants of the Wilson-Cowan model [166] introduced to study temporal evolution

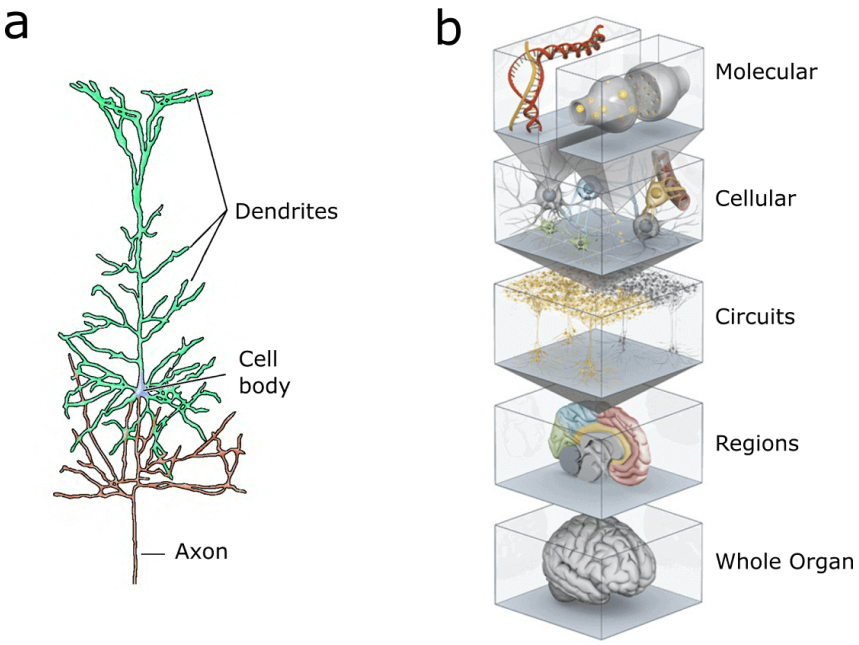

Figure 2: (**a**) Schematic of a neuron illustrating its three main components: the dendrites, the cell body and the axon. From [122], pp. 3, Fig. 1.2E. (**b**) Different spatial scales in neuronal modeling. From *Scientific American*, vol. 306, no. 6, pp. 54.

of mean firing rates of interacting excitatory and inhibitory populations of neurons[1]. Similar to first models of single neurons, this is a phenomenological model, i.e. it only describes the firing rates, and does not account for the biophysical details of neural firing. Neural mass models that include more realistic aspects of interacting neural populations have been successfully used to explain neuroimaging data. One example of such approach is the work of Jansen and Rit, who considered strengths of intra-population connections taking into account the anatomy of the cortex and used the resulting model to investigate epileptic seizures [82].

Average mean activity of neuronal populations in neural mass models is studied as a function of time only. When the spatial component is taken into account and it is continuous, we speak of *neural field models*. These models are usually cast as nonlocal differential equations and are used to model neural activity at the *macroscopic* scale. Neural fields are the focus of this Thesis and in what follows we provide the historical overview of neural field theories.

The first neural field theory dates back to the 1950's and the work of Beurle [14]. His formulation accounted for a continuum approximation of the network of purely excitatory cells and was capable of supporting

[1]The Wilson-Cowan neural field model that we discuss later is a spatial extension of this local neural mass model, although Wilson and Cowan did not use the term *neural mass* explicitly.

various forms of activity with spatial and temporal organization, including plane waves, spherical and circular waves and vortices. The activity patterns in Beurle's model were shown to be unstable, meaning that as a consequence of any deviation form the equilibrium the activity either dies out or saturates. Stabilizing brain activity can be achieved by incorporating inhibition in the model, which was later done by Griffith [69]. This approach did not prove successful, mainly because it did not account for excitatory and inhibitory synaptic connections explicitly. The formulation of neural field models that is commonly used today is due to work of Wilson and Cowan in the 1970's. They proposed a model with two inter- and self-connected layers of excitatory and inhibitory neurons which is considered a cornerstone of neural field models that are in use today. We discuss the iconic work of Wilson and Cowan below.

2.2 Wilson-Cowan model

The Wilson-Cowan model was first introduced in network (or space-clamped) form in [166], followed by a spatially extended (or continuum) version of the model in [167]. The latter can be written as a pair of partial integro-differential equations

$$\tau_E \frac{\partial u_E(x,t)}{\partial t} = -u_E(x,t) + f_E\left(\int_{\mathbb{R}} w_{EE}(x-y)u_E(y,t)\mathrm{d}y - \int_{\mathbb{R}} w_{IE}(x-y)u_I(y,t)\mathrm{d}y + I_E(x,t)\right), \tag{2.1a}$$

$$\tau_I \frac{\partial u_I(x,t)}{\partial t} = -u_I(x,t) + f_I\left(\int_{\mathbb{R}} w_{EI}(x-y)u_E(y,t)\mathrm{d}y - \int_{\mathbb{R}} w_{II}(x-y)u_I(y,t)\mathrm{d}y + I_I(x,t)\right). \tag{2.1b}$$

This two-layer model describes the activity of excitatory and inhibitory populations of neurons coupled together. We now discuss the various terms that appear in (2.1).

The variables $u_E(x,t)$ and $u_I(x,t)$ describe the spatial and temporal evolution of mean level of activity of interacting excitatory and inhibitory populations. The temporal scale of the dynamics of each population is determined by time constants $\tau_{E,I}$. Functions $f_{E,I}$ are nonlinear activation functions, in [167] taken as sigmoids bounded to values between 0 and 1

$$f_i(x) = 1/[1 + e^{-\beta_i(x-\theta_i)}], \qquad i = E, I, \tag{2.2}$$

where the steepness β_i and threshold θ_i depend on the population type $i = E, I$.

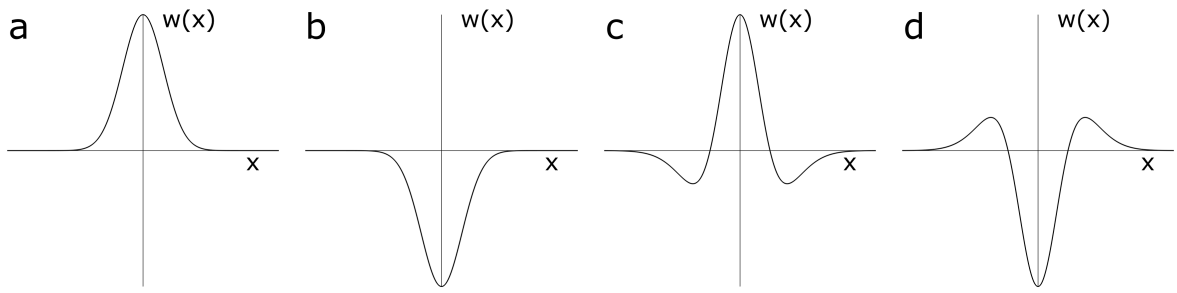

Figure 3: Examples of connectivity functions $w(x)$ given by (2.3) are shown. The interactions can be classified into four types: purely excitatory (**a**); purely inhibitory (**b**); "lateral-inhibition" or "Mexican hat" (**c**); "lateral excitation" or "inverted Mexican hat" (**d**).

The connectivity strength from population $a = E, I$ to population $b = E, I$ is given by $w_{ab}(x - y)$. It depends only on the distance between neurons x and y and not on their position, i.e. it is translationally invariant. This function is typically either Gaussian or exponential. Its usual form is given by

$$w(x) = A_1 e^{-(x/\sigma_1)^2} - A_2 e^{-(x/\sigma_2)^2}, \tag{2.3}$$

where all parameters are non-negative.

The interactions given by (2.3) can be classified into four types [51]:

(a) excitatory, when $A_2 = 0$;

(b) inhibitory, when $A_1 = 0$;

(c) lateral-inhibitory, when $\sigma_2 > \sigma_1$ and $A_1 > A_2$;

(d) lateral-excitatory, when $\sigma_1 > \sigma_2$ and $A_2 > A_1$.

Examples of different connectivity types are given in Figure 3.

We note that the original Wilson-Cowan model includes refractoriness modeled by multiplying the firing rates by

$$1 - r_i u_i(x, t), \qquad i = E, I, \tag{2.4}$$

where r_i is proportional to the refractory period of the population u_i. We omitted it here for simplicity since it usually does not appear in modern uses of the model. Moreover, it was observed that refractory terms effectively rescale the parameters of the nonlinearities $f_{E,I}$ [120].

To simplify their model and gain insights about its solutions, Wilson and Cowan employed a technique known as *time coarse graining* that was first used to study some problems of statistical physics. In the

space-clamped model [166], it was applied by replacing the time integrals present in the equations by their temporal averages, i.e., coarse-grained variables. This allowed Wilson and Cowan to perform the phase plane analysis to determine the stability of fixed points of the neuronal dynamics. They observed multiple stable fixed points, hysteresis loops and limit cycles in their model and concluded that upon choosing physiologically reasonable values of the parameters, the temporally coarse-grained equations are valid [166].

Time coarse graining was used also in the spatially extended model [167] and yielded a system (2.1). Wilson and Cowan found numerically that depending on the values of model parameters, there exist three categories of solutions: active transients, spatially localised limit cycles, and spatial patterns that reflect some properties of prior stimuli. It was postulated that each type of solution corresponds to a distinct type of neural tissue present in different areas of the brain [167]. Among these solutions, the spatial patterns, or steady states, are the most important for this Thesis. Spatially inhomogeneous steady states are peaks of elevated activity first generated by prior stimulus pattern and then sustained by recurrent interactions until removed by a sufficiently strong inhibitory input [167]. They are believed to be the analogue of *short-term memory*, i.e. memory holding task relevant information on the time scale of seconds, as shown in studies with primates [62, 167]. Apart from modeling the memory function, the Wilson-Cowan model has been applied to address a number of problems in computational neuroscience and has been extended in many ways since its introduction in the 1970's. For a recent review we refer the reader to [32, 40, 86].

2.3 Amari model

The next milestone for neural field theory was the seminal work of Amari [3]. He proposed a model in which interacting excitatory and inhibitory neurons are mixed in a single population. The reduced dimensionality of the resulting model allowed him for more rigorous analysis of the steady state solutions. In what follows we show how the Amari model can be derived from the Wilson-Cowan equations.

Under some assumptions the excitatory and inhibitory populations of system (2.1) can be lumped together into a single equation. In particular we assume that inhibition is faster than excitation (i.e., $\tau_I \ll \tau_E$), f_I is linear (i.e., $f_I(u) = u$), and that the recurrent inhibition w_{II} is neglected (i.e., $w_{II} = 0$) (see e.g. [51] and Chapter 12 of [53]).

We begin by setting $\tau_I = 0$, thus the activity $u_I(x,t)$ is stationary at the time scale of the excitation τ_E.

We solve (2.1b) for $u_I(x,t)$

$$u_I(x,t) = \int_{\mathbb{R}} w_{IE}(x-y)u_E(y,t)\mathrm{d}y + I_I(x,t). \tag{2.5}$$

After substituting (2.5) into (2.1a) and dropping subscripts we obtain the single population model

$$\tau\frac{\partial u(x,t)}{\partial t} = -u(x,t) + f\left(\int_{\mathbb{R}} w(x-y)u(y,t)\mathrm{d}y + I(x,t)\right), \tag{2.6}$$

where $w(x-y) = w(x,y)$ represents a mixture of the excitatory and inhibitory interactions

$$w(x-y) = w_{EE}(x) - \int_{\mathbb{R}} w_{EI}(x-y)w_{IE}(y)\mathrm{d}y, \tag{2.7}$$

and the input $I(x,t)$ is given by

$$I(x,t) = I_E(x,t) - \int_{\mathbb{R}} w_{EI}(x-y)I_I(y,y)\mathrm{d}y. \tag{2.8}$$

When the nonlinearity in 2.6 is placed inside the convolution term, we obtain the Amari equation from his seminal paper [3]

$$\tau\frac{\partial u(x,t)}{\partial t} = -u(x,t) + \int_{\mathbb{R}} w(x-y)f(u(y,t))\mathrm{d}y + I(x,t) + h, \tag{2.9}$$

where we have included a constant external input h whose role we describe below.

We note that the formulations (2.6) and (2.9) are identical in the mathematical sense since they both support the existence of the stationary activity patterns that we consider in this thesis. Equation (2.6) is referred to as an activity-based model with $u(x,t)$ representing the neural firing rate, whereas (2.9) is a voltage-based model, with $u(x,t)$ representing the membrane potential.

For his model, Amari assumed that the firing rate function is a Heaviside function, i.e., it is effectively a sigmoid function (2.2) in the limit $\beta \longrightarrow \infty$ that can be written as

$$f(u) = H(u) = \begin{cases} 0 & \text{if} \quad u \leq \theta, \\ 1 & \text{otherwise}, \end{cases} \tag{2.10}$$

where θ is the firing threshold. Amari set θ to zero and then added a spatially homogeneous (usually negative) input h to the field to adjust the bias. This is equivalent to setting input h to zero and having the threshold θ as a parameter [3, 51]. The choice of the Heaviside firing rate function greatly facilitates the mathematical analysis of solutions of the model (but see Kishimito and Amari [89] for a generalization of results to the case of a sigmoid nonlinearity). It allowed Amari to construct explicit solutions and apply linear stability analysis to his model. We discuss Amari's approach in more detail in Chapter 5.

Amari also assumes that the connectivity function $w(x)$ is of lateral inhibition type (see Fig. 3c). Connectivity that takes both positive and negative values is crucial for a field comprising a single population of both excitatory and inhibitory neurons. Although the single population model integrating both types of neurons is less realistic in the biological sense, it has the advantage of mathematical tractability [51].
In the absence of inhomogeneous input $I(x,t)$, Amari found in his model four different types of equilibrium solutions:

(i) $\emptyset$-solution in which no region is excited, i.e. $u \leq 0$ for all x;

(ii) ∞-solution in which the whole region is excited, i.e. $u > 0$ for all x;

(iii) a-solution, or localized excitation, in which the excited region is a finite interval of length a;

(iv) (a,b)-solution which is $b-$periodic with an excited region of length a.

In [3] Amari proves the existence and stability of the four types of solutions. He showed that the type of solutions that the field dynamics supports depends on the connectivity strength described by $w(x,y)$ and the homogeneous input $h < 0$. The first two types of solutions are trivial. Among the remaining types, localized, stable activity patterns also known as "activity bumps" have attracted most attention since they are thought to represent a neural correlate of a memory function, as we already mentioned while discussing Wilson-Cowan model. We discuss bumps and their application to the modeling of working memory in more detail in the next section and devote Chapter 5 to their analysis. Other applications of Amari type neural fields where bump solutions play a central role include the modeling of orientation tuning in the primary visual cortex [23, 73], head-direction cells in rats [175], and robot navigation [20], to mention but a few examples. Periodic solutions of (2.9) received by far less attention in the literature, however see [94].

2.4 Bumps and working memory

The concept of working memory (WM) refers to the short-term maintenance and manipulation of sensory information on the timescale of seconds that is considered crucial for execution of many cognitive tasks [11]. The neural processes underpinning working memory are typically studied in non-human primates during delayed response tasks [62]. Those experiments suggest that a neural correlate of WM is persistent neural activity that is sustained in the brain in the absence of inputs from the external world. This kind of input-specific persistent activity has been observed in prefrontal cortex (PFC) and other cortical areas

such as the posterior parietal cortex and the inferotemporal cortex [63, 130]. Two types of encoding continuous-valued information in self-sustained activity can be distinguished [160]:

- **Spatial working memory** is based on a position code. It is studied for instance in delayed oculomotor tasks, in which a saccadic eye movement of a subject is guided by the memorized spatial position of a visual cue [62]. During such tasks, neurons tuned to the continuous parameter stimulus position respond with persistent activity. The level of activity reflects the similarity between their preferred "position" and the external input. When the neurons are ordered along a line by their preferred position, the self-sustained neural population activity is visualized as a spatially localized activity bump. The peak position of this bump thus encodes the specific value of the external cue [3, 25].

- **Parametric working memory** is based on a rate code. It has been studied for instance in delayed somatosensory discimination tasks, in which the encoded analog quantity is stimulus frequency [130]. The experiments revealed persistent neural activity which varies monotonically with stimulus frequency. A specific frequency is thus encoded by the firing rate and not by the position of a bump in parametric space as in spatial WM.

A possible mechanism for self-sustained neuronal activity is synaptic reverberation, i.e., circulation of excitation and inhibition in a recurrently connected neural network [74]. The idea is that the network connectivity is such that the activity triggered by external inputs evolves toward some privileged activity states that are stable in time, referred to as *attractor states* [177]. A particularly insightful theoretical framework, which has been frequently used in the past to explain experimental data, is the continuous bump attractor network [3, 25, 33]. Typically, the recurrent interactions within the network are organized in a way that neurons encoding similar values of the continuous variable excite each other, whereas cells encoding dissimilar values inhibit each other. Due to the assumed spatial symmetry of the connectivity function, bumps are neutrally stable [3]. They can be located at any position along a continuum of parameter values.

Direct experimental evidence supporting the bump attractor hypothesis comes from studies on the monkey prefrontal cortex during WM tasks [168]. In the frequently used oculomotor paradigm an animal is required to remember the spatial location of one or more briefly presented visual stimuli. Several seconds after stimulus offset the monkey has to execute a saccade toward the remembered location. At the beginning of maintenance period, neurons tuned to the spatial cue evolve a bump of elevated activity. The observed diffusive drift in the bump position during the maintenance period correlates with spatial

errors of the saccadic eye movements. Continuous attractor networks explain this loss of memory precision over time by assuming that sources of additive noise cause bump drift [168].

Despite their success in many applications, the explanatory power of classical bump attractor networks is still limited since the bump shape is exclusively determined by the recurrent interactions. A more sophisticated circuit-based model should regulate the rate of persistent activity depending on the qualitative and quantitative characteristic of the preceding inputs. It has been shown for instance that the level of persistent activity during the delay period of a spatial WM task correlates with stimulus contrast [34]. The internal memory representation can also be modulated by additional spatially informative cues [96, 164]. Moreover, there is recent experimental evidence that input-specific persistent activity is not static but may systematically change (e.g., ramp up) during the delay period [25]. Several cellular and network mechanisms have been proposed that are able to stabilize graded levels of population activity, based on intracellular or network-level computations, which in general proved to be a nontrivial problem [134].

A recent neural field model proposed by Carroll and colleagues suppports a continuum of bump amplitudes [30]. It consists of separate excitatory and inhibitory populations that are intra- and interconnected with distance-dependent connectivity functions. However, the field model is structurally unstable since the network parameters and the nonlinear firing function (necessary of piecewise linear shape) must be tuned precisely (see also [92]). In particular, the recurrent excitation must be inversely proportional to the slope of the nonlinearity to show a monotonic dependency of the bump amplitude on input strength. Since any deviation from the fine tuning destroys the continuity of the attractor, the biological plausibility of the working memory model is limited. The novel dynamic field model presented and analyzed in this thesis supports a two-dimensional bump attractor, determined by a continuum of bump positions and bump amplitudes. Importantly, the attractor state is robust to changes in the nonlinearity and (mild) perturbations of the network structure.

2.5 General remarks on neural field models

We first make some comments on the domain of integration, or spatial extend, (called Ω henceforth) of the neural field equations. So far we considered models defined on the real line, i.e. on a one-dimensional infinite domain. Modeling the activity of a finite number of neurons using an integro-differential equation defined on an infinite domain at first may not seem biologically plausible. However, given that there are approximately 86 billion neurons in the human brain, the continuum limit of the dense neural network

seems to be justified. Usually the spatial extend of a neural field is taken as $\mathbb{R}^d$ or a subset of $\mathbb{R}^d$, $d = 1, 2, 3$. The majority of examples in the literature concerns one-dimensional models ($d = 1$). Taken as a model of pattern formation in cortical tissue, one-dimensional neural fields are relatively easy to study and provide insights that can be extended to higher-dimensional and more realistic models. Two-dimensional neural fields ($d = 2$) can be regarded as models of a piece of cortical tissue where its thickness is neglected. They are more biologically plausible compared to the one-dimensional case and provide richer dynamics, but at the expense of higher computational cost (see e.g. [24, 149]). Neuronal tissue with its thickness taken into account can be modeled using a three-dimensional field model ($d = 3$). Due to the high computational complexity of the three-dimensional convolution describing the spatial interactions, this case did not receive much attention so far.

The next natural consideration is the choice of boundary conditions, which is in particular important for numerical integration of neural field equations. Neural fields are primarily studied on either infinite or periodic domains. When approximating the infinite domain the boundaries of the domain are left "open". For studying spatially localized patterns, the domain should be large enough so that the spatial extend of the connectivity function is much smaller than the domain size. This ensures that the localized activity in the model is sufficiently far from the edges of the domain to prevent boundary effects that may affect the pattern formation process [51]. Another common approach is to use periodic boundary conditions (see e.g., [73, 175]).

We now discuss an important difference between the two neural field formulations given by (2.6) and (2.9), following the explanation in [51]. The model defined by (2.6) is usually referred to as an activity based model, whereas (2.9) is referred to as a voltage based model. The difference between the two forms lies in the biological interpretation of the variable $u(x, t)$ and the time constant τ. For the activity based model, it is assumed that the shape of the postsynaptic potential depends only on the nature of the presynaptic population that caused it. In this case, the variable $u(x, t)$ represents the *firing rate* and τ is called the *membrane time constant* of the model. The assumption for the voltage based model is that the postsynaptic potential has the same shape regardless of the presynaptic population that caused it and depends only on the postsynaptic cell. Here, $u(x, t)$ is referred to as the *synaptic drive* and τ is called the *synaptic time constant*. The choice of the formulation depends thus on the biological considerations for the model (see e.g., [120]). The two formulations are closely related and conversion between them can be made upon appropriate change of variables [51].

Finally, for completeness, we note that equations similar to (2.6) and (2.9) have been studied from a purely

mathematical perspective. They are of the Hammerstein type [72] and have been investigated recently in e.g., [5].

3 The dynamic neural field approach to robotics

3.1 The Dynamic Field Theory (DFT)

The Dynamic Field Theory (DFT) is a biologically-inspired modeling language that has been used to model neural processes that account for a vast number of behaviors and cognitive abilities [137]. This broad range of topics includes but is not limited to target selection of the saccadic system [91], the planning of reaching movements [12, 50], the perception of motion [81] and the synthesis of cognitive behaviors such as memory, learning or decision making in autonomous robots [21, 139].

As basic building blocks, DFT uses dynamic neural fields (DNFs) introduced in Chapter 2 [3, 166, 167]. The particular mathematical form typically employed is Amari's formulation given by (2.9) since it allows analytical treatment [3]. Different to the classical models that were applied to explain neural pattern formation on the cortical surface or in cortical areas, the fields in DFT applications are defined over continuous metric dimensions relative to which information is being represented such as space, orientation, color or other stimulus features. Activation bumps are the elementary units of representation in the DFT framework. They encode the memory of a specific value along the metric dimension. From a dynamical systems point of view bumps represent fixed point attractors.

DFT models typically consists of several coupled neural fields. They describe how external inputs (e.g., form sensory systems) drive the activation in the distributed neural network in order to generate sensory-motor behaviors. The activation patterns described by means of DFT in general do not correspond to the total activation of a given neural population but rather represent a projection of the neural activity into a lower-dimensional parametric space relevant to a given task [47, 137, 138].

3.2 DFT and robotics

In the area of robotics, the DFT approach has been first used to design autonomous robot architectures for navigation tasks. This allowed for endowing the so-called attractor dynamics approach with memory and decision making functionalities [21, 139]. Using DFT-based control architectures proved successful in addressing two serious shortcomings in robotics research [46]. First, the absence of knowledge representations in robotic systems was hindering the progress toward endowing the robots with cognitive abilities. Second, there was a need for general architectures for system integration that can be analyzed theoretically [46].

The DFT framework has been also employed for developing control architectures for human-robot interaction tasks. It provided means for endowing robots with high-level cognitive functions such as action understanding, decision making and memory [48, 49]. The DFT-based architectures are organized as large scale networks of interconnected neural fields that encode task-specific knowledge in their activation patterns. We show in Fig. 4 an example of such multi-layered architecture for decision making in human-robot joint action [16]. Each individual field is modeled using variants of Amari's equation. In this formulation, the stability of attractor solutions depends on the model parametrization and the current inputs [3]. In general, the stability of each part of a complex dynamical system does not ensure the stability of the system as a whole. However, if the coupling strength is weak, meaning that the external inputs to a field site are weak compared to the inputs mediated by the recurrent interactions within the field, the existence and stability of the desired attractor states can be guaranteed. The design of large scale architectures of coupled fields is thus possible [138].

3.3 Building complex architectures with DNFs

3.3.1 Attractor states in DNFs

The state of the field dynamics is determined by two factors, the strenght of neural connections and external inputs. In the absence of inputs, the field converges to the *resting state*, assumed by convention as a negative value, i.e., $u(x) = -h$. When localized input $I(x)$ is applied to the field, there are two possible scenarios, depending on the input strength. In the case of weak input, that is not strong enough to bring the field activity above the firing threshold, the field operates in the *input driven regime*. The integral term in the field equation (2.9) vanishes, i.e., $u(x) = I(x) - h$, and the field dynamics simply reproduces

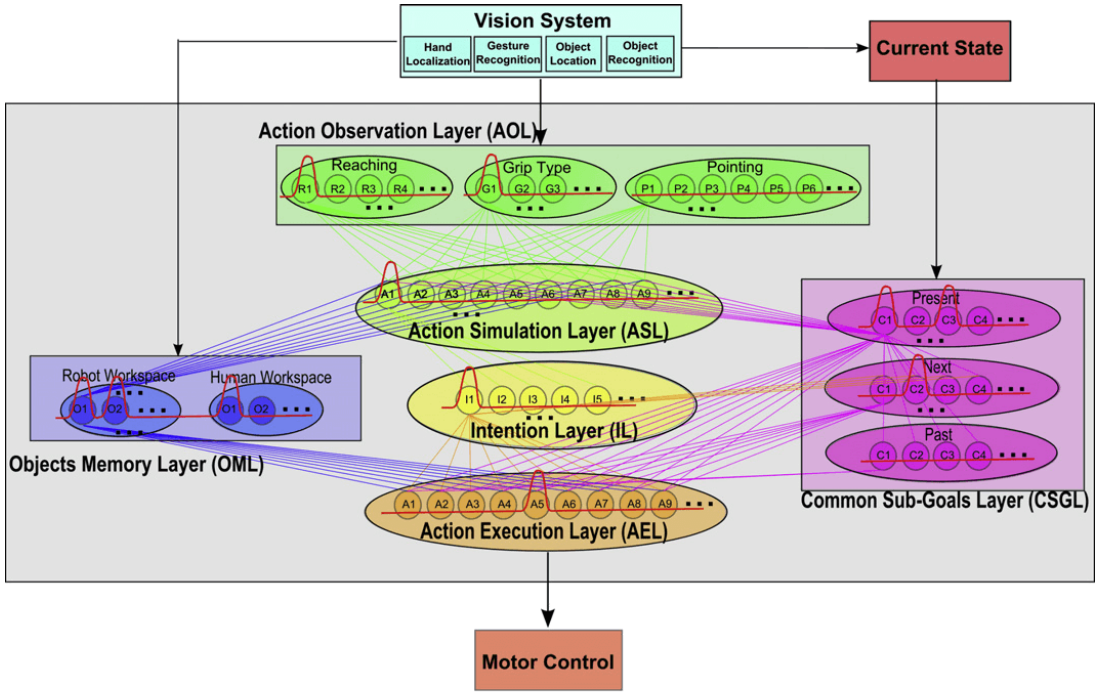

Figure 4: Multi-layered DFT architecture for human-robot joint action [16]. Each layer contains one or more neural populations encoding task specific information which are coupled to neural populations in other layers.

the input pattern. When the input is strong enough to bring the field activity locally above the threshold, the field generates a localized activation pattern. The lateral interactions begin to take effect, with short-range excitation amplifying the field response at stimulated sites, and long-range inhibition suppressing field locations outside the area with suprathreshold activity. This activity pattern is however only transient in nature. When the input is removed, the field relaxes back to the resting state.

In a *self-sustaining state*, these patterns may persist in the field even in the absence of input. Under appropriate conditions on the connectivity function and the parameter h, the field dynamics is bistable, with a stable resting state coexisting with a stable, self-sustaining bump of activity. We illustrate this in Figure 5. The ability to switch between the two attractor states is crucial for building DNF models. The resting state is destabilized by a sufficiently strong input giving rise to a bump of activity that persists when the input is removed, which can be regarded as implementing a *memory* function. The stable bump may in turn be removed by a sufficiently strong negative input, that brings the field back to the stable resting state. This implements a *forgetting* mechanism in applications of the DFT approach.

So far we considered the case of a single localized external input. When multiple inputs are present, the response of the field depends on the choice of the connectivity function $w(x)$. Typical choices include

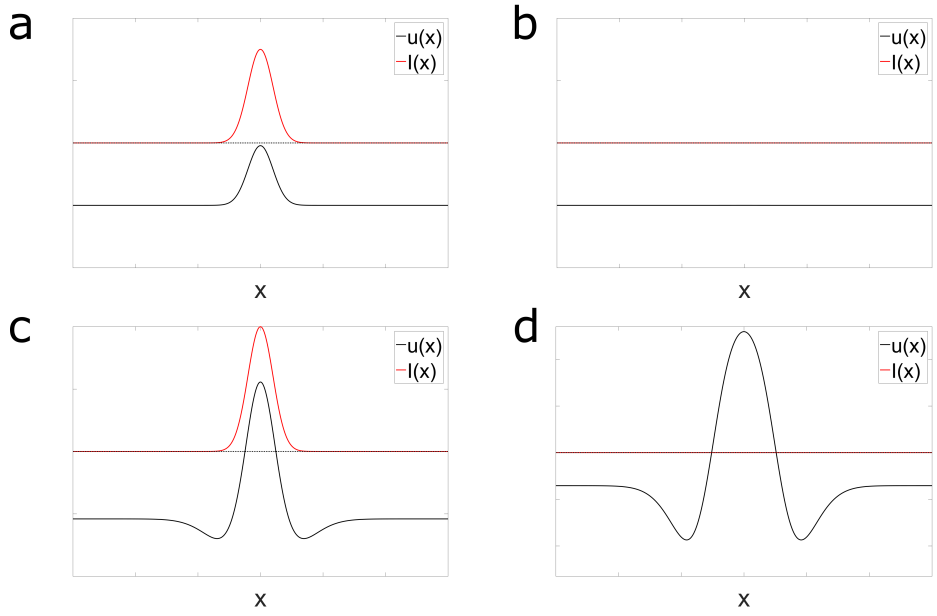

Figure 5: Switching between different attractor states in a neural field model. Weak transient input (**a**) doesn't bring the field activity above the threshold (dotted line), and when the input is removed, the field relaxes back to the resting state (**b**). Stronger input (**c**) brings the activity above the threshold and a self-sustained bump solution evolves (**d**).

a strong lateral inhibition component. The inhibition leads to suppression of activation at field sites that receive weaker input and as a consequence only one localized activity pattern persists in the field. We illustrate this in Figure 6. In DNF models, this competition is a basis of a *decision* process, since only the strongest of multiple inputs will trigger the evolution of a bump. Coupling functions of oscillatory type changes sign infinitely often, therefore regions of excitation exist also at larger distances and as a consequence more than one bump may persist in the field [98]. In this case, the field dynamics may develop several bumps in response to multiple inputs, providing a *multi-item memory* function.

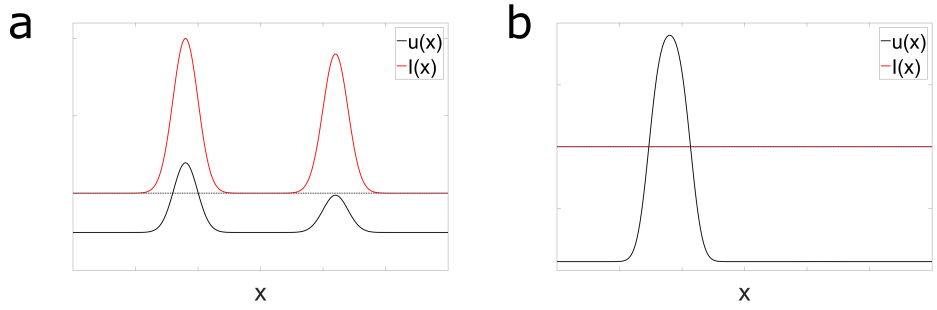

Figure 6: Decision process in a neural field model. When two inputs are presented in parallel (**a**), a bump solution evolves only at the location receiving the stronger input (**b**).

3.3.2 Coupling between DNFs

Complex DNF architectures capable of explaining and generating sensory-motor behaviors consist of multiple coupled fields. This coupling is implemented by using the activity of one field as an input to another field. Depending on the function of a specific coupling, there might be additional computations performed on this activity. It can be for instance first convolved with an additional kernel describing a specific interaction between the fields, or multiplied with the output of the step function acting on this activation to ensure that only suprathreshold activity is used as input. In Amari's field equation (2.9), the input term $I(x,t)$, represents the summed input at site x from external sources (e..g, sensors) and/or connected fields.

We now use a toy DNF model consisting of three coupled one-dimensional fields (Figure 7) to explain the idea of inter-field coupling that should facilitate the understanding of more complex DNF architectures that we introduce in later chapters. Imagine that the field on top, u_1, contains a stable activation pattern that was initially created with some input from sensors or another connected field.

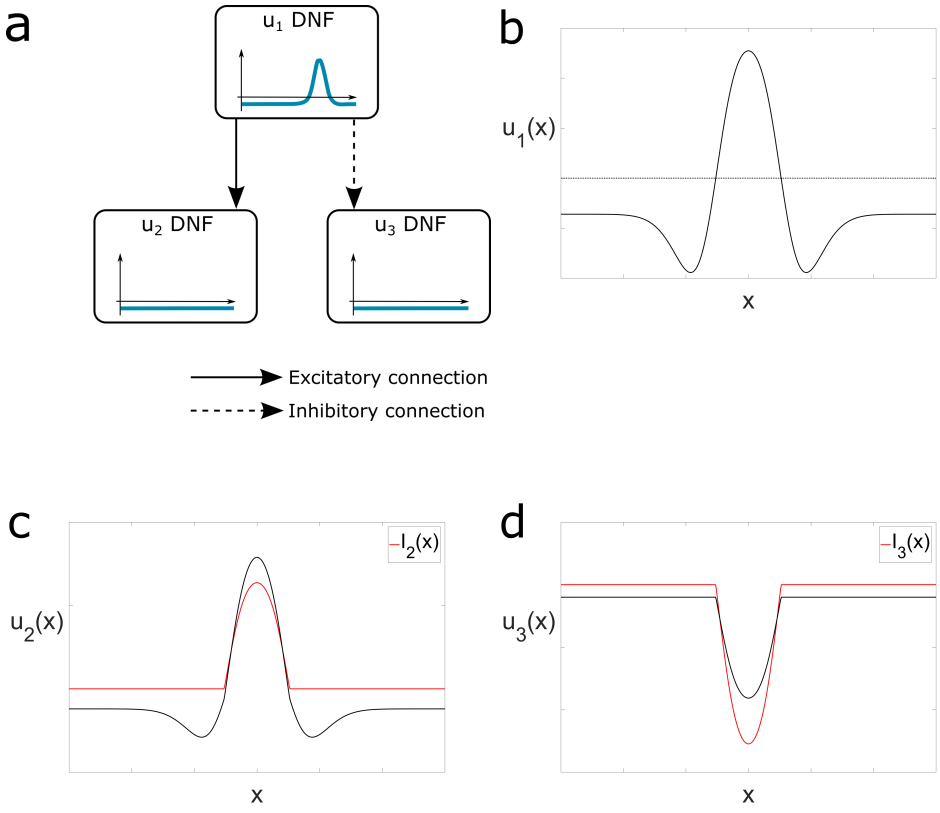

Figure 7: Toy DNF model. (**a**) Sketch of the model architecture containing three coupled neural fields, $u_{1,2,3}$. Dashed lines indicate inhibitory connections, solid lines excitatory connections. (**b**) Bump attractor, (**c,d**) activity patterns (black line) together with the localized input (red line). The dotted line in (**b**) indicates the threshold $\theta = 0$.

The two fields on bottom, u_2 and u_3, receive the activity of u_1 field as an input. Excitatory (inhibitory) connections are given by positive (negative) input. Figure 7c-d shows the activation pattern (black line) in the presence of the external input (red line). In this example only suprathreshold activity of u_1 should have an effect on the remaining fields, therefore we multiply u_1 with a nonlinear transfer function such as for instance the Heaviside step function with threshold $\theta = 0$. The excitatory or inhibitory inputs to the fields u_2 and u_3, respectively, are then given by $I_2(x) = \epsilon_2 u_1(x) f(u_1(x))$ and $I_3(x) = -\epsilon_3 u_1(x) f(u_1(x))$, where $\epsilon_2, \epsilon_3 > 0$ are scaling factors which guarantee that the field dynamics is not dominated by the external input. Note that the activity pattern in Fig. 7c would converge to the bump attractor when the additive input is switched off whereas the activity in Fig. 7d would converge to the stable resting state. Functionally, the suppression below resting state in the presence of the inhibitory input can be used for instance to guarantee that excitatory input from another field is not able to drive the evolution of a bump at this site.

3.4 Example of a complex architecture: DNF model of sequence learning

3.4.1 Sequence learning

The ability to encode, store and recall sequences of events is an essential component of intelligent behaviour. Almost all of our daily routine tasks are embedded in a sequential context. Fluent execution of sequential activities very often requires the information about both the ordinal and temporal sequence structure. Experimental evidence from physiological and behavioral studies suggests that the neural mechanisms underlying both ordinal and temporal structure of sequences are closely related, however, this is still a matter of considerable debate in the experimental literature (see e.g., [43, 152]).

One of the main theories for serial order is the ordinal theory [75]. According to this theory, sequence elements can be stored along a common dimension, and serial order is defined by the relative values of that dimension. In [70], the serial order is assumed to be stored in an activation gradient, where the representation of each item in the sequence is stronger than the subsequent one. The sequence retrieval is an iterative process of selecting the strongest element, which is then reset by feedback inhibition so that the next strongest element can be selected. This process continues until all elements of the sequence are retrieved. Due to the competitive read-out mechanism this theory is also referred to as competitive

queuing (CQ) [78]. For reviews of different serial order theories we refer the reader to e.g. [75, 79].

The DNF-based approach to learning joint order-timing representations of sequences belongs to the CQ model class. The main idea is that the serial order is encoded by means of multi-bump solutions forming an activation gradient, with the highest bump representing the first event, and the lowest bump the last one [56]. This is inspired by neurophysiological evidence showing that neuronal populations encoding different sequence elements appear to be activated in parallel at the beginning of sequence execution with a neural activation level representing the ordinal position [7]. The activation gradient in the neural field is achieved by combining the field dynamics with a state-dependent threshold accommodation dynamics for the firing rate function [36]. As a consequence, the strength of the population representation of each event is a function of elapsed time since sequence onset.

3.4.2 DNF model of learning joint order and timing representations

The DNF model introduced in [56] and extended in [57] consists of two parts: sequence learning and sequence recall (see Figure 8). This division corresponds to the two phases of the behavioral paradigm used for studying sequence learning [127]. The dimensions over which the fields are spanned are the dimensions guiding sequence learning. In the experiment described in [57], a robot learned by observing a teacher to first memorize and subsequently execute from memory a precisely timed musical sequence. The sequence of notes was coded using colored squares displayed on a computer screen, hence, the fields are spanned over the dimension color.

The goal of the sequence learning phase is to establish the activation gradient containing all elements of the observed sequence. The learned multi-bump pattern is stored in the sequence memory field u_{mem} and serves as a subthreshold input to the decision field u_{de}. The sequence recall phase starts with the increase of the baseline activity in u_{de} that brings the subthreshold activation pattern closer to the threshold. When the element with the highest activation reaches this threshold, a bump evolves, which corresponds to the recall of the specific element. In the robotics experiment, the time of crossing the threshold starts the behavior, that is, the robot presses the corresponding color key on the keyboard (for a video with an example of the experiments see `http://marl.dei.uminho.pt/public/videos/PianoTask.mp4`). Mediated by excitatory connections, a bump evolves in the working memory field $u_w m$ which subsequently suppresses the bump in the decision field $u_d e$ due to inhibitory feedback connections. This dynamic process continues until all the elements in the sequence are retrieved and stored in working memory as being executed.

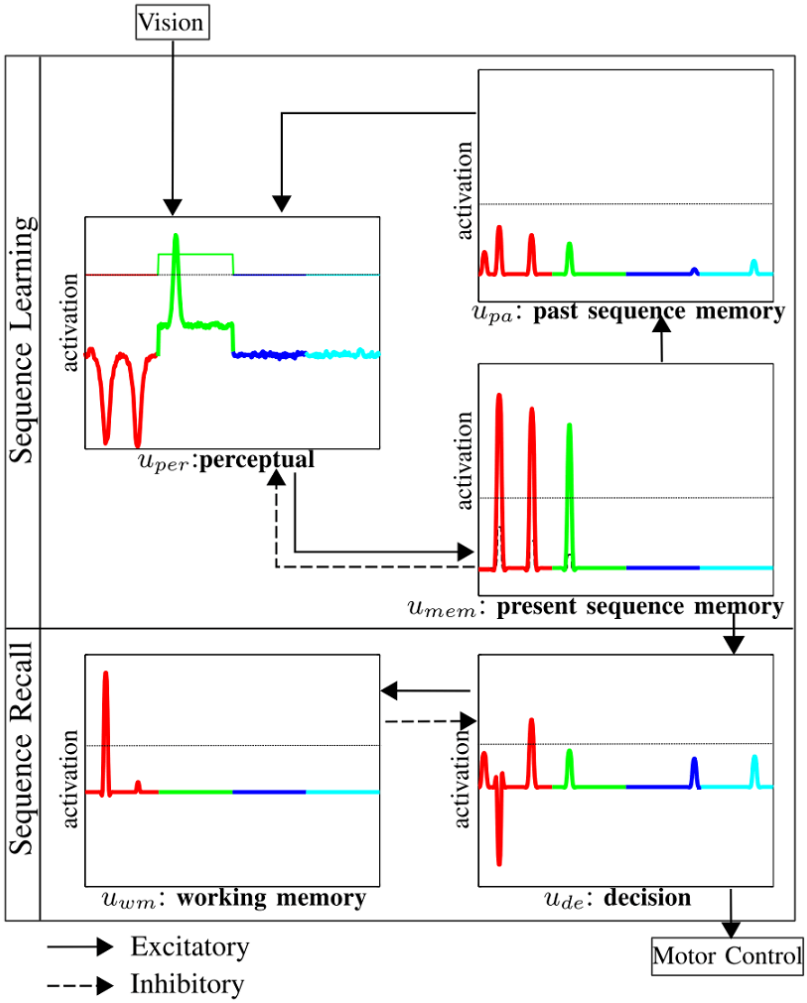

Figure 8: Schematic view of the DNF architecture used in [57] consisting of several interconnected fields implementing sequence learning and sequence recall.

The model of learning sequential task was later extended in [171] by specifically addressing the important role of sensory feedback about executed actions for the learning process. This extension allowed us to address the important challenge of adaptive action timing in dynamic environments.

3.4.3 Adaptive timing

In the musical sequence example [57], the motor delays that may affect the timing of sequence execution were negligible (and constant) since the robot's fingers were positioned directly above the keyboard. However in more complex scenarios with varying movement times of component actions, motor delays will destroy the learned timing pattern. This is particularly important for robots interacting with people in dynamic environments. For instance, in the case of in an object transfer task between robot and human,

the temporal precision of the robot action has a greater weight for the subjective experience rating than the spatial precision as demonstrated in a recent user study of human-robot interaction [90].

Motivated by these findings, we proposed an extension to the DNF model that addresses the challenge of adaptive action timing [171]. The sequence learning process is analogous to the original version of the model [57]. An important difference is that the learned sequence representation can be precisely adjusted during the sequence recall phase of the experiment. Since the memory of a sequence is encoded in an activation gradient that stores the relative timing of events, by adjusting the amplitudes of bumps in the gradient we can fine tune this timing pattern.

The main change in the model is the addition of two fields, representing the internal simulation of learned sequence execution and the perception of the sensory feedback about executed actions. The sensory feedback is present only when the action is accomplished, meaning that in the first execution of a memorized sequence, the learned timing is delayed by the movement execution time. The time courses of the activities in the two added fields are compared during the sequence recall phase in order to detect the temporal mismatch between them. Based on detected mismatch, the original gradient in the sequence memory is adjusted, and this adapted gradient is used in subsequent execution trials. The fine tuning of the original memory representation is achieved by a simple learning rule that we adapted from [1]. Based on a difference between the expected timing and the actually executed timing of action, the learning rule adapts the resting level of the field containing the copy of original memory representation, resulting in changed timing of actions in the next sequence recall trial. When the action is delayed, the resting level is increased in order to start the movement earlier in subsequent trial. If the action is executed too early, the resting level is reduced to delay movement onset.

In Figure 9 we illustrate the effect of the local adaptation of the resting level h on the time course of the bump evolution in the decision field. The resting level was increased locally for the bump centered at position x_3, and decreased for the remaining two bumps centered at x_1 and x_2 (Fig. 9b). This means that the first action, represented by the highest bump, is recalled earlier in a subsequent trial, whereas the remaining two actions are recalled at later times. We illustrate this in Figure 9c-d, where the times courses of activity at the field locations $x_{1,2,3}$ are shown. Relatively small changes of the gradient result in differences in the time when each bump reaches the decision threshold θ, marked as $t_{1,2,3}$. Parameter h may be also adapted globally, to adjust the onset time of the whole sequence without affecting the relative timing pattern encoded in the activation gradient [171].

The model of adaptive action timing was tested in different robotics experiments [173], [Wojtak et al.,

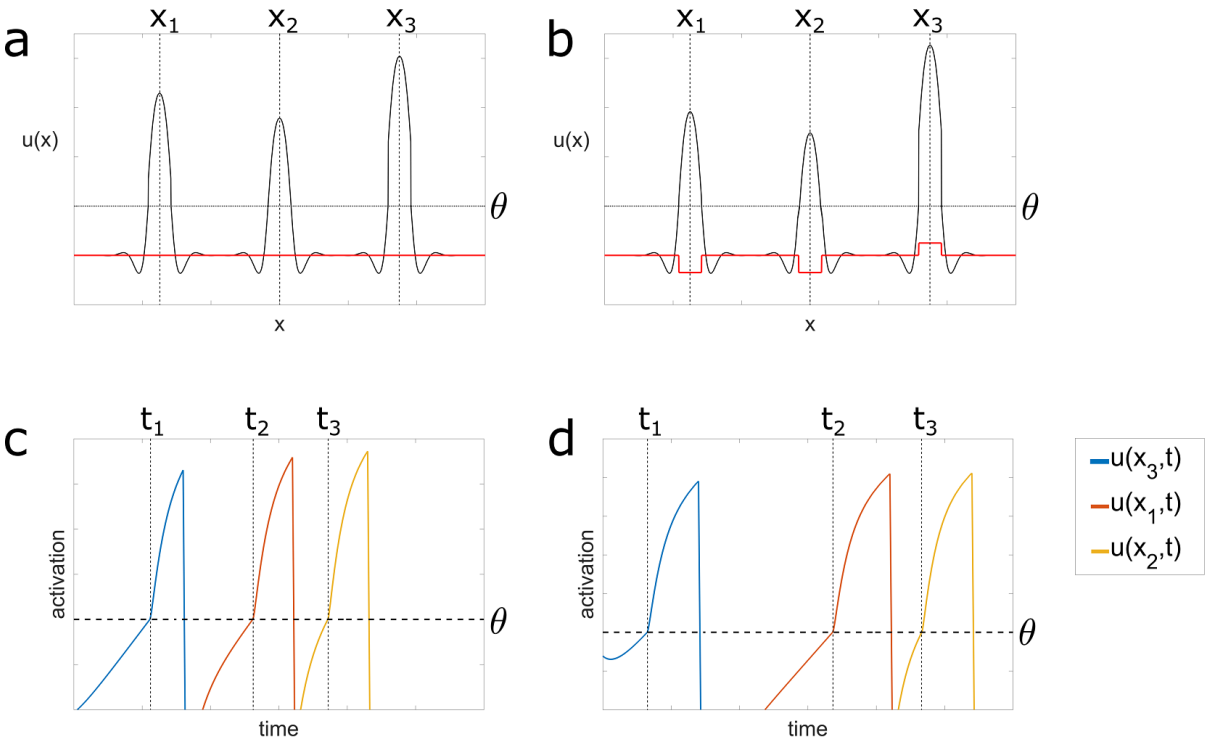

Figure 9: Local h-level adaptation of individual bumps in a memory field: (**a**) before adaptation, (**b**) after adaptation. The adapted h-level (red line) results in bumps with changed amplitudes. Panels (**c**) and (**d**) show the time courses of field locations corresponding to the bump centers, $x_{1,2,3}$, before and after h-level adaptation, respectively.

in preparation]. Different sequential task settings have been designed that are closely inspired by realistic scenarios in service (e.g., assisting a disabled person during drinking) and industrial (e.g., joint assembly of electronic equipment) applications [173], [Wojtak et al., in preparation]. All scenarios require a tight synchronization of actions between human and robot to minimize waiting time, and thus, to guarantee fluent task execution. The experiments included two distinct learning and adaptation phases. First, the robot learns the order and timing of joint task execution by observing the performance of two human "teachers". Subsequently, the robot replaces one human in the team and tries to jointly execute the task with the remaining "teacher". To achieve fluency, the robot has to adapt in repeated interaction trials its movement timing to the (predictable) time course of actions performed by the partner. The robot's adaptive timing capacity is further challenged by 1) the interaction with different users in the same task, and 2) by systematic changes in the timing of specific subtasks executed by the human partner.

Figure 10 depicts an example of a human-robot cooperation in which the robot transfers different objects in the correct order and at the expected time to a human operator [Wojtak et al., in preparation].

The robot adapts the timing of its actions over several joint execution trials by taking into account the action timing of the human partner. We show snapshots of the handovers (with time stamps indicating seconds) during the first (top) and the third (bottom) joint execution trial. It can be clearly seen that the execution fluency greatly improves due to the robot's adaptive movement timing capacity.

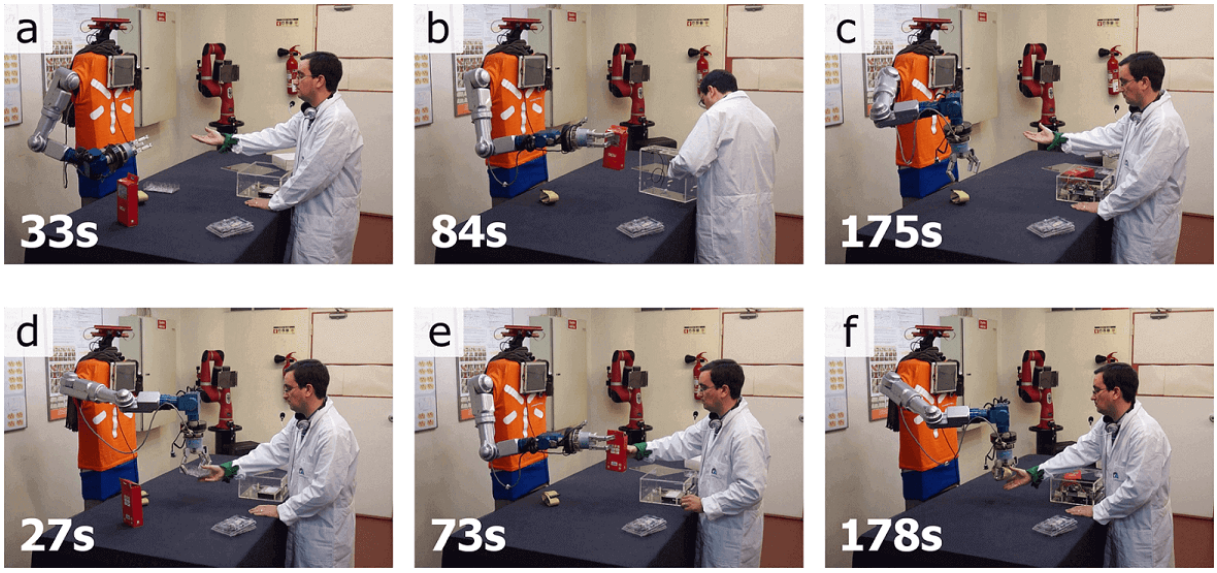

Figure 10: Example of a human-robot cooperation scenario. Snapshots of the handovers (with time stamps indicating seconds) during the first (**a** - **c**) and the third (**d** - **f**) joint execution trial.

3.5 Motivation for the new model

In the Amari model used for building DNF architectures, the bump solution has a unique shape exclusively determined by the recurrent interactions within the network. This means that the input characteristics (e.g., strength or duration) are not reflected in the bump profile. In order to create input dependent bump solutions with different amplitudes and shapes (e.g. reflecting different input durations), additional mechanisms such as for instance a threshold accommodation dynamics used in sequence learning model are necessary. Another important issue for applications concerns the creation of a stable multi-bump solution in response to a series of sensory inputs. Even if such solution exists when the stimuli are presented simultaneously, when they are presented sequentially, the additional inhibition created by existing bumps in the field might be too strong for subsequent stimuli to overcome. In the Amari model, this challenge has been addressed by using a special type of connectivity function, the oscillatory kernel proposed in [98], which supports the existence of input-driven multi-bump solutions [55]. However, being able to create stable multi-bumps with different classes of connectivity function would benefit many applications.

In the following, we present a new neural field model that responds to these shortcomings of the classical models. It provides a two-dimensional bump attractor, determined by a continuum of bump positions and bump amplitudes. The model may be applied as a robust neural integrator representing input strength and duration in the bump amplitude without a need to rely on any additional processing mechanisms such as for instance a threshold accommodation dynamics [58]. Moreover, due to a reduced activity suppression by neighboring bumps, the creation of stable multi-bump solutions is possible even with a connectivity function of lateral inhibition type used by Amari [3] in his seminal work.

4 Novel two-field model

4.1 Derivation of the neural field model

We extend the model studied by Amari [3] by coupling a second neural field, v, to the system. Our model thus reads

$$\tau_u \frac{\partial u(\mathbf{x},t)}{\partial t} = -u(\mathbf{x},t) + v(\mathbf{x},t) + \int_\Omega w(\mathbf{x},\mathbf{x}') f(u(\mathbf{x}',t)-\theta)\mathrm{d}\mathbf{x}' + I(\mathbf{x},t), \tag{4.1a}$$

$$\tau_v \frac{\partial v(\mathbf{x},t)}{\partial t} = -v(\mathbf{x},t) + u(\mathbf{x},t) - \int_\Omega w(\mathbf{x},\mathbf{x}') f(u(\mathbf{x}',t)-\theta)\mathrm{d}\mathbf{x}', \tag{4.1b}$$

where the spatial domain Ω is $\mathbb{R}^d$ or a subset of $\mathbb{R}^d$. We study the model for the cases $d = 1$ and $d = 2$, but higher dimensions could be in principle considered as well with the presented mathematical techniques. In numerical simulations of the model we apply "open" boundary conditions unless otherwise stated. This means that the value attained by the field at the boundary of the domain is determined by the initial condition and inputs to the field. We ensure that the domain is large enough so that the activity patterns are sufficiently far from the domain boundaries. We note however that we are not restricted to this specific setting, and other choices of boundary conditions could be employed, e.g. periodic boundary conditions or Dirichlet boundary conditions [67]. The variables $u(\mathbf{x},t)$ and $v(\mathbf{x},t)$ represent neural activities at position $\mathbf{x} \in \Omega$ at a time $t \in \mathbb{R}^+$.

The parameters τ_u and τ_v define the timescales of field u and v, respectively, and $I(\mathbf{x},t)$ represents a time-dependent, localized input centered at site $\mathbf{x}$ of the u-field.

Term $w(\mathbf{x},\mathbf{x}')$ denotes the strength of connections between neurons, is assumed to depend on the Euclidean distance, so that $w(\mathbf{x},\mathbf{x}') = w(|\mathbf{x}-\mathbf{x}'|)$. Hence, the 1D and 2D neural fields are homogeneous and isotropic (translationally/rotationally invariant). Following Amari [3], we know that the network can support a stable stationary bump solution when $w(\mathbf{x})$ satisfies the following conditions

(H_1) $w(\mathbf{x})$ is symmetric, i.e. $w(-\mathbf{x}) = w(\mathbf{x})$ for all $\mathbf{x} \in \mathbb{R}^d$;

(H_2) $w(\mathbf{x})$ is continuous on $\mathbb{R}^d$ and $\int w(\mathbf{x}')\mathrm{d}\mathbf{x}'$ is finite;

(H_3) $w(\mathbf{x}) > 0$ on an interval $(-\overline{\mathbf{x}}, \overline{\mathbf{x}})$, and $w(-\overline{\mathbf{x}}) = w(\overline{\mathbf{x}}) = 0$;

(H_4) $w(\mathbf{x})$ is decreasing on $(0, \overline{\mathbf{x}}]$;

(H_5) $w(\mathbf{x}) < 0$ on $(-\infty, -\overline{\mathbf{x}}) \cup (\overline{\mathbf{x}}, \infty)$.

The conditions are for the 1D case and can be generalized to 2D. Conditions (H_1), (H_2) and (H_4) are general requirements for a tractable mathematical analysis, whereas conditions (H_3) and (H_5) result in "lateral inhibition" type interactions [51]. In particular, condition (H_3) yields that nearby neurons excite each other, while (H_5) ensures mutually inhibitory influence of neurons at distances greater than a certain value $\overline{\mathbf{x}}$.

Common examples of $w(\mathbf{x})$ satisfying conditions $(H_1) - (H_5)$ are a coupling function with constant lateral inhibition

$$w_{lat}(\mathbf{x}) = A_{lat} e^{\left(-\mathbf{x}^2/2\sigma_{lat}^2\right)} - g_{lat}, \qquad A_{lat} > 0, \sigma_{lat} > 0, g_{lat} > 0, \tag{4.2}$$

and the Mexican hat function given by the difference of two Gaussians

$$w_{mex}(\mathbf{x}) = A_{ex} e^{\left(-\mathbf{x}^2/2\sigma_{ex}^2\right)} - A_{in} e^{\left(-\mathbf{x}^2/2\sigma_{in}^2\right)} - g_{mex}, \tag{4.3}$$

where $A_{ex} > A_{in} > 0$ and $\sigma_{in} > \sigma_{ex} > 0$ and $g_{mex} > 0$.

To enable stable multi-bump solutions in the neural field equation (2.9), Laing et al. [98] extended the work of Amari [3] by introducing the oscillatory connectivity function

$$w_{osc}(\mathbf{x}) = e^{-b|\mathbf{x}|}(b \sin|\mathbf{x}| + \cos(\mathbf{x})), \qquad b > 0, \tag{4.4}$$

where the parameter b controls the rate at which the oscillations decay with distance.

In a study addressing the conditions on multiple localized inputs $I(\mathbf{x}, t)$ that guarantee the evolution of a multi-bump pattern [55], the periodically modulated function (4.4) has been adapted in in the following way

$$w_{osc}(\mathbf{x}) = e^{-b|\mathbf{x}|}(b \sin|\alpha\mathbf{x}| + \cos(\alpha\mathbf{x})), \qquad b > 0, \tag{4.5}$$

where the parameter $0 < \alpha \leq 1$ is added to control the distances of the zero crossings of $w(\mathbf{x})$.

The couplings (4.4) and (4.5) satisfy (H_1) and (H_2), and also the following properties

(H_6) $w(\mathbf{x})$ is an oscillatory function that tends to zero as $x \to \pm\infty$;

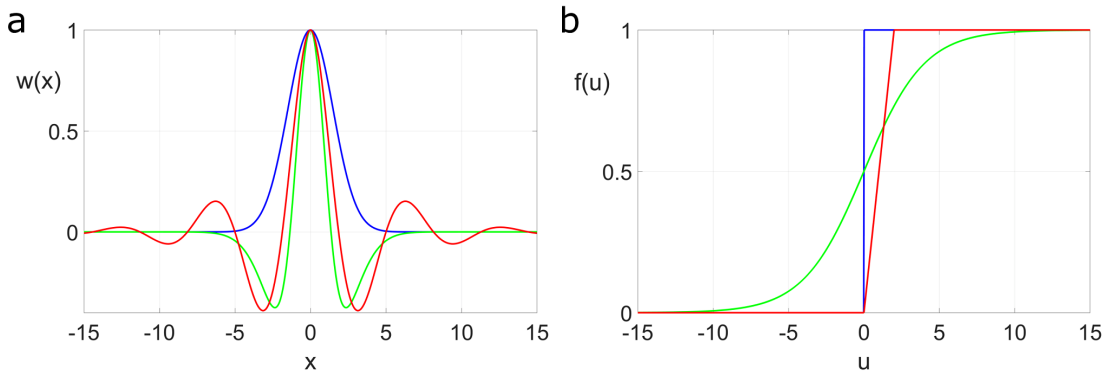

Figure 11: (**a**) Connectivity functions $w(x)$ given by (4.2) with $A_{lat} = 1$, $\sigma_{lat} = 1.5$ (blue curve), (4.3) with $A_{ex} = 2$, $\sigma_{ex} = 1$, $A_{inh} = 1$, $\sigma_{inh} = 2$ and $g_{mex} = 0$ (green curve) and (4.4) with $A = 1$, $b = 0.3$ (red curve). (**b**) Activation functions given by (4.6) (blue curve), (4.7) with $\beta = 0.5$ (green curve) and (4.8) with $\beta = 0.5$ (red curve). Threshold $\theta = 0$.

(H_7) $w(0) > 0$ and $w(\mathbf{x})$ changes sign infinitely often on $(0, \infty)$.

We show examples of coupling functions given by (4.2) - (4.4) in Figure 11a.

The term $f(u)$ denotes the firing rate function with threshold $\theta \geq 0$. To simplify the analytical work, Amari assumed $f(u)$ as a Heaviside step function, that is

$$f(u) = H(u) = \begin{cases} 0, & u \leq \theta, \\ 1, & u > \theta. \end{cases} \tag{4.6}$$

Other possible choices are the sigmoid function with slope parameter β

$$f(u) = \frac{1}{1 + e^{(-\beta(u-\theta))}}, \tag{4.7}$$

and the piecewise linear function

$$f(u) = \begin{cases} 0, & u \leq \theta, \\ \beta(u - \theta), & \theta < u \leq \theta + 1/\beta, \\ 1, & u > \theta + 1/\beta. \end{cases} \tag{4.8}$$

Examples of functions (4.6) - (4.8) are depicted in Figure 11b.

Amari derives his scalar neural field model of coupled excitatory and inhibitory subpopulations by assuming that the long ranged inhibitory feedback in the network is infinitely fast. This ensures that the spread of self-sustained excitation remains localized in a region activated by external input. To understand the role of the v-field of the two-field model in the pattern formation process, it is helpful to consider

also different time scales for the two fields (see Figure 12). In the limit case $\tau_v \longrightarrow 0$, the v-field is at quasi-equilibrium with

$$v(\mathbf{x}, t) = u(\mathbf{x}, t) - \int_\Omega w(\mathbf{x}, \mathbf{x}') f(u(\mathbf{x}', t) - \theta) \mathrm{d}\mathbf{x}'. \tag{4.9}$$

Substituting this expression into the u-equation of (4.1) yields

$$\frac{\partial u(\mathbf{x}, t)}{\partial t} = I(\mathbf{x}, t). \tag{4.10}$$

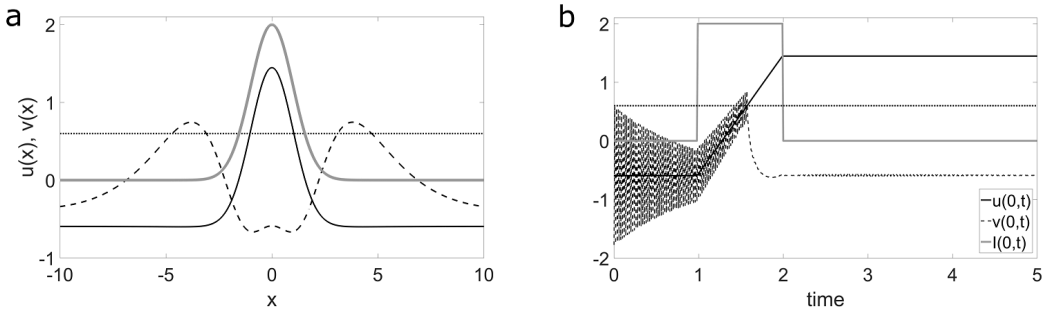

Figure 12: (**a**) Solution at time $t = 50$ of the model (4.1) with $\tau_v = 0.005$. (**b**) Time evolution of center positions of field u and v from panel **a**. Input (grey line) with $A_I = 2$, $\sigma_I = 1$ and $d = 1$ was applied at time $t = 1$. Kernel w given by (4.3) with $A_{ex} = 2.5$, $\sigma_{ex} = 1.5$, $A_{inh} = 1.25$, $\sigma_{inh} = 3.5$ and $w_{inh} = 0.1$. $K = 0$, $\theta = 0.6$.

The u-field thus implements a perfect temporal integration of external inputs if fast local feedback loops counterbalance any input-induced changes in the recurrent interactions. Interestingly, a distinct subclass of inhibitory interneurons has been described in WM tasks that show sustained activity with "inverted spatial tuning" relative to nearby excitatory neurons [176]. Such opposed tuning is consistent with a spatial integration of excitation with the inverted connectivity profile of the u-field. Its functional role is not clear however. Based on a cortical microcircuit model, it has been suggested that these interneurons might serve to stabilize working memory by virtue of disinhibiting excitatory neurons that have already been activated by a stimulus held in memory [159]. In the two-field model, balanced inhibitory feedback ensures that persistent activity at any time represents the time integral of past inputs to a specific field location. In addition, the spatial integration with an inverted Mexican hat connectivity propagates excitation outwards from stimulated regions, thus reducing the effect of lateral inhibition in the u-field [124].

4.2 Spatially homogeneous field model

To understand the pattern formation process of the two-field model and its dependence on initial conditions and external input it is instructive to first discuss a one-dimensional, spatially homogeneous version of

system (4.1) in which all field sites integrate with the same weight the activity from neighboring neurons. The dynamics of the resulting space-clamped system can be analyzed using phase plane techniques. It is given by

$$\frac{\mathrm{d}q_u}{\mathrm{d}t} = -q_u + q_v + W \times f(q_u - \theta) + I, \tag{4.11a}$$

$$\frac{\mathrm{d}q_v}{\mathrm{d}t} = -q_v + q_u - W \times f(q_u - \theta). \tag{4.11b}$$

The constant $W > 0$ is chosen without loss of generality to represent the integral of the kernel w

$$W = \int_{-\infty}^{\infty} w(y)\mathrm{d}y. \tag{4.12}$$

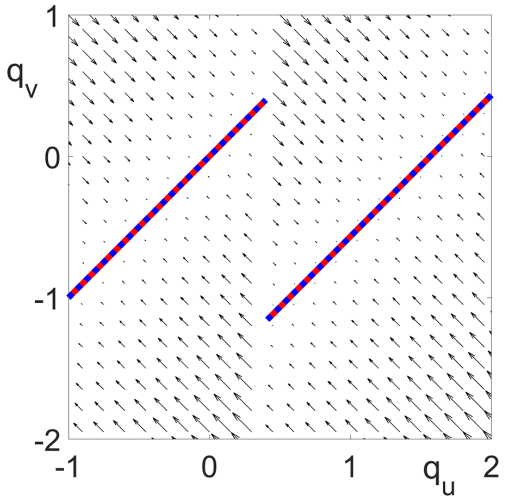

Figure 13: Phase portrait and nullclines of the system (4.11) with $\theta = 0.4$ and $I = 0$. Blue line represents the q_u-nullcline and the red line the q_v-nullcline. Parameters of the kernel used to calculate W in (4.12) are $A_{ex} = 2$, $A_{in} = 1$, $\sigma_{ex} = 1.25$, $\sigma_{in} = 2.5$ and $w_{inh} = 0$.

Fig. 13 depicts the phase portrait of system (4.11) in the absence of input. Equilibrium points lie on a line with positive slope and a discontinuity at threshold θ. For a suprathreshold initial value $q_u(0) > \theta$ and $q_v(0) = 0$, the system converges to an equilibrium point with $q_u > q_u(0)$ which increases monotonically with increasing $q_u(0)$. Solution curves are also represented by straight lines indicating that the sum of q_u and q_v remains constant over time, $q_u + q_v = K$. For the specific choice $K = 1$, Fig. 14 shows the solution curve together with the q_u-nullcline and the q_v-nullcline definded by $\mathrm{d}q_u/\mathrm{d}t = 0$ and $\mathrm{d}q_v/\mathrm{d}t = 0$, respectively. The intersections of the two nullclines represent equilibrium points of the dynamical system, their location and number depends on the values for K and θ. For the case $K \geq 2\theta$, there is a single equilibrium point which is stable. For $K < 2\theta$, there are three three equilibrium points. One of them, (q^*_{u2}, q^*_{v2}),

is unstable, whereas the remaining two points (q^*_{u1}, q^*_{v1}) and (q^*_{u3}, q^*_{v3}) are stable. The equilibrium point to which the system converges is determined by the initial values $(q_u(0), q_v(0)) = (q_u(0), 1 - q_u(0))$ as summerized in Table 1.

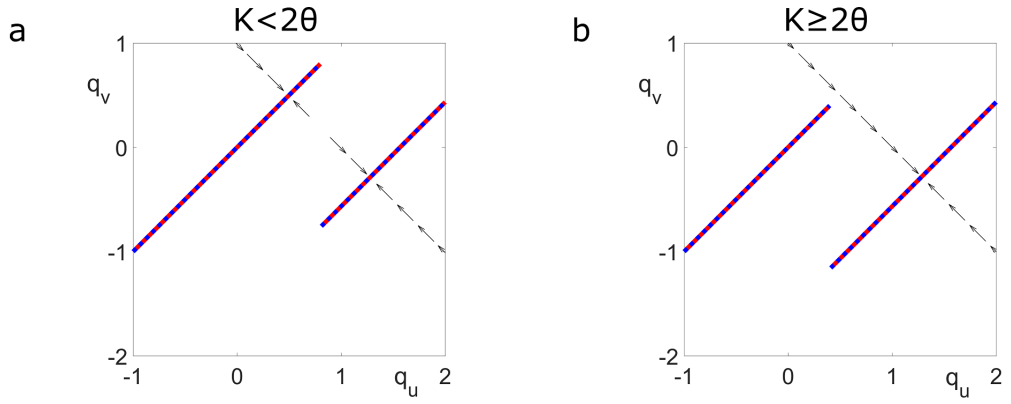

Figure 14: Phase portrait and nullclines of the system (4.11) with the initial condition $q_u(0) + q_v(0) = K$. (**a**) $K = 1$, $\theta = 0.8$. There are three equilibrium points at $(q^*_{u1}, q^*_{v1}) = (0.5, 0.5)$, $(q^*_{u2}, q^*_{v2}) = (0.8, 0.2)$, $(q^*_{u3}, q^*_{v3}) = (1.28, -0.28)$. (**b**) $K = 1$, $\theta = 0.4$. There is one equilibrium point at $(q^*_u, q^*_v) = (1.28, -0.28)$.

For the two-field model, the discussion of the qualitative behavior of the reduced model suggests the existence of a bump solution with a unique shape satisfying $u(x) + v(x) = K$ as long as the initial conditions satisfy $u(x, 0) + v(x, 0) = K$ and $u(x, 0) > \theta$ holds. In this case, the two-field model is expected to behave as the classical Amari model. For the case that K is not a constant, $u(x, 0)+v(x, 0) = K(x)$, bumps with a monotonic dependence on initial conditions can be expected. As a particularly relevant example for applications, we study in Chapter 7 numerically the case $v(x, 0) = 0 \quad \forall x$ and $u(x, 0)$ with Gaussian shape which reflects an initial condition set by localized input.

Initial value $q_u(0)$	$K < 2\theta$	$K \geq 2\theta$
$q_u \leq \frac{K}{2}$	$\left(\frac{K}{2}, \frac{K}{2}\right)$	$\left(\frac{K+W}{2}, \frac{K-W}{2}\right)$
$\frac{K}{2} < q_u \leq \theta$	$(\theta, K - \theta)$	
$q_u > \theta$	$\left(\frac{K+W}{2}, \frac{K-W}{2}\right)$	

Table 1: Fixed points of the system (4.11) with the condition $q_u(0) + q_v(0) = K$.

We start our investigation by analyzing the existence and stability of bump solutions for the Amari model (Chapter 5) and the two-field model (Chapter 6) for one and two spatial dimensions.

5 Stability analysis of the Amari model

5.1 Introduction

In this Chapter we analyze the existence and stability of stationary single bump solutions in the Amari model without external inputs [3] using three different methods. First, we review the results from Amari's seminal paper [3] using his linear stability analysis approach. We then study bump solutions using a Lyapunov functional [95, 118]. Finally we employ Pinto's and Ermentrout's stability analysis [121]. The focus is on bump solutions in one spatial dimension. However, using Pinto's and Ermentrout's method we extend the analysis also to the two dimensional case. Here a specific coupling function of lateral inhibition type ("wizard hat") is used to ease the mathematical analysis.

Following Amari's analysis of the one-dimensional field equation

$$\frac{\partial u(x,t)}{\partial t} = -u(x,t) + \int_{\mathbb{R}} w(x-y) f(u(y,t)-\theta)\mathrm{d}y, \tag{5.1}$$

we assume f to be the Heaviside function with threshold θ given by (4.6). The connectivity functions we consider are a Gaussian kernel with constant lateral inhibition given by (4.2) and a Mexican hat function given by (4.3).

5.2 Amari's linear stability analysis

Using the Heaviside function, Amari has shown that the behavior of a bump solution can be described by tracking the boundaries between states of high and low activity. It is thus possible to reduce the analysis of pattern formation in the model formalized by an integro-differential equation to the simpler problem of analyzing the dynamics of boundary points governed by ODEs.

Let $R[u(x,t)]$ be the region over which the field is excited

$$R[u(x,t) > \theta] = (x_1(t), x_2(t)), \tag{5.2}$$

and let the gradients of $u(x,t)$ at the boundaries x_1 and x_2 of the excited region be

$$c_1 = \frac{\partial u(x_1,t)}{\partial x}, \qquad -c_2 = \frac{\partial u(x_2,t)}{\partial x}. \tag{5.3}$$

After a short period of time $\mathrm{d}t$, the excited region changes to

$$R[u(x,t+\mathrm{d}t) > \theta] = (x_1(t+\mathrm{d}t), x_2(t+\mathrm{d}t)). \tag{5.4}$$

The boundaries of the excited region satisfy

$$\text{at time } t: \quad u(x_i,t) = \theta, \tag{5.5a}$$

$$\text{at time } t+\mathrm{d}t: \quad u(x_i+\mathrm{d}x_i, t+\mathrm{d}t) = \theta, \tag{5.5b}$$

where $x_i(t+\mathrm{d}t) = x_i + \mathrm{d}x_i, i = 1,2.$

A first order Taylor expansion of the latter equation yields

$$\frac{\partial u(x_i,t)}{\partial x}\mathrm{d}x_i + \frac{\partial u(x_i,t)}{\partial t}\mathrm{d}t = 0, \qquad i = 1,2, \tag{5.6}$$

for infinitesimally small $\mathrm{d}x_i$ and $\mathrm{d}t$.

We can then rewrite (5.1) at $x = x_i(t)$ as

$$\frac{\partial u(x_i,t)}{\partial t} = -u(x_i,t) + \int_{x_1(t)}^{x_2(t)} w(x,y)\mathrm{d}y. \tag{5.7}$$

Since $u(x_i,t) = \theta$, we have from (6.2a)

$$\frac{\partial u(x_i,t)}{\partial t} = -\theta + W(x_2 - x_1), \tag{5.8}$$

where

$$W(x) = \int_0^x w(y)\mathrm{d}y. \tag{5.9}$$

We have

$$\frac{\mathrm{d}x_1}{\mathrm{d}t} = \left.\frac{-\partial u/\partial t}{\partial u/\partial x}\right|_{x=x_1} = -\frac{1}{c_1}\left(-\theta + W(x_2 - x_1)\right), \tag{5.10a}$$

$$\frac{\mathrm{d}x_2}{\mathrm{d}t} = \left.\frac{\partial u/\partial t}{\partial u/\partial x}\right|_{x=x_2} = \frac{1}{c_2}\left(-\theta + W(x_2 - x_1)\right). \tag{5.10b}$$

We can then describe the change of length of the excited region $\Delta(t) = x_2(t) - x_1(t)$

$$\frac{\mathrm{d}\Delta}{\mathrm{d}t} = \left(\frac{1}{c_1} + \frac{1}{c_2}\right)\left(-\theta + W(\Delta)\right). \tag{5.11}$$

The existence of a solution of width $\Delta = x_2 - x_1$ is determined by the roots of

$$W(\Delta) = \theta. \tag{5.12}$$

The stability condition is that a steady state of width Δ is stable if

$$W'(\Delta) < 0, \tag{5.13}$$

and unstable otherwise.

We plot examples of the existence condition (5.12) for the lateral inhibition kernel (4.2) and the Mexican hat kernel (4.3) in Figure 16.

The number of bump solutions that the field can support in the absence of input depends on the connectivity function $w(x)$ and the value of θ. Amari defines

$$W_{max} = \max_{x>0} W(x), \qquad W_\infty = \lim_{x\to\infty} W(x) \tag{5.14}$$

and gives the sets of equilibrium solutions for three cases

Case I_1: $W_\infty > 0$; $2W_\infty > W_{max}$,

Case I_2: $W_\infty > 0$; $2W_\infty < W_{max}$,

Case II: $W_\infty < 0$.

We show in Fig. 15 the set of possible equilibrium solutions for the case $W_\infty < 0$ as a function of θ.

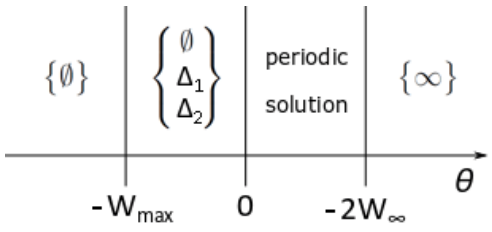

Figure 15: Diagram showing the sets of equilibrium solutions in the Amari model for the case of $W_\infty < 0$ for various values of θ in the absence of input [3] where $\emptyset$ denotes a solution in which no region is excited and ∞ is a solution in which the whole region is excited. Solutions $\Delta_1 < \Delta_2$ are bumps with widths Δ_1 and Δ_2, respectively. Solution Δ_1 is unstable, the remaining solutions are stable.

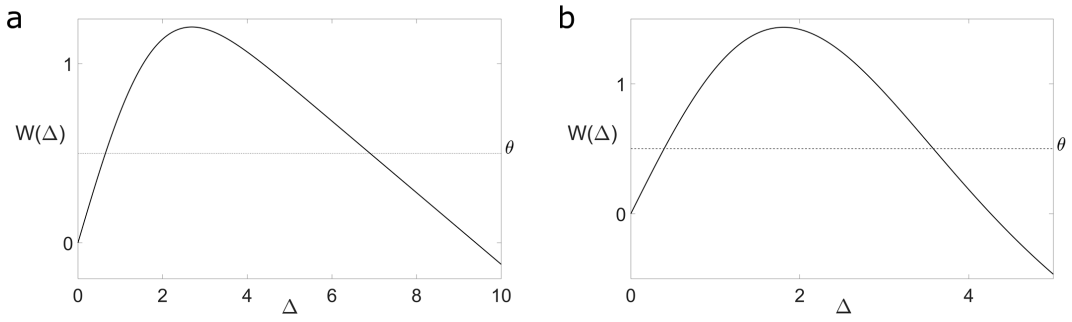

Figure 16: Bump existence in the Amari model for a lateral inhibition kernel (4.2) with $A_{lat} = 1$, $\sigma_{lat} = 1.5$, $w_{inh} = 0.2$ (**a**) and Mexican hat kernel (4.3) with $A_{ex} = 3$, $\sigma_{ex} = 1.5$, $A_{inh} = 1.5$, $\sigma_{inh} = 3$ and $w_{inh} = 0.2$ (**b**). In both panels the threshold is $\theta = 0.5$ (dotted line). In panel (**a**) there exist two solutions with $\Delta_1 = 0.64$ (unstable) and $\Delta_2 = 6.9$ (stable). In panel (**b**) we have two solutions with $\Delta_1 = 0.39$ (unstable) and $\Delta_2 = 3.58$ (stable).

5.3 Lyapunov method

The stability of stationary solutions of the neural field equations can be also determined using the Lyapunov method [61], as it was done previously in e.g. [39, 95, 118]. Stable and unstable bump solutions correspond to local minima and local maxima of a Lyapunov functional, respectively. We summarize the results for the Amari model below.

The Lyapunov functional for the Amari model (5.1) is given by

$$E[u] = -\frac{1}{2}\int_\Omega\int_\Omega w(x-y)f(u(x,t)-\theta)f(u(y,t)-\theta)\mathrm{d}x\mathrm{d}y + \int_\Omega\int_0^{u(x,t)} f'(s)s\mathrm{d}s. \quad (5.15)$$

For a Heaviside firing rate it becomes

$$E[u] = -\frac{1}{2}\int_\Omega\int_\Omega w(x-y)f(u(x,t)-\theta)f(u(y,t)-\theta)\mathrm{d}x\mathrm{d}y + \theta\int_\Omega f(u(x,t)-\theta)\mathrm{d}x. \quad (5.16)$$

For a bump of width $\Delta = (x_2 - x_1)$ we have

$$E(\Delta) = -\frac{1}{2}\int_{x_1}^{x_2}\int_{x_1}^{x_2} w(x-y)\mathrm{d}x\mathrm{d}y + \theta(x_2 - x_1). \quad (5.17)$$

Using (5.9) we obtain

$$E(\Delta) = -\int_0^\Delta W(x)\mathrm{d}x + \theta\Delta. \quad (5.18)$$

In Fig. 17 we show examples of the Lyapunov functional for the Amari model (5.1). We plot $E(\Delta)$ for two choices of the connectivity function $w(x)$, and in both cases E has one local maximum and one local minimum, corresponding to the unstable and stable bump solution, respectively.

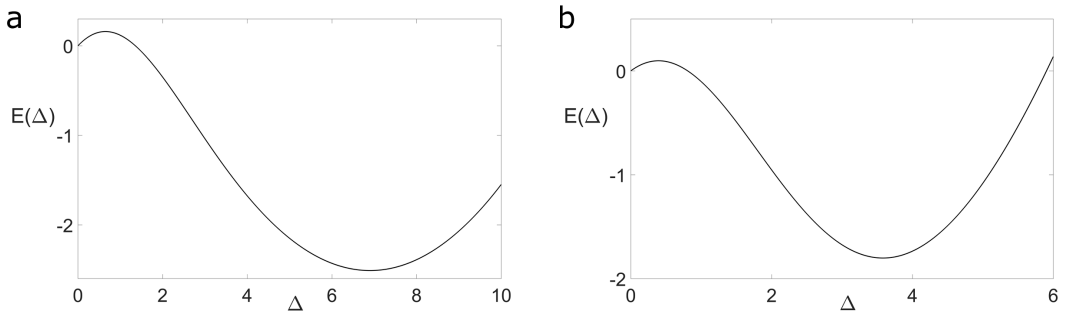

Figure 17: Plot of $E(\Delta)$ given by (5.18) for the Amari model (5.1) with a lateral inhibition kernel (4.2) (**a**) and Mexican hat kernel (4.3) (**b**). In (**a**), there is a local maximum at $\Delta_1 = 0.64$ and a local minimum at $\Delta_2 = 6.9$. In (**b**), there is a local maximum at $\Delta_1 = 0.39$ and a local minimum at $\Delta_2 = 3.58$. Parameters as in Fig. 16.

5.4 Pinto's and Ermentrout's perturbation approach

The final stability analysis method that we consider is the one used by Pinto and Ermentrout [121]. The approach is based on the analysis of the eigenvalues of the system linearized around the steady state. The field model analyzed in [121] consists of two separate populations of excitatory and inhibitory neurons with different time scales. In the limit case of instantaneous inhibition, the authors showed that their approach reproduces Amari's results. We study the Amari model using the linearization approach in both one and two spatial dimensions by first investigating the existence of single bump solutions and then determining their stability.

5.4.1 1D Amari model

Existence of bumps

Consider an equilibrium solution $U(x) = \lim_{t\to\infty}(u(x,t))$ satisfying

$$U(x) = \int_{-\infty}^{\infty} w(|x-y|) f(U(y-\theta))\mathrm{d}y. \tag{5.19}$$

Let $R[U] = \{x | U(x) > \theta\}$ be the region over which the field is excited. We can then rewrite (5.19) as

$$U(x) = \int_{R[U]} w(|x-y|)\mathrm{d}y. \tag{5.20}$$

For a stationary bump of width $\Delta = x_2 - x_1$ the excited region is then given by the interval (x_1, x_2) and equation (5.20) takes the form

$$U(x) = \int_{x_1-x}^{x_2-x} w(y)\mathrm{d}y. \tag{5.21}$$

Knowing that $U(x_1) = U(x_2) = \theta$ and setting $x = x_1$ and $x = x_2$, respectively, we have

$$\theta = \int_0^{x_2 - x_1} w(y)\mathrm{d}y, \tag{5.22a}$$

$$\theta = \int_{x_1 - x_2}^{0} w(y)\mathrm{d}y. \tag{5.22b}$$

We set $x_1 = -\frac{\Delta}{2}$ and $x_2 = \frac{\Delta}{2}$ and obtain the following necessary condition for the existence of a bump

$$\theta = W(\Delta). \tag{5.23}$$

In the case of a kernel with homogeneous lateral inhibition or a Mexican hat coupling function, it follows from condition (5.23) that there is a maximum of two bump solutions for a given value of θ, one wide and one narrow, as illustrated in Fig. 18. Condition (5.23) is the same as the existence condition obtained using Amari's stability analysis, (5.12).

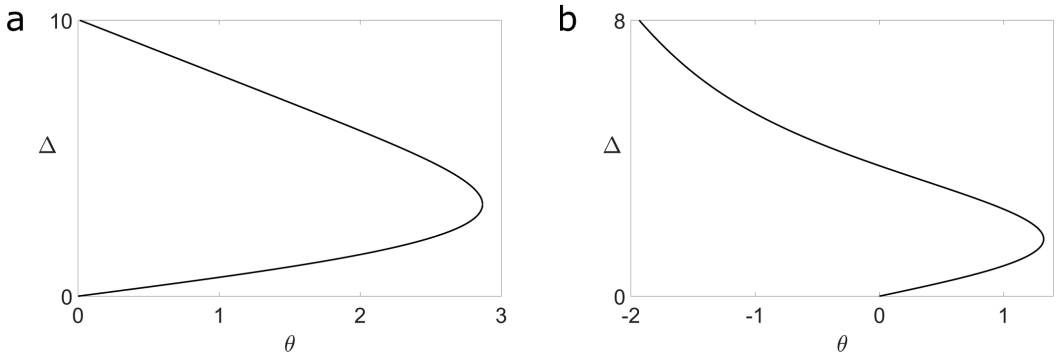

Figure 18: Bump width Δ as a function of θ in the Amari model for a lateral inhibition kernel (4.2) with $A_{lat} = 2$, $\sigma_{lat} = 2$, $w_{inh} = 0.5$ (**a**) and Mexican hat kernel (4.3) with $A_{ex} = 3$, $\sigma_{ex} = 1.4$, $A_{inh} = 1.5$, $\sigma_{inh} = 3$ and $w_{inh} = 0.2$ (**b**).

Stability of bumps

To analyze the stability of a bump, we consider the equilibrium solution (5.19) and introduce a change in width of the excited region under a small time-dependent perturbation ψ

$$u(x,t) = U(x) + \psi(x,t). \tag{5.24}$$

Combining equations (5.1) and (5.24) we obtain

$$\frac{\partial}{\partial t}[U(x,t) + \psi(x,t)] = -[U(x,t) + \psi(x,t)] + \int_{-\infty}^{\infty} w(|x-y|) f(U(y) + \psi(y,t) - \theta)\mathrm{d}y. \tag{5.25}$$

Using first order Taylor expansion, we get

$$\frac{\partial\psi(x,t)}{\partial t} = -U(x,t) - \psi(x,t) + \int_{-\infty}^{\infty} w(|x-y|)[f(U(y)-\theta) + f'(U(y)-\theta)\psi(y,t)]\mathrm{d}y + \ldots, \quad (5.26)$$

which reduces to

$$\frac{\partial\psi(x,t)}{\partial t} = -\psi(x,t) + \int_{-\infty}^{\infty} w(|x-y|)f'(U(y)-\theta)\psi(y,t)\mathrm{d}y. \quad (5.27)$$

Since the formal derivative of the step function is the Dirac delta function $\frac{\partial H}{\partial u} = \delta(u-\theta)$ we have

$$\begin{aligned}\int_{\infty}^{\infty} w(x-y)H'(U(y)-\theta)\psi(y,t)\mathrm{d}y &= \int_{\infty}^{\infty} w(x-y)\delta(U(y)-\theta)\psi(y,t)\mathrm{d}y \\ = \int \frac{w(x-U^{-1}(z))\delta(z-\theta)\psi(U^{-1}(z),t)\mathrm{d}z}{|U'(U^{-1}(z))|} &= \frac{w(x-x_1)\psi(x_1,t)}{|U'(x_1)|} + \frac{w(x-x_2)\psi(x_2,t)}{|U'(x_2)|}.\end{aligned} \quad (5.28)$$

Assuming that solutions are of the separable form $\psi(x,t) = e^{\lambda t}(\psi(x))$, Equation (5.27) gives

$$\lambda\psi(x) = -\psi(x) + \frac{w(x-x_1)\psi(x_1)}{|U'(x_1)|} + \frac{w(x-x_2)\psi(x_2)}{|U'(x_2)|}. \quad (5.29)$$

By setting $x = x_1$ and $x = x_2$, respectively, we have the two equations

$$\lambda\psi(x_1) = -\psi(x_1) + \frac{w(0)\psi(x_1)}{|U'(x_1)|} + \frac{w(\Delta)\psi(x_2)}{|U'(x_2)|}, \quad (5.30a)$$

$$\lambda\psi(x_2) = -\psi(x_2) + \frac{w(\Delta)\psi(x_1)}{|U'(x_1)|} + \frac{w(0)\psi(x_2)}{|U'(x_2)|}. \quad (5.30b)$$

In order to determine $|U'(x)|$ we differentiate equation (5.21) and get

$$U'(x) = [w(x_1-x) - w(x_2-x)]. \quad (5.31)$$

Since $\Delta = x_2 - x_1$, we get

$$|U'(x_i)| = w(0) - w(\Delta), \qquad i = 1, 2. \quad (5.32)$$

We can then write the system (5.30) in the matrix form

$$A \cdot \begin{bmatrix}\psi(x_1)\\ \psi(x_2)\end{bmatrix} = \begin{bmatrix}0\\0\end{bmatrix},$$

where the matrix A is given by

$$A = \begin{bmatrix}\lambda + 1 - a & -b\\ -b & \lambda + 1 - a\end{bmatrix},$$

with the parameters a and b defined as

$$a = \frac{w(0)}{c}, \qquad b = \frac{w(\Delta)}{c}, \tag{5.33}$$

where

$$c = |U'(x_{1,2})|. \tag{5.34}$$

The eigenvalues of A read

$$\lambda_{\pm} = -1 + a \pm b. \tag{5.35}$$

We then have

$$\lambda_{-} = 0, \qquad \lambda_{+} = \frac{2w(\Delta)}{w(0) - w(\Delta)}. \tag{5.36}$$

$\lambda_{-} = 0$ is an expected result of the translation invariance of the bump solutions due to the assumed spatial symmetry of the coupling function $w(x)$. The solution is stable if $Re(\lambda_{+}) < 0$. Hence, the stability condition is that a bump with width Δ is stable if

$$w(\Delta) < 0. \tag{5.37}$$

In Fig. 19 we plot the stability results for the two coupling functions used. In both cases, the solution curve consists of two branches, the upper branch with wider bumps is stable (solid lines), whilst the lower branch of narrow bumps is unstable (dashed lines). The two branches merge at the saddle-node bifurcation where the stability change occurs.

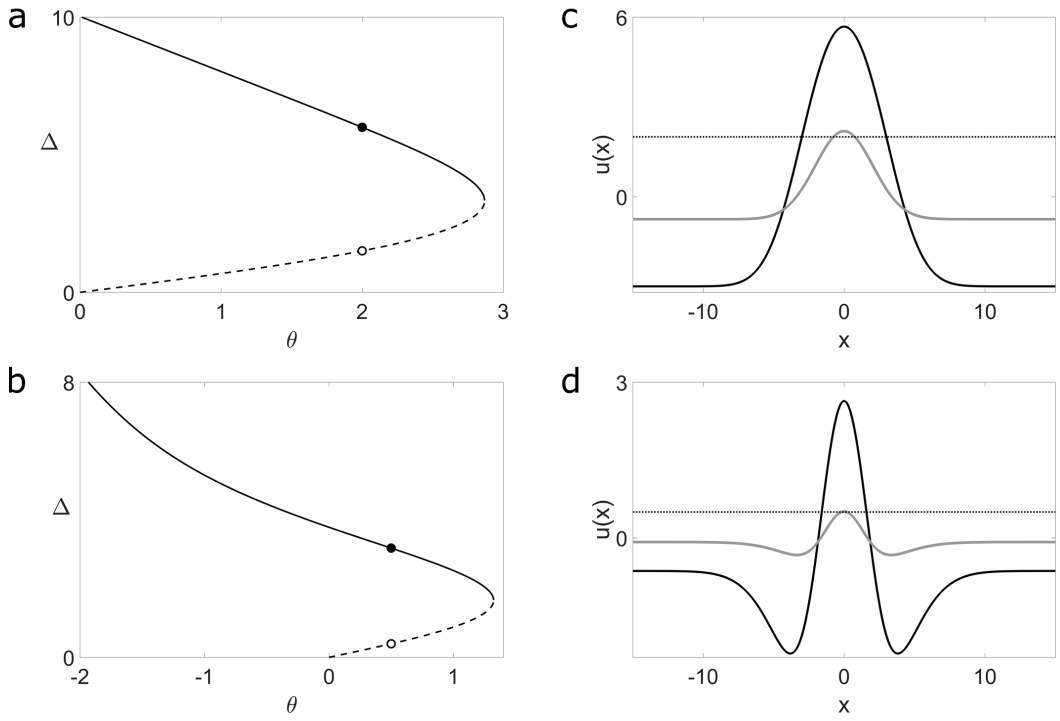

Figure 19: Bump stability in the Amari model for a lateral inhibition kernel (4.2) (**a**) and Mexican hat kernel (4.3) (**b**). Solid (dashed) lines shows branches of stable (unstable) solutions. (**c** and **d**) Examples of stable (black lines) and unstable (grey lines) bump solutions corresponding to the filled (unfilled) dots in panels **a** and **b**. (**c**) Bump widths are $\Delta_1 = 1.51$ (unstable bump) and $\Delta_2 = 5.99$ (stable bump), threshold $\theta = 2$. (**d**) Bump widths are $\Delta_1 = 0.39$ (unstable bump) and $\Delta_2 = 3.17$ (stable bump), threshold $\theta = 0.5$. Remaining parameters as in Fig. 18.

5.4.2 2D Amari model

We now study the two-dimensional analog of (5.1)

$$\frac{\partial u(\mathbf{r},t)}{\partial t} = -u(\mathbf{r},t) + \int_{\mathbb{R}^2} w(\mathbf{r}-\mathbf{r}')f(u(\mathbf{r}',t))\mathrm{d}\mathbf{r}', \tag{5.38}$$

where $\mathbf{r} = (r,\phi)$, $r \in \mathbb{R}^+$ and $\phi \in [0, 2\pi)$. The firing rate function $f(u)$ is taken again as a Heaviside function with threshold θ given by (4.6). We consider a wizard hat weight distribution given by a combination of modified Bessel functions of the second kind [24, 149]

$$w(r) = \frac{2}{3\pi}(K_0(r) - K_0(2r) - A(K_0(r/\sigma) - K_0(2r/\sigma))). \tag{5.39}$$

An example of the rotationally symmetric function (5.39) is depicted in Fig. 20. As can be clearly seen, it combines local excitation with surround inhibition.

Existence of bumps

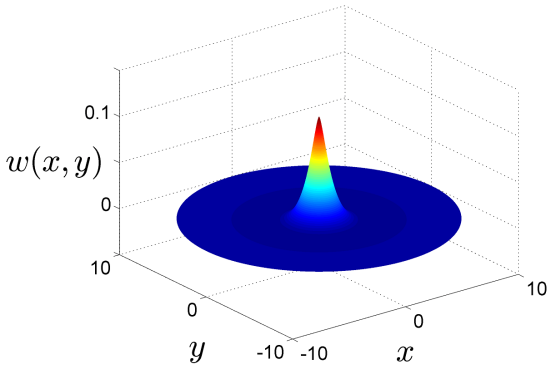

Figure 20: Weight distribution given by a combination of modified Bessel functions of the second kind as defined in (5.39). Weight parameters are $A = 1/4$ and $\sigma = 2$.

We consider a circularly symmetric bump solution of radius R such that $u(\mathbf{r}, t) = U(r)$ with $U(R) = \theta$, $U(r) > \theta$ for $r < R$, $U(r) < \theta$ for $r > R$ and $U(r) \to 0$ as $r \to \infty$.

A stationary solution of equation (5.38) then gives

$$U(r) = \int_0^{2\pi} \int_0^R w(|\mathbf{r} - \mathbf{r}'|) r' \mathrm{d}r' \mathrm{d}\phi, \tag{5.40}$$

which using $|\mathbf{r} - \mathbf{r}'| = \sqrt{r^2 + r'^2 - 2rr' \cos\phi}$ we can rewrite as

$$U(r) = \int_0^{2\pi} \int_0^R w(\sqrt{R^2 + r'^2 - 2Rr' \cos\phi}) r' \mathrm{d}r' \mathrm{d}\phi. \tag{5.41}$$

The double integral in (5.41) can be calculated using the Fourier transforms and Bessel function identities.

We start with expressing $w(r)$ as a 2D Fourier transform using polar coordinates

$$w(r) = \frac{1}{2\pi} \int_{\mathbb{R}^2} e^{i\mathbf{r}\cdot\mathbf{k}} \widehat{w}(\mathbf{k}) \mathrm{d}\mathbf{k} = \frac{1}{2\pi} \int_0^\infty \left(\int_0^{2\pi} e^{ir\rho\cos\phi} \widehat{w}(\rho) \mathrm{d}\phi \right) \rho \mathrm{d}\rho, \tag{5.42}$$

where $\widehat{w}$ denotes the Fourier transform of w and $\mathbf{k} = (\rho, \phi)$. Using the integral representation

$$\frac{1}{2\pi} \int_0^{2\pi} e^{ir\rho\cos(\phi - \zeta)} \mathrm{d}\rho = J_0(\rho r), \tag{5.43}$$

where J_0 is the Bessel function of the first kind, we express $w(r)$ in terms of its Hankel transform of order zero

$$w(r) = \int_0^\infty \widehat{w}(\rho) J_0(\rho r) \rho \mathrm{d}\rho, \tag{5.44}$$

which, when substituted into (5.40), gives

$$U(r) = \int_0^{2\pi} \int_0^R \left(\int_0^\infty \widehat{w}(\rho) J_0(\rho|\mathbf{r} - \mathbf{r}'|) \rho \mathrm{d}\rho \right) r' \mathrm{d}r' \mathrm{d}\zeta'. \tag{5.45}$$

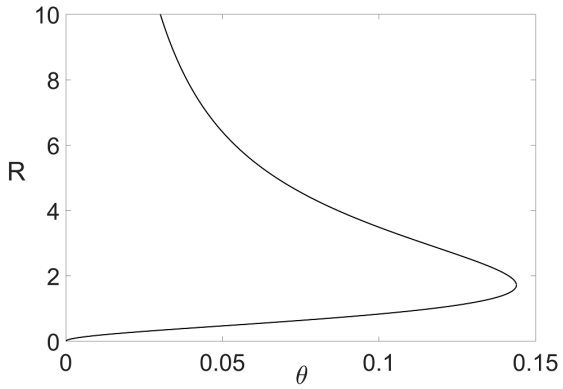

Figure 21: The bump radius is plotted as a function of θ for the Amari model. The coupling function is given by 5.39, with $A = 1/4$ and $\sigma = 2$.

We reverse the order of integration and use the addition theorem

$$J_0(\rho\sqrt{r^2 + r'^2 - 2rr'\cos\zeta'}) = \sum_{m=0}^{\infty} \epsilon_m J_m(\rho r) J_m(\rho r') \cos m\zeta', \tag{5.46}$$

where $\epsilon_0 = 1$ and $\epsilon_n = 2$ for $n \geq 1$. Then using the identity

$$J_1(\rho R)R = \rho \int_0^R J_0(\rho r')r'\mathrm{d}r', \tag{5.47}$$

we obtain

$$U(r) = 2\pi R \int_0^{\infty} \widehat{w}(\rho) J_0(\rho r) J_1(\rho R)\mathrm{d}\rho. \tag{5.48}$$

Knowing that $U(R) = \theta$, we obtain the following necessary condition for the existence of a bump

$$\theta = 2\pi R \int_0^{\infty} \widehat{w}(\rho) J_0(\rho r) J_1(\rho R)\mathrm{d}\rho. \tag{5.49}$$

For the wizard hat coupling function there is a maximum of two bump solutions as shown in Fig. 21. In the next section we investigate the stability of the solutions.

Stability of bumps

In the following, we determine the linear stability of radially symmetric solutions. As in the one-dimensional case, we study the stability of solutions with respect to small perturbations of the bump boundary. We consider different possible perturbations of the circular boundary exhibiting D_n symmetry. Some examples of low-order perturbations are shown in Figure 22.

We consider a steady state

$$U(\mathbf{r}) = \int_{\mathbb{R}^2} w(\mathbf{r} - \mathbf{r}') f(U(\mathbf{r}'))\mathrm{d}\mathbf{r}', \tag{5.50}$$

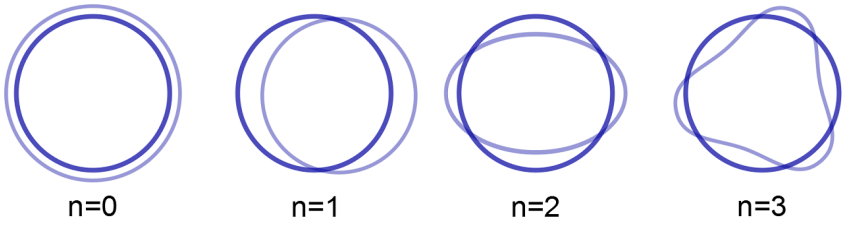

Figure 22: Examples of low-order perturbations of the bump boundary exhibiting D_n symmetry.

and introduce time-dependent perturbations of the circular boundary

$$u(\mathbf{r}, t) = U(\mathbf{r}) + \psi(\mathbf{r}, t). \tag{5.51}$$

We then look for solutions of the form

$$\psi(\mathbf{r}, t) = e^{\lambda t}\psi(\mathbf{r}), \tag{5.52}$$

and get the eigenvalue equation

$$\lambda\psi(\mathbf{r}) = -\psi(\mathbf{r}) + \int_{\mathbb{R}^2} w(\mathbf{r} - \mathbf{r}')\delta(U(\mathbf{r}') - \theta)\psi(\mathbf{r}')\mathrm{d}\mathbf{r}'. \tag{5.53}$$

Using polar coordinates we can rewrite (5.53) as

$$\begin{aligned}\lambda\psi(r, \phi) &= -\psi(r, \phi) \\ &+ \int_0^{2\pi} \mathrm{d}\phi' \int_0^{\infty} r'\mathrm{d}r' w(\sqrt{r^2 + r'^2 - 2rr'\cos\phi})\delta(U(r') - \theta)\psi(r', \phi - \phi').\end{aligned} \tag{5.54}$$

We then look for solutions of the form

$$\psi(r, \phi) = e^{in\phi}\psi(r), \tag{5.55}$$

where n is the number of modes of the boundary perturbation (see Fig. 22).

Equation (5.54) then takes form

$$\lambda\psi(r) = -\psi(r) + \int_0^{2\pi} \mathrm{d}\phi' R w(\sqrt{r^2 + R^2 - 2rR\cos(\phi - \phi')})\frac{\psi(R)e^{-in\phi}}{|U'(R)|}. \tag{5.56}$$

We set $r = R$ and get

$$\lambda\psi(R) = -\psi(R) + \int_0^{2\pi} \mathrm{d}\phi R w(R\sqrt{2 - 2\cos\phi})\frac{\psi(R)e^{-in\phi}}{|U'(R)|}. \tag{5.57}$$

The eigenvalues of 5.57 read

$$\lambda_{-1} = -1, \tag{5.58a}$$

$$\lambda_n = -1 + \frac{R}{|U'(R)|}\int_0^{2\pi} \mathrm{d}\phi w(R\sqrt{2-2\cos\phi}))e^{-in\phi}. \tag{5.58b}$$

Note that λ_n is real, since after setting

$$\sqrt{2-2\cos\phi} = 2\sin\left(\frac{\phi}{2}\right), \tag{5.59}$$

and rescaling ϕ we have

$$Im\{\lambda_n\} = -\frac{2R}{|U'(R)|}\int_0^{\pi} w(2R\sin(\phi))\sin(2n\phi)\mathrm{d}\phi = 0, \tag{5.60}$$

i.e., the integrand is odd-symmetric about $\frac{\pi}{2}$. Hence,

$$\lambda_n = Re\{\lambda_n\} = -1 + \frac{R}{|U'(R)|}\int_0^{2\pi} w(2R\sin(\phi/2))\cos(n\phi)\mathrm{d}\phi, \tag{5.61}$$

with the integrand even-symmetric about $\frac{\pi}{2}$.

We evaluate the integral in (5.61) using Bessel functions

$$\begin{aligned}
&\int_0^{2\pi} w(2R\sin(\phi'/2))\cos(n\phi')\mathrm{d}\phi' \\
&= \int_0^{2\pi}\left(\int_0^{\infty}\widehat{w}(\rho)J_0(\rho(2R\sin(\phi'/2)))\rho\mathrm{d}\rho\right)\cos\phi'\mathrm{d}\phi' \\
&= 2\pi\int_0^{\infty}\widehat{w}(\rho)J_n(\rho R)J_n(\rho R)\rho\mathrm{d}\rho.
\end{aligned} \tag{5.62}$$

We then differentiate (5.48) with respect to r

$$U'(R) = 2\pi R\int_0^{\infty}\widehat{w}(\rho)J_1(\rho R)J_1(\rho R)\rho\mathrm{d}\rho. \tag{5.63}$$

We can now rewrite the eigenvalues as

$$\lambda_{-1} = -1, \tag{5.64a}$$

$$\lambda_n = -1 + \frac{\int_0^{\infty}\widehat{w}(\rho)J_n(\rho R)J_n(\rho R)\rho\mathrm{d}\rho}{\int_0^{\infty}\widehat{w}(\rho)J_1(\rho R)J_1(\rho R)\rho\mathrm{d}\rho}. \tag{5.64b}$$

It follows from (5.64b) that $\lambda_1 = 0$, which is the result of the translation invariance of the system. The points of azimuthal stability determined by the conditions $\lambda_n = 0$ for $n = 0, 2, \ldots, 7$ are shown in the Fig. 23.

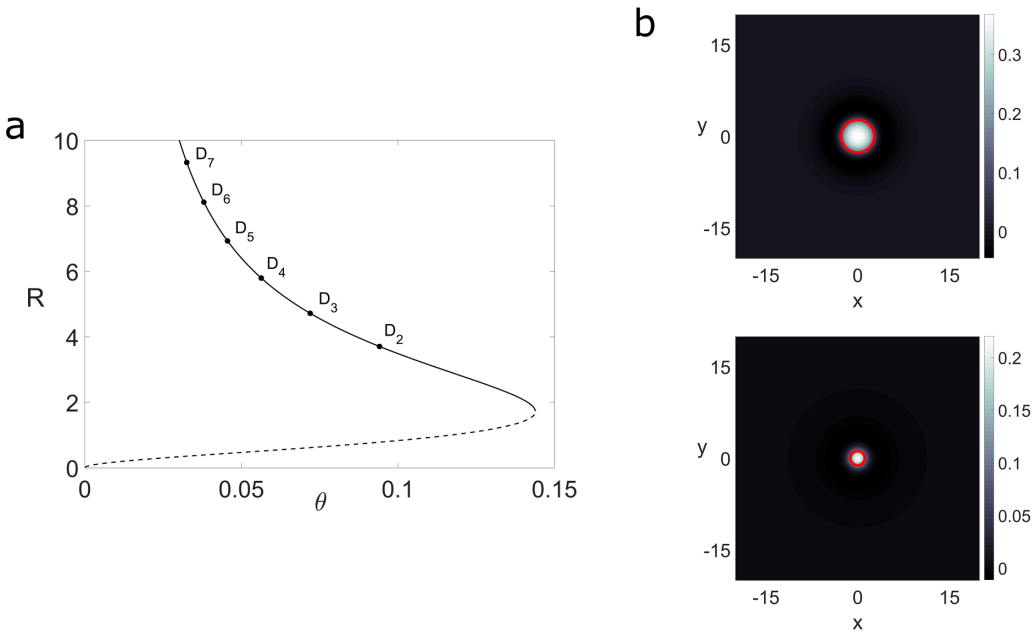

Figure 23: (**a**) Bump radius R as a function of θ for the wizard hat weight distribution (5.39) with $A = 1/4$ and $\sigma = 2$. Solid line: stable solutions, dashed line: unstable solutions. Dots show points along the branch where bumps become unstable to planar perturbations with D_n symmetry. (**b**) Examples of stable solution with radius $R = 2.65$ (top) and unstable solution with radius $R = 1.11$ (bottom) for $\theta = 0.125$. The red circle is the boundary of the bump where $U(R) = \theta$.

5.5 Conclusion

In this chapter, we have discussed three methods that can be used to determine the stability of bump solutions of the Amari model: Amari's linear stability analysis, the Lyapunov method and Pinto and Ermentrout's perturbation approach. With all three methods, we studied the one dimensional model with a Heaviside firing rate function and two choices of the connectivity kernel. Pinto's and Ermentrout's perturbation approach was also used to study the model in two dimensions. All three methods, as expected, yield the same result: the co-existrence of a wider stable bump and a narrower unstable bump.

6 Stability analysis of the two-field model

6.1 Introduction

In this Chapter, we apply the three stability analysis methods presented in previous chapter to the two-field model, starting with the one-dimensional case

$$\frac{\partial u(x,t)}{\partial t} = -u(x,t) + v(x,t) + \int_{\mathbb{R}} w(x-y) f(u(y,t)-\theta)\mathrm{d}y, \tag{6.1a}$$

$$\frac{\partial v(x,t)}{\partial t} = -v(x,t) + u(x,t) - \int_{\mathbb{R}} w(x-y) f(u(y,t)-\theta)\mathrm{d}y, \tag{6.1b}$$

where $f(u)$ is taken again as a Heaviside function (4.6) with threshold θ. Our choice of the coupling function $w(x)$ is again the kernel with a spatially homogeneous inhibition (4.2) and the Mexican hat (4.3) function for the one-dimensional model and the wizard hat function (5.39) for the two-dimensional case.

6.2 Amari's linear stability analysis

Using formulas (5.2) - (5.6), we rewrite (6.1) at $x = x_i(t)$ as

$$\frac{\partial u(x,t)}{\partial t} = -u(x,t) + v(x,t) + \int_{x_1(t)}^{x_2(t)} w(|x-y|)\mathrm{d}y, \tag{6.2a}$$

$$\frac{\partial v(x,t)}{\partial t} = -v(x,t) + u(x,t) - \int_{x_1(t)}^{x_2(t)} w(|x-y|)\mathrm{d}y. \tag{6.2b}$$

Since $u(x_i,t) = \theta$ and $u(x_i,t) + v(x_i,t) = K$, using (5.9) we have from (6.2a)

$$\frac{\partial u(x_i,t)}{\partial t} = -2\theta + K + W(x_2 - x_1), \qquad i = 1,2. \tag{6.3}$$

We obtain the system of ODEs for the boundary points x_1 and x_2

$$\frac{\mathrm{d}x_1}{\mathrm{d}t} = \left.\frac{-\partial u/\partial t}{\partial u/\partial x}\right|_{x=x_1} = -\frac{1}{c_1}\left(-2\theta + K + W(x_2 - x_1)\right), \tag{6.4a}$$

$$\frac{\mathrm{d}x_2}{\mathrm{d}t} = \left.\frac{\partial u/\partial t}{\partial u/\partial x}\right|_{x=x_2} = \frac{1}{c_2}\left(-2\theta + K + W(x_2 - x_1)\right). \tag{6.4b}$$

We can then describe the change of length of the excited region, $\Delta(t) = x_2(t) - x_1(t)$,

$$\frac{\mathrm{d}\Delta}{\mathrm{d}t} = \left(\frac{1}{c_1} + \frac{1}{c_2}\right)\left(-2\theta + K + W(\Delta)\right). \tag{6.5}$$

The existence of a solution of width $\Delta = x_2 - x_1$ is determined by the roots of

$$F(\Delta) = -2\theta + K + W(\Delta) = 0. \tag{6.6}$$

The steady state of width Δ is stable if

$$\frac{\mathrm{d}F(\Delta)}{\mathrm{d}\Delta} < 0, \tag{6.7}$$

and unstable otherwise. We plot examples of function $F(\Delta)$ in Figure 24.

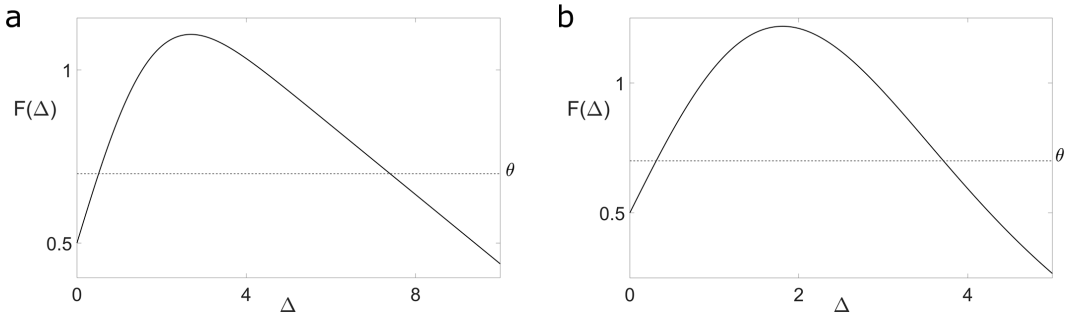

Figure 24: Bump existence in the two-field model (6.1) for a lateral inhibition kernel (4.2) with $A_{lat} = 1$, $\sigma_{lat} = 1.5$, $w_{inh} = 0.2$ (**a**) and Mexican hat kernel (4.3) with $A_{ex} = 3$, $\sigma_{ex} = 1.5$, $A_{inh} = 1.5$, $\sigma_{inh} = 3$ and $w_{inh} = 0.2$ (**b**). In both panels the threshold is $\theta = 0.7$ (dotted line). In panel (**a**) there exist two solutions with $\Delta_1 = 0.51$ (unstable) and $\Delta_2 = 7.4$ (stable). In panel (**b**) we see two solutions with $\Delta_1 = 0.31$ (unstable) and $\Delta_2 = 3.71$ (stable).

6.3 Lyapunov method

We now derive the Lyapunov functional for the two-field model (6.1). The functional can be written as

$$E[u] = -\frac{1}{2}\int_\Omega\int_\Omega w(x-y)f(u(x,t)-\theta)f(u(y,t)-\theta)\mathrm{d}x\mathrm{d}y + (2\theta - K)\int_\Omega f(u(x,t)-\theta)\mathrm{d}x. \tag{6.8}$$

For a bump of width $\Delta = (x_2 - x_1)$ we have

$$E(\Delta) = -\frac{1}{2}\int_{x_1}^{x_2}\int_{x_1}^{x_2} w(x-y)\mathrm{d}x\mathrm{d}y + (2\theta - K)\,(x_2 - x_1). \tag{6.9}$$

Using (5.9), we obtain

$$E(\Delta) = -\int_0^{\Delta} W(x)\mathrm{d}x + (2\theta - K)\,\Delta. \tag{6.10}$$

We plot examples of function $E(\Delta)$ in Figure 25. Similar to the Amari model, for both connectivity functions considered we observe one local maximum and one local minimum, corresponding to unstable and stable bump solutions, respectively.

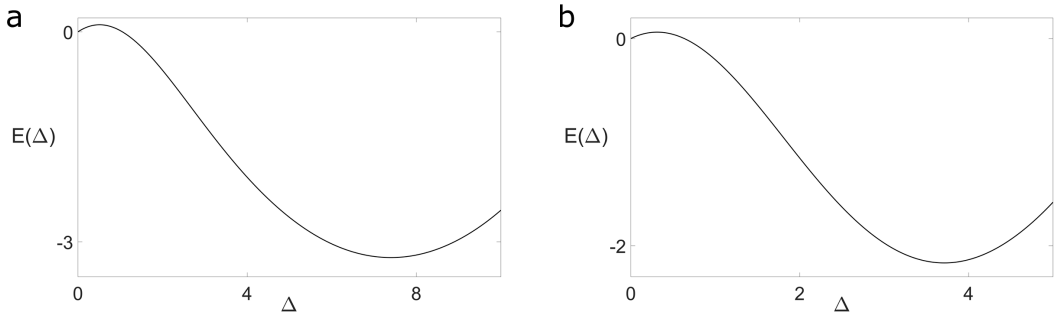

Figure 25: Plot of $E(\Delta)$ given by (5.18) for the two-field model (6.1) with a lateral inhibition kernel (4.2) (**a**) and Mexican hat kernel (4.3) (**b**). In (**a**), there is a local maximum for $\Delta_1 = 0.51$ and a local minimum for $\Delta_2 = 7.4$. In (**b**), there is a local maximum for $\Delta_1 = 0.31$ and a local minimum for $\Delta_2 = 3.71$. Parameters as in Fig. 24.

6.4 Pinto's and Ermentrout's perturbation approach

In this section, we explore the existence and stability of the steady state of the two-field model using Pinto and Ermentrout's stability analysis [121]. We first analyze the model solutions in one spatial dimension. Our analysis is then extended to two spatial dimensions in Section 6.4.2.

6.4.1 1D two-field model

Existence of bumps

We start by constructing stationary bump solutions $u(x,t) = U(x)$, $v(x,t) = V(x)$ that satisfy

$$U(x) = V(x) + \int_{-\infty}^{\infty} w(x-y) f(U(x-y) - \theta)\mathrm{d}y, \tag{6.11a}$$

$$V(x) = U(x) - \int_{-\infty}^{\infty} w(x-y) f(U(x-y) - \theta)\mathrm{d}y. \tag{6.11b}$$

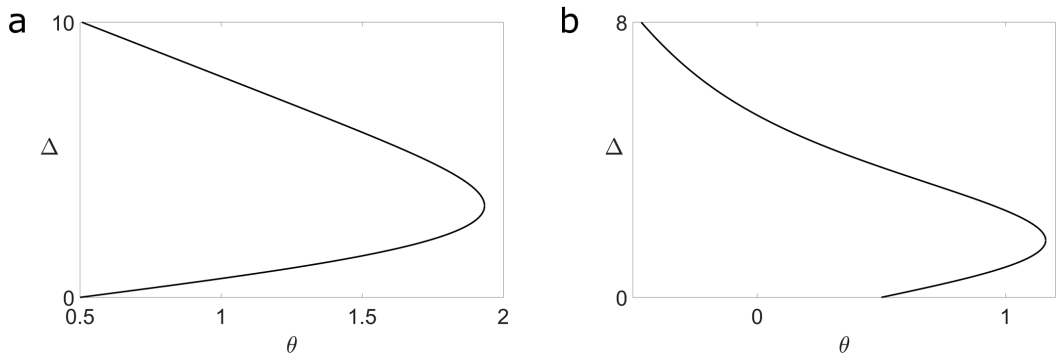

Figure 26: Bump width Δ as a function of θ in the two-field model for a lateral inhibition kernel (4.2) with $A_{lat} = 2$, $\sigma_{lat} = 2$, $w_{inh} = 0.5$ (**a**) and Mexican hat kernel (4.3) with $A_{ex} = 3$, $\sigma_{ex} = 1.4$, $A_{inh} = 1.5$, $\sigma_{inh} = 3$ and $w_{inh} = 0.2$ (**b**). Here, $K = 1$.

For a single bump solution of width $\Delta = x_2 - x_1$, the excited region is the interval $x \in (x_1, x_2)$. The system (6.11) then reduces to

$$U(x) = V(x) + \int_{x_1 - x}^{x_2 - x} w(y)\mathrm{d}y, \tag{6.12a}$$

$$V(x) = U(x) - \int_{x_1 - x}^{x_2 - x} w(y)\mathrm{d}y. \tag{6.12b}$$

We now use (6.12a) to determine the existence of stationary solutions of the model. Knowing that at the bump boundaries $U(x_1) = U(x_2) = \theta$ holds, and setting $x = x_1$ and $x = x_2$, respectively, we have

$$\theta = V(x_1) + \int_{0}^{x_2 - x_1} w(y)\mathrm{d}y, \tag{6.13a}$$

$$\theta = V(x_2) + \int_{x_1 - x_2}^{0} w(y)\mathrm{d}y. \tag{6.13b}$$

We use (5.9) and set $x_1 = -\frac{\Delta}{2}$ and $x_2 = \frac{\Delta}{2}$. Since $V(x) = K - U(x)$, we obtain the following necessary conditions for the existence of a bump

$$\theta = \frac{K + W(\Delta)}{2} = F(\Delta). \tag{6.14}$$

If $\frac{K}{2} < \theta < \frac{K + W_{max}}{2}$, there are two values, Δ_1 and Δ_2, that satisfy (6.14), that is, there are two one-bump solutions with different widths for the same value of θ. If $0 < \theta \leq \frac{K}{2}$, there is one value of Δ that satisfies (6.14). Hence, as in the case of the Amari model, there is maximum of two solutions for a given value of θ for both connectivity functions considered, which we illustrate in Fig. 26.

Stability of bumps

Having determined the existence of single bump solutions in our model, we now use the perturbation approach to derive the stability conditions. We start with introducing the change in width of the excited region under small perturbations $\psi(x,t)$ and $\zeta(x,t)$

$$u(x,t) = U(x) + \psi(x,t), \tag{6.15a}$$

$$v(x,t) = V(x) + \zeta(x,t). \tag{6.15b}$$

Linearizing (6.1) about U leads to the following evolution equations for the perturbations

$$\frac{\partial\psi(x,t)}{\partial t} = -\psi(x,t) + \zeta(x,t) + \int_{-\infty}^{\infty} w(|x-y|)f'(U(y)-\theta)\psi(y,t)\mathrm{d}y, \tag{6.16a}$$

$$\frac{\partial\zeta(x,t)}{\partial t} = -\zeta(x,t) + \psi(x,t) - \int_{-\infty}^{\infty} w(|x-y|)f'(U(y)-\theta)\psi(y,t)\mathrm{d}y. \tag{6.16b}$$

We use (5.28) and assume separable perturbations $(\psi(x,t),\zeta(x,t)) = e^{\lambda t}(\psi(x),\zeta(x))$. We obtain the following eigenvalue equations

$$(\lambda+1)\psi(x) = \zeta(x) + \frac{w(x-x_1)\psi(x_1)}{|U'(x_1)|} + \frac{w(x-x_2)\psi(x_2)}{|U'(x_2)|}, \tag{6.17a}$$

$$(\lambda+1)\zeta(x) = \psi(x) - \frac{w(x-x_1)\psi(x_1)}{|U'(x_1)|} - \frac{w(x-x_2)\psi(x_2)}{|U'(x_2)|}. \tag{6.17b}$$

We eliminate $\zeta(x)$ from (6.17a) using (6.17b)

$$(\lambda+1)\psi(x) = \frac{\psi(x) - \frac{w(x-x_1)\psi(x_1)}{|U'(x_1)|} - \frac{w(x-x_2)\psi(x_2)}{|U'(x_2)|}}{\lambda+1} + \frac{w(x-x_1)\psi(x_1)}{|U'(x_1)|} + \frac{w(x-x_2)\psi(x_2)}{|U'(x_2)|}. \tag{6.18}$$

To calculate $|U'(x_i)|$ we differentiate equation (6.12a) to get

$$U'(x) = V'(x) + [w(x_1-x) - w(x_2-x)], \tag{6.19}$$

and since $\Delta = x_2 - x_1$, knowing that $V(x) = K - U(x)$, we have

$$|U'(x_i)| = \left|\frac{K' + w(x_1-x_i) - w(x_2-x_i)}{2}\right| = \frac{K' + w(0) - w(\Delta)}{2}, \qquad i = 1,2, \tag{6.20}$$

thus since $K' = 0$ we have

$$|U'(x_{1,2})| = \frac{w(0) - w(\Delta)}{2}. \tag{6.21}$$

By setting $x = x_1$ and $x = x_2$ in (6.18) we obtain the system of equations

$$A \cdot \begin{bmatrix} \psi(x_1) \\ \psi(x_2) \end{bmatrix} = \begin{bmatrix} 0 \\ 0 \end{bmatrix},$$

where the matrix A is given by

$$A = \begin{bmatrix} \lambda + 1 - \dfrac{1+a}{\lambda+1} - a & \dfrac{b}{\lambda+1} - b \\ \dfrac{b}{\lambda+1} - b & \lambda + 1 - \dfrac{1+a}{\lambda+1} - a \end{bmatrix},$$

with the parameters a and b defined as

$$a = \frac{w(0)}{|U'(x_{1,2})|}, \qquad b = \frac{w(\Delta)}{|U'(x_{1,2})|}. \tag{6.22}$$

The eigenvalues of A satisfy

$$\frac{\lambda^2 \left(a^2 - 2a(\lambda+2) - b^2 + (\lambda+2)^2\right)}{(\lambda+1)^2} = 0. \tag{6.23}$$

The eigenvalues of A read

$$\lambda_{1,2} = 0, \tag{6.24}$$

$$\lambda_{3,4} = a \pm b - 2. \tag{6.25}$$

The existence of two zero eigenvalues reflects the underlying translation symmetry of the two-field model. The bump is marginally stable with respect to shifts in space as well as shifts in the amplitude.

The remaining eigenvalues are

$$\lambda_3 = a - b - 2 = \frac{2\left(w(0) - w(\Delta)\right)}{w(0) - w(\Delta)} - 2 = 0 \tag{6.26}$$

and

$$\lambda_4 = a + b - 2 = \frac{2\left(w(0) + w(\Delta)\right)}{w(0) - w(\Delta)} - 2 = 0, \tag{6.27}$$

thus, the stability of the bump will be determined by the sign of $w(\Delta)$. Hence, a steady state of width Δ is stable if

$$w(\Delta) < 0. \tag{6.28}$$

Fig. 27 demonstrates the stability of one-bump solutions. They come in pairs, and with increasing threshold θ the two solutions annihilate in a saddle-node bifurcation. Therefore, for threshold values with two existing bump solutions, only the larger bump is stable.

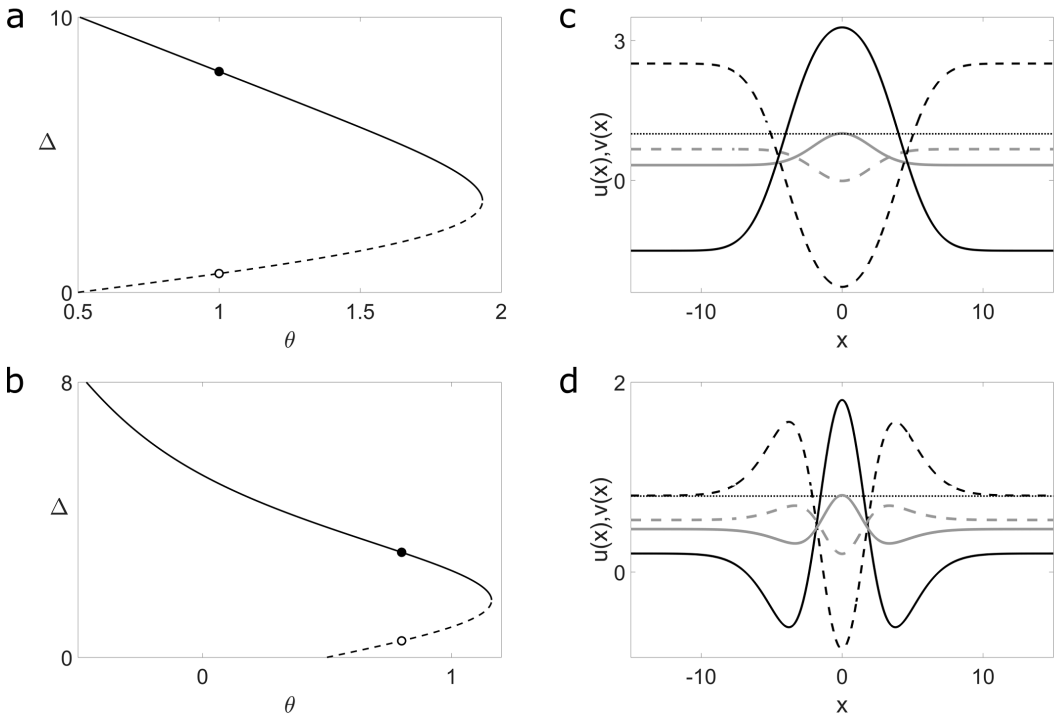

Figure 27: Bump stability in the two-field model for a lateral inhibition kernel (4.2) (**a**) and Mexican hat kernel (4.3) (**b**). Solid (dashed) lines show branches of stable (unstable) solutions. (**c** and **d**) Examples of stable (black lines) and unstable (grey lines) bump solutions correspond to the filled (unfilled) dots in the panels on the left. (**c**) Solution widths are $\Delta_1 = 0.68$ (unstable bump) and $\Delta_2 = 8.03$ (stable bump), threshold $\theta = 1$. (**d**) Solution widths are $\Delta_1 = 0.48$ (unstable bump) and $\Delta_2 = 3.05$ (stable bump), threshold $\theta = 0.8$. Remaining parameters as in Fig. 26.

6.4.2 2D two-field model

In what follows, we analyze the two-field neural field model in two spatial dimensions. The model reads

$$\frac{\partial u(\mathbf{r},t)}{\partial t} = -u(\mathbf{r},t) + v(\mathbf{r},t) + \int_{\mathbb{R}^2} w(\mathbf{r}-\mathbf{r}')f(u(\mathbf{r}',t))\mathrm{d}\mathbf{r}', \tag{6.29a}$$

$$\frac{\partial v(\mathbf{r},t)}{\partial t} = -v(\mathbf{r},t) + u(\mathbf{r},t) - \int_{\mathbb{R}^2} w(\mathbf{r}-\mathbf{r}')f(u(\mathbf{r}',t))\mathrm{d}\mathbf{r}', \tag{6.29b}$$

where $\mathbf{r} = (r,\phi)$, $r \in \mathbb{R}^+$ and $\phi \in [0, 2\pi)$. We consider a wizard hat weight distribution given by (5.39).

Existence of bumps

We consider a radially symmetric bump solution of radius R such that $u(\mathbf{r},t) = U(r)$ with $U(R) = \theta$, $U(r) > \theta$ for $r < R$, $U(r) < \theta$ for $r > R$ and $U(r) \to 0$ as $r \to \infty$. A stationary solution of system

(6.29) then gives

$$U(r) = V(r) + \int_0^{2\pi} \int_0^R w(|\mathbf{r} - \mathbf{r}'|) r' \mathrm{d}r' \mathrm{d}\phi, \tag{6.30a}$$

$$V(r) = U(r) - \int_0^{2\pi} \int_0^R w(|\mathbf{r} - \mathbf{r}'|) r' \mathrm{d}r' \mathrm{d}\phi. \tag{6.30b}$$

Using $|\mathbf{r} - \mathbf{r}'| = \sqrt{r^2 + r'^2 - 2rr' \cos\phi}$ we rewrite system (6.30) as

$$U(r) = V(r) + \int_0^{2\pi} \int_0^R w(\sqrt{R^2 + r'^2 - 2Rr' \cos\phi}) r' \mathrm{d}r' \mathrm{d}\phi, \tag{6.31a}$$

$$V(r) = U(r) - \int_0^{2\pi} \int_0^R w(\sqrt{R^2 + r'^2 - 2Rr' \cos\phi}) r' \mathrm{d}r' \mathrm{d}\phi. \tag{6.31b}$$

The double integral in (6.31) can be calculated using the Fourier transforms and Bessel function identities in the same way as for the Amari model. We use formulas (5.42) - (5.44) to get

$$U(r) = V(r) + \int_0^{2\pi} \int_0^R \left(\int_0^\infty \widehat{w}(\rho) J_0(\rho|\mathbf{r} - \mathbf{r}'|) \rho \mathrm{d}\rho \right) r' \mathrm{d}r' \mathrm{d}\phi', \tag{6.32a}$$

$$V(r) = U(r) - \int_0^{2\pi} \int_0^R \left(\int_0^\infty \widehat{w}(\rho) J_0(\rho|\mathbf{r} - \mathbf{r}'|) \rho \mathrm{d}\rho \right) r' \mathrm{d}r' \mathrm{d}\phi'. \tag{6.32b}$$

We reverse the order of integration and use the addition theorem as in (5.46) and use the identity (5.47) to obtain

$$U(r) = V(r) + 2\pi R \int_0^\infty \widehat{w}(\rho) J_0(\rho r) J_1(\rho R) \mathrm{d}\rho, \tag{6.33a}$$

$$V(r) = U(r) - 2\pi R \int_0^\infty \widehat{w}(\rho) J_0(\rho r) J_1(\rho R) \mathrm{d}\rho. \tag{6.33b}$$

Knowing that $U(R) = \theta$ and $K = U(r) + V(r)$ we get the following necessary condition for the existence of a bump

$$\theta = \frac{K}{2} + \pi R \int_0^\infty \widehat{w}(\rho) J_0(\rho r) J_1(\rho R) \mathrm{d}\rho. \tag{6.34}$$

For the wizard hat coupling function, as in the case of the Amari model, there is a maximum of two bump solutions as shown in Fig. 28. In the next section we investigate the stability of these solutions.

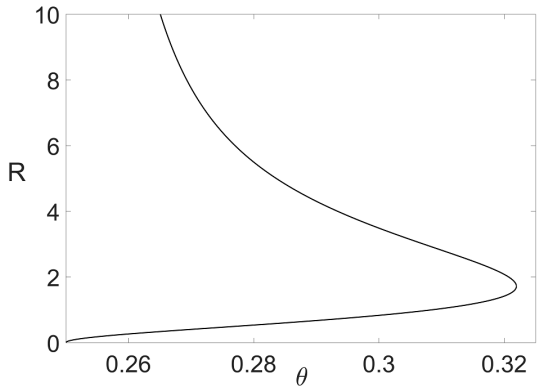

Figure 28: Bump radius R as a function of θ for the two-field model. The coupling function is given by 5.39, with $A = 1/4$ and $\sigma = 2$. Here, $K = 0.5$.

Stability of a 2D bump

In the following we determine the linear stability of radially symmetric solutions. As for the previous case, we study the stability with respect to small perturbations of the bump boundary. We consider different possible perturbations of the circular boundary exhibiting D_n symmetry (see Figure 22).

The stationary solution is given by

$$U(\mathbf{r}) = V(\mathbf{r}) + \int_{\mathbb{R}^2} w(\mathbf{r} - \mathbf{r}') f(U(\mathbf{r}'))\mathrm{d}\mathbf{r}', \tag{6.35a}$$

$$V(\mathbf{r}) = U(\mathbf{r}) - \int_{\mathbb{R}^2} w(\mathbf{r} - \mathbf{r}') f(U(\mathbf{r}'))\mathrm{d}\mathbf{r}'. \tag{6.35b}$$

We introduce time-dependent perturbations of the circular boundary

$$u(\mathbf{r}, t) = U(\mathbf{r}) + \psi(\mathbf{r}, t), \tag{6.36a}$$

$$v(\mathbf{r}, t) = V(\mathbf{r}) + \zeta(\mathbf{r}, t). \tag{6.36b}$$

We then look for solutions of the separable form

$$(\psi(\mathbf{r}, t), \zeta(\mathbf{r}, t)) = e^{\lambda t}(\psi(\mathbf{r}), \zeta(\mathbf{r})), \tag{6.37}$$

and get

$$\lambda\psi(\mathbf{r}) = -\psi(\mathbf{r}) + \zeta(\mathbf{r}) + \int_{\mathbb{R}^2} w(\mathbf{r} - \mathbf{r}')\delta(U(\mathbf{r}') - h)\psi(\mathbf{r}')\mathrm{d}\mathbf{r}', \tag{6.38a}$$

$$\lambda\zeta(\mathbf{r}) = -\zeta(\mathbf{r}) + \psi(\mathbf{r}) - \int_{\mathbb{R}^2} w(\mathbf{r}-\mathbf{r}')\delta(U(\mathbf{r}')-h)\psi(\mathbf{r}')\mathrm{d}\mathbf{r}'. \tag{6.38b}$$

We rewrite system (6.38) as

$$\begin{aligned}\lambda\psi(r,\phi) &= -\psi(r,\phi) + \zeta(r,\phi)\\ &+ \int_0^{2\pi}\mathrm{d}\phi' \int_0^{\infty} r'\mathrm{d}r' w(\sqrt{r^2+r'^2-2rr'\cos\phi})\delta(U(r')-h)\psi(r',\phi-\phi'),\end{aligned} \tag{6.39a}$$

$$\begin{aligned}\lambda\zeta(r,\phi) &= -\zeta(r,\phi) + \psi(r,\phi)\\ &- \int_0^{2\pi}\mathrm{d}\phi' \int_0^{\infty} r'\mathrm{d}r' w(\sqrt{r^2+r'^2-2rr'\cos\phi})\delta(U(r')-h)\psi(r',\phi-\phi').\end{aligned} \tag{6.39b}$$

We look for solutions of the form

$$(\psi(r,\phi),\zeta(r,\phi)) = e^{in\phi}(\psi(r),\zeta(r)), \tag{6.40}$$

where n is the number of modes of the boundary perturbation (see Fig. 22). System (6.39) then takes the form

$$\begin{aligned}\lambda\psi(r)e^{in\phi} &= -\psi(r)e^{in\phi} + \zeta(r)e^{in\phi}\\ &+ \int_0^{2\pi}\mathrm{d}\phi' \int_0^{\infty} r'\mathrm{d}r' w(\sqrt{r^2+r'^2-2rr'\cos(\phi-\phi')})\delta(U(r')-h)\psi(r')e^{in(\phi-\phi')},\end{aligned} \tag{6.41a}$$

$$\begin{aligned}\lambda\zeta(r)e^{in\phi} &= -\zeta(r)e^{in\phi} + \psi(r)e^{in\phi}\\ &- \int_0^{2\pi}\mathrm{d}\phi' \int_0^{\infty} r'\mathrm{d}r' w(\sqrt{r^2+r'^2-2rr'\cos(\phi-\phi')})\delta(U(r')-h)\psi(r')e^{in(\phi-\phi')}.\end{aligned} \tag{6.41b}$$

After dividing both sides by $e^{in\phi}$ we have

$$\begin{aligned}\lambda\psi(r) &= -\psi(r) + \zeta(r)\\ &+ \int_0^{2\pi}\mathrm{d}\phi' R w(\sqrt{r^2+R^2-2rR\cos(\phi-\phi')})\frac{\psi(R)e^{-in\phi}}{|U'(R)|},\end{aligned} \tag{6.42a}$$

$$\begin{aligned}\lambda\zeta(r) &= -\zeta(r) + \psi(r)\\ &- \int_0^{2\pi}\mathrm{d}\phi' R w(\sqrt{r^2+R^2-2rR\cos(\phi-\phi')})\frac{\psi(R)e^{-in\phi}}{|U'(R)|}.\end{aligned} \tag{6.42b}$$

We set $r = R$ and get

$$\begin{aligned}\lambda\psi(R) &= -\psi(R) + \zeta(R)\\ &+ \int_0^{2\pi}\mathrm{d}\phi R w(R\sqrt{2-2\cos\phi})\frac{\psi(R)e^{-in\phi}}{|U'(R)|},\end{aligned} \tag{6.43a}$$

$$\begin{aligned}\lambda\zeta(R) &= -\zeta(R) + \psi(R) \\ &\quad - \int_0^{2\pi} \mathrm{d}\phi R w(R\sqrt{2-2\cos\phi}) \frac{\psi(R)e^{-in\phi}}{|U'(R)|}.\end{aligned} \tag{6.43b}$$

The system (6.43) can be written as

$$A \cdot \begin{bmatrix} \psi(R) \\ \zeta(R) \end{bmatrix} = \begin{bmatrix} 0 \\ 0 \end{bmatrix},$$

where the matrix A is given by

$$A = \begin{bmatrix} \lambda + 1 - S_n & -1 \\ -1 + S_n & \lambda + 1 \end{bmatrix},$$

with

$$S_n = \frac{R}{|U'(R)|} \int_0^{2\pi} \mathrm{d}\phi w(R\sqrt{2-2\cos\phi}) e^{-in\phi}. \tag{6.44}$$

Then, we find that

$$(\lambda + 1 + S_n)(\lambda + 1) - (-1 + S_n)(-1 + S_n) = 0. \tag{6.45}$$

Hence the eigenvalues of A are

$$\lambda_{-1} = 0, \tag{6.46}$$

$$\lambda_n = -2 + S_n. \tag{6.47}$$

Note that λ_n is real, since after setting

$$\sqrt{2-2\cos\phi} = 2\sin\left(\frac{\phi}{2}\right), \tag{6.48}$$

and rescaling θ we have

$$Im\{\lambda_n\} = -\frac{2R}{|U'(R)|} \int_0^{\pi} w(2R\sin(\phi))\sin(2n\phi)\mathrm{d}\phi = 0, \tag{6.49}$$

i.e., the integrand is odd-symmetric about $\frac{\pi}{2}$. Hence,

$$\lambda_n = Re\{\lambda_n\} = -2 + \frac{R}{|U'(R)|} \int_0^{2\pi} w(2R\sin(\phi/2))\cos(n\phi)\mathrm{d}\phi, \tag{6.50}$$

with the integrand even-symmetric about $\frac{\pi}{2}$.

We evaluate the integral in (6.50) using Bessel functions (5.62) and differentiate (6.33a) with respect to r

$$U'(R) = V'(R) - 2\pi R \int_0^{\infty} \widehat{w}(\rho) J_1(\rho R) J_1(\rho R) \rho \mathrm{d}\rho. \tag{6.51}$$

Knowing that $K = U(r) + V(r)$ we have

$$U'(R) = \frac{K'}{2} - \pi R \int_0^\infty \widehat{w}(\rho) J_1(\rho R) J_1(\rho R) \rho \mathrm{d}\rho. \tag{6.52}$$

We can now write the eigenvalues of A as

$$\lambda_{-1} = 0, \tag{6.53}$$

$$\lambda_n = -2 + \frac{4\pi R}{K' + 2\pi R} \frac{\int_0^\infty \widehat{w}(\rho) J_n(\rho R) J_n(\rho R) \rho \mathrm{d}\rho}{\int_0^\infty \widehat{w}(\rho) J_1(\rho R) J_1(\rho R) \rho \mathrm{d}\rho}. \tag{6.54}$$

Since $K' = 0$ we have

$$\lambda_{-1} = 0, \tag{6.55}$$

$$\lambda_n = -2 + 2 \frac{\int_0^\infty \widehat{w}(\rho) J_n(\rho R) J_n(\rho R) \rho \mathrm{d}\rho}{\int_0^\infty \widehat{w}(\rho) J_1(\rho R) J_1(\rho R) \rho \mathrm{d}\rho}. \tag{6.56}$$

Unlike in the Amari model, we have $\lambda_{-1} = 0$ (compare with (5.64a)). We conclude that this zero eigenvalue results from the bump being marginally stable to perturbations of the amplitude. It follows from (6.56) that $\lambda_1 = 0$, which is the result of the spatial translation invariance of the system. For $n = 0, 2, \ldots, 7$, we plot the points of azimuthal stability determined by the conditions $\lambda_n = 0$ in Fig. 29.

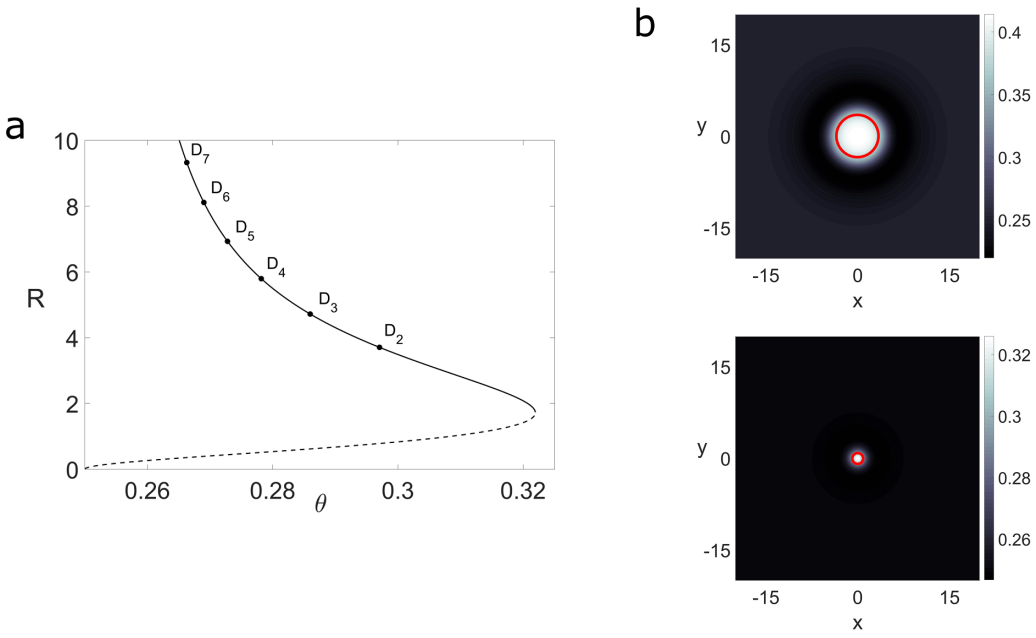

Figure 29: (**a**) Bump radius R as a function of θ in the two-field model for the wizard hat weight distribution (5.39) with $A = 1/4$ and $\sigma = 2$. Dots show points along the branch where bumps become unstable to planar perturbations with $D_2 \dots D_7$ symmetry. (**b**) Examples of stable solution with radius $R = 3.49$ (top) and unstable solution with radius $R = 0.83$ (bottom) for $\theta = 0.3$. The red circle indicates the boundary of the bump where $U(R) = \theta$. Here, $K = 0.5$.

6.5 Conclusion

In this chapter, we have demonstrated that all three methods that we used for analyzing the Amari model can be generalized to the analysis of the two-field model. We used a similar setting as in the previous chapter, i.e. lateral inhibition and Mexican hat kernels in one dimension, and a wizard hat function in two dimensions. The main conclusion is that with respect to the existence and stability of single bump solutions the two models show the same qualitative behavior. Single bumps appear in pairs, with the narrower bump being unstable and the wider bump being stable.

7 Numerical analysis of N-bump solutions

7.1 Introduction

In the previous chapter, we concentrated our efforts on the stability analysis of single bump solutions in neural field models following Amari's seminal work [3]. It was shown later by Laing et al. [98] that the Amari model with Mexican-hat kernel and Heaviside step function does not support stable N-bump solutions consisting of $N \geq 2$ disjoint areas of excitation. Numerical evidence suggest, however, that stable N-bumps might exist if a sigmoid function is used and the individual bumps are separated by a distance where the interaction strength is weak [37]. The search for general conditions supporting stable N-bump solutions has triggered investigation on connectivity functions with more than one zero crossing. It has been shown by Laing et al. [98] that a connectivity function of oscillatory type (4.4), with alternating regions of lateral excitation and lateral inhibition, supports stable multi-bump solutions. This line of research has been later extended by Ferreira et al. [55] to include also conditions on the external inputs that are able to trigger the evolution of these attractor solutions.

The goal of this chapter is threefold. First, to verify in numerical model simulations the hypotheses suggested by the analysis of the space-clamped model (4.11) that the two-field model supports bump solutions with the shape depending on the initial conditions. Second, to introduce numerical bifurcation techniques that allow us to find and to track as model parameters vary single and multi-bump solutions of the two-field model with lateral inhibition kernel. Third, to directly compare N-bump solutions and their dependence on model parameters for the Amari and the two-field model with oscillatory interaction kernel. There exist several software packages available for carrying out the numerical continuation, such as AUTO-07P [42], Matlab package MATCONT [41] and C++ library Trilinos [135], to give but a few examples. These tools were designed for low-dimensional problems and are not suitable for analysing high-dimensional systems of equations that result from the discretization of the neural field equations [97]. A possible workaround is to reduce the neural field equation to equivalent ODE (when $\Omega \subset \mathbb{R}$) or PDE (when $\Omega \subset \mathbb{R}^2$)

formulation that show the same qualitative behavior of the pattern formation process. Both strategies have been used in neural field literature. Examples of ODE formulations can be found in [71, 98, 154]; PDEs were used in [38, 99, 100]. This reduction makes it possible to apply standard continuation packages to investigate the behavior of neural field models. A commonly used tool is AUTO-07P (standalone or embedded in software package XPPAUT [52]), as for example in [38, 71, 98, 100]. The Trilinos library has been also used to study behavior of neural field equations [124, 153, 154].

For the present work, we choose to follow the approach outlined in [123] and adapt the Matlab code available in [8]. It allows us to find steady state solutions of both the Amari model and the two-field model with an oscillatory coupling function or a Mexican hat coupling function. The main advantage of this method is that it can be applied directly to the full model, without the need to rely on ODE or PDE aproximations. This is possible due to the usage of Newton–GMRES solvers combined with a fast Fourier transform (FFT) employed for computing the convolution term [123]. Since the continuation method requires that the transfer function is differentiable, we use a sigmoid function with a sufficiently large slope parameter β to approximate the step function.

An immediate question is which parameter(s) we should choose for the numerical continuation. For the oscillatory kernel, we decide to use as examples the firing threshold θ and parameter b of the kernel, and fix the remaining parameters of the models. This choice allows us to compare our results with findings in literature, where N-bump solutions of neural field equations have been studied numerically in terms of both θ (e.g., [9, 37, 99]) and b (e.g., [45, 98]). For the Mexican hat coupling function, we use threshold θ as a continuation parameter. It is important to keep in mind that the bifurcation methods used in this chapter can be applied to study other model parameters as well.

7.2 Numerical bifurcation method

7.2.1 Pseudo-arclength continuation

Numerical continuation is a method for finding solutions of equations

$$F(\mathbf{v}, p) = 0, \tag{7.1}$$

where $\mathbf{v}$ is the $(M+1)$-dimensional column vector with components $u_0, u_1, \ldots, u_M$, and $F : \mathbb{R}^M \times \mathbb{R} \to \mathbb{R}^M$. We can find stable solutions of (7.1) by numerically integrating the system for a sufficiently long time. Both stable and unstable solutions of (7.1) can be found using Newton's method, starting sufficiently close

to them. By repeating this step and varying parameter p we obtain a branch of solutions to (7.1), the procedure known as natural parameter continuation [68]. The main disadvantage of this approach is that it fails if a branch contains fold points, i.e. turning points with respect to the parameter p.

One way to overcome this limitation is to drop the natural parametrization by p and use some other parameterization, which is the main idea of the pseudo-arclength continuation method proposed by Keller [85]. We give a brief overview of the method below.

Instead of the natural parametrization by p, the curve Γ is now parametrised by arclength s, thus $\Gamma(s) = (\mathbf{v}(s), p(s))$ is a curve of solutions to $F(\mathbf{v}, p)$. Given one of the solutions of (7.1), $(\mathbf{v}_0, p_0)$, we want to find a nearby solution, $(\mathbf{v}_1, p_1)$, which also satisfies (7.1). It must also satisfy the pseudo-arclength condition

$$(\mathbf{v}_1 - \mathbf{v}_0)^T \dot{\mathbf{v}}_0 + (p_1 - p_0)\dot{p}_0 - \Delta s = 0, \tag{7.2}$$

where Δs is the pseudo-arclength stepsize, $(\dot{\mathbf{v}}_0, \dot{p}_0)$ is the tangent vector to the curve at $(\mathbf{v}_0, p_0)$, normalized to have length 1 and a superscript T indicates transpose. The overdot indicates differentiation with respect to arclength, s. Geometrically it means that we find a solution $(\mathbf{v}_1, p_1)$ of the equation $F(\mathbf{v}, p) = 0$ in a hyperplane that is both a distance Δs from the point on the curve $(\mathbf{v}_0, p_0)$ and perpendicular to the direction vector $(\dot{\mathbf{v}}_0, \dot{p}_0)$, see Figure 30.

To find point $(\mathbf{v}_1, p_1)$, we use the following Newton iteration to solve (7.1) and (7.2) simultaneously for $(\mathbf{v}(s), p(s))$

$$\begin{pmatrix} \mathbf{v}_1^{(i)} \\ p_1^{(i)} \end{pmatrix} = \begin{pmatrix} \mathbf{v}_1^{(i-1)} \\ p_1^{(i-1)} \end{pmatrix} - J_{(i-1)}^{-1} \begin{pmatrix} F(\mathbf{v}_1^{(i-1)}, p_1^{(i-1)}) \\ (\mathbf{v}_1^{(i-1)} - \mathbf{v}_0)^T \dot{\mathbf{v}}_0 + (p_1^{(i-1)} - p_0)\dot{p}_0 - \Delta s \end{pmatrix}, \tag{7.3}$$

for $i = 1, 2, \ldots, (M+1)_{(M+1)}$, where

$$J_{(i)} = \begin{pmatrix} F_v & F_p \\ \dot{\mathbf{v}}_0 & \dot{p}_0 \end{pmatrix} \tag{7.4}$$

is the $(M+2) \times (M+2)$ Jacobian of the augmented system, and the partial derivatives are evaluated at $(\mathbf{v}_1^{(i)}, p_1^{(i)})$. The stability of the point $(\mathbf{v}_1, p_1)$ depends on the eigenvalues of F_v evaluated at this point. Next points on the curve of solutions are found in successive Newton iterations.

7.2.2 Problem setting

Here we give an overview of the set up of our system and describe how Avitabile's numerical continuation software [8] can be applied to neural field models. Our approach is explained for the Amari model, the

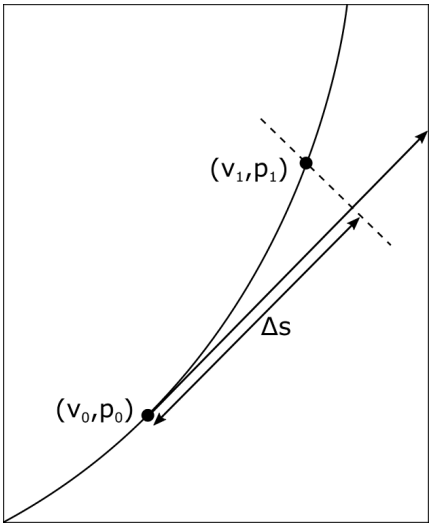

Figure 30: A scheme of the relation expressed by (7.2). The solid line indicates the curve of solutions, and the tangent to this curve at (v_0, p_0) is shown by an arrow.

extension to two fields is straightforward. We consider the model

$$\frac{\partial u(\mathbf{x},t)}{\partial t} = -u(\mathbf{x},t) + \int_\Omega w(\mathbf{x},\mathbf{x}')f(u(\mathbf{x}',t)-\theta)\mathrm{d}\mathbf{x}' + g(\mathbf{x}), \tag{7.5}$$

posed on a domain Ω which is a subset of $\mathbb{R}^d$. In the following we use fields with dimensions $d = 1$ and $d = 2$. We choose a finite domain sufficiently large that there is no activity near the boundaries in order to imitate the infinite domain. In particular, for one-dimensional models we assume the domain $\Omega : [-L, L]$, $L = 12\pi$, which we discretise over a uniform grid of $N = 2^{16}$ points.

The firing rate function is the sigmoidal function given by (4.7). We employ two types of lateral connectivity, the classical Mexican hat function (4.3) and the decaying oscillatory function (4.4).

The term $g(\mathbf{x})$ represent weak external input ($g(\mathbf{x}) \ll 1$). Its role is to break the translational invariance of the system so that we can apply Newton iterations directly to (7.5) [123].

Numerical computations of the model (7.5) are performed, discretizing a large but finite domain $\Omega = [-L, L]^d$ with N evenly distributed grid points in each spatial direction and imposing periodic boundary conditions. We approximate u on a grid $\Omega_N = \{(x_i, y_j)\}_{i,j=1}^N$ and collect the corresponding approximate values of u in a vector **u**

$$u_{ij} \approx u(x_i, y_i), \qquad \mathbf{u} = \{u_{ij}\}_{i,j=1}^N \in \mathbb{R}^{N^d}. \tag{7.6}$$

Similarly, we get vectors **w**, **f(u)**, **g** $\in \mathbb{R}^{N^d}$ for the approximations to w, $f(u)$ and g, respectively. Further, we introduce the discrete convolution,

$$(u * v)_{ij} \approx \mathcal{F}^{-1}(\mathcal{F}(u)\mathcal{F}(v))(x_i, y_i), \qquad \mathbf{u} * \mathbf{v} = \{(u * v)_{ij}\}_{i,j=1}^N \in \mathbb{R}^{N^d}, \tag{7.7}$$

where $\mathcal{F}$ and $\mathcal{F}^{-1}$ is the Fourier transform and its inverse, respectively. The spatially discrete version of the evolution equation (7.5) is thus given by

$$\dot{\mathbf{u}} = -\mathbf{u} + \mathbf{w} * \mathbf{f}(\mathbf{u}). \tag{7.8}$$

For numerical continuation of steady states of (7.5), we solve the system of algebraic equations

$$\mathbf{F}(\mathbf{u}) = -\mathbf{u} + \mathbf{w} * \mathbf{f}(\mathbf{u}) = \mathbf{0}, \tag{7.9}$$

whose associated Jacobian-vector product is given by

$$\mathbf{J}(\mathbf{u})\mathbf{v} = -\mathbf{v} + \mathbf{w} * (\mathbf{f'}(\mathbf{u})\mathbf{v}), \quad \mathbf{u}, \mathbf{v} \in \mathbb{R}^N, \tag{7.10}$$

where $\mathbf{f'}(\mathbf{u}) = \operatorname{diag}(f'(u_{11}), \ldots, f'(u_{NN})) \in \mathbb{R}^{N\times N}$. We solve the system (7.9) iteratively using the Newton generalised minimal residual method (Newton-GMRES) implemented in MATLAB and continue the solution with a secant method using the code adapted from [8]. Eigenvalue computations are also performed using the Jacobian-vector products (7.10).

7.3 Mexican hat kernel

In this section we study both neural field models in one spatial dimension ($d = 1$). We consider the Mexican hat connectivity function (4.3) and steep sigmoidal firing rate function (4.7) using $\beta = 50$ as an example.

7.3.1 Amari model

We begin our numerical study with the Amari model (7.5). First we integrate the model with the initial activation profile at $t = 0$ given by

$$u(x, 0) = A_u e^{\left(-x^2/2\sigma_u^2\right)}. \tag{7.11}$$

Weak external inhomogeneous input $g(x)$ is given by

$$g(x) = G_0 e^{\left(-x^2/2\sigma_g^2\right)}, \tag{7.12}$$

where $G_0 = 0.001$ and $\sigma_g = \sqrt{10}$. In Figure 31 we show the 1-bump solution of the Amari model with a Mexican hat kernel (4.3) for a set of three different initial profiles (7.11). As expected for the Amari model, the shape of the solution is determined solely by the connectivity function $w(x)$ and is not affected by the initial state of the field. Every initial condition converged to the same bump attractor.

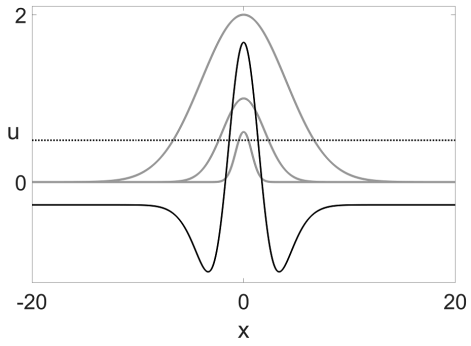

Figure 31: One-bump solution of the Amari model (7.5) (black) for a set of three different initial profiles (7.11) (grey) with parameters: $A_u = 2$, $\sigma_u = 4$ (wide curve), $A_u = 1$, $\sigma_u = 2$ (intermediate curve), $A_u = 0.6$, $\sigma_u = 0.75$ (narrow curve). The kernel $w(x)$ is given by (4.3) with $A_{ex} = 2$, $A_{in} = 1$, $\sigma_{ex} = 1.25$, $\sigma_{in} = 2.5$ and $w_{inh} = 0.1$. Threshold $\theta = 0.5$ (dotted line).

We now perform numerical continuation of the solution shown in Fig. 31 using the threshold θ as a continuation parameter. The resulting solution curve is depicted in Figure 32. The curve consists of an upper branch of stable solutions and a lower branch of unstable solutions that connect in a saddle-node bifurcation. The numerical continuation technique thus confirms the analytical result of Chapter 6.

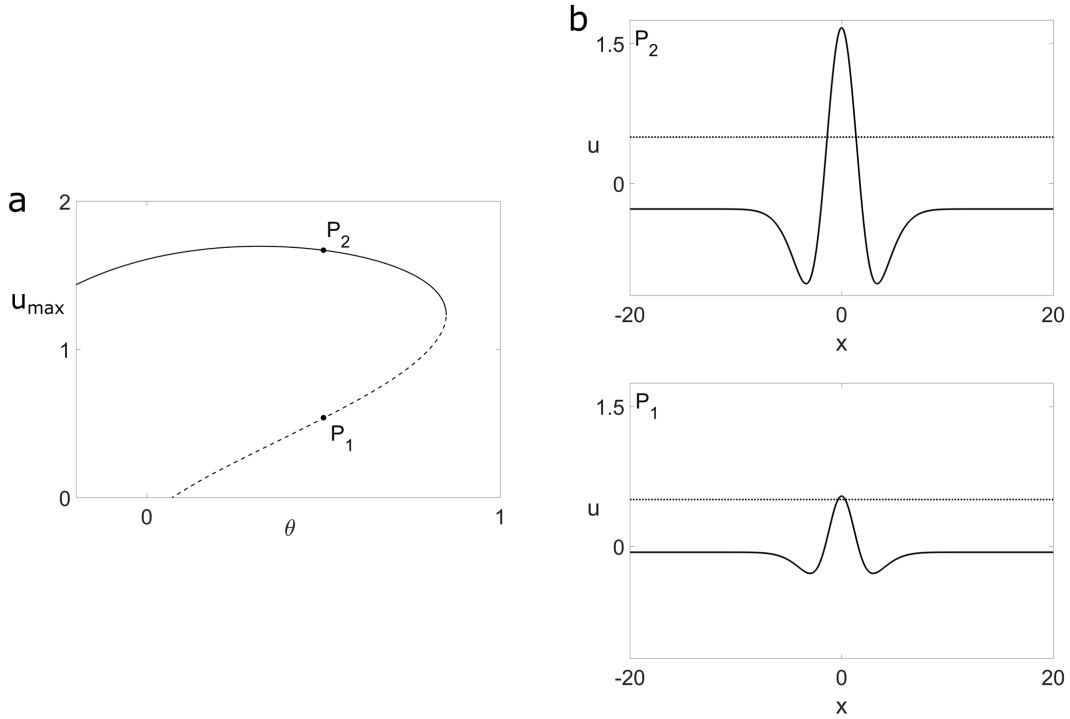

Figure 32: (**a**) Bifurcation curve showing one-bump solutions of (7.5) with a Mexican hat kernel (4.3) as the parameter θ is varied. Solid (dashed) lines represent stable (unstable) solutions. (**b**) Examples of solutions at points P_1 (unstable) and P_2 (stable) for $\theta = 0.5$ (dotted line). Parameters of the kernel as in Fig. 31.

7.3.2 Two-field model

We now investigate localized activation patterns of the two-field model

$$\frac{\partial u(\mathbf{x},t)}{\partial t} = -u(\mathbf{x},t) + v(\mathbf{x},t) + \int_\Omega w(\mathbf{x},\mathbf{x}')f(u(\mathbf{x}',t)-\theta)\mathrm{d}\mathbf{x}', \tag{7.13a}$$

$$\frac{\partial v(\mathbf{x},t)}{\partial t} = -v(\mathbf{x},t) + u(\mathbf{x},t) - \int_\Omega w(\mathbf{x},\mathbf{x}')f(u(\mathbf{x}',t)-\theta)\mathrm{d}\mathbf{x}', \tag{7.13b}$$

with the Mexican hat kernel (4.3).

To highlight the difference to the Amari model we focus on two results, 1) the dependence of the bump shape on initial conditions, and 2) the existence of numerically stable two-bump solutions.

Model with initial condition $u(x,0)+v(x,0)=K$

The initial conditions for $u(x,0)$ and $v(x,0)$ are given by

$$u(x,0) = A_u e^{\left(-x^2/2\sigma_u^2\right)}, \tag{7.14a}$$

$$v(x,0) = K - u(x,0), \tag{7.14b}$$

where K is a constant. The Gaussian pattern is used in the initial state of the u-layer to ensure that a localized solution evolves in the field.

We show in Figure 33 example solutions of (7.13) for two different values of the threshold θ. These values correspond to the two cases considered in Section 4.2 when discussing the space-clamped field equation: $K < 2\theta$ and $K \geq 2\theta$. The first case, with $K = 1$ and $\theta = 0.8$, is depicted in panels (**a**) and (**b**). If the initial state of the u-field (7.14a) is below the threshold θ, both fields converge to a uniform subthreshold activity value $u(x) = v(x) = K/2$ (panel **a**). If its value is higher than θ, a stable one-bump solution evolves (panel **b**).

We now consider the second case ($K \geq 2\theta$). In Figure 33, we show one-bump solution that evolved from a wider (panel **c**) and a narrower (panel **d**) initial condition (7.14). Consistent with the Amari case, the same bump solution independent of the initial conditions evolves.

We now perform numerical continuation of the model (7.13a) with initial profile (7.14) with $K = 1$, $A_u = 1$ and $\sigma_u = 1$, using threshold θ as a continuation parameter. The resulting solution curve is depicted in Figure 34. The curve consists of an upper branch of stable solutions and a lower branch of unstable solutions.

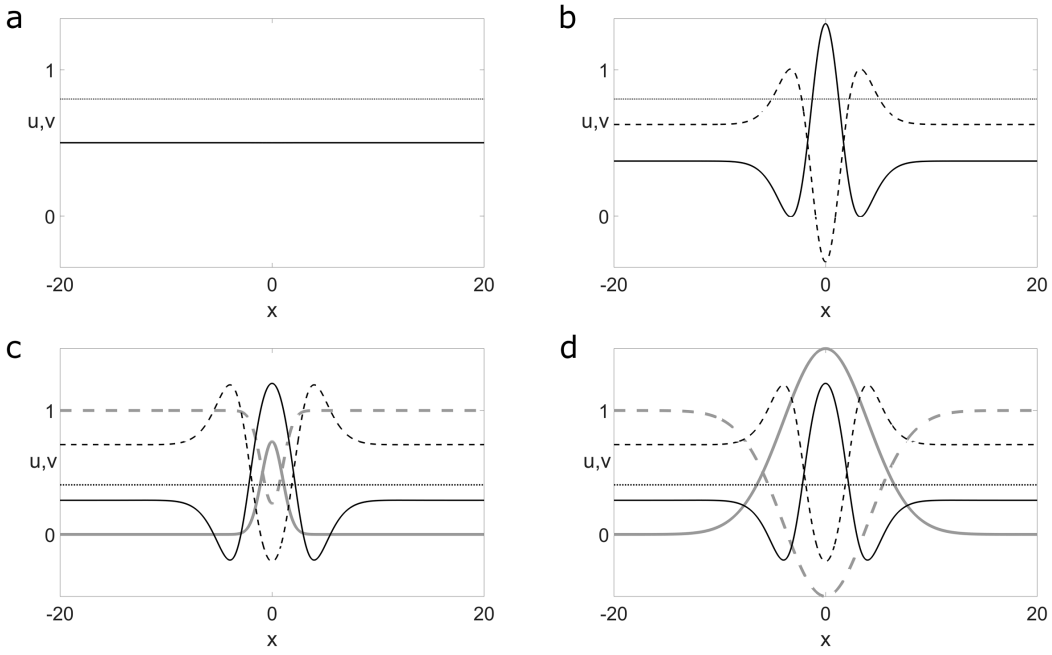

Figure 33: Solutions at time $t = 50$ of the two-field model (7.13) (black lines) for different initial profiles (7.14) with $K = 1$. (**a**) $u(x) = v(x) = 0.5$, $\theta = 0.8$. (**b**) $u(0,t) = 1.315$, $v(0,t) = -0.315$, $\theta = 0.8$. (**c**) $A_u = 0.75$, $\sigma_u = 1$, $u(0,t) = 1.22$, $v(0,t) = -0.22$, $\theta = 0.4$. (**d**) $A_u = 1.5$, $\sigma_u = 4$, $u(0,t) = 1.22$, $v(0,t) = -0.22$, $\theta = 0.4$. The kernel $w(x)$ is given by (4.3) with $A_{ex} = 2$, $A_{in} = 1$, $\sigma_{ex} = 1.25$, $\sigma_{in} = 2.5$ and $w_{inh} = 0.1$. Threshold $\theta = 0.5$ (dotted line). Compare with the fixed points in Fig. 14.

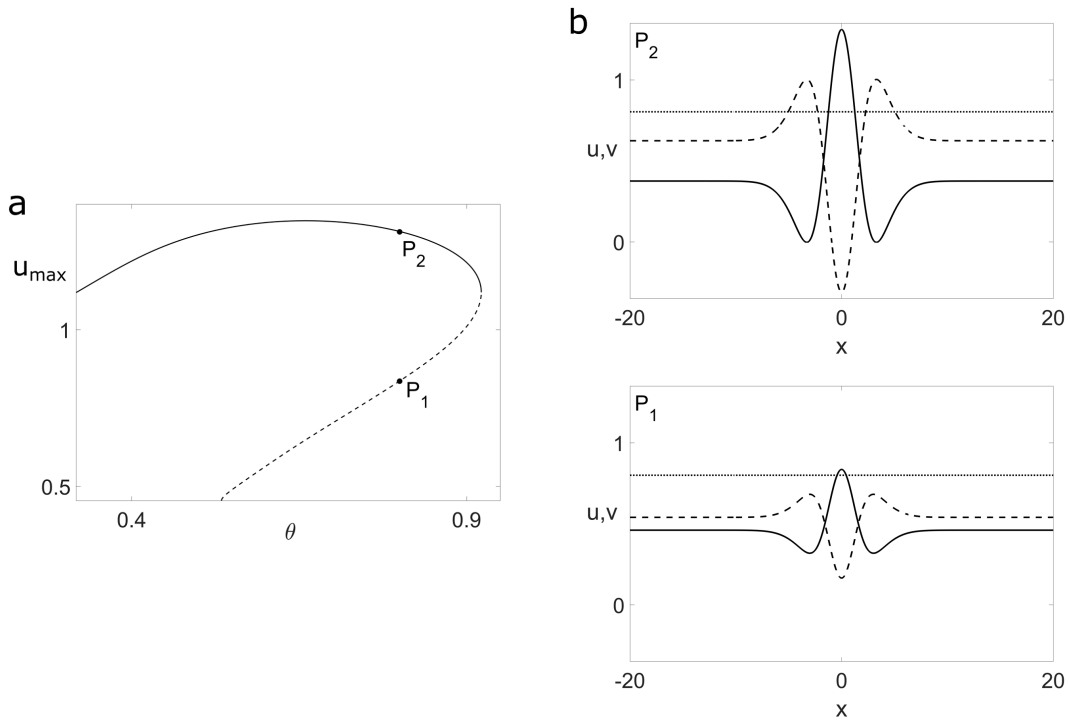

Figure 34: (**a**) Bifurcation curve showing one-bump solutions of (7.13a) with a Mexican hat kernel (4.3) as the parameter θ is varied. Solid (dashed) lines represent stable (unstable) solutions. (**b**) Examples of solutions at points P_1 (unstable) and P_2 (stable) for $\theta = 0.8$ (dotted line). Parameters of the kernel as in Fig. 33.

Model with initial condition $u(x,0)+v(x,0)=K(x)$

Now instead of using a constant value for the initial sum, $u(x,0)+v(x,0)=K$, we choose the sum to be a Gaussian function and investigate how this choice affects the bump solutions.

The inhomogeneous initial condition for is given by

$$u(x,0)=v(x,0)=K_n(x)/2, \quad K_n(x)=\sum_{j=1}^{n} A_{K_j} e^{\left(-(x-x_{K_j})^2/2\sigma_K^2\right)}. \tag{7.15}$$

We show in Figure 35 one-bump solutions of (7.13) that evolved from wider (panel **a**) and narrower (panel **b**) initial condition (7.15). Unlike the previous example (7.14), different initial conditions now lead to different bump solutions with a shape determined by the initial condition. Using wider (narrower) Gaussian function $K(x)$ leads to evolution of a wider (narrower) bump.

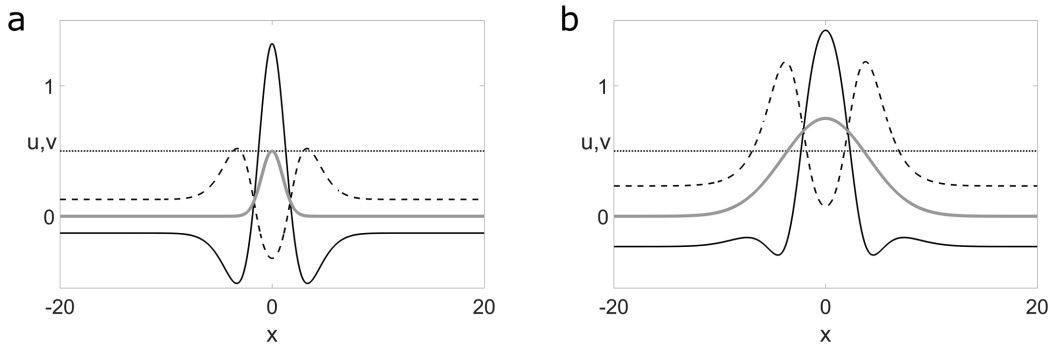

Figure 35: One-bump solution of the two-field model (7.13) (black lines) for two different initial profiles (7.15) (grey) with $A_{K_1}=0.75$, $\sigma_{K_1}=1$, $x_{K_1}=0$ (**a**) and $A_{K_1}=1.5$, $\sigma_{K_1}=4$, $x_{K_1}=0$ (**b**). Parameters of the kernel as in Fig. 33. Threshold $\theta=0.5$ (dotted line).

We now perform numerical continuation of the model (7.13) with initial profile (7.15) with $A_{K_1}=1$ and $\sigma_{K_1}=1$, using threshold θ as a continuation parameter. The resulting solution curve is depicted in Figure 36 (top left). Again, we can see an upper branch consisting of stable solutions and lower branch with unstable solutions. There is also an additional branch of stable subthreshold bumps, which does not exist in the Amari model, satisfying $u(x,t)=v(x,t)=K(x)/2$ for any value $\theta>0.57$.

In order to study the relation between the shape of the initial condition (7.15) and the solution structure of the model, we perform numerical continuation of bump solutions analogously to the previous example, but with a wider Gaussian profile in $K(x)$. The resulting bifurcation curve is shown in Figure 36 (top right). We can see the same co-existence of an upper (stable) and a lower (unstable) branch of suprathreshold solutions as before and a branch of stable subthreshold solutions for $\theta>1.07$. Increasing the width of $K(x)$ results in a larger range of parameter values θ for which a stable one-bump exists.

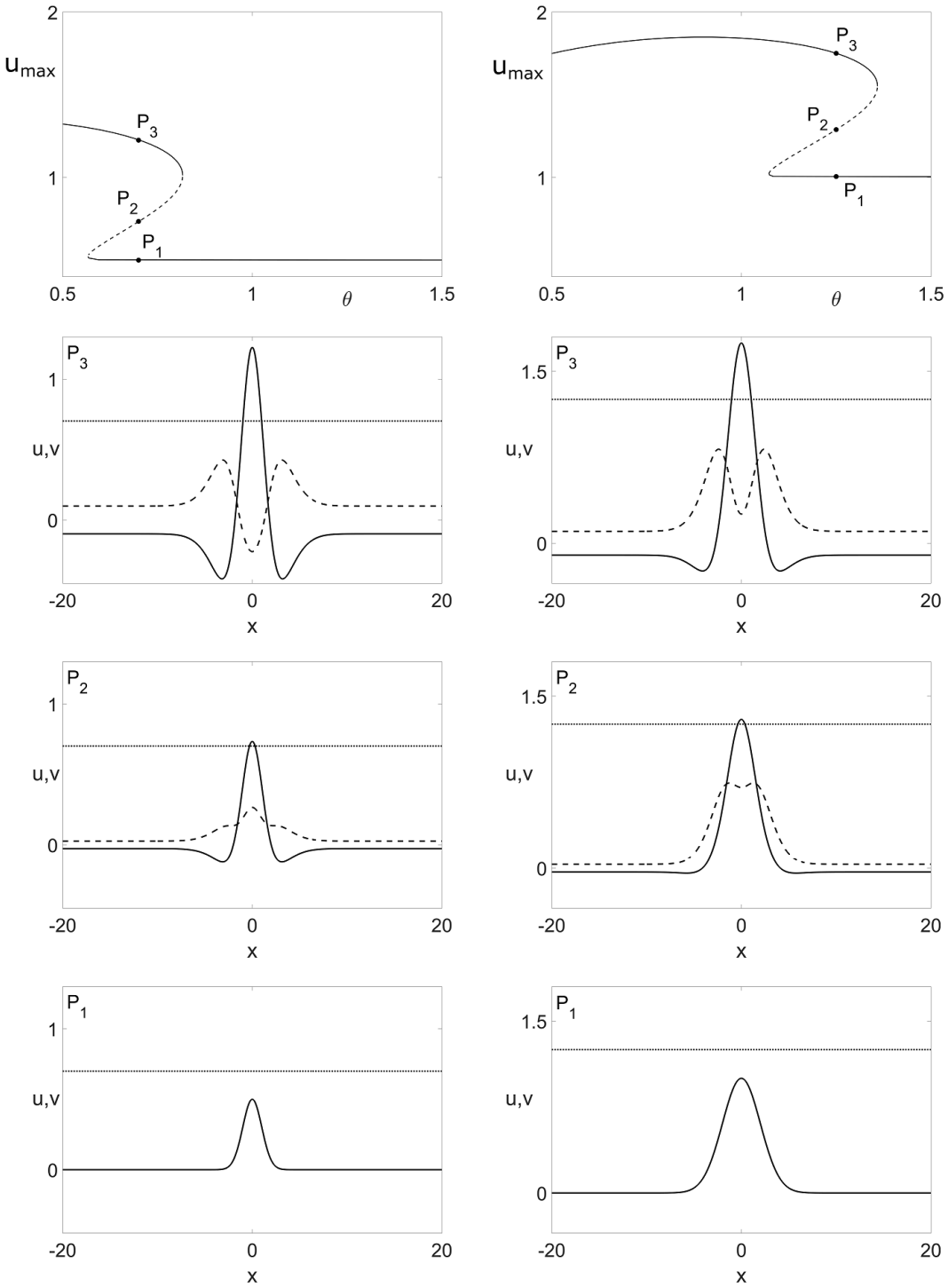

Figure 36: Top row: Bifurcation curve showing one-bump solutions of (7.13a) with the initial condition (7.15) with $A_{K_1} = 1$, $\sigma_{K_1} = 1$, $x_{K_1} = 0$ (left) and $A_{K_1} = 2$, $\sigma_{K_1} = 2$, $x_{K_1} = 0$ (right) as the parameter θ is varied. Solid (dashed) lines represent stable (unstable) solutions. Examples of solutions at points P_1, P_3 (stable) and P_2 (unstable) for a narrower and a wider profile of $K(x)$ are shown in the left and right column, respectively. Threshold $\theta = 0.8$ (left column) and $\theta = 1.25$ (right column) (dotted line). Parameters of the kernel as in Fig. 33.

Next we look at two-bump solutions of (7.13) obtained with a bimodal initial condition $K_2(x)$ given by (7.15). Figure 37 shows the resulting bifurcation curve as θ is varied. We can see an upper (stable) and lower (unstable) branch of suprathreshold solutions exist and a branch of stable subthreshold solutions with $u(x) = v(x) = K(x)/2$ for $\theta > 0.80$.

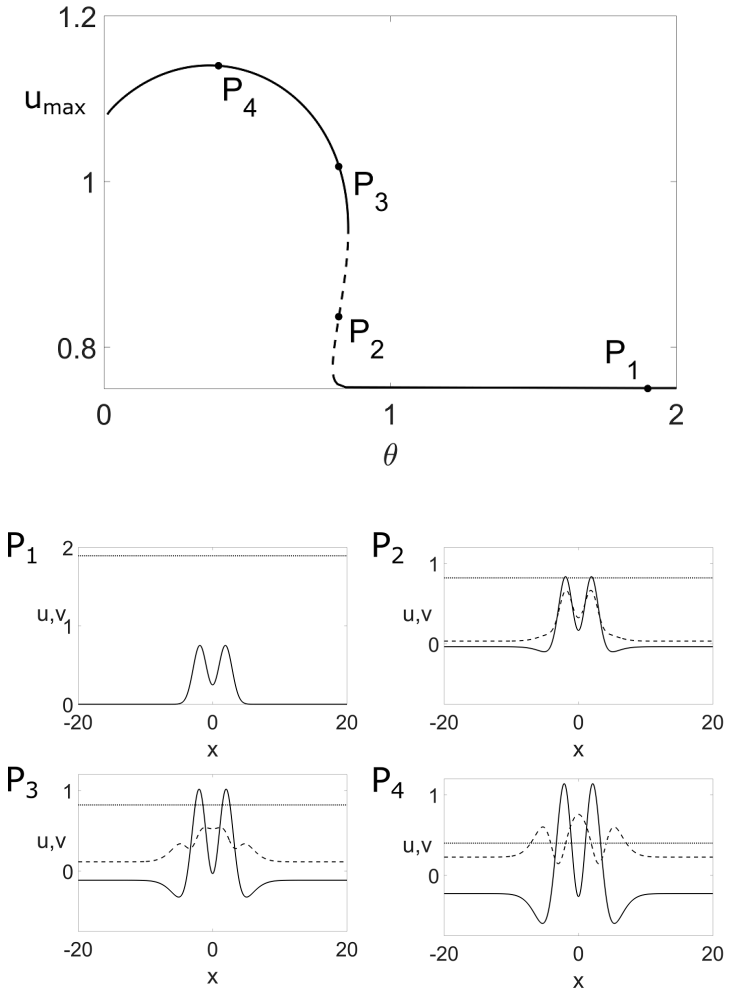

Figure 37: Bifurcation curve showing two-bump solutions of (7.13a) with the initial condition (7.15) with $A_{K_{1,2}} = 1.5$, $\sigma_{K_{1,2}} = 1$, $x_{K_{1,2}} = \pm 1.9$ as the parameter θ is varied. Solid (dashed) lines represent stable (unstable) solutions. Examples of two-bump solutions at points P_1, P_3, P_4 (stable) and P_2 (unstable) are shown. Threshold θ (dotted line): $\theta = 1.9$ (P_1), $\theta = 0.82$ (P_2 and P_3), $\theta = 0.4$ (P_4). Parameters of the kernel as in Fig. 33.

To evaluate the dependence of the inter-peak distance on model parameters, Fig. 38 depicts the bifurcation curve when the lateral inhibition parameter σ_{inh} is varied. As illustrated by the two pairs of stable and unstable two-bumps, (P2,P3) and (P1,P4), respectively, the distance decrease with increasing σ_{inh}. It is important to stress that the two bumps exist at a distance where the boundary points of a bump receive different levels of inhibition form the second bump since there is a gradient in the lateral inhibition

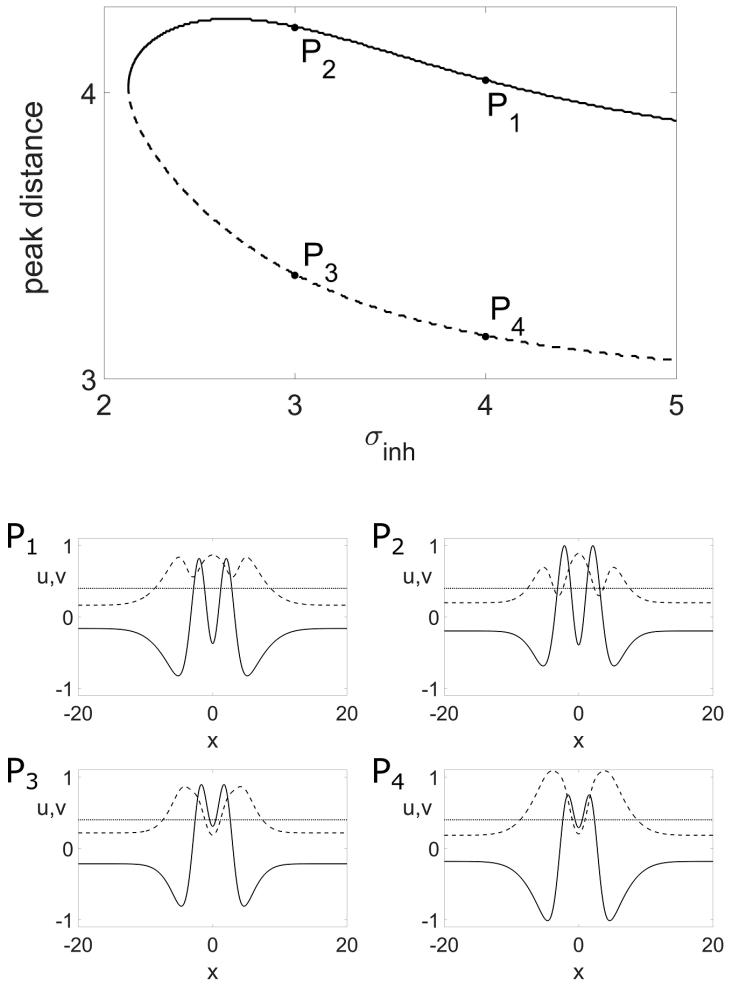

Figure 38: Bifurcation curve showing two-bump solutions of (7.13a) with the initial condition (7.15) with $A_{K_{1,2}} = 1.5$, $\sigma_{K_{1,2}} = 1$, $x_{K_{1,2}} = \pm 1.9$ as the parameter σ_{inh} is varied. Solid (dashed) lines represent stable (unstable) solutions. Examples of two-bump solutions at points P_1, P_2 (stable) and P_3, P_4 (unstable) are shown. $\sigma_{inh} = 3$ (P_2 and P_3), $\sigma_{inh} = 4$ (P_1 and P_4). Remaining parameters as in Fig. 33.

profile of the Mexican-hat coupling. In the Amari model, this inhibition gradient causes a continuous drift of the bump in opposite direction. The observed "bump repulsion" effect has been already discussed by Amari [3].

We now study three-bump solutions of (7.13) as the parameter θ varies from 2 to 0, starting from a trimodal initial condition $K_3(x)$ given by (7.15). The bifurcation curve and some example solutions are shown in Fig. 39. We can again see a subthreshold solution with $u(x) = v(x) = K(x)/2$ (P_1 in Fig. 39). As θ decreases, the solution undergoes a fold bifurcation giving rise to branch segment with solutions consisting of a single bump flanked by two subthreshold patterns (solutions P_2 and P_3). As we move further along the solution curve, the middle bump decreases below threshold θ, while two outside bumps becoming suprathreshold. As a result, we see a branch segment with two-bump solutions separated by a

subthreshold bump in the middle (solutions P_4 and P_5). The middle bump increases, eventually reaching threshold θ and we can observe a branch of three-bump solutions (P_6 and P_7 in Fig. 39).

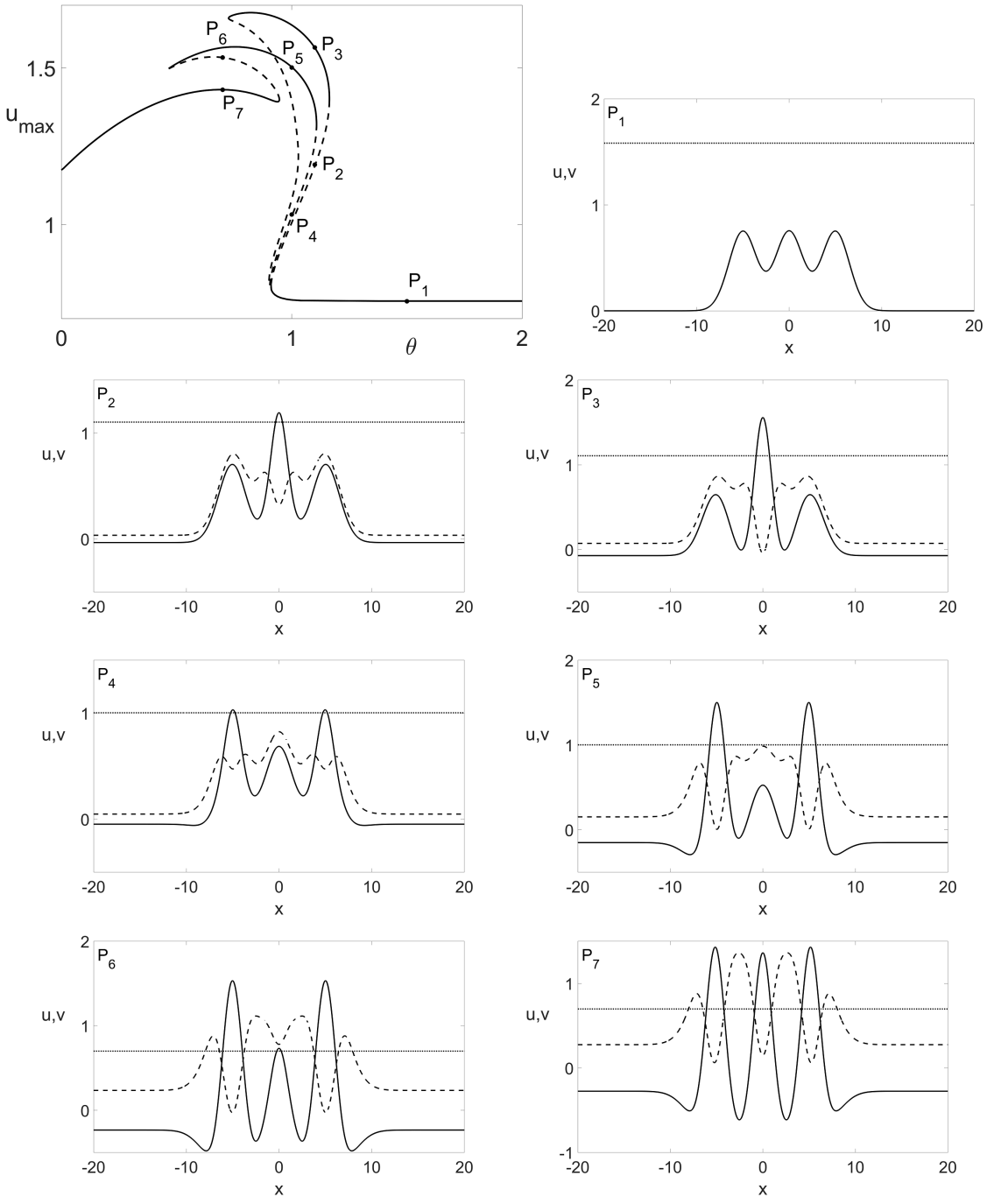

Figure 39: Bifurcation curve showing three-bump solutions of (7.13a) with the initial condition (7.15) with $A_{K_j} = 1.5$, $\sigma_{K_j} = 1.5$, $x_{K_{1,2,3}} \in \{-5, 0, 5\}$ as the parameter θ is varied. Solid (dashed) lines represent stable (unstable) solutions. Examples of bump solutions at points P_1 to P_7 are shown. The kernel $w(x)$ is given by (4.3) with $A_{ex} = 2.5$, $A_{in} = 1$, $\sigma_{ex} = 0.8$, $\sigma_{in} = 2$ and $w_{inh} = 0.1$. For details see the text.

7.4 Oscillatory kernel

In this section, we study both neural field models with oscillatory connectivity function (4.4) in one and two spatial dimensions. The firing rate function is again a steep sigmoidal function (4.7).

7.4.1 Amari model

For one spatial dimension ($d = 1$), we find N-bump solutions by numerically integrating the model with the initial condition

$$u(x,0) = I\cos\left(\frac{lx}{L}\right)\exp\left(-\left(lx/L\right)^2\right), \tag{7.16}$$

where I controls the amplitude and $l > 0$ is the parameter allowing to vary the width of the initial condition, with the width of $u(x,0)$ increasing as l is decreased.

We concentrate on symmetric solutions with an odd number of bumps only. We note that other N-bump solutions exist, e.g. solutions with an even number of bumps.

Once a stable solution is found using the numerical integration, we can select a specific model parameter and compute branches of solutions using numerical continuation method as described before. We begin with the firing threshold, θ. Figure 40, panel (**a**), illustrates the resulting solution branches. We plot the maximum activation level $u_{max}(x) \quad x \in \Omega$, as a function of the continuation parameter, θ. The solid (dashed) lines represent stable (unstable) solutions. We observe a characteristic bifurcation structure called *snaking* in the neural field literature [9, 98, 123]. The solution curve undergoes a series of fold bifurcations, with two additional bumps added to the solution at each fold on the left side of the curve.

As we ascend the snaking curve, the solution branches come closer to each other. We plot the L_2 norm of the solution, $||u||_2$, as the function of θ in the panel (**b**), so that the separation of branches is better visible.

For $N \in \{1,3,5,7\}$, N-bump solutions come in pairs of bumps which differ in the maximum value u_{max}. Only the pattern with the stronger activation is stable, which mirrors the analytical result of one-bump solutions [3, 35]. Examples of solution pairs chosen from the computed branches are displayed in Figure 40, panel (c). As θ increases, pairs of stable and unstable solutions annihilate in saddle-node bifurcations. We terminate our numerical computations with $N = 7$ when the bump solutions approach the limits of the finite domain Ω.

We now perform the continuation with respect to the parameter b, that determines the amplitude of the oscillations in the connectivity function $w(x)$ [98]. We investigate 1- and 3-bump solutions and show the

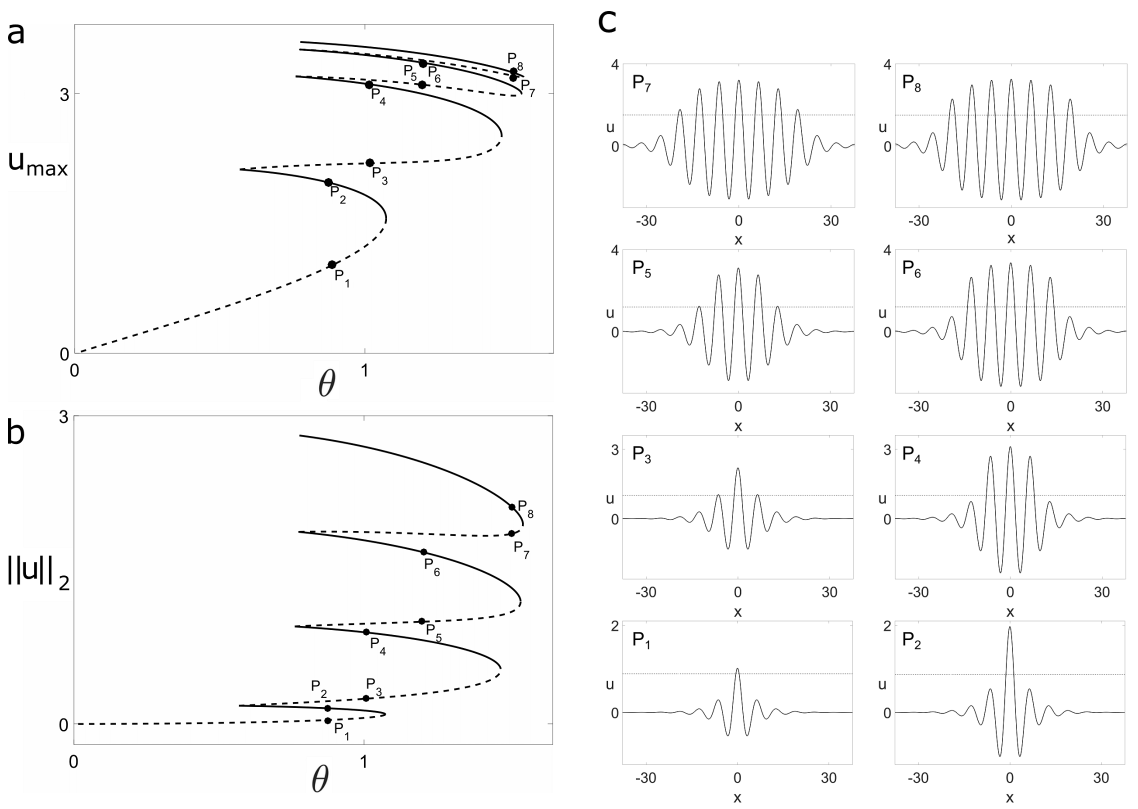

Figure 40: Bifurcation curves showing 1-, 3-, 5- and 7-bump solutions of (7.5) where θ is the continuation parameter. Solid (dashed) lines represent stable (unstable) solutions. (**a**) u_{max} is plotted as a function of θ. (**b**) $||u||_2$ is plotted as a function of θ. (**c**) Several examples of solutions at points P_1 to P_8 are shown. The initial condition for the solutions is given by (7.16) with $I = 4$ and $l = 12$. Remaining parameters: $b = 0.2$ and $\beta = 50$.

results in Figure 41. Panel (**a**) shows the global maximum of $u(x)$ as a function of b; panel (**b**) shows the L_2 norm of u as a function of b. A selection of solution examples is shown in panel (**c**).

Similar as for parameter θ, the 1- and 3-bump solutions come in pairs of one stable solution and one unstable solution that are destroyed in saddle-node bifurcations. As parameter b increases, the curves representing families of 1- and 3-bump solutions come closer together and finally overlap. This is caused by the fact that higher values of b affect the oscillations on the borders of 1- and 3-bump solutions, but the maximum activation value u_{max} does not change. The separation of solution curves is better visible when we plot the L_2 norm as a function of b (panel (**b**)). Again, we can see a *snaking* phenomenon, i.e. the solutions acquire more bumps as the solution norm increases. This finding was already described in [98].

We now consider model (7.5) in two spatial dimensions, i.e. the domain Ω is now a subset of $\mathbb{R}^2$. We discretise $\Omega : [-32, 32]^2$ using a uniform grid of $2^{11} \times 2^{11}$ points. The weak external inhomogeneous

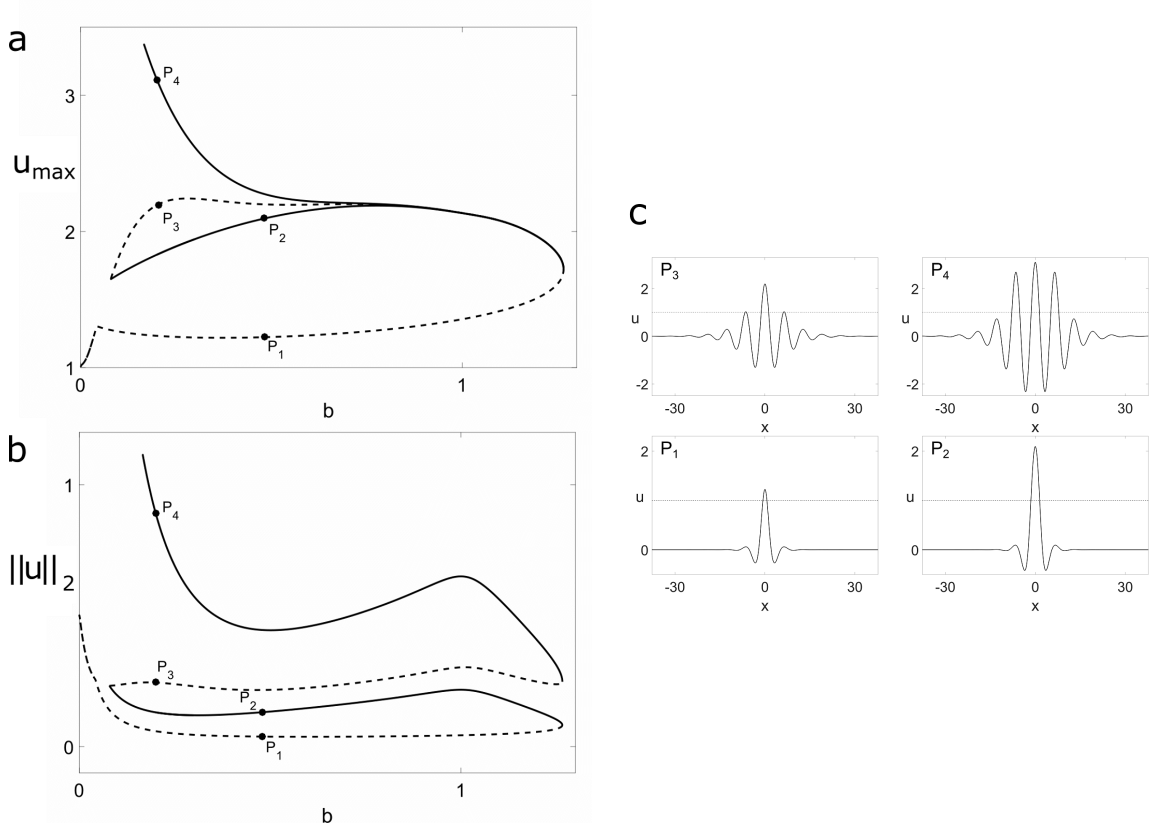

Figure 41: Bifurcation curves showing 1- and 3-bump solutions of (7.5) where b is the continuation parameter. Solid (dashed) lines represent stable (unstable) solutions. (**a**) u_{max} is plotted as a function of b. (**b**) $||u||_2$ is plotted as a function of b. (**c**) Several examples of solutions at points P_1 to P_4 are shown. The initial condition for the solutions is given by (7.16) with $I = 4$ and $l = 12$. Remaining parameters: $\theta = 1$ and $\beta = 50$.

input $g(\mathbf{x})$ is given by

$$g(\mathbf{x}) = G_0 \exp\left(-\frac{x^2 + y^2}{\sigma_g^2}\right), \tag{7.17}$$

where $G_0 = 0.001$ and $\sigma_g = \sqrt{10}$. It brakes the translational invariance of the system and allows us to apply the numerical continuation method to the model. The initial profile $u(\mathbf{x}, 0)$ is given by

$$u(\mathbf{x}, 0) = 8 \exp\left(-\frac{x^2 + y^2}{6}\right). \tag{7.18}$$

We numerically integrate the equation (7.5) with the initial condition (7.18) to a steady state. Next we continue this solution with θ as the continuation parameter. The result is shown in Figure 42 where we plot the maximum of u as a function of θ. As in the one-dimensional model, the solutions come in pairs: one solution with the larger value u_{max} is stable and the other with a smaller u_{max} is unstable. The stability changes at saddle-node bifurcations. As the maximum value of u continues to increase, stable one-bump

solution change into unstable "bump-with-ring" solution, i.e. a central bump surrounded by one ring (not shown). This behavior was previously described in [99, 100].

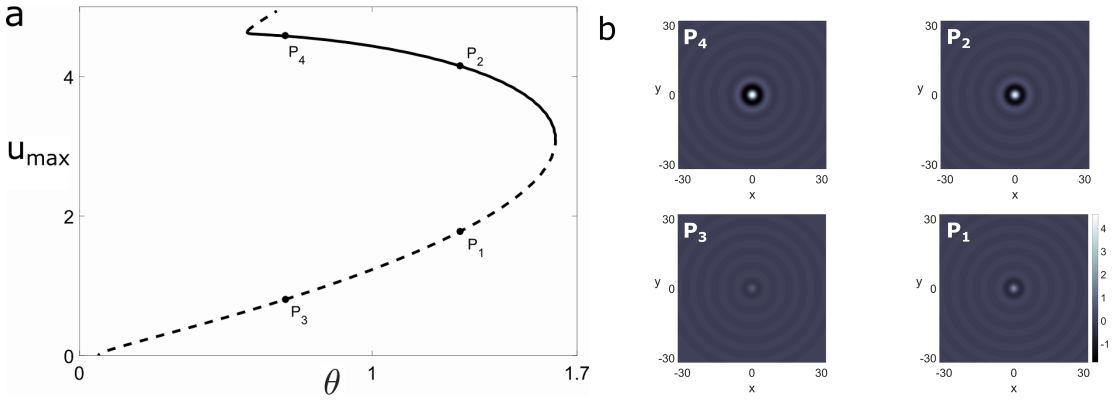

Figure 42: (**a**) Bifurcation curve showing 1-bump solutions of (7.5) as the parameter θ is varied. As the maximum of u increases, the one-bump solution changes into a "bump-with-ring" solution. (**b**) Several examples of solutions at points P_1 to P_4 are shown. Remaining parameters: $b = 0.4$ and $\beta = 30$.

7.4.2 Two-field model

We now consider the two-field model (7.13) where $f(u)$ and $w(x)$ are given by (4.7) and (4.4), respectively. We first consider the one-dimensional model, with initial condition analogous to (7.16)

$$u(x,0) = I\cos\left(\frac{lx}{L}\right)\exp\left(-\left(\frac{lx}{L}\right)^2\right), \tag{7.19a}$$

$$v(x,0) = K - u(x,0), \qquad K = 1, \tag{7.19b}$$

where I is the amplitude of the initial profile and $l > 0$ controls its width.

We now find the solution curves of (7.13) using numerical continuation, starting again with θ as a continuation parameter. The results are displayed in Figure 43. Comparing the solution branches with those of the Amari model (Figure 40), we can see that the addition of a second field equation to the model did not introduce any qualitative changes to the solution structure. As in the Amari model, N-bump solutions come in pairs of one stable and one unstable solution, annihilating in saddle-nodes bifurcations as θ increases. Snaking behavior of N-bump solutions is clearly visible when looking at the L_2 norm of the solution plotted as a function of θ (panel (b) of Figure 43).

Next we look at the N-bump solutions of (7.13) as the parameter b varies. Figure 44 shows the resulting bifurcation diagrams. We can see again pairs of stable and unstable solutions that annihilate one another

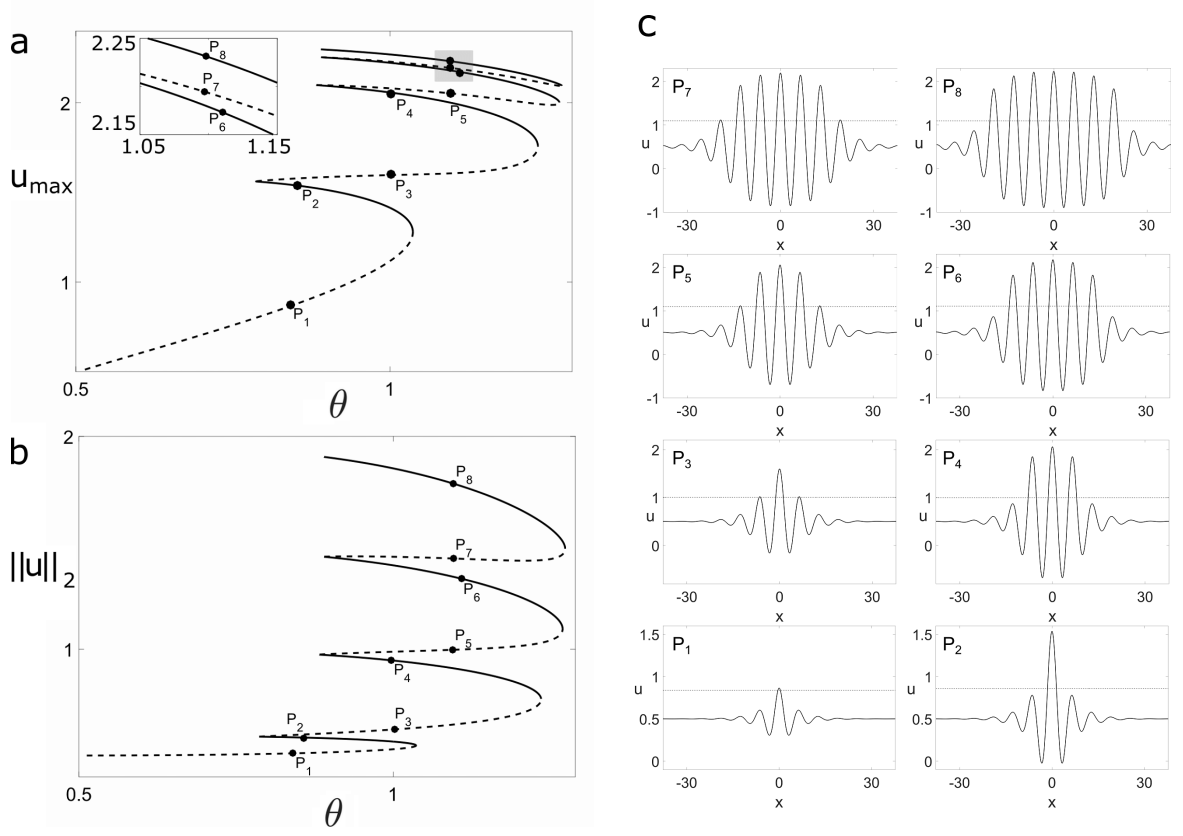

Figure 43: Bifurcation curves showing 1-, 3-, 5- and 7-bump solutions of (7.13a) where θ is the continuation parameter. Solid (dashed) lines represent stable (unstable) solutions. (**a**) u_{max} is plotted as a function of θ. (**b**) $||u||_2$ is plotted as a function of θ. (**c**) Several examples of solutions at points P_1 to P_8 are shown. The initial condition for the solutions is given by (7.19) with $I = 4$ and $l = 12$. Remaining parameters: $b = 0.2$ and $\beta = 50$. Compare with Figure 40.

in saddle-node bifurcations as b is increased. When plotting the global maximum of u as a function of b (panel (**a**)), the curves of 1-, 3- and 5-bump solutions approach one another and finally overlap as b increases. By plotting the L_2 norm of u as a function of b, we can clearly see a separation of solution branches (panel (b)). The snaking structure is again present. Representative solutions are shown in panel (c). Similarly as for parameter θ, the solution structure resembles qualitatively that of the Amari model (compare Figure 41).

We now consider model (7.13) in two spatial dimensions, i.e. now $\Omega \subset \mathbb{R}^2$. We discretise the domain $\Omega : [-32, 32]^2$ using a grid of $2^{10} \times 2^{10}$ points and integrate (7.13) to a steady state. To break the translational symmetry of the system we apply the weak input $g(\mathbf{x})$ given by (7.17). The initial condition is given by

$$u(\mathbf{x}, 0) = 5 \exp\left(-\frac{x^2 + y^2}{6}\right). \tag{7.20a}$$

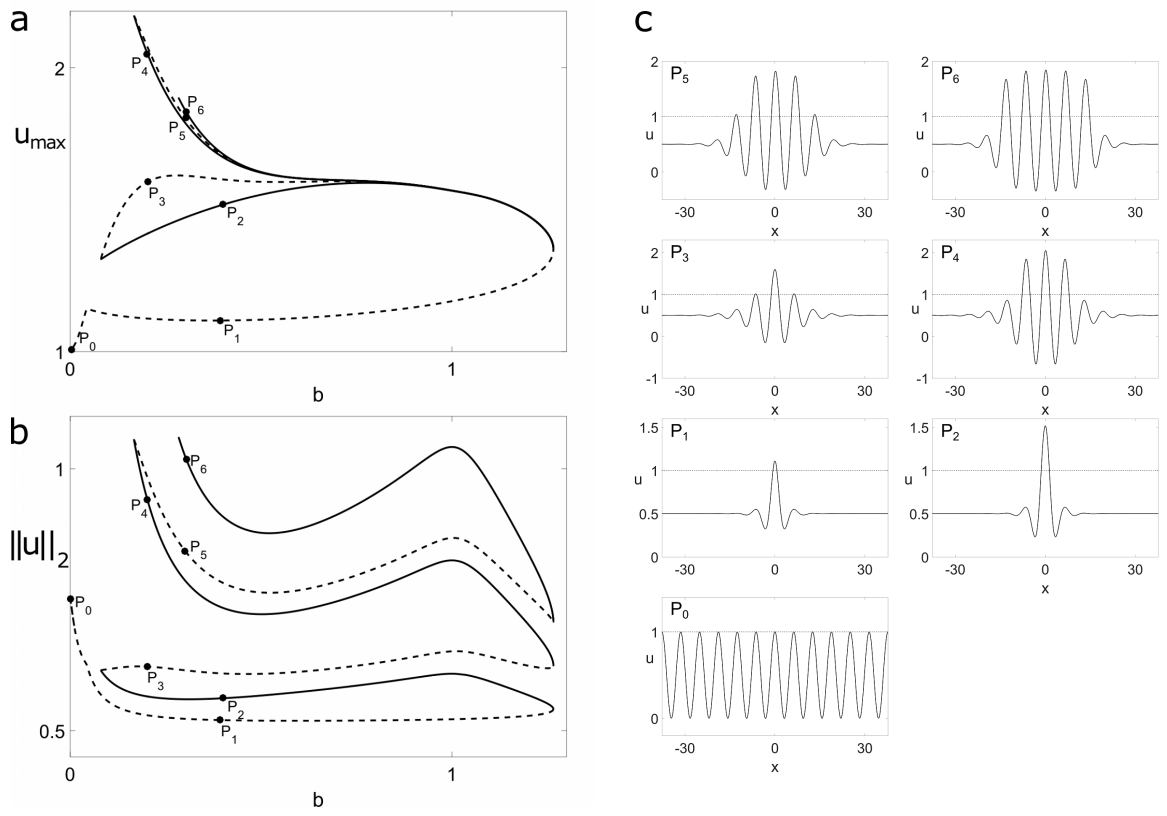

Figure 44: Bifurcation curves showing 1-, 3- and 5-bump solutions of (7.13a) where b is the continuation parameter. Solid (dashed) lines represent stable (unstable) solutions. (**a**) u_{max} is plotted as a function of b. (**b**) $||u||_2$ is plotted as a function of b. (**c**) Several examples of solutions at points P_0 to P_6 are shown. The initial condition for the solutions is given by (7.19) with $I = 4$ and $l = 12$. Remaining parameters: $\theta = 1$ and $\beta = 50$. Compare with Figure 41.

$$v(\mathbf{x}, 0) = K - u(\mathbf{x}, 0), \qquad K = 0.5. \tag{7.20b}$$

We now find solution curves in terms of the parameter θ using numerical continuation. The solution structure is again similar to that of the Amari model. This becomes clear when looking at Figure 45, where we show the bifurcation diagram for the two-dimensional model (compare Figure 42). The solutions occur again in pairs and bump stability changes at saddle node bifurcations. With increasing maximum values of u, a stable one-bump solution changes into unstable "bump-with-ring" solution, as previously observed in the Amari model.

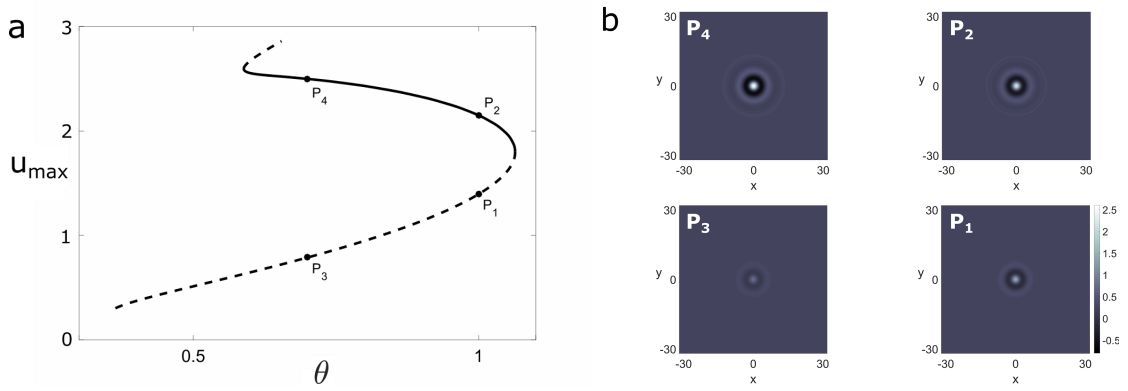

Figure 45: (**a**) Bifurcation curve showing 1-bump solutions of (7.13a) as the parameter θ is varied. As the maximum of u increases, the 1-bump solution transition into a bump-with-ring solution, i.e. a central bump surrounded by one ring. (**b**) Several examples of solutions at points P_1 to P_4 are shown. Remaining parameters: $b = 0.4$ and $\beta = 30$. Compare with Figure 42.

7.5 Conclusion

In this chapter we have used numerical continuation techniques to analyze localized solutions of both the Amari model and the two-field model.

In Section 7.3 we considered the classical Mexican hat connectivity function. For the Amari model, we observed in the bifurcation diagram an upper branch of stable one-bump solutions and a lower branch of unstable one-bump solutions. The resulting bifurcation curve for single bumps in the two-field model is qualitatively the same as in the Amari model when the sum of the initial conditions is spatially homogeneous. These results match, as expected, our analytical findings of the previous chapter. We then extended our numerical investigation of the two-field model to the case with spatially inhomogeneous initial conditions with a typical Gaussian shape. In addition to single bump solutions, we found also stable two- and three-bump solutions, which is not observed in the case of the Amari model. We note that those solutions are obtained with a sigmoidal firing rate function, since the Heaviside function cannot be used in the numerical continuation method [123]. We believe however that the choice of sufficiently large steepness parameter value β approximates the step function well.

Section 7.4 was dedicated to the study of N-bump solutions in both models with oscillatory coupling function. Using the Amari model in 1D, we confirmed results known from the literature including bifurcation curves with the typical snaking structure. Similarly, the snaking phenomenon is also observed in the two-field model, with qualitatively the same bifurcation structure and stability of bump solutions. In an extension of the numerical continuation method to the two-dimensional case we identified for both models a whole range of threshold values θ for which stable and unstable one-bump solutions coexist.

8 Working memory application[1]

8.1 Introduction

In this chapter we study input-driven solutions of the novel two-field model introduced in Chapter 4. In particular we are interested in multi-bump solutions triggered by external inputs and their application to working memory modeling. First we look at the existence and stability of N-bump solutions in the two-field model and discuss their impact on modeling different cognitive functions. We then systematically compare the pattern formation process in the Amari and the two-field model in tasks with multiple memory items. Specifically, we are interested to understand how input-induced variations of the memory strength affect the inference of nearby memory traces and their spatial drift in response to random activity fluctuations.

We consider the Amari model given by (2.9) and the two-field model given by (9.1) with the weight function taken as Mexican-hat (4.3). The firing rate function $f(u)$ is chosen as a Heaviside function with threshold θ given by (4.6). The time-dependent external input $I(x,t)$ to the u-field is modeled as one or more Gaussians centered at positions x_{c_j}:

$$I(x,t) = (H_{t_0}(t) - H_{t_1}(t)) \sum_j A_{I_j} e^{\left(-(x-x_{c_j})^2/2\sigma_I^2\right)}, \tag{8.1}$$

where $H_{t_0}(t)$ and $H_{t_1}(t)$ represent step functions with threshold t_0 and t_1, respectively, so that the input starts at $t = t_0$ and ends at $t = t_1$. Input strength is controlled by $A_{I_j} > 0$.

8.2 Existence and stability of N-bump solutions

It is well know that continuous attractor networks have difficulties to simultaneously stabilize multiple bumps due to the constraints imposed by lateral inhibition and the interference between nearby patterns [3, 162]. This limitation has been addressed in computational studies by introducing additional processing

[1] The content of this chapter is based on [169].

mechanism such as short-term synaptic facilitation [129] or by using interaction kernels that are not of lateral-inhibition type [55, 101]. However, already Amari [4] pointed out that for the connectivity function (4.3) stable multiple bumps may exist at distances, $|x| > x_c$, where the lateral inhibition is constant (see e.g. [84] for a WM application). It is straightforward to derive a condition for the existence of a N-bump which is constrained by the summed inhibition that a bump receives from the $N-1$ neighboring patterns. Without loss of generality, we assume that the bump is located in the interval $\left[-\frac{\Delta}{2}, \frac{\Delta}{2}\right]$ and that the remaining $N-1$ pulses are located in the intervals $\left[x_1 - \frac{\Delta}{2}, x_1 + \frac{\Delta}{2}\right]$, $\left[x_2 - \frac{\Delta}{2}, x_2 + \frac{\Delta}{2}\right]$, ..., $\left[x_{N-1} - \frac{\Delta}{2}, x_{N-1} + \frac{\Delta}{2}\right]$, with $x_{i+1} - x_i > \Delta + x_s$, $i = 1, 2, \ldots, N-1$. That is, $u(x) > \theta$ for $x \in \left[-\frac{\Delta}{2}, \frac{\Delta}{2}\right] \cup \left[x_1 - \frac{\Delta}{2}, x_1 + \frac{\Delta}{2}\right] \cup \ldots \cup \left[x_{N-1} - \frac{\Delta}{2}, x_{N-1} + \frac{\Delta}{2}\right]$, and $u(x) \leq \theta$ elsewhere.
Equilibrium solutions of the two-field model are given by

$$U(x) = V(x) + \int_{-\frac{\Delta}{2}}^{\frac{\Delta}{2}} w(y)\mathrm{d}y + \int_{x_1-\frac{\Delta}{2}}^{x_1+\frac{\Delta}{2}} w(y)\mathrm{d}y + \ldots + \int_{x_{N-1}-\frac{\Delta}{2}}^{x_{N-1}+\frac{\Delta}{2}} w(y)\mathrm{d}y, \tag{8.2a}$$

$$V(x) = U(x) - \int_{-\frac{\Delta}{2}}^{\frac{\Delta}{2}} w(y)\mathrm{d}y - \int_{x_1-\frac{\Delta}{2}}^{x_1+\frac{\Delta}{2}} w(y)\mathrm{d}y - \ldots - \int_{x_{N-1}-\frac{\Delta}{2}}^{x_{N-1}+\frac{\Delta}{2}} w(y)\mathrm{d}y. \tag{8.2b}$$

Since at the boundaries of a bump $U(-\frac{\Delta}{2}) = U(\frac{\Delta}{2}) = \theta$, $U(x) + V(x) = K$ and

$$\int_{x_i-\frac{\Delta}{2}}^{x_i+\frac{\Delta}{2}} w(y)\mathrm{d}y = -\Delta g_{mex}, \tag{8.3}$$

we get the existence condition for N-bump solutions

$$F(\Delta) = -2\theta + K + W(\Delta) - (N-1)\Delta\, g_{mex} = 0. \tag{8.4}$$

The width of an individual bump of a N-bump solution can be thus found graphically by looking on the intersection of the plot of $W(\Delta)$ with the line $2\theta - K + (N-1)\Delta g_{mex}$. Fig. 46 shows an example for the case $K = 2\theta$ and $N = 2$. The maximum number of stable bumps that the specific connection function supports is $N = 6$. A further increase of lateral inhibition would destabilize the bumps since $\mathrm{d}W(\Delta)/\mathrm{d}\Delta > 0$.

The analogous condition for the existence of a N-bump solutions in the Amari model is given by

$$F(\Delta) = -\theta + W(\Delta) - (N-1)\Delta\, g_{mex} = 0. \tag{8.5}$$

For the example of Fig. 46, the maximum number of bumps reduces in this case to $N = 3$.

We show in the next section that different to the Amari model [101], the two-field model supports the existence and stability of true two-bump solutions for which the inter-peak distance is smaller than x_c.

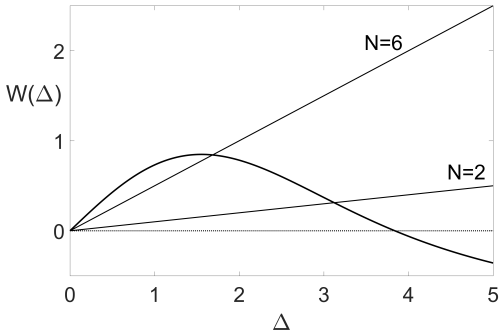

Figure 46: Existence of N one-bump solutions in the two-field model with the Mexican hat kernel (4.3). Threshold $\theta = 0.5$ and $K = 1$. Straight lines show the condition (8.4) for $N = 2$ and $N = 6$. Kernel w is given by (4.3) with $A_{ex} = 2$, $A_{in} = 1$, $\sigma_{ex} = 1.25$, $\sigma_{in} = 2.5$ and $g_{mex} = 0.1$.

8.3 Input driven bump solutions

In working memory applications, classical bump attractor models implement the encoding and maintenance of briefly presented visual input as an all-or-none process. The information is either stored in a self-stabilized bump with a shape defined by the recurrent interactions or the information is completely lost since neural activity decays back to resting state. However, a growing body of experimental evidence indicates that this binary classification may be insufficient as a description of WM storage, because the representational quality of WM items may differ depending on sensory attributes of the input or task demands. For instance, the salience of the visual input manipulated through varying stimulus strength (or contrast) is known to affect WM representations. Consistent with the notion of memory-associated persistent activity, a graded modulation of sustained population activity as a function of stimulus contrast has been described in a WM task. Figure 47 shows various bump solutions of the two-field integrator model in which input attributes are systematically varied. In panels (a) and (b), the attractor network converts a transient input into a persistent output which is proportional to the input amplitude. A comparison of panels (a) and (c) illustrates that the bump also represents faithfully input width. This property can be exploited for instance to encode uncertainty in the sense of an explicit probability code [109]. Higher uncertainty is then represented by a wider activation pattern across the neural population tuned to a continuous input feature (e.g., representing ranges of movement direction, [12]). In panel (d), the localized input of panel (a) is applied but lasting three times as long. The bump amplitude (measured above threshold) is three times larger, as expected by perfect integration. The two-field model can thus be used to model the encoding of input duration [172] if one assumes that the input amplitude is first normalized by upstream sensory processing [29]. Figure 48 shows the temporal evolution of a bump in an example in which the input strength changes

over time. Such a nonstationary input stream can be expected in any natural environment. Again, the bump amplitude reflects the total external input applied to the population. The observed "ramping" activity is a hallmark of "drift-diffusion" models of decision making which assume the continuous accumulation of sensory and other evidence to a threshold (for review see [22]). Importantly, to work as a robust neural integrator over a longer timescale of a decision process, the network dynamics should hold the activity level without significant decay or growth when an input signal vanishes. Figure 49 shows this integrator property in an example in which two inputs are presented sequentially at the same field site $x = 0$. As can be seen in the time evolution plot, the population activity stabilizes at a constant level after cessation of the inputs at times t_3 and t_5, respectively.

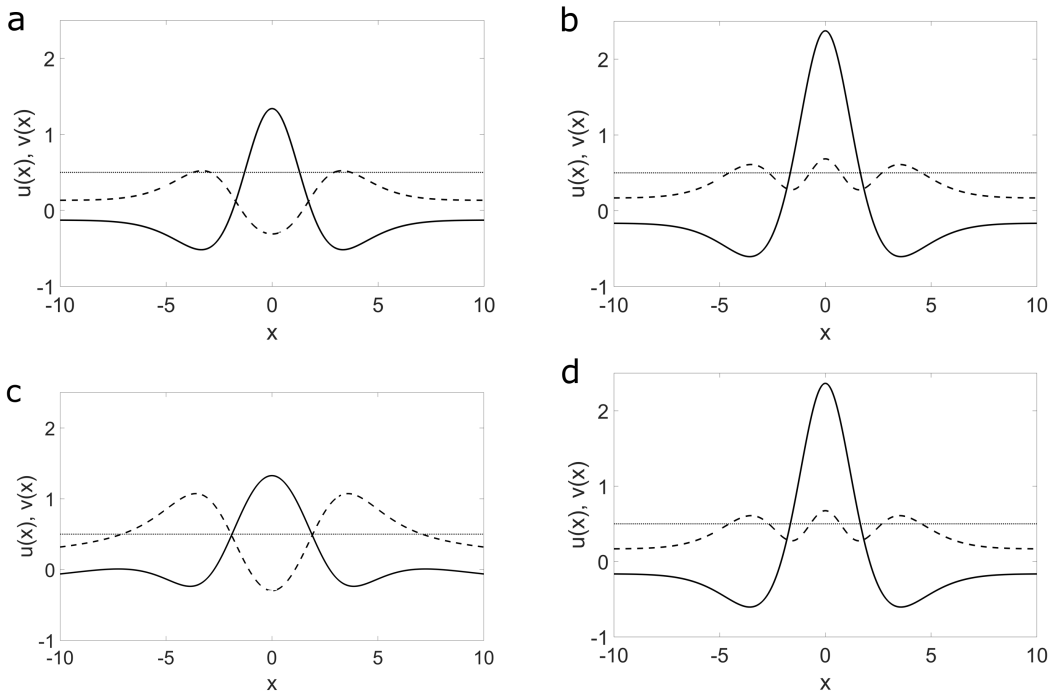

Figure 47: Solutions at time $t = 50$ of the model (9.1) created with transient inputs $I(x,t)$ given by (8.1) with variation of (**b**) input strength A_I, (**c**) input width σ_I and (**d**) input duration d_I. Parameters of the inputs: (**a**) $A_{I_j} = 1, \sigma_{I_j} = 1, d_{I_j} = 1$ (**b**) $A_{I_j} = 3, \sigma_{I_j} = 1, d_{I_j} = 1$ (**c**) $A_{I_j} = 1, \sigma_{I_j} = 6, d_{I_j} = 1$ (**d**) $A_{I_j} = 1, \sigma_{I_j} = 1, d_{I_j} = 3$. The kernel w is given by (4.3) with $A_{ex} = 2$, $A_{in} = 1$, $\sigma_{ex} = 1.25$, $\sigma_{in} = 2.5$ and $g_{mex} = 0.1$. Threshold $\theta = 0.5$ (dotted line), $K = 0$.

The existence of stable multi-bump solutions shown in Section 8.2 does not necessarily mean that their evolution can be triggered by external inputs. In field models of lateral inhibition type, any existing suprathreshold activity will amplify the fast inhibitory feedback and suppress further excitatory activity. This means that in order to create an input-driven multi-bump no processing advantage should be given to a specific subpopulation in terms of the timing and the strength of the input. For the two-field model, the competitive

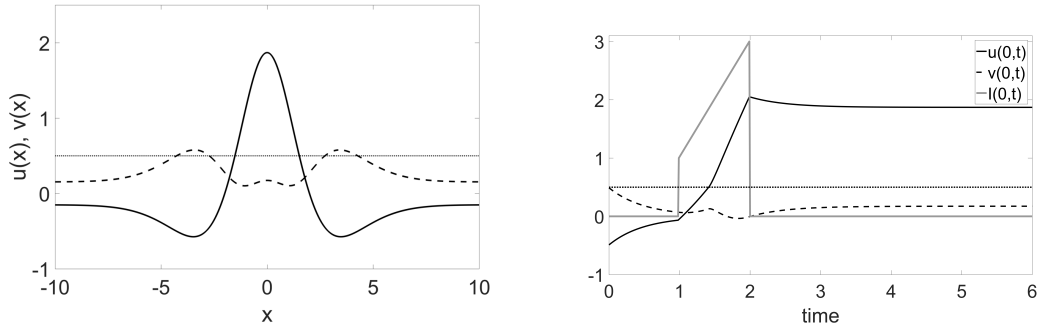

Figure 48: Effect of applying a dynamic input with continuously increasing strength. Parameters of the input: $A_{I_j} = [1, 3], \sigma_{I_j} = 1, d_{I_j} = 3$. The kernel w is given by (4.3) with $A_{ex} = 2$, $A_{in} = 1$, $\sigma_{ex} = 1.25$, $\sigma_{in} = 2.5$ and $g_{mex} = 0.1$. Threshold $\theta = 0.5$ (dotted line), $K = 0$.

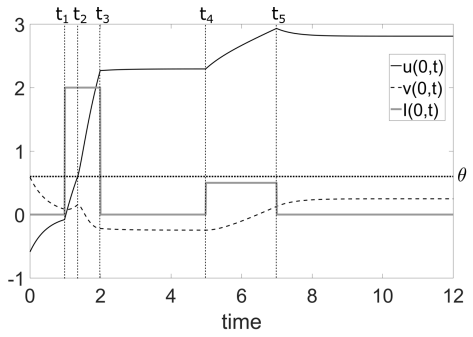

Figure 49: Time evolution of center positions of field u and v during integration of two transient inputs. At time $t = 1$ we apply an input with $A_{I_j} = 2$, $\sigma_{I_j} = 1$ and $d_{I_j} = 1$. Then at time $t = 5$ we apply an input with $A_{I_j} = 0.5$, $\sigma_{I_j} = 1$ and $d_{I_j} = 2$. $K = 0$, $\theta = 0.6$.

effect of lateral inhibition is predicted to be counterbalanced to some extent since the spatial integration of the v-field with an inverted Mexican hat profile propagates excitation outwards from stimulated regions. Figure 50 shows that in both models a three-bump solution evolves when three identical, transient inputs are applied at the same time. The situation is different for a sequential stimulation protocol (Figure 51). In the Amari case, only the first input triggers the evolution of a bump whereas the more balanced dynamics of the two-field model stabilizes again a three-bump solution. It is worth noting that suppression effects due to lateral inhibition can be also observed in the two-field model. In the next section we show that when inputs with different amplitudes are applied, the bump representation of a weaker input may become suppressed below threshold.

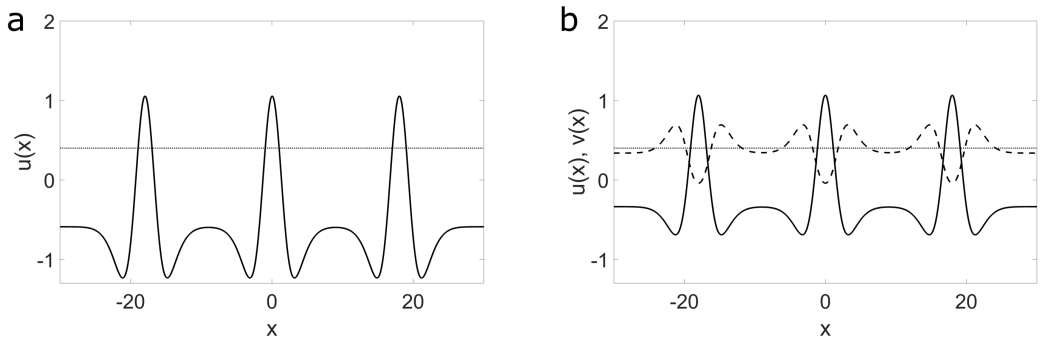

Figure 50: Solutions of the Amari model (**a**) and the two-field model (**b**) at time $t = 50$ created with simultaneous inputs. Input $I(x,t)$ with $A_{I_j} = 1, \sigma_{I_j} = 1, d_{I_j} = 1$ was applied at time $t = 1$. The kernel w is given by (4.3) with $A_{ex} = 2$, $A_{in} = 1$, $\sigma_{ex} = 1.25$, $\sigma_{in} = 2.5$ and $g_{mex} = 0.1$. Threshold $\theta = 0.4$ (dotted line), $K = 0$.

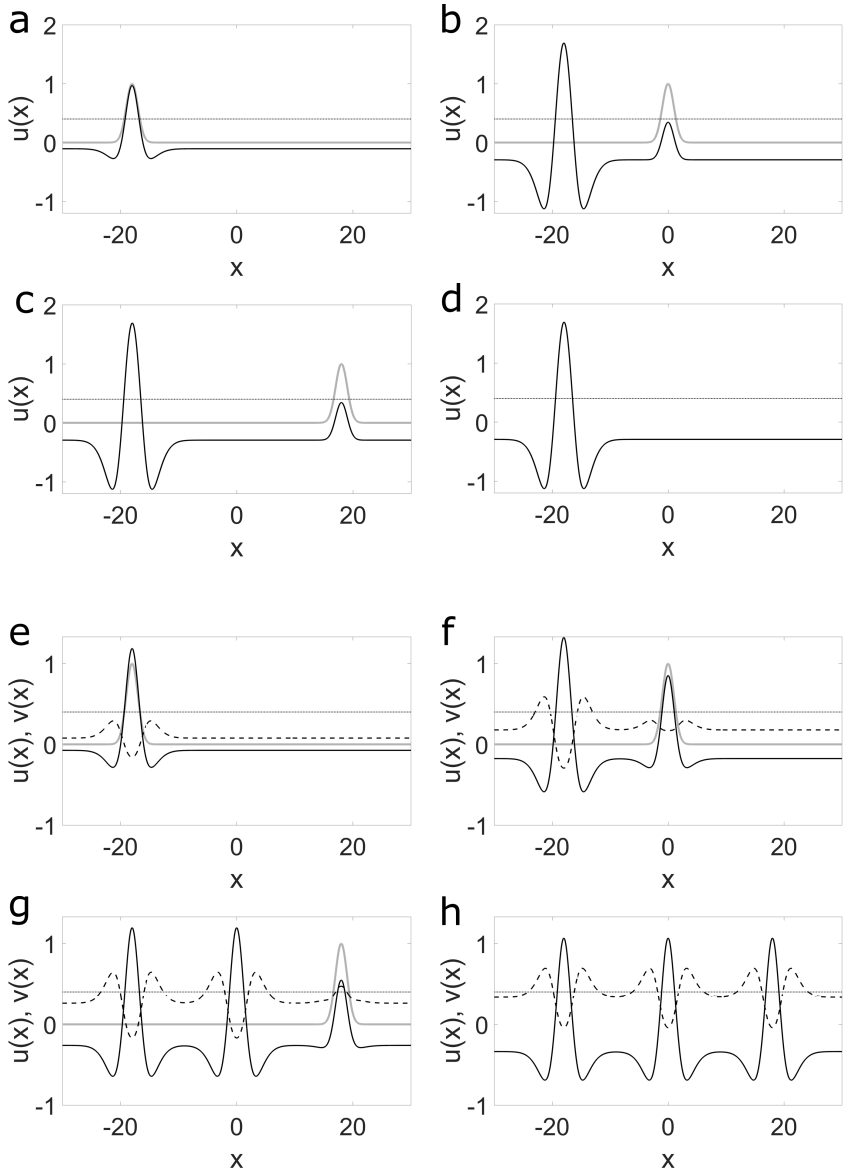

Figure 51: Solutions of the Amari model (**a**-**d**) and the two-field model (**e**-**h**) created with sequential inputs. Inputs $I(x,t)$ (gray lines) applied at times $t_1 = 1$, $t_2 = 10$ and $t_3 = 20$. Snapshots taken at times: $t = 2$ (**a** and **e**), $t = 11$ (**b** and **f**), $t = 21$ (**c** and **g**), $t = 50$ (**d** and **h**). Remaining parameters of the inputs: $A_{I_j} = 1, \sigma_{I_j} = 1, d_{I_j} = 1$. Parameters of the kernel as in Fig. 50. Threshold $\theta = 0.4$ (dotted line), $K = 0$.

8.3.1 Retro-cuing task

The representational quality of WM items is not only shaped by bottom-up input features as discussed above but may be also modulated by top-down signals representing task demands [164]. A behavioral paradigm that has attracted considerable interest over the last decade is retro-cuing (for an overview see [145]). It shows that memory performance can be enhanced by a cue indicating the most relevant item for the current task goals, even when the cue is applied long after the input array has been removed. A simple application of prioritizing an item during WM maintenance is a task in which the spatial location of two equally task-relevant movement targets has to be memorized, the information about the location to visit first may vary and becomes available only later during the task. The exact mechanisms underlying the retro-cueing benefit are still debated but recent modeling and experimental work suggests that top-down signals generate neural contrast by enhancing the neural population representations of the cued item and inhibiting activity of items irrelevant to current task goals [13, 65]. As illustrated in Figure 52, this view is consistent with the dynamics of the integrator model when a second transient input is applied to one of the two fields sites that had already developed a bump in response to a first input. In the context of the mentioned application, it is interesting to note that a neural activation gradient is the hallmark of so-called competitive cueing models of serial order [127]. In dynamic field implementations of this model class, a competitive winner-take-all dynamics in a decision field, which receives the memory gradient as input, is used to recall the stored serial order [58].

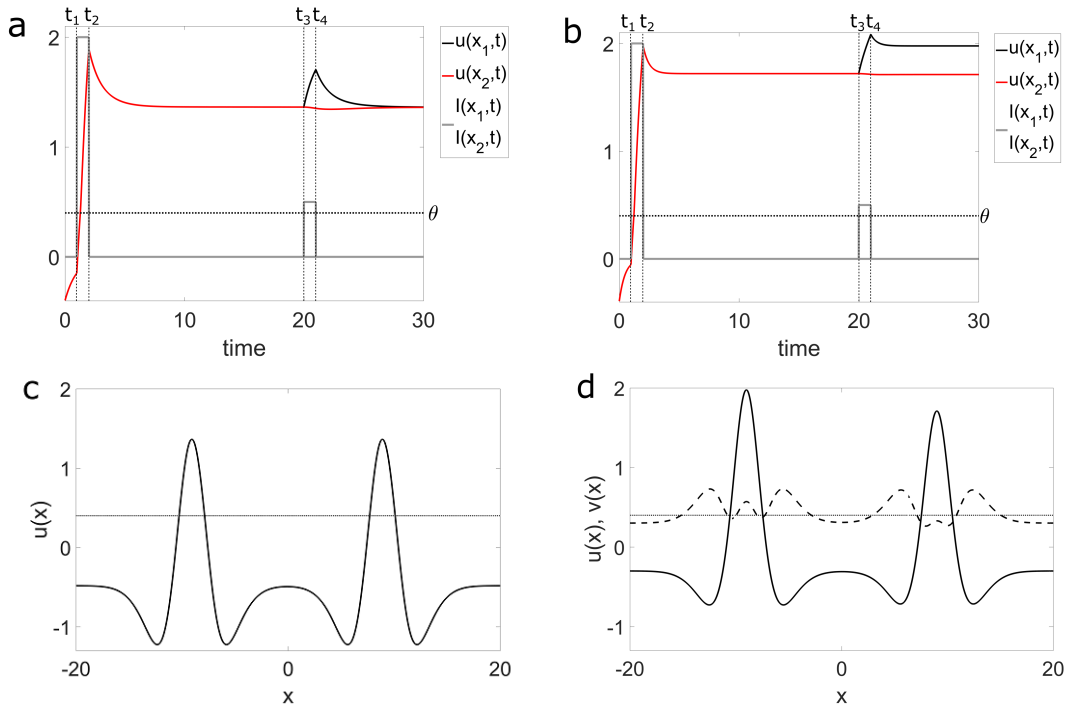

Figure 52: Retro-cuing task in the Amari model (**a** and **c**) and in the two-field model (**b** and **d**). Bumps are created with two inputs (grey lines) with $A_{I_j} = 2$ applied simultaneously at time $t_1 = 1$ at positions $x_1 = -9$ and $x_2 = 9$. At a later time $t_3 = 20$ an additional weak input with $A_{I_3} = 0.5$ is applied to one of the memories at x_1. (**a** and **b**) Temporal evolution of sites x_1 (black lines) and x_2 (red lines) in both models. (**c** and **d**) Snapshots showing the final solutions at time $t = 50$. Remaining parameters of the inputs: $\sigma_{I_j} = 1, d_{I_j} = 1$. The kernel w is given by (4.3) with $A_{ex} = 2$, $A_{in} = 1$, $\sigma_{ex} = 1.25$, $\sigma_{in} = 2.5$ and $g_{mex} = 0.1$. Threshold $\theta = 0.4$ (dotted line), $K = 0$.

Recent findings in functional magnetic resonance imaging (fMRI) studies using a retro-cueing paradigm have challenged the assumption that multiple items can be concurrently represented in an active state of persistent neural activity [131, 146]. The findings have been interpreted as evidence that only the currently most task-relevant item is maintained in an persistent state whereas the memories of currently unattended items are stored in stimulus-selective patterns of short-term synaptic facilitation. Computational models show that such latent "activity-silent" memory traces in the neural network can be restored into an active state by retro-cues or other non-specific read-out signals [115, 150]. However, the findings of the neurophysiological experiments are not conclusive since the applied data analysis technique might not be sensitive enough to detect the signatures of weak sustained neural activity associated with unattended items ([114], see [148] for neural evidence of multiple active WM representations). In fact, a recent modeling study based on the DNF framework convincingly showed that all key experimental findings of the fMRI retro-cue study [146] could be reproduced relying entirely on sustained neural activity for WM representations [136]. The existence of subthreshold bumps in the two-field model supports the notion that also

weak population activity can be sustained over behaviorally relevant timescales. Figure 53 simulates the same retro-cue task like in Figure 52 but with weaker initial inputs and stronger cue. The field develops again a two-bump but with a closer to threshold activation level. The main difference is that the population representation of the un-cued item now appears to be suppressed below threshold. Figure 54 shows that like in the computational studies of the activity-silent WM mechanism, the application of an unspecific input signal that does not provide any spatial information is sufficient to restore the subthreshold memory trace into a suprathreshold activity pattern.

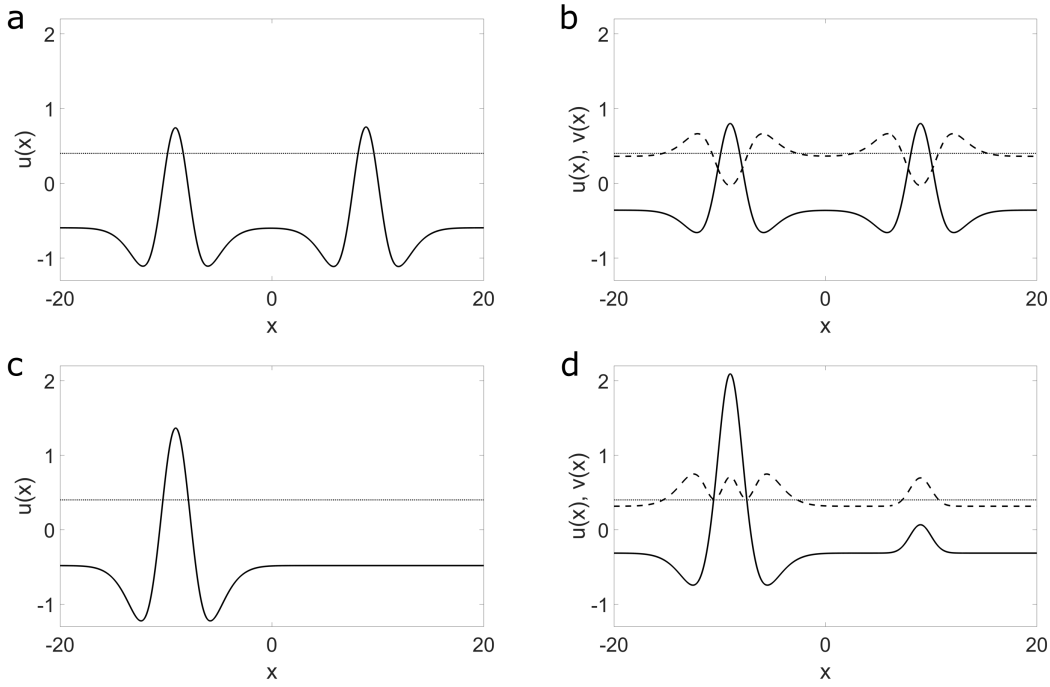

Figure 53: Retro-cuing task in the Amari model (left column) and in the two-field model (right column). Top row: Snapshots at time $t = 20$ showing bumps created with two inputs with $A_{I_j} = 0.75$. Bottom row: Snapshots at time $t = 50$ showing solutions after applying an additional input with $A_{I_3} = 2$ to one of the memories. Remaining parameters of the inputs: $\sigma_{I_j} = 1, d_{I_j} = 1$. The kernel w is given by (4.3) with $A_{ex} = 2$, $A_{in} = 1$, $\sigma_{ex} = 1.25$, $\sigma_{in} = 2.5$ and $g_{mex} = 0.2$. Threshold $\theta = 0.4$ (dotted line), $K = 0$.

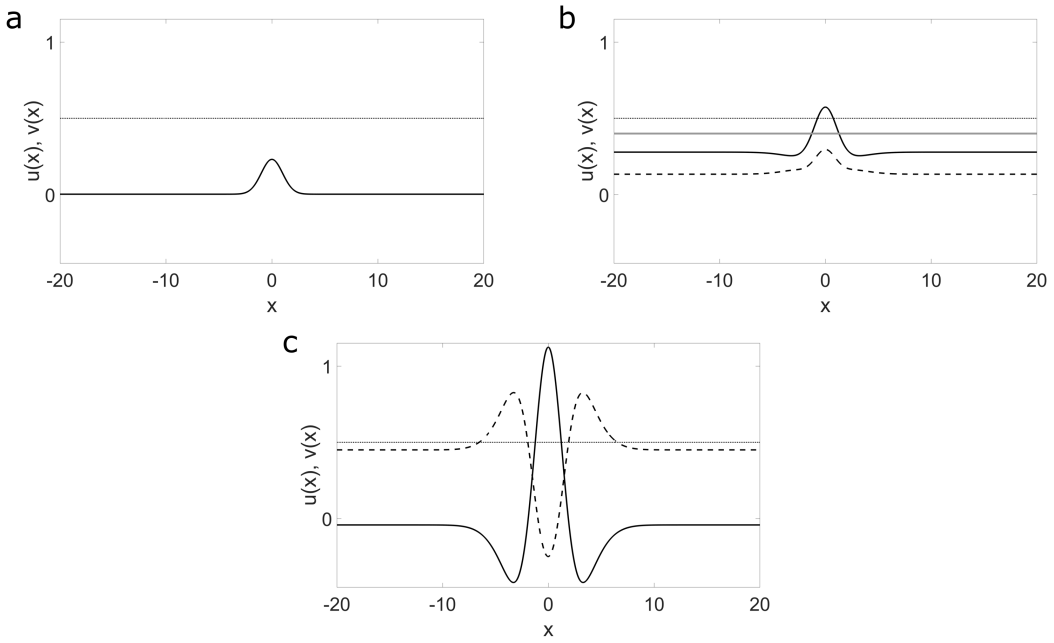

Figure 54: Recovery of a "forgotten" memory (subthreshold bump) using unspecific input. (**a**) Snapshot at time $t = 9$. Solution created with input with $A_{I_j} = 0.45$ applied at time $t = 1$ for duration $d_{I_j} = 1$. (**b**) Snapshot at time $t = 11$. A spatially constant input $I(x) = 0.4$ (grey line) is applied at time $t = 10$ for duration $d_I = 1$. (**c**) Snapshot at time $t = 50$. Parameters of the kernel as in Fig. 53. $K = 0$, $\theta = 0.5$.

8.3.2 Interacting bumps

An attractive feature of continuous attractor models is that they accurately explain errors in WM and other behavioral tasks as a distance-dependent interaction between two or more neural population representations [2, 47, 84, 165]. DNF models of lateral-inhibition type connectivity predict that when two transient inputs are presented in close proximity, the network dynamics exhibits an attraction effect [3, 93]. As shown in Figure 55, the Amari model makes the strong prediction that there is no possibility to independently store very similar points on a feature dimension since the two initially disjoint activity patterns will merge. This attraction effect has been exploited for instance to model target selection of fast saccadic eye movements that are known to land between two close targets ("averaging saccades" [165]). However, the finding in a WM task of no performance impairment when items in memory are similar has challenged the generality of the averaging hypothesis of simultaneously processed nearby feature values [106]. The two-field model develops in response to the same transient inputs a brought activation pattern with two peaks which is clearly distinguishable from a one-bump solution triggered by a single input. Interestingly, a recent experiment investigating a possible neural substrate of saccadic averaging in the superior colliculus (SC) reports that the simultaneous stimulation of two nearby SC sites evokes a single merged activation pattern centered between the two sites [156]. Consistent with the prediction of the two-field model, the

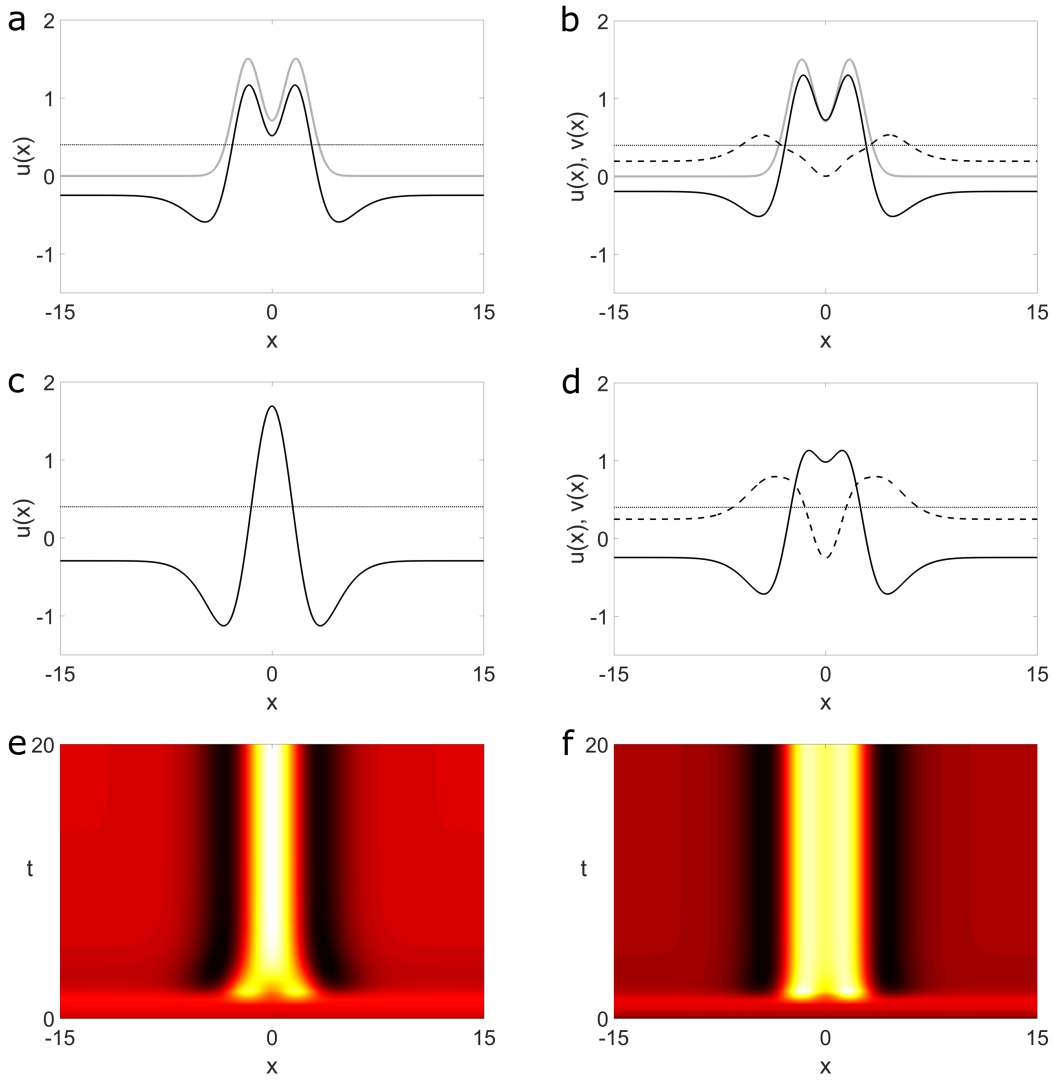

Figure 55: Merging bumps in the Amari model (left column) and in the two-field model (right column). Bumps created with two inputs with $A_{I_j} = 1.5, \sigma_{I_j} = 1, d_{I_j} = 1$, applied at time $t = 1$ at positions $x_{c_{1,2}} = \pm 1.7$. (**a** and **b**) Snapshots at time $t = 2$ when input (gray lines) is still present. (**c** and **d**) Steady states at time $t = 50$. (**e** and **f**) Time courses of models' activities. The kernel w is given by (4.3) with $A_{ex} = 2$, $A_{in} = 1$, $\sigma_{ex} = 1.25$, $\sigma_{in} = 2.5$ and $g_{mex} = 0.1$. Threshold $\theta = 0.4$ (dotted line), $K = 0$.

spread of activation appears to be significantly wider than the localized activity pattern induced by a single stimulation. In WM applications, a downstream read-out mechanism might interpret the existence of the two peaks and the relatively suppressed activity at the intermediate position as evidence for the storage of two similar inputs [106]. An attraction effect still manifests since the peak distance is smaller than the original input distance [2].

For larger input distances, both models show a repulsion effect for which direct neurophysiological and behavioral evidence has been also described [2, 47]. The predicted magnitude of the repulsion effect differs significantly however (Figure 56). The two localized inputs, which overlap to some extent, set the

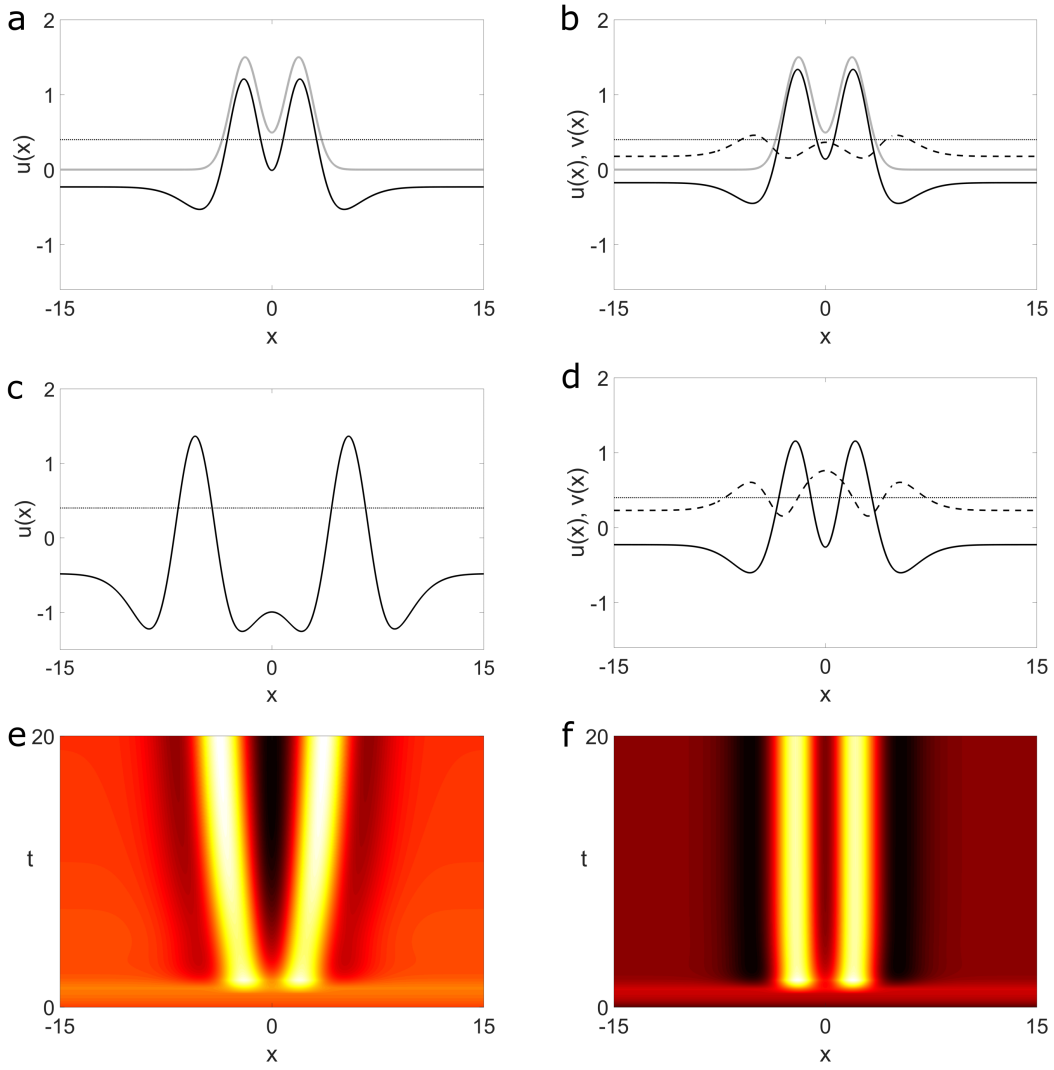

Figure 56: Repulsive bumps in the Amari model (left column) and in the two-field model (right column). Bumps created with two inputs with $A_{I_j} = 1.5, \sigma_{I_j} = 1, d_{I_j} = 1$, applied at time $t = 1$ at positions $x_{c_{1,2}} = \pm 1.9$. (**a** and **b**) Snapshots at time $t = 2$ when input (gray lines) is still present. (**c** and **d**) Steady states at time $t = 200$. (**e** and **f**) Time courses of models' activities. The kernel w is given by (4.3) with $A_{ex} = 2$, $A_{in} = 1$, $\sigma_{ex} = 1.25$, $\sigma_{in} = 2.5$ and $g_{mex} = 0.1$. Threshold $\theta = 0.4$ (dotted line), $K = 0$. The solution in panel **d** is solution P_4 shown in Fig. 37.

dynamics of the two-field model in the basin attraction of a two-bump solution with an inter-peak distance larger than the input distance. In the Amari case, the attractor state represents two independent bumps located at a further increased distance for which the mutual inhibitory interaction is constant. As shown in Fig. 38, the magnitude of the repulsion effect depends on the spatial shape of the lateral inhibition controlled by the parameter σ_{inh}.

A third type of distance-dependent interaction effect discussed in continuous attractor models is bump annihilation [93, 162]. It may occur when a bump is closely flanked by two others. Figure 57 shows an

example simulation of the Amari model where the summed lateral inhibition of the two flanking bumps suppresses the input-induced suprathreshold activity at the intermediate position $x = 0$, resulting in a complete memory loss. Bump annihilation thus limits the number of items that can be simultaneously stored in a field of a given size. The situation is different for the integrator model where a weaker but still subthreshold bump stabilizes at $x = 0$. With inputs closer to threshold, the intermediate bump becomes suppressed below threshold but the activity still remains sustained. Recent experimental findings support the notion of a neural encoding and maintenance of weak visual inputs into WM that do not reach the threshold for conscious perception but may still affect goal-directed behavior [143]. Models of the capacity limits of working memory are silent on this issue [150]. Future research might attempt to more directly test the hypothesis that sustained subthreshold activity constitutes a neural substrate of conscious and unconscious memory.

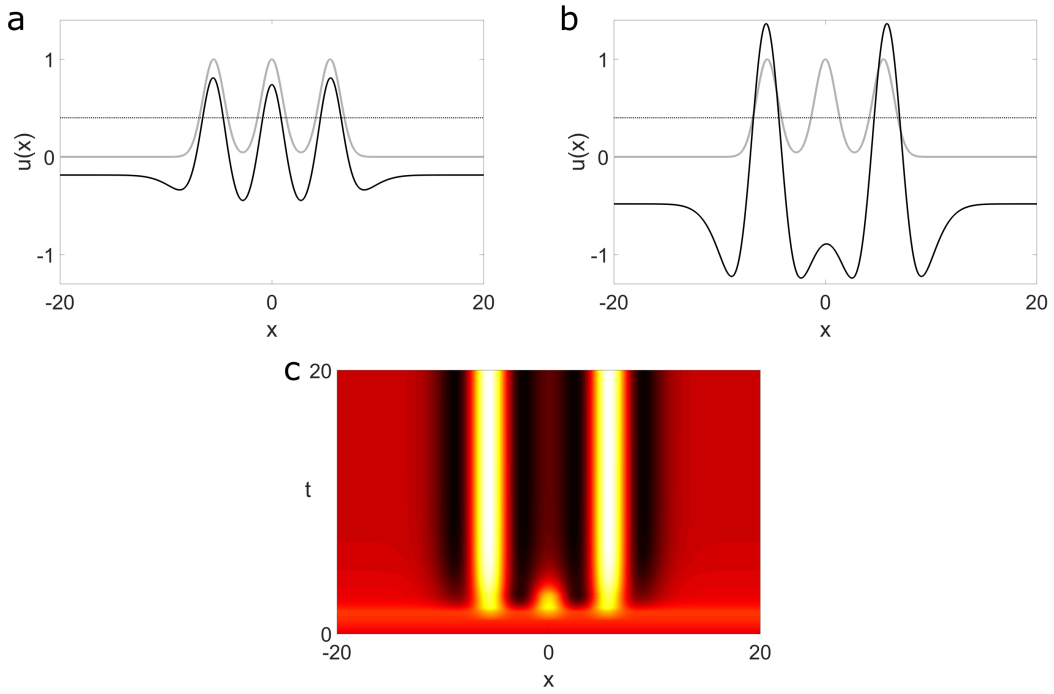

Figure 57: Bump annihilation in the Amari model. (**a**) Snapshot at time $t = 2$ when input (gray line) is still present. (**b**) Steady state at time $t = 100$. (**c**) Time course of model activity. Bumps created with three inputs with $A_{I_j} = 1, \sigma_{I_j} = 1, d_{I_j} = 1$, applied at time $t = 1$ at positions $x_{1,2,3} \in \{-5.5, 0, 5.5\}$. The kernel w is given by (4.3) with $A_{ex} = 2$, $A_{in} = 1$, $\sigma_{ex} = 1.25$, $\sigma_{in} = 2.5$ and $g_{mex} = 0.2$. Threshold $\theta = 0.4$ (dotted line).

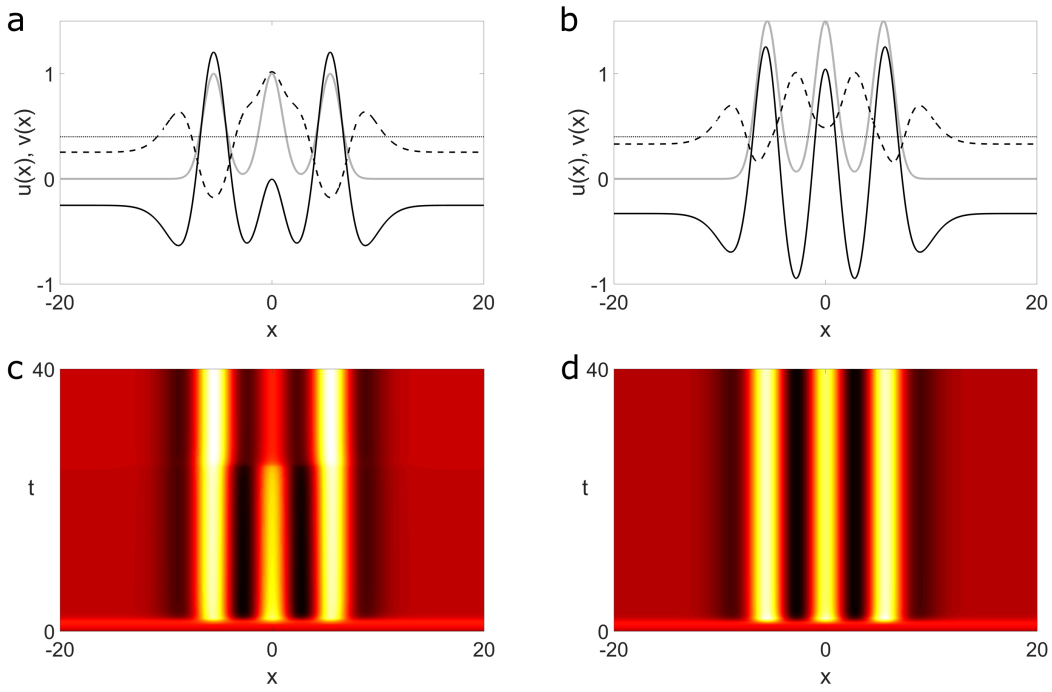

Figure 58: Three-bump solutions of the two-field model. (**a** and **b**) Steady states at time $t = 100$. (**c** and **d**) Time courses of model activities. Bumps created with three inputs (gray lines) with $A_{I_j} = 1$ (left column) and $A_{I_j} = 1.5$ (right column) applied at time $t = 1$ at positions $x_{1,2,3} \in \{-5.5, 0, 5.5\}$. Remaining input parameters $\sigma_{I_j} = 1$, $d_{I_j} = 1$. The kernel w is given by (4.3) with $A_{ex} = 2$, $A_{in} = 1$, $\sigma_{ex} = 1.25$, $\sigma_{in} = 2.5$ and $g_{mex} = 0.2$. Threshold $\theta = 0.4$ (dotted line), $K = 0$.

8.3.3 Bump drift and bump interaction in the stochastic integrator model

To evaluate the impact of random fluctuations on the evolution and maintenance of input-driven bumps of the two-field model, we use a stochastic version of the field equations with additive noise. It is given by

$$\frac{\partial u(\mathbf{x},t)}{\partial t} = -u(\mathbf{x},t) + v(\mathbf{x},t) + \int_\Omega w(\mathbf{x},\mathbf{x}') f(u(\mathbf{x}',t) - \theta)\mathrm{d}\mathbf{x}' + I(\mathbf{x},t) + \epsilon^{1/2}\mathrm{d}W(\mathbf{x},t), \tag{8.6a}$$

$$\tau_v \frac{\partial v(\mathbf{x},t)}{\partial t} = -v(\mathbf{x},t) + u(\mathbf{x},t) - \int_\Omega w(\mathbf{x},\mathbf{x}') f(u(\mathbf{x}',t) - \theta)\mathrm{d}\mathbf{x}', \tag{8.6b}$$

where $\mathrm{d}W(x,t)$ is the increment of a spatially correlated Wiener process such that

$$\langle \mathrm{d}W(x,t) \rangle = 0, \tag{8.7}$$

$$\langle \mathrm{d}W(x,t)\mathrm{d}W(y,s) \rangle = C(x-y)\delta(t-s)\mathrm{d}t\mathrm{d}s, \tag{8.8}$$

and $\epsilon \ll 1$ is the noise amplitude.

Closely following the conceptually related bump attractor model of Carroll and colleagues [30], we choose

a cosine spatial correlation function

$$C(x) = \pi \cos(x). \tag{8.9}$$

The correlation function $C(x-y)$ can be related directly to a spatial filter $\mathcal{F}(x-y)$. The term $\mathrm{d}W(x,t)$ can be defined by convolving a spatially white noise process $\mathrm{d}\mathcal{Y}(x,t)$, satisfying $\langle \mathrm{d}\mathcal{Y}(x,t)\rangle = 0$ and $\langle \mathrm{d}\mathcal{Y}(x,t)\mathrm{d}\mathcal{Y}(y,s)\rangle = \delta(x-y)\delta(t-s)\mathrm{d}t\mathrm{d}s$ with the filter $\mathcal{F}(x-y)$ such that

$$\mathrm{d}W(x,t) = \int_\Omega \mathcal{F}(x-y)\mathrm{d}\mathcal{Y}(y,t)\mathrm{d}y, \tag{8.10}$$

where $\mathcal{F}(x-y) = C(x-y)$. The noise term is added to the u-equation only. This allows us to directly compare the simulations of the two-field model with the behavior of the Amari model defined by the u-equation. Our simulations show that adding the same noise model also to the v-equation does not change the qualitative model predictions reported here.

8.3.3.1 Bump drift

Due to the neutral stability of a bump in a continuous attractor network, random noise may lead to a drift of the bump in the absence of tuned external input [28, 30, 87]. Stochastic dynamic field models thus predict a time-dependent loss of precision of WM representations. Direct neurophysiological and behavioral evidence for this prediction comes from a recent study using a spatial WM paradigm in which a monkey had to make saccadic eye movements to a remembered target. The results showed that the recalled location deviates on a trial-by-trial basis precisely in the direction of the drift of the tuned population activity at the end of the delay period [168].

Figure 59 shows for a single run of the stochastic integrator the bump drift at a fixed time (a) and in a space-time plot (b). Larger drifts represent larger errors of the memorized location relative to the location represented by the neural activity during input presentation at time $t = 0$ at position $x = 0$. Since recall precision is known to be influenced by bottom-up sensory salience and top-down factors like retro-cues, the bump amplitude representing the quality or strength of the item memory should affect the drift rate. We tested this prediction in simulations of the stochastic model with inputs of varying strength (100 simulations for each strength). As shown in panel (c), the variance of the bump center position decreases systematically with increasing bump amplitude. For the highest amplitude tested, the fluctuations over time around the true input position are rather small. This dependence of the drift on input strength is consistent with the results obtained with the DNF model proposed by Carroll and colleagues [30]. Since there is no dependence of bump shape on input features in the Amari model, there is a unique drift pattern.

For the present parameter setting, it is comparable with the pattern observed with input strength $A_I = 3$ of the two-field model.

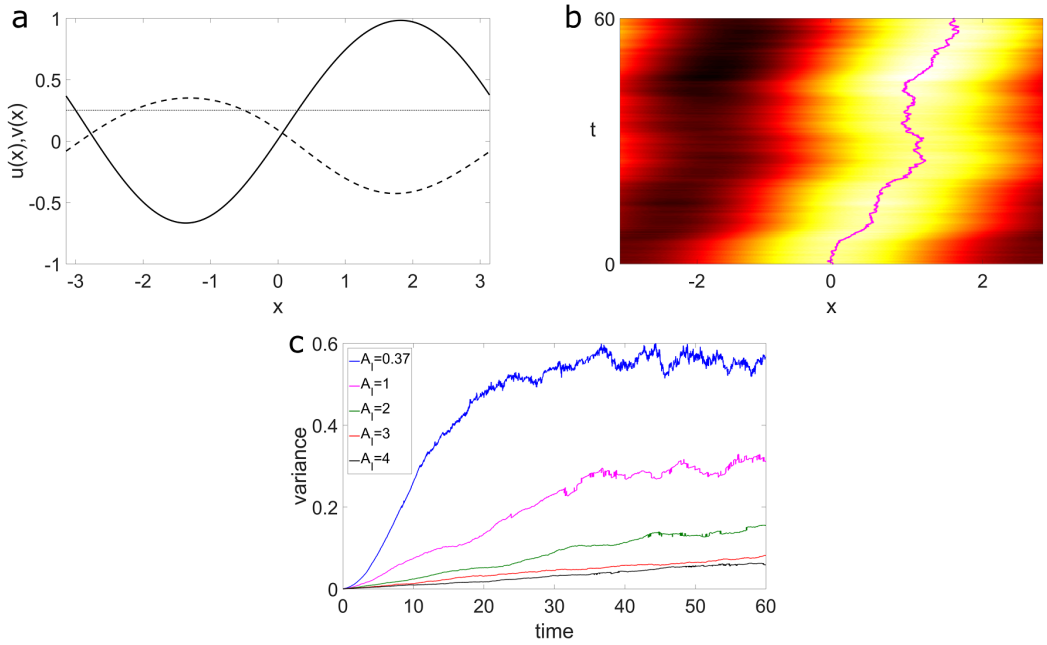

Figure 59: Bump diffusion in the stochastic two-field model. (**a**) Bump solution at time $t = 60$. The initial condition is a bump centered at $x = 0$. (**b**) Space-time plot showing the bump drift. (**c**) Variance of the bump's position computed for $N = 100$ numerical simulations of the model with different input strengths A_I. Remaining input parameters $\sigma_{I_j} = 1$, $d_{I_j} = 1$. The kernel w is given by (4.3) with $A_{ex} = 2$, $A_{in} = 1$, $\sigma_{ex} = 1.5$, $\sigma_{in} = 2.5$ and $g_{mex} = 0.3$. Threshold $\theta = 0.25$ (dotted line), $K = 0$, $\epsilon = 0.005$, $L = \pi$, $\mathrm{d}x = 0.01$, $\mathrm{d}t = 0.01$.

8.3.3.2 Bump interaction

As we have shown in section 8.3.2, recall precision in continuous attractor models also depends on potential interference of nearby memory traces. We have therefore also tested the behavior of the stochastic integrator model with two simultaneously presented inputs. They were placed at a critical distance where in the deterministic case a repulsion effect manifests and a small reduction of the input distance ($2\,\mathrm{d}x$, where $\mathrm{d}x$ is the numerical mesh size) causes attraction. Figure 60 (a) shows overlaid activity profiles of an evolving two-bump solution taken at a fixed time in different model simulations. As can be clearly seen, the additive noise causes a switching between either attraction or repulsion in different trials. Panel (b) shows that the magnitude of the interference effect appears to be greatly reduced when stronger inputs are applied. Panel (c) show this dependence on input strength/bump amplitude in a more quantitative manner by plotting the variance of the inter-peak distance as a function of time. To allow a direct comparison, Figure

61 depicts, for the same input distance, the activity pattern at a fixed time in two runs of the stochastic Amari model. It develops either a single bump (a) or a two-bump with repulsion (b). The model simulations show that the single bump may be the result of a suppressive interaction or a fast merging of the input-induced activity patterns.

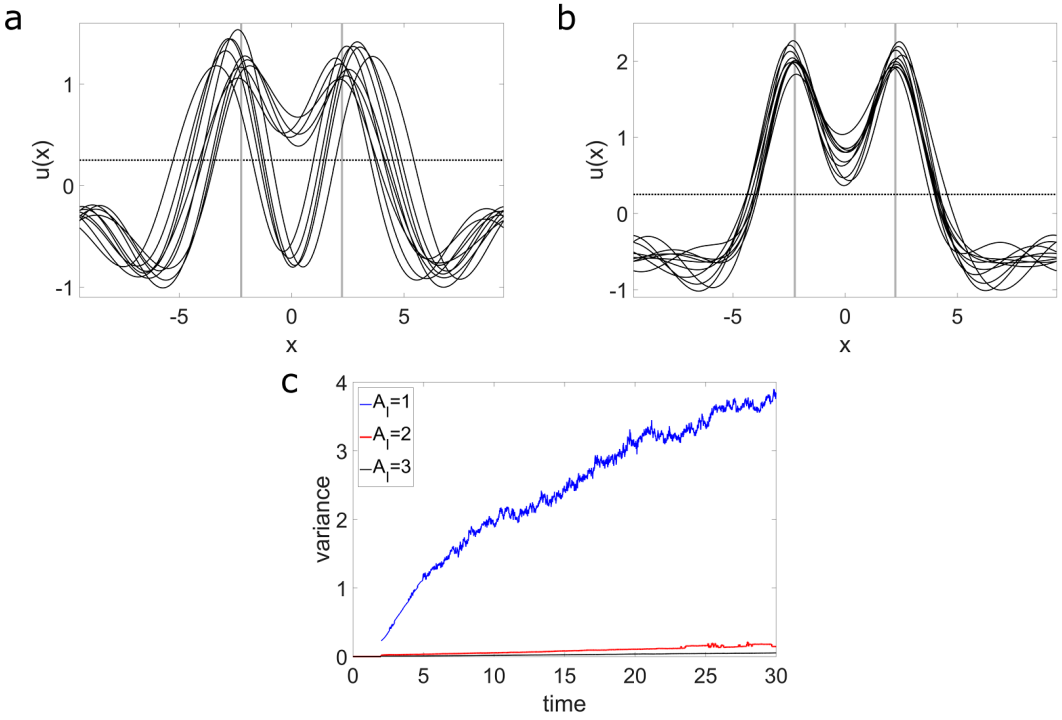

Figure 60: Bump attraction/repulsion due to noise in the two-field model. Sample profiles of u-field of the model at time $t = 30$ created with two inputs with $A_{I_j} = 1$ (**a**) and $A_{I_j} = 3$ (**b**). The percentage of "merged" solutions for inputs with amplitudes $A_I \in \{1, 2, 3\}$ in $N = 500$ trials was respectively 60%, 98% and 100%. (**c**) Variance of the inter-peak distance as a function of time computed for $N = 500$ numerical simulations of the model for different input strengths A_I. The inputs with amplitudes $A_{I_j} = 1$, $A_{I_j} = 2$, $A_{I_j} = 3$, are applied at positions $x_{1,2} = \pm 2.25$. Remaining parameters of the inputs are $\sigma_{I_j} = 1$ and $d_{I_j} = 1$. The kernel w is given by (4.3) with $A_{ex} = 2$, $A_{in} = 1$, $\sigma_{ex} = 1.5$, $\sigma_{in} = 2.5$ and $g_{mex} = 0.1$. Threshold $\theta = 0.25$ (dotted line), $K = 0$, $\epsilon = 0.0025$, $L = 3\pi$, $\mathrm{d}x = 0.01$, $\mathrm{d}t = 0.01$.

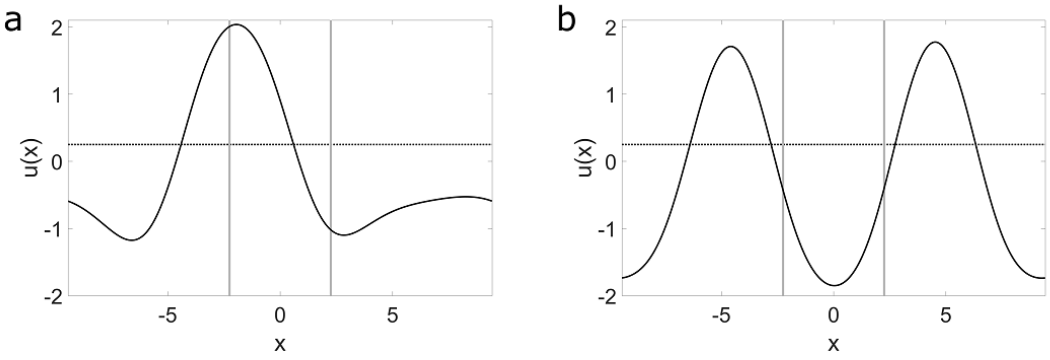

Figure 61: Bump merging (**a**) and repelling (**b**) in the Amari model due to noise. The inputs with amplitudes $A_1 = 1$ are applied at positions $x_{1,2} = \pm 2.25$. Remaining parameters of the inputs are $\sigma_I = 1$ and $d = 1$. The kernel w is given by (4.3) with $A_{ex} = 2$, $A_{in} = 1$, $\sigma_{ex} = 1.5$, $\sigma_{in} = 2.5$ and $g_{mex} = 0.1$. Threshold $\theta = 0.25$ (dotted line), $\epsilon = 0.0025$, $L = 3\pi$, $\mathrm{d}x = 0.01$, $\mathrm{d}t = 0.01$.

8.3.4 Gated integrator model

The two-field model performs a continuous integration of input streams of any strength. This is a desirable feature for decision making since also weak evidence may bias decision processes involving multiple alternatives. One potential problem with the perfect integrator mechanism is that the pure accumulation of noise at field sites without specific input may in principle lead to the creation of bumps. Other neuro-inspired integrator models solve this problem by implementing circuit-based gating mechanism that control the minimum level of evidence entering the accumulation process [27, 92]. We propose a simple extension of the two-field model in which the coupling between the two layers is gated by a threshold function $g(u)$. A step function with threshold $\kappa \leq \theta$ is used for simplicity. The model reads

$$\frac{\partial u(\mathbf{x},t)}{\partial t} = -u(\mathbf{x},t) + v(\mathbf{x},t)g(u(\mathbf{x},t)-\kappa) + \int_\Omega w(\mathbf{x},\mathbf{x}')f(u(\mathbf{x}',t)-\theta)\mathrm{d}\mathbf{x}' + I(\mathbf{x},t) + \epsilon^{1/2}\mathrm{d}W(\mathbf{x},t), \tag{8.11a}$$

$$\frac{\partial v(\mathbf{x},t)}{\partial t} = -v(\mathbf{x},t) + u(\mathbf{x},t)g(u(\mathbf{x},t)-\kappa) - \int_\Omega w(\mathbf{x},\mathbf{x}')f(u(\mathbf{x}',t)-\theta)\mathrm{d}\mathbf{x}'. \tag{8.11b}$$

Functionally, the state-dependent gating mechanism delays the perfect integration of evidence until a target location is selected by an initial input of strength $A_I > \kappa$, rendering a bump creation by accumulated (weak) noise unlikely. Figure 62 (left column) compares the pattern formation in response to an input at $x = 0$ in the stochastic model without (a and b) and with gating mechanism using different gating thresholds κ (c,d,e and f). Without gating mechanism, in addition to the input-driven bump at $x = 0$ various noise-induced bumps at other locations develop.

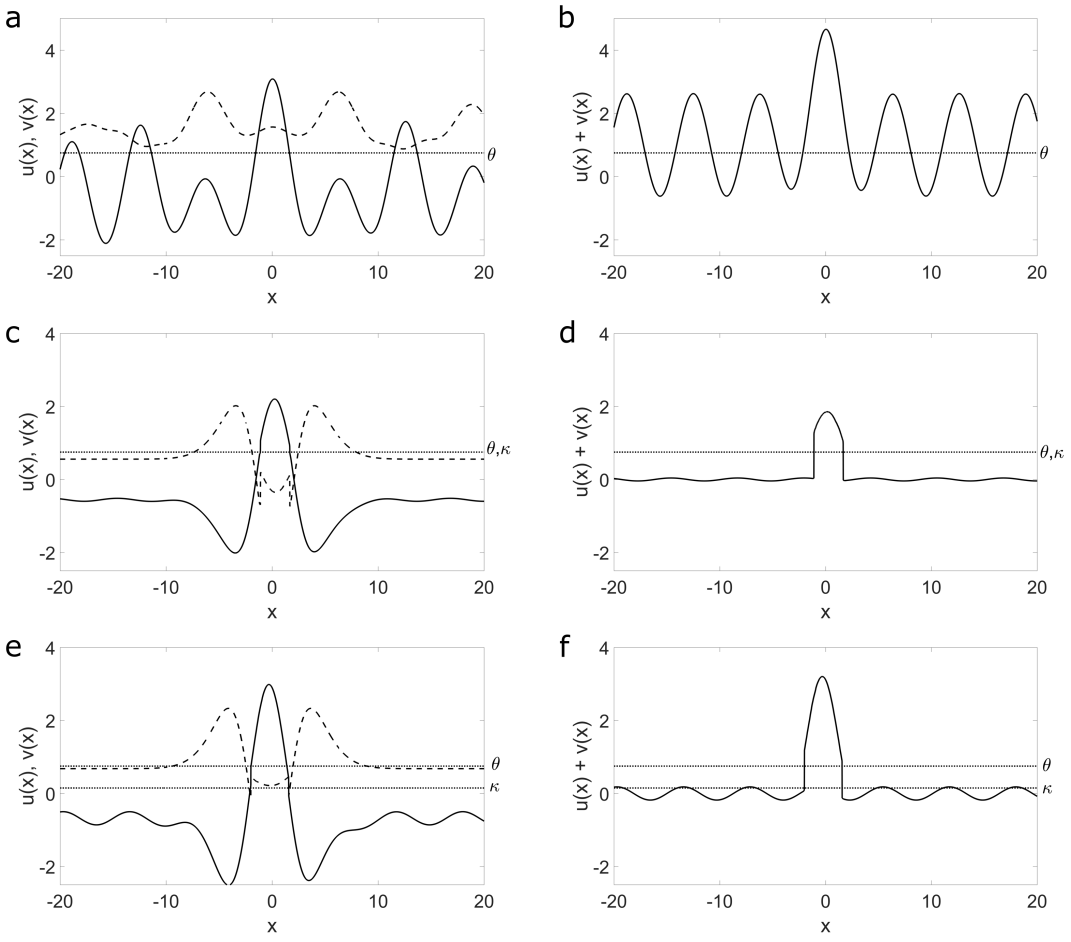

Figure 62: Simulations of the two-field model (8.11) with different values of threshold κ and the Mexican hat function given by (4.3) with $A_{ex} = 3$, $A_{in} = 1.5$, $\sigma_{ex} = 1.4$, $\sigma_{in} = 3$ and $g_{mex} = 0.2$, $\theta = 0.75$, $K = 1$. Spatial fluctuations as given by a cosine-correlated noise with $\epsilon = 0.005$. Bumps created with input with $A_{I_j} = 2, \sigma_{I_j} = 1.5, d_{I_j} = 1$, applied at $x = 0$. (**a**,**b**) no gating; (**c**,**d**) $\kappa = \theta = 0.75$; (**e**,**f**) $\kappa = 0.15$.

The impact on noise integration can be seen when comparing the sum of $u(x)$ and $v(x)$, representing the total of accumulated external input and noise. For the gating case, the integral represents the bell-shaped input slightly corrupted by noise and small random fluctuations at other field sites whereas for the case without gating, the integral represents a clearly suprathreshold multi-bump pattern. It is important to notice that the gating mechanisms do not destroy the existence of subthreshold bumps since for sites x with $u(x) > \kappa$ a continuous integration of weak inputs is still supported.

The gating mechanism is also important for resetting stimulus-selective persistent activity to a homogeneous resting state. In WM applications of continuous attractor networks, it is typically assumed that a switch between a bump attractor and a stable resting state can be achieved by applying a transient inhibitory input to all neurons [28]. Figure 63 illustrates this “forgetting” mechanism in a model simulation

without noise. The neural integrator first develops a bump in response to a localized excitatory input which is followed by a strong decrease in activation when at time $t = 21$ the homogeneous inhibition is applied to the u-field. Functionally, the two fields become decoupled since $g(u) < \kappa, \forall x$, and the subthreshold activity in both layers converges to the homogeneous resting state, $u = v = 0$ as predicted by the Amari model [3].

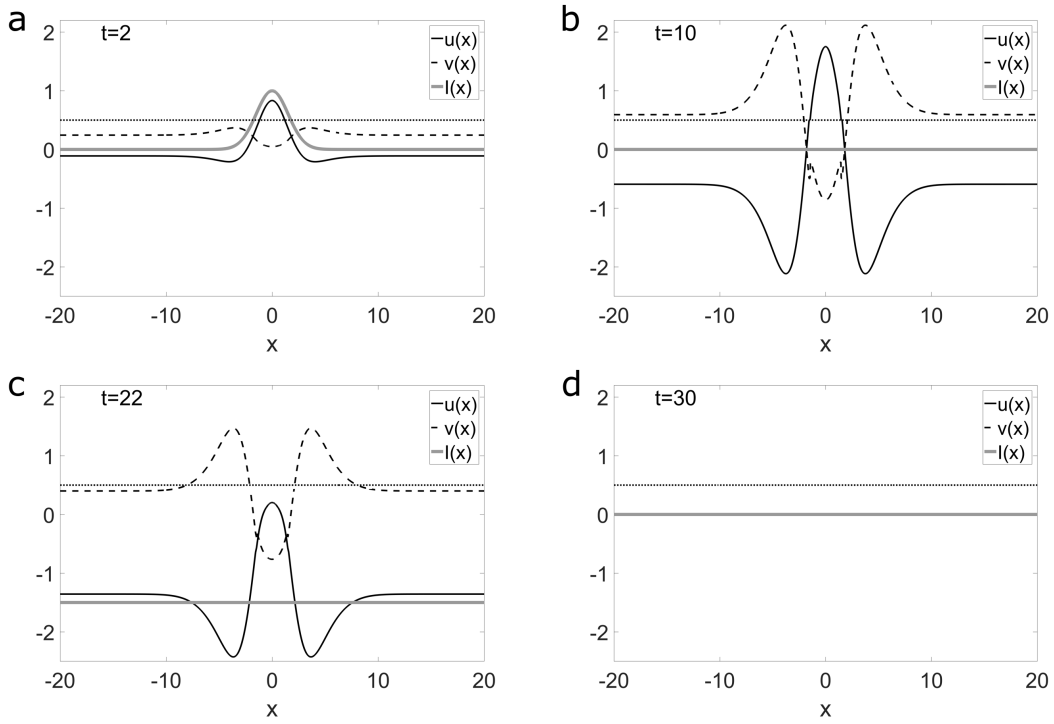

Figure 63: Forgetting mechanism. A bump is first triggered by localized input applied at $t = 1$ (**a** and **b**). This is followed by a decay to resting state (**c** and **d**) when at time $t = 21$ a homogeneous inhibitory input is applied to the u-field of the two-field model (8.11). The connectivity function is given by (4.3) with $A_{ex} = 3$, $A_{in} = 1.5$, $\sigma_{ex} = 1.4$, $\sigma_{in} = 3$ and $g_{mex} = 0.2$. The localized input is defined by $A_{I_j} = 1, \sigma_{I_j} = 1.5, d_{I_j} = 1$ and the homogeneous inhibition by $A = -1.5$ and $d_{I_j} = 1$. Thresholds $\kappa = \theta = 0.5$ (dotted line), $K = 1$.

8.4 Conclusion

In this chapter, we have presented a bump attractor model which is able to sustain localized activity patterns evoked by external inputs which differ in shape *and* amplitude. The model simulations demonstrate that the network dynamics not only supports the encoding of a single input value in the bump position but also the storage of additional stimulus attributes like uncertainty, intensity or duration in the bump shape. Moreover, the model works as a robust neural integrator since the bump amplitude faithfully reflects the accumulation

of input signals over time. This contrasts with the behavior of most attractor networks applied in working memory and decision making tasks in which the stable state corresponds to a stereotyped pattern of activity exclusively determined by the recurrent interactions within the network. The input dependence is achieved by combining a lateral-inhibition type network connectivity with local inhibitory and excitatory feedback mechanisms that are able to stabilize input-induced changes of the population activity at any level.

Using an identical parameter set allowed us to directly compare the performance of the two-field model with the classical Amari model. The network with the balanced local feedback exhibits several distinct features. First, two stable regions of excitation may exist at a distance where a gradient in the lateral inhibition profile predicts a merging or drifting of the bumps in the Amari model. Moreover, the lateral feedback excitation of the two-field model facilitates in general the formation of memory bumps. This is particularly evident in a sequential stimulus protocol in which lateral inhibition in the Amari model may prevent the encoding of an input in a stable activity pattern. This is true even for the case of a spatially uniform lateral inhibition for which a multi-bump solution exists. The two-field model thus predicts a higher working memory capacity without the need to refer to additional processing mechanism like top-down excitation [44] or a stimulus-selective synaptic facilitation [115]. Second, the activation pattern induced by two nearby inputs does not merge completely into in a single bump at an intermediate position but displays a wide plateau in its profile. This result is consistent with the prediction of biophysically realistic bump attractor networks [162] and has been described in electrophysiological stimulation studies [156]. The higher uncertainty expressed by the wider activity distribution could be used by a downstream read-out system in cue integration and decision making tasks. Third, the two-field model supports the existence of stable subthreshold activity patterns. In the context of the retro-cuing paradigm, we have argued that such patterns might represent less-salient items that become suppressed below threshold by means of lateral inhibition from bumps representing cued items. The experimental observation that neural memory representations often degrade to a large extent during the delay period has been taken as evidence for an active-silent state of working memory encoded in synaptic changes [115]. The model simulations however suggest that postulating such a latent memory state might not be necessary at least for the retro-cuing task [136]. The information represented by weak sustained activity is not lost but can be restored with a spatially unspecific cue.

Unlike in bistable attractor models of Amari type, the baseline activity of the neural integrator is not a stable state. A forgetting mechanism can thus not be implemented by simply applying a sufficiently strong

inhibitory input that destabilizes existing bumps. For working memory applications, we have proposed a simple gating mechanism for the local feedback which restores the stable resting state of the Amari model without destroying the existence of subthreshold bump solutions.

The possibility to represent stimulus attributes in the bump shape allows us to make predictions about the impact of for instance input strength (or contrast) on working memory performance. Simulations of the stochastic version of the two-field model reveal that the noise-induced drift of a single bump in the continuous attractor network decreases with increasing bump amplitude associated with stronger inputs. Larger bump amplitudes also greatly reduce the interaction effects of two input-induced bumps at a critical distance which can be described as repulsion or attraction when considering the relative peak positions.

9 DNF model for measuring and reproducing time intervals[1]

9.1 Introduction

In this chapter, we use the model of a robust neural integrator introduced in Chapter 4 to investigate in numerical simulations neuro-inspired processing mechanism that can be used to endow robots with the capacity to measure and produce time intervals in a highly flexible manner. We review recent neurophysiological evidence suggesting that the neural computational principles supporting this capacity may be understood from a dynamical systems perspective: Inputs and initial conditions determine how a recurrent neural network evolves from a "resting state" to a state triggering the action. During measurement, the temporal accumulation of input leads to the evolution of a self-stabilized bump whose amplitude reflects elapsed time. During production, the stored information is used to reproduce on a trial-by-trial basis the time interval either by adjusting input strength or initial condition of the integrator. We discuss the impact of the results on our goal to endow autonomous robots with a human-like temporal cognition capacity for natural human-robot interactions.

9.2 Interval reproduction task

Our successful interaction with an inherently dynamic environment requires the capacity to perceive elapsed time and to produce highly timed motor responses. Humans and other animals are able to generate time intervals in the range of tens of milliseconds to several seconds in anticipation of sensory events (e.g., a color change of a traffic light) without a clock or any external device [64, 110]. Moreover, the temporal control of behavior often shows a striking flexibility [125], allowing the adjustment of movement initiation time based on a single or very few observations of environmental changes (e.g. a prolonged amber phase). How the nervous system manages to flexibly process temporal information in

[1] The content of this chapter is based on [172].

the service of behavioral goals is currently an active research field (for a recent review see [119]). A recent experiment in which monkeys were trained to measure different sample intervals (demarcated by two time markers) and immediately afterward reproduce it by a proactive saccade to a predefined target, reveals new insights into the neural processing mechanisms [83]. We show the experimental setup for the interval reproduction task from [83] in Figure 64. The main finding during the production epoch is a monotonic

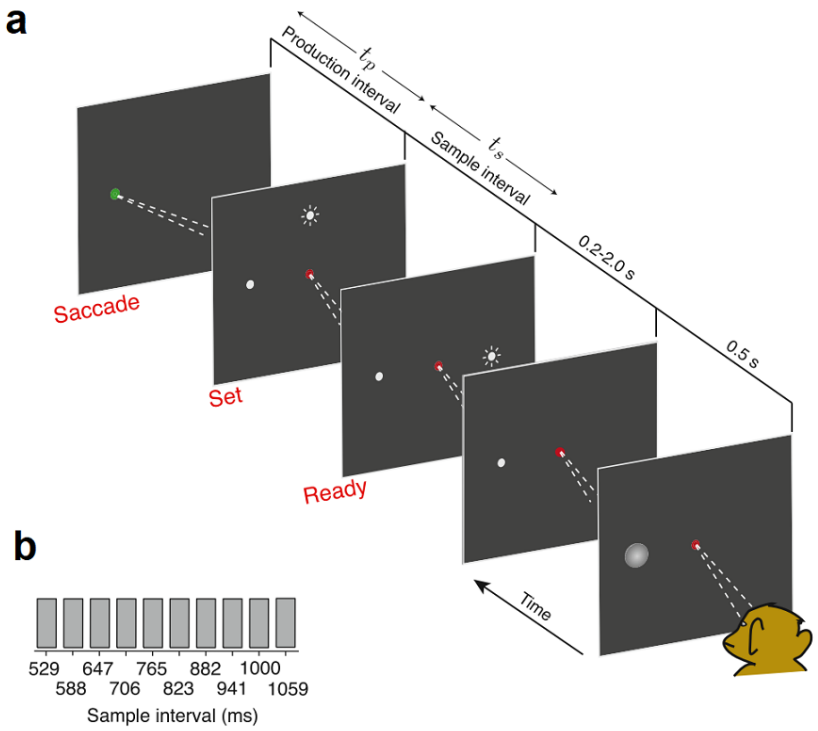

Figure 64: (**a**) Experimental setup for the "Ready, Set, Go" (RSG) task. In the measurement epoch (ME), monkeys measured a sample interval, marked by two cues: "Ready" and "Set". In the production epoch (PE), monkeys had to reproduce the sample interval by making a saccadic eye movement to a visual target (there was no explicit "Go" signal). Sample intervals were drawn randomly from a discrete uniform distribution with values ranging between 529 and 1,059 ms (**b**). From [83], Figure 1A-B.

increase of neural population activity to a fixed threshold value associated with saccade onset. Such a ramp-to-threshold dynamics has been described previously in a wide range of brain areas during timing tasks [119]. The interesting novelty of this study is the observation that the population activity at the end of the measuring epoch (ME) predicts on a trial-by-trial basis the buildup rate during the production epoch (PE) and consequently anticipates the time of the upcoming motor response. Longer sample intervals are associated with higher firing rates at the end of ME and shallower buildup rates during PE. Averaged neural responses during both ME and PE epochs are shown in Figure 65.

Most computational models of ramping activity explain the accumulation of temporal evidence as a

result of a network mechanism in which positive and negative feedback is mediated by recurrent connections between neurons [126, 142]. However, well known problems with these integrator models are the requirement to fine tune network connections and the lack of robustness to perturbations [105]. Moreover, changes in the network structure (e.g., through Hebbian synaptic modification) are assumed to tune the slope of ramping activity to a new sample interval [126]. Here we use a novel model of a robust neural integrator [170] based on the theoretical framework of dynamic neural fields [138] to test a dynamical systems view on flexible measurement and reproduction of time intervals [125]. The basic assumption is that temporal flexibility can be readily understood in terms of inputs and initial conditions that control the speed with which the neural population activity in the recurrent network evolves. Our primary goal is not to explain in detail the experimental data in [83], but to investigate in numerical model simulations neuro-inspired processing mechanism that may be used in the future to endow autonomous robots with a sophisticated action timing capacity for more natural human-robot interactions [19, 49].

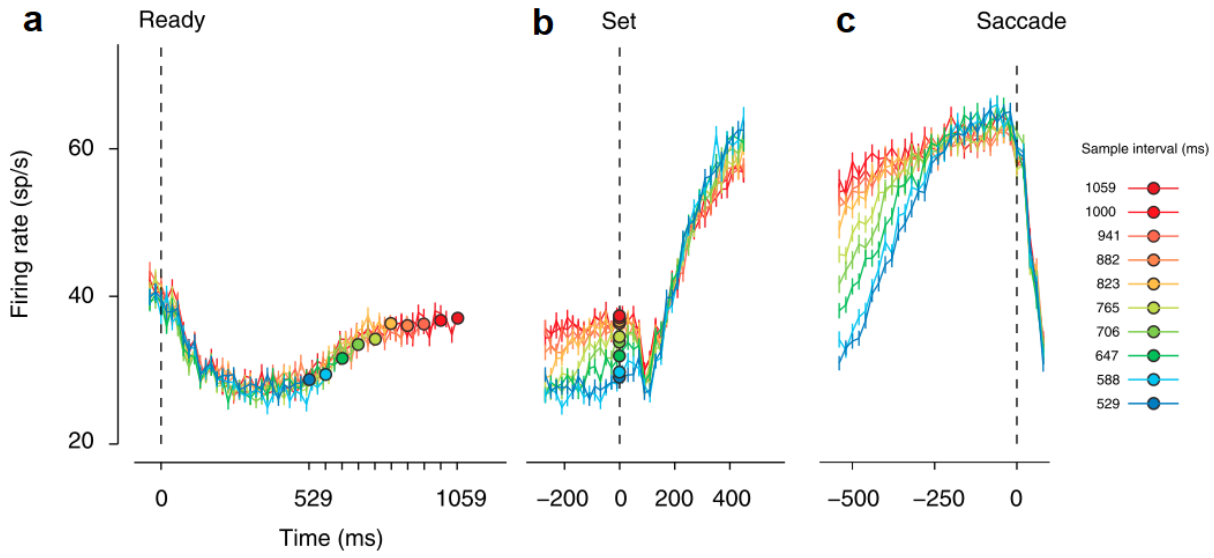

Figure 65: Plots of the population-average neural responses during the RSG task. Sample intervals are indicated by colors (see legend). (**a**) Response averages aligned to the time of "Ready". Each trace terminates at the time of the corresponding "Set" (filled circles). Activity declines initially and then increases monotonically with elapsed time. (**b**) Response averages aligned to the time of "Set". (**c**) Response averages aligned to the time of saccade. Trials with shallower buildup rate resulted in longer production intervals, and conversely, trials with steeper buildup rate were followed by shorter production intervals. From [83], Figure 2C-E.

9.3 The model

In the applications, neural fields are typically spanned over continuous dimensions such as direction, position or color. Following the experimental setup in [83], we assume for the present study that the neurons in the field represent the target of the saccadic eye movement triggered at the end of PE which is identified by movement direction. The presentation of the target input triggers the evolution of a localized activation pattern or bump encoding the specific parameter value. To represent not only the nature of the input but also the accumulation of temporal evidence we have to assume that the recurrent interactions between the neurons in the field are able to stabilize a bump solution with a continuum of amplitudes. To ensure this we employ a novel field model that we introduced in Chapter 4

$$\frac{\partial u(x,t)}{\partial t} = -u(x,t) + v(x,t) + \int_\Omega w(|x-y|) f(u(y,t)-\theta)\mathrm{d}y + I(x,t) + \epsilon^{1/2}\mathrm{d}W(x,t), \quad \text{(9.1a)}$$

$$\frac{\partial v(x,t)}{\partial t} = -v(x,t) + u(x,t) - \int_\Omega w(|x-y|) f(u(y,t)-\theta)\mathrm{d}y, \quad \text{(9.1b)}$$

posed on a one-dimensional domain $\Omega \subset \mathbb{R}$. The firing rate function $f(u)$ is taken here as a Heaviside step function (4.6) with threshold θ. The function $I(x,t)$ represents the time varying external input to field u. The additive noise term $\mathrm{d}W(x,t)$ describes the increment of a spatially dependent Wiener process with noise amplitude $\epsilon \ll 1$. It allows us, in principle, to test predictions about the variability of time measurements, an interesting issue that goes beyond the scope of this chapter.

The lateral inhibition type connectivity kernel has a "Mexican-hat" shape given by (4.3). The parameter values used throughout this chapter are $A_{ex} = 3$, $A_{in} = 1.5$, $\sigma_{ex} = 1$, $\sigma_{in} = 3$, $g_{mex} = 0.5$.

We apply the same coupling function to the v-field with a negative sign. The shape of the distance-dependent synaptic strengths thus represents an inverted Mexican-hat with inhibition dominating at shorter and excitation at longer distances.

Numerical simulations of the model were done in Julia [15] using a forward Euler method with time step $\Delta_t = 0.001$ and spatial step $\Delta_x = 0.005$, on a finite domain Ω with length $L = 60$. To compute the spatial convolution of w and f we employ a fast Fourier transform (FFT), using Julia's package `FFTW` with functions `fft` and `ifft` to perform the Fourier transform and the inverse Fourier transform, respectively.

9.4 Simulation results

In the following numerical examples, we consider a target input given by the Gaussian function

$$I(x) = A_I e^{\left(-(x-x_c)^2/2\sigma_I^2\right)}, \tag{9.2}$$

centered at position $x_c = 0$, with standard deviation $\sigma_I = 2$. The input strength, A_I, differs for the time interval measurement and the time interval reproduction epochs of the experiment (see below). For simplicity, we assume that the interval to measure is defined by the duration of the external input and not by two additional time markers like in the experiments. We leave the interesting issue of potential differences in subjective time measurements with "filled" intervals as opposed to "unfilled" intervals demarcated by time markers for future studies [161]. The temporal integration process thus starts from a homogeneous activity baseline when at time $t = 0$ the suprathreshold target input is presented. Following [83], we use for the numerical tests time intervals in the range of 500 to 1000 ms.

For the reproduction epoch we distinguish two situations. 1) Like for the measurement epoch, the temporal accumulation process starts from a homogeneous initial condition with the presentation of the target input. The input strength is inversely proportional to the bump amplitude reached during ME. 2) The evolution of the population activity starts without external input from a non-homogeneous initial condition. The pre-activation of neurons representing the target direction is inversely proportional to the bump amplitude reached during ME.

9.4.1 Measuring time intervals

The following simulations illustrate how the neural trajectory in the u-field evolves in response to the localized external input specifying the target direction. Fig. 66 depicts three examples of steady state solutions that are the result of the temporal input integration over different time intervals. The shape of the self-stabilized bumps reflects the fact that a longer accumulation time results in a higher bump amplitude. A closer inspection of the duration-height dependency using more time intervals reveals that the relationship is approximately linear (Fig. 67).

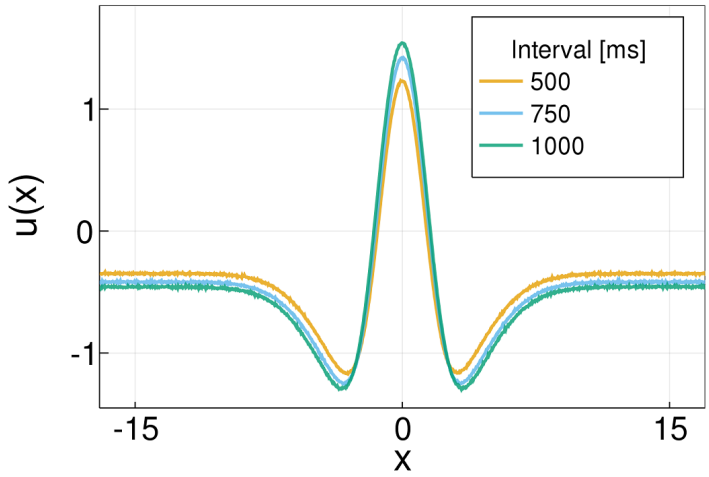

Figure 66: Example of three steady state solutions of the u-field of (9.1) resulting from applying three sample intervals of durations $d_{s_j} \in \{500, 750, 1000\}$, respectively. The amplitude of the external input given by (9.2) is $A_I = 1.75$, the threshold for the Heaviside function $f(u)$ is $\theta = 0.25$.

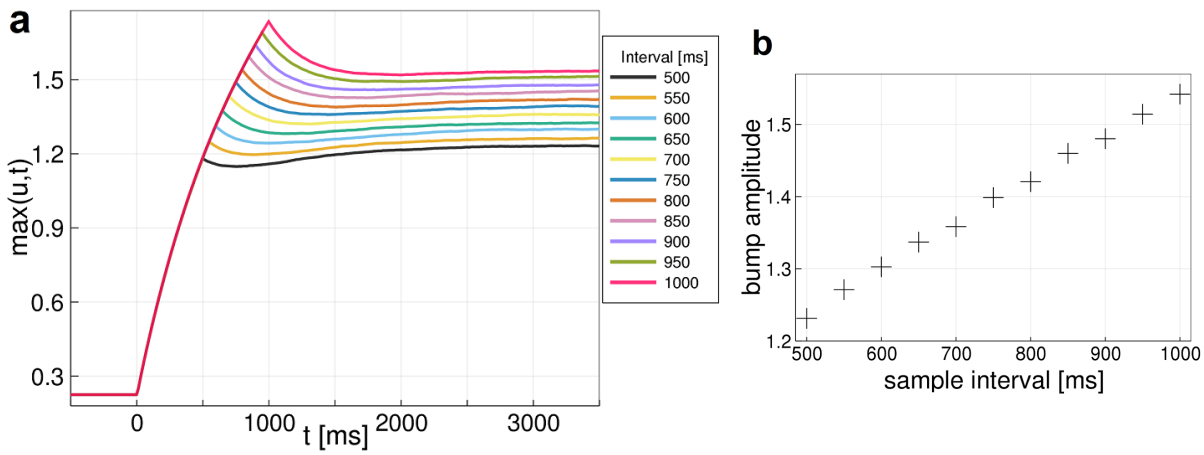

Figure 67: (**a**) Time courses of activity in the u-field during the interval measuring epoch. (**b**) Bump amplitude at the end of the measuring epoch as a function of sample interval length.

9.4.2 Reproducing time intervals - varying inputs

For the reproduction epoch we apply the same external input, $I(x,t)$, like for the time interval measurement but chose in accordance with the qualitative experimental findings in [83] the input strength in dependence of the bump amplitude reached in ME. The following relation is used for the model simulations:

$$A_I = \frac{1}{\ln(u_{max})}, \tag{9.3}$$

where u_{max} is maximum of the steady state solution in the u-field in the preceding measurement epoch. Fig. 68 shows the input amplitudes, A_I, for the range of measured intervals. The application of the

suprathreshold input triggers in all cases the evolution of a bump solution. Fig. 69 compares the evolution of population activity for all tested intervals. As can be clearly seen when comparing the slopes of the curves, input strength controls the time course of the neural trajectories. Since the strength of the input is inversely proportional (on a logarithmic scale) to interval length, population activity resulting from stronger inputs will reach the fixed read-out threshold, $h_R = 2$, earlier, producing shorter time intervals for movement initiation. Conversely, localized activity integrating weaker inputs reach this threshold later in time, resulting in longer production intervals. After reaching the threshold, h_R, the activity in both fields is reset to the initial resting state. The production interval is measured as the interval between the onset of the input $I(x, t)$ at $t = 0$ and the time when the u-activity reaches the threshold.

Fig. 70 compares directly the values of measured and produced intervals. For the tested range, the results reveal a very good match with a slight overestimation of the shortest intervals and a slight underestimation of the longest intervals (see also Table 2).

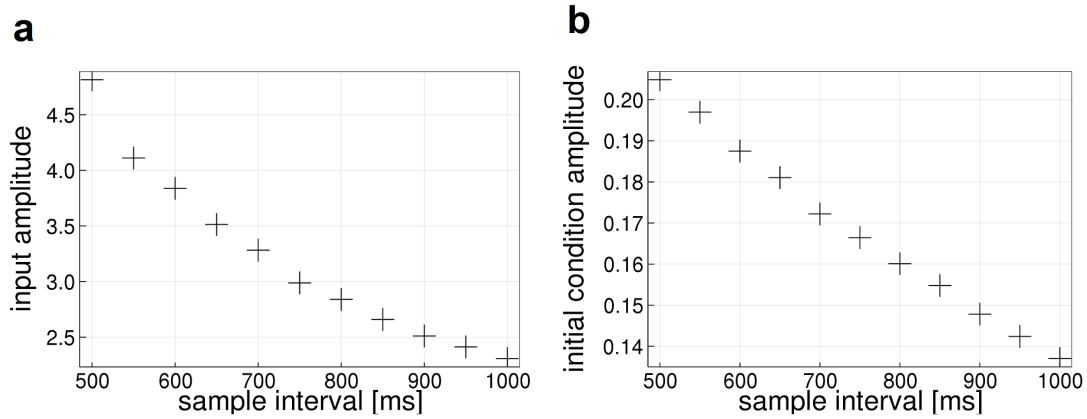

Figure 68: (**a**) Strength of the input during the interval production epoch as a function of sample interval length. (**b**) Strength of the initial condition during the interval production epoch as a function of sample interval length.

9.4.3 Reproducing time intervals - varying initial conditions

To test the hypothesis that an adequate choice of initial condition for the population dynamics of the reproduction epoch may be sufficient to account for a flexible reproduction of measured time intervals, we proceed as follows. The numerical simulations do not start from a homogeneous resting state. Instead, the population centered at position x_c representing the planned movement direction appears to be pre-activated at time $t = 0$. The amplitude of the preshape depends on the outcome of the preceding

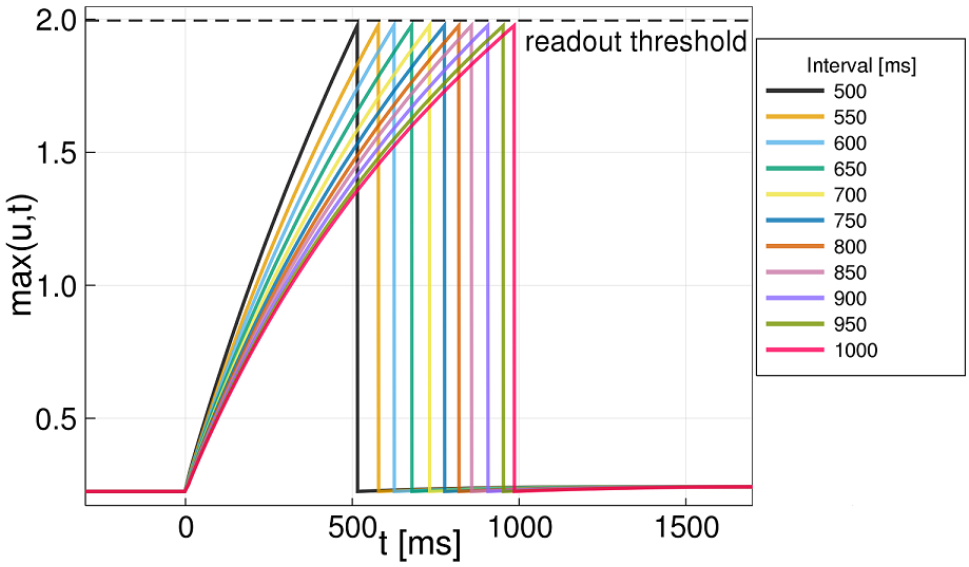

Figure 69: Time courses of activity in the u-field during the interval production epoch. Threshold reaching time is determined by the input strength.

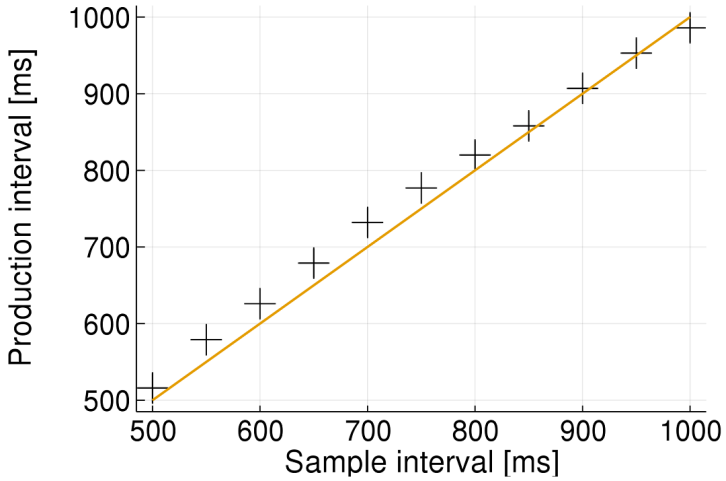

Figure 70: Production intervals as a function of sample intervals. Goodness of fit $R^2 = 0.99$.

measuring epoch in the following manner:

$$u(x,0) = \frac{1}{\alpha e^{(u_{max})}} e^{\left(-(x-x_c)^2/8\right)}, \qquad v(x,0) = K - u(x,0), \tag{9.4}$$

where u_{max} is maximum activity of the steady state solution in the u-layer reached during ME, and α is a constant scaling factor for the preshape amplitude which decreases with increasing u_{max}. The role of the constant K can be understood by noting that the subthreshold population dynamics ($f(u) = 0$) has the equilibrium solution $u(x) = v(x)$. By choosing $K > 2h$ one can ensure that the dynamics of the coupled populations will reach the threshold h necessary to drive the evolution of a bump. For the numerical tests we use $K = 0.5$, $h = 0.22$ and $\alpha = 1.25$. The initial condition may be set for instance by a transient

sample interval	500	550	600	650	700	750	800	850	900	950	1000
produced interval (external inputs)	516	579	626	679	732	777	820	858	907	953	986
produced interval (initial conditions)	518	604	676	741	793	820	862	893	923	950	972

Table 2: Values (in milliseconds) of sample and produced intervals.

input controlling the bell-shaped pre-activation and by a transient "go" signal (e.g., the second flash in the monkey experiment) controlling K and consequently the onset of the temporal evolution at $t = 0$. Figure 71 shows the time course of activity of the u-field for all measured intervals. The initial preshape amplitude predicts motor timing. Stronger preshapes are associated with shorter production intervals. Since no external input is applied, the neural trajectory is identical for all intervals once the threshold for the bump formation is reached. The difference in timing is thus completely explained by the speed with which the subthreshold trajectory reaches threshold, which in turn is determined by the activation gap between $u(x, 0)$ and h. Figure 72 directly compares the measured and produced intervals. The coefficient of determination, $R^2 = 0.95$, indicates that the numerical results fit still quite well the model of a perfect measuring/production match, albeit with larger errors compared to the model with external input (see also Table 2).

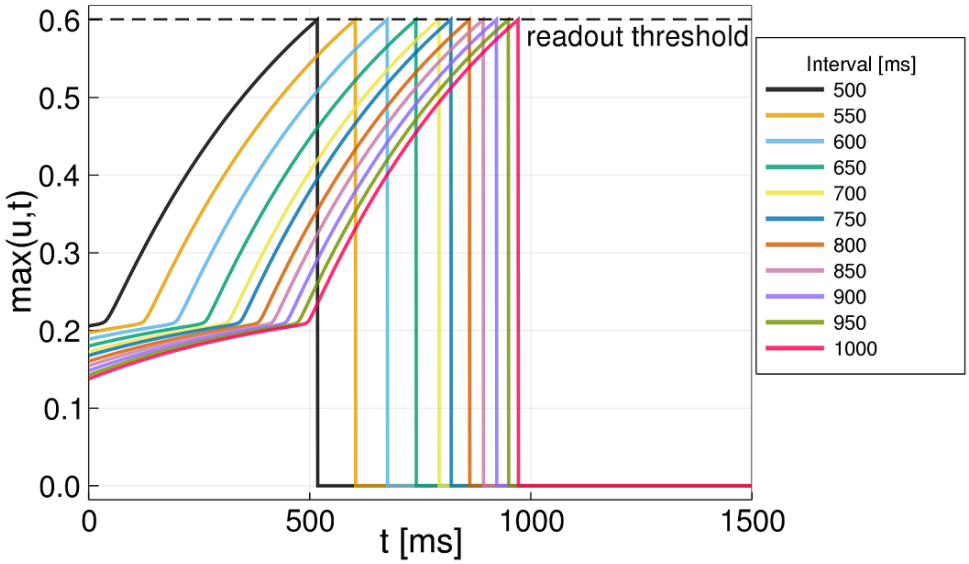

Figure 71: Time courses of activity in the u-field during the interval production epoch. The instants of reaching the read-out threshold, $h_R = 0.6$, vary systematically in dependence of the initial condition of the field dynamics.

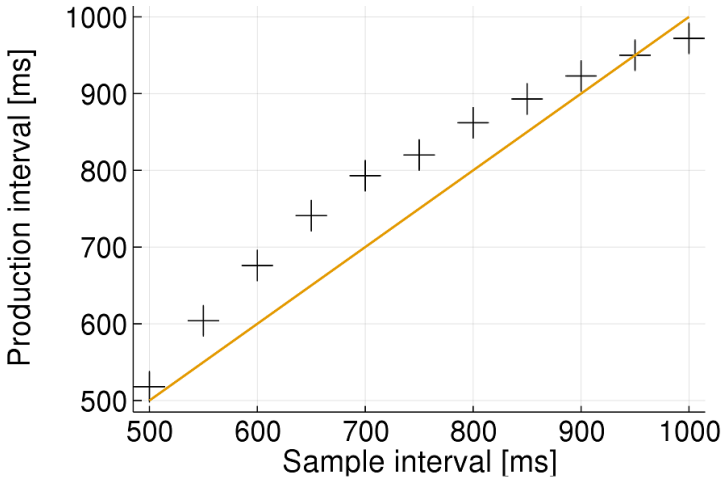

Figure 72: Production intervals as a function of sample intervals. Goodness of fit $R^2 = 0.95$.

9.5 Application to robotics

The results of our simulation study support the notion that neural computational principles of flexible timing may be captured by a dynamical systems perspective. Closely balanced excitation and inhibition in a spatially structured neural network explain the temporal integration and maintenance of external inputs. The information about elapsed time stored in the bump amplitude can be used on a trial-by-trial basis to reproduce the time interval either by adjusting input strength or initial condition of the neural integrator. This affects the speed or the onset of the neural trajectory towards the bump attractor, respectively. The field model shares with other recurrent network models the assumption that the neural mechanisms for timing are closely integrated with the processing of other stimulus attributes like for instance movement direction [112, 119].

There are several open issues with the current model implementation. First of all, since the input is continuously integrated, not only its duration but also its strength will influence the bump amplitude and consequently the interval measurement. The "strength normalization" issue can be solved by not integrating the input directly but instead a bump from a connected neural field which is triggered and deleted by transient signals (e.g., input onset and offset). In classical neural field models, the shape of such a memory bump is exclusively determined by the recurrent interactions within the network [3, 48]. Moreover, recurrent interactions are known to increase the signal-to-noise ratio, making the integration process more robust compared to the direct integration of a potentially weak and noisy input. Interestingly, the usage of a memory bump in the integration process might also explain the finding that "filled" intervals are typically judged as lasting longer than "unfilled" intervals of the same duration [161]. Since a stationary

bump solution of the field equation with a lasting external input has a slightly larger amplitude compared to a bump triggered by a brief, transient input, the temporal integration in the "filled" condition predicts a larger bump amplitude in the measurement field compared to the "unfilled" condition.

A second issue concerns the scaling of intervals to values outside the measured range by instruction or symbolic cues [157]. The effective bump height during reproduction should reflect this additional information. We have recently proposed and tested a simple and effective adaptation rule for the bump height based on the comparison between the produced time course of population activity and the neural trajectory of a reference or synchronization signal indicating the expected timing [171].

Our ultimate application goal for the model is to advance towards a human-like temporal cognition capacity for autonomous robots [113]. We are planning to test the model as part of an existing dynamic field control architecture for natural human-robot cooperation [49]. The continuous real-time synchronization of decision and actions with a human partner requires flexible perception and production of time intervals, fully integrated in other cognitive processes without reference to external computer clocks. A concrete example of human-robot collaboration is an assembly paradigm in which a robot assistant hands over a series of objects to the human worker. Findings in recent experiments directly comparing human-human and human-robot handovers stress the importance of temporal aspects of the robot's actions [66, 90]. Being able to adapt to the user by minimizing the human's waiting time is considered crucial for user acceptance and satisfaction. Figure 73 presents a sketch of a possible model implementation in the context of a cooperative object transfer task. The robot has first to measure the duration of individual assembly steps. This could be achieved for instance in a learning by demonstration paradigm in which the robot watches a human teacher executing the assembly work (assuming that all objects are within reach, [144]). Time measurement starts when the robot observes the teacher reaching for a specific object and stops when he/she reaches for the next one. The input to the measurement field is thus a self-stabilized bump in a memory field representing the object currently manipulated. During joint task execution, the robot uses the temporal information stored in the bump amplitude to prepare the complementary action of holding out the next object for the user. The temporal integration of the object memory bump with an amplitude given by equation 9.3 causes ramping activity in the time reproduction field. Reaching the pre-defined activation threshold at the end of the interval to be estimated is associated with the initiation of the object transport to the exchange position. Due to motor delays, the object exchange may still not be in perfect synchrony. A perceived temporal mismatch between the expected and the realized event timing (e.g., user picking object from robot hand) can be used to adapt in a single trial the initial resting state in the

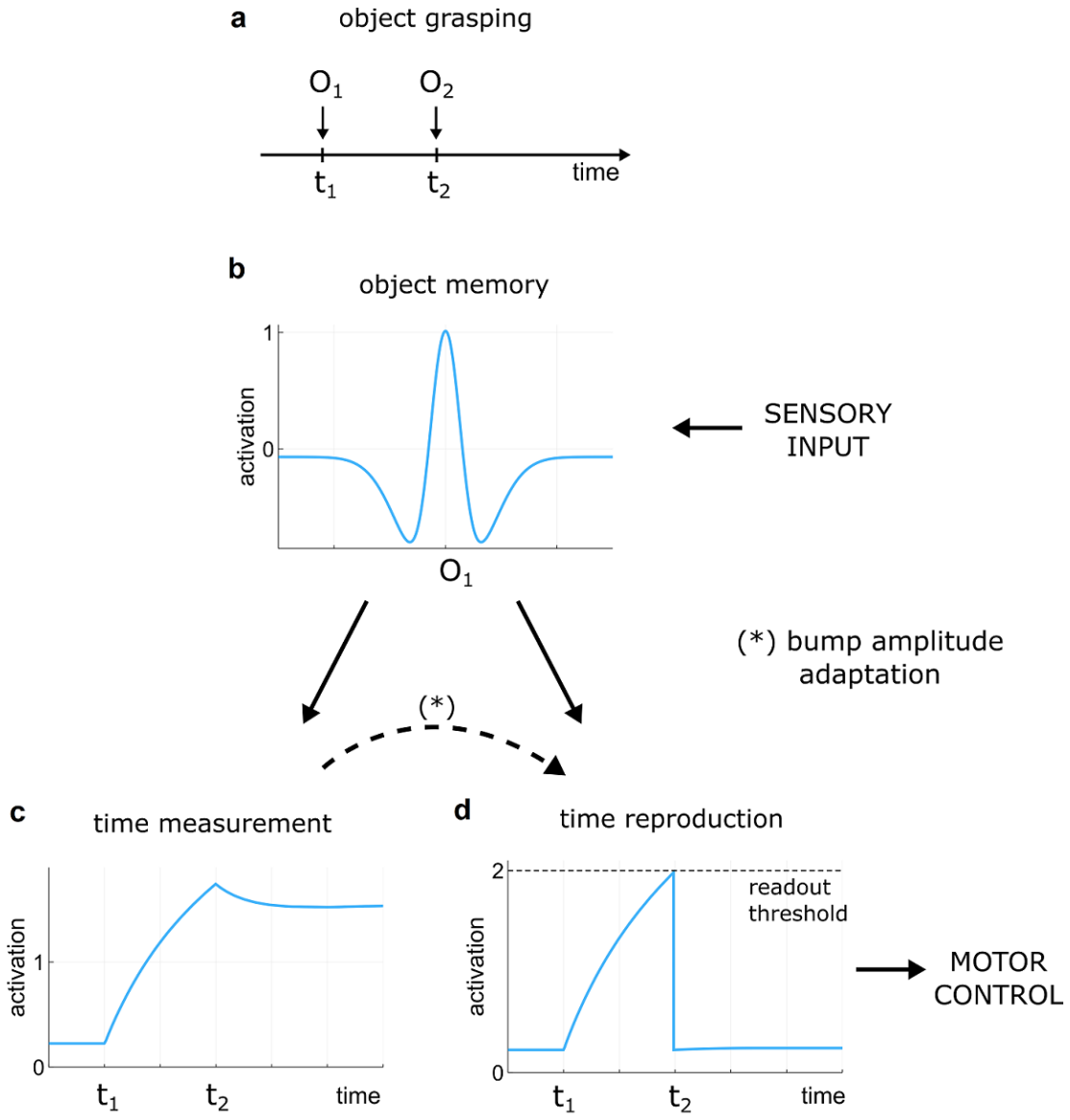

Figure 73: Object handover task. (**a**) The robot has to measure the time interval, $[t_1, t_2]$, between two consecutive graspings of object O_1 and object O_2. (**b**) Visual input from the camera system, characterizing the first object (e.g., object color), drives the evolution of a bump in an object memory field. (**c**) Time course of the temporal integration of the object memory in the measurement field during the interval $[t_1, t_2]$. (**d**) The measured duration is recalled in the reproduction field by integrating the memory bump with an amplitude defined by the measurement bump in (**c**). Reaching the readout threshold is associated with the initiation of the object transfer to the exchange position.

reproduction field in order to compensate systematic motor delays [171]. We are currently studying how the choice of the time scale of the robust neural integrator ($\tau = 1$ in the present study) affects precision timing for time intervals that are relevant for human-robot interactions.

9.6 Conclusion

We presented an application of the novel neural field model introduced in Chapter 4 to robustly measure and produce time intervals. Our results are in line with the recent evidence suggesting that neural computational principles of flexible timing may be captured by a dynamical systems perspective. The model may be incorporated as a part of larger DNF control architecture for natural human-robot collaboration to advance toward a human-like temporal cognition capacity for robots.

10 DNF model for planning of a robotics assistant[1]

10.1 Introduction

This chapter presents an application of the two-field model as a part of DNF architecture for sequence learning and planning of a robotics assistant. The two-field model is used to perform temporal integration of external and internal inputs of any strength. The accumulation of inputs in persistent activity of neural populations during sequence learning leads to formation of an activation gradient encoding the sequential order of memorized events. This information is then recalled from the memory in the sequence planning phase. The work presented in this chapter complements our earlier research on a DNF architecture for natural human-robot cooperation. The main advantage of using the two-field model is the robust representation of accumulated evidence in localized activation patterns, without a need to rely on additional processing mechanisms.

As a first robotics experiment we chose a pipe assembly task in which a robot first watches a human assistant grasping a series of pipes to hand them over to an operator performing the assembly steps. The goal for the robot is to learn the serial order of handovers to subsequently substitute the human assistant in the joint task. Order learning is guided by the information provided by the vision system about the color and the length of each pipe. During observation, the neural integrator of a memory field establishes a gradient of persistent activations over distinct neural subpopulations tuned to a specific color-length combination. The integration time from input onset to the end of the assembly sequence defines the level of persistent activity. Consequently, the neural representation of the first pipe to be grasped has the highest activation whereas the representation of the last pipe has the lowest. During joint execution, the competitive neurodynamics of a decision field, which receives the stable activation gradient as input, drives the sequential initiation of proactive handovers of all pipes in the correct order.

[1] The content of this chapter is based on [174].

10.2 Experimental setup

For the experiment, we used the collaborative robot Sawyer designed by the company "Rethink Robotics". It is featured by a 7 degrees of freedom robot arm with 1.26 meters reach that operates in work cells defined for humans. The "head" mounted on top consists of a LCD display and a camera system. An additional camera system is mounted on the arm. We used the head camera to provide the information about length and color at the moment when the "giver" has transported the pipe to the exchange position and the "receiver" touches it. During joint task execution, the reach-grasp-transport trajectory of the robot arm to a pre-defined exchange position is generated using the "HUMP" planner developed by our group [140]. It guarantees human-like features of the robot arm movements.

10.3 DNF model for sequence learning and planning

10.3.1 Model equations

We now briefly describe the two neural field models used to build the DNF architectures discussed in this chapter and later in Chapter 11.

We employ the Amari model

$$\tau \frac{\partial u(\mathbf{x}, t)}{\partial t} = -u(\mathbf{x}, t) + \int_{\Omega} w(\mathbf{x}, \mathbf{x}') f(u(\mathbf{x}', t) - \theta) \mathrm{d}\mathbf{x}' - h + I(\mathbf{x}, t) + \epsilon^{1/2} \mathrm{d}W(\mathbf{x}, t), \tag{10.1}$$

and the two-field model

$$\begin{aligned} \tau \frac{\partial u(\mathbf{x}, t)}{\partial t} &= -u(\mathbf{x}, t) + v(\mathbf{x}, t) + \int_{\Omega} w_{mex}(\mathbf{x}, \mathbf{x}') f(u(\mathbf{x}', t) - \theta) \mathrm{d}\mathbf{x}' \\ &\quad + I(\mathbf{x}, t) + \epsilon^{1/2} \mathrm{d}W(\mathbf{x}, t), \end{aligned} \tag{10.2a}$$

$$\tau \frac{\partial v(\mathbf{x}, t)}{\partial t} = -v(\mathbf{x}, t) + u(\mathbf{x}, t) - \int_{\Omega} w_{mex}(\mathbf{x}, \mathbf{x}') f(u(\mathbf{x}', t) - \theta) \mathrm{d}\mathbf{x}'. \tag{10.2b}$$

In this chapter, spatial domain Ω is a subset of $\mathbb{R}^d$ with $d = 1$ and $d = 2$. The parameter $\tau > 0$ defines the time scale, $I(\mathbf{x}, t)$ represents a time-dependent, localized input centered at site $\mathbf{x}$, and $h > 0$ defines the stable resting state of a field without external input. Term $w(\mathbf{x}, \mathbf{x}')$ is the synaptic weight distribution which determines the connection strength between interacting neurons at positions $\mathbf{x}$ and $\mathbf{x}'$.

We use three different weight distributions w: a Gaussian function minus a constant given by (4.2), a Mexican hat function given by (4.3), and an oscillatory connectivity function given by (4.4). Firing rate

function f is the Heaviside function defined in (4.6) with the threshold chosen as $\theta = 0$ [3]. Finally, the additive noise term $\mathrm{d}W(\mathbf{x}, t)$ describes the increment of a spatially dependent Wiener process with amplitude $\epsilon \ll 1$. We use the noise term to break the symmetry in decision processes in which different choices get equal or nearly equal support from input sources. Model parameters, initial conditions and implementation details are given in the Appendix B.

10.3.2 Model architecture

Figure 74 presents a sketch of the DNF model implemented as part of the control architecture of the robot Sawyer. It consists of several interconnected two-dimensional fields spanned over the input dimensions $(x, y) = (\text{length, color})$.

The model generalizes an earlier one-dimensional sequence learning model which we have applied to teach a robot by demonstration a color-coded musical sequence [57]. From a computational perspective, the important innovation is that the neural integrator simplifies the processing and storage of serial information. No additional neural mechanisms (e.g., a threshold accommodation dynamics used in [57]) have to be applied to account for stable bumps with varying amplitudes.

The perceptual field u_{per}, governed by the Amari equation (10.1) with kernel (4.2), receives a two-dimensional Gaussian input representing the length-color combination of a specific pipe that the vision system detects at the exchange position. The neural dynamics in the sequence memory layer is governed by the coupled neural integrator equations, u_m and v_m, given by (10.2) with kernel (4.3). The u_m-field receives two types of excitatory input (solid lines):

$$I(x, y, t) = u_{per}(x, y, t) f(u_{per}(x, y, t)) + I_c f(u_m(x, y, t)). \tag{10.3}$$

The first term on the right side describes the input from the perceptual field at position (x, y) where sensory information has triggered the evolution of a suprathreshold activity pattern. Through inhibitory feedback connections (dashed line), the bump in u_{per} becomes destabilized (and the input disappears) once a memory bump in (u_m, v_m) has been established at the corresponding position. The second term describes a constant input I_c to all neurons in u_m, which is defined by the summed suprathreshold activation in the "sequence onset" field u_{on}:

$$I_c = \kappa \int_{\{x : u_{on}(x) \geq 0\}} f(u_{on}(x)) \mathrm{d}x, \tag{10.4}$$

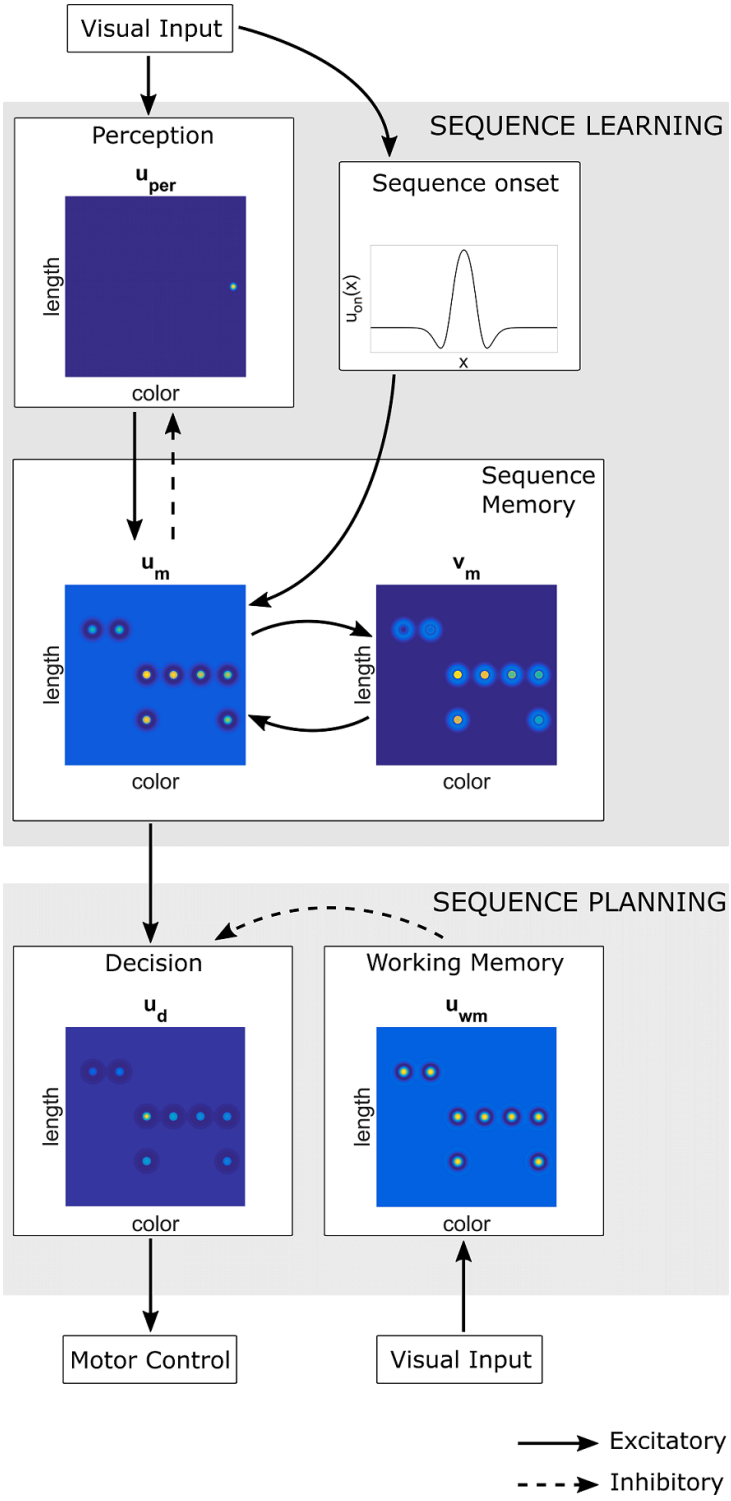

Figure 74: Schematic view of the DNF model with several interconnected fields implementing sequence learning and sequence planning.

where $\kappa > 0$ defines the input strength.

A bump in this one-dimensional field represents the memory of an additional color cue that signals to the robot the onset of the sequence demonstration. Due to the multiplicative gating by the suprathreshold

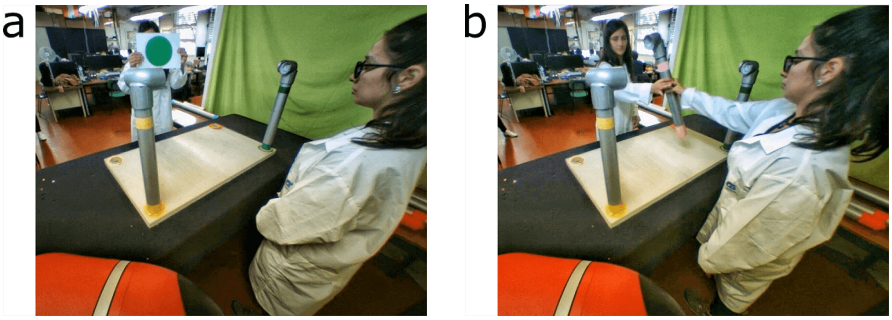

Figure 75: Perceptual input to the u_{on} field (**a**) and the u_{per} field (**b**) during sequence learning phase.

activity, $f(u_m)$, the integration of the constant input, I_c, manifests only at sites where the transient input from u_{per} has already driven the evolution of a bump. As a consequence, the earlier a certain pipe has been manipulated during demonstration, the higher is its memory bump. An activation gradient established in (u_m, v_m) thus encodes serial order. Gradient-based modeling approaches to serial order are known in the literature as competitive cuing or ordinal models [127]. The integration of the constant input stops when a second color cue (not shown), signaling the end of the sequence demonstration, destabilizes the bump in u_{on}.

During joint execution of the assembly task, the choice which pipe to manipulate next is made in the decision field u_d governed by equation (10.1) with kernel (4.2). It receives the stationary activation gradient of u_m as subthreshold, excitatory input:

$$I(x, y) = u_m(x, y). \tag{10.5}$$

The planning and execution of the whole sequence starts with the sequence onset signal. It triggers the continuous increase of the baseline activity h_d. A simple linear dynamics is used with a time scale $\tau_d = 1/\kappa$ controlled by the strength parameter $\kappa > 0$:

$$\tau_d \frac{\mathrm{d}h_d(t)}{\mathrm{d}t} = \int\limits_{\{x:u_{on}(x)\geq 0\}} f(u_{on}(x))\mathrm{d}x, \; h_d(t_0) = h_{d_0} < 0. \tag{10.6}$$

The subpopulation of u_d with highest pre-activation reaches the threshold for creating a bump first. The moment of reaching the threshold is used to trigger the reach-to-grasp movement towards the specific pipe. The bump is destabilized by inhibitory input (dashed line) from a bump in the working memory field u_{wm} which is initially driven by visual input. This input indicates that the hand of the human worker has reached the exchange position to receive the pipe. Subsequently, the neural representation of the next pipe to be manipulated by the robot becomes active in u_d. This autonomous planning process continues until the memory representation of the last pipe with the lowest pre-activation has been processed. To

enable stable multi-bump solutions in the working memory field u_{wm} governed by the two-dimensional Amari equation (10.1), an oscillatory connectivity function (4.4) is used.

10.4 Results

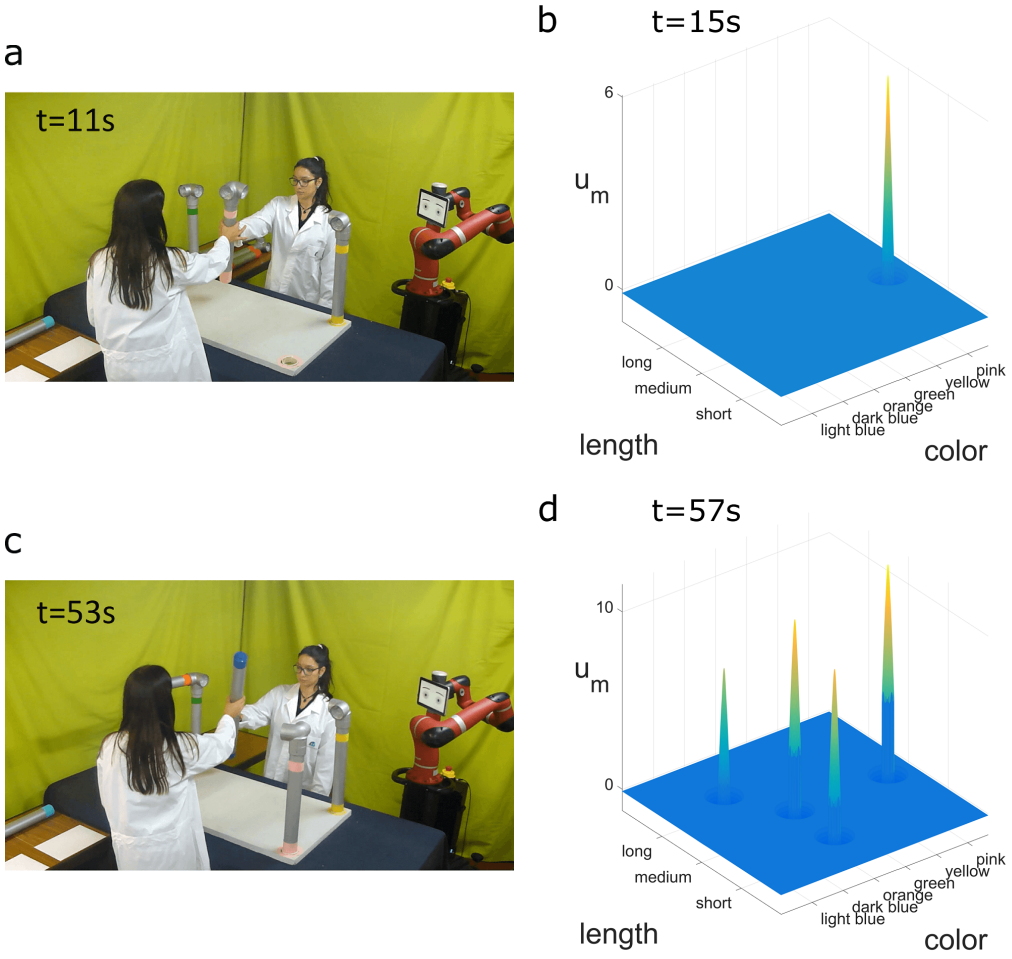

Figure 76: Snapshots of the sequence demonstration (**a** and **c**) and corresponding bump formation in the memory field u_m spanned over the dimensions color and length (**b** and **d**).

The robot Sawyer watches the human assistant handing over 4 pipes to the worker in the following order: pink-medium ⟶ orange-medium ⟶ orange-short ⟶ dark-blue-long. Figure 76 shows two snapshots at the beginning and the end of the demonstration together with the corresponding activity patterns in the sequence memory field. At time $t = 15$**s** a single bump has evolved representing the pink-medium pipe. Immediately after the transfer of the dark-blue-long pipe, at time $t = 57$**s**, all 4 pipes are represented in memory with bump amplitudes reflecting serial order. Figure 77 depicts the time course of the sequential

bump formation relative to sequence onset at time $t = 0$.

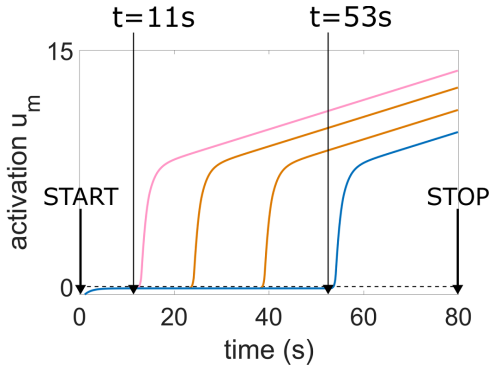

Figure 77: Temporal evolution of population activities in the memory field u_m during sequence demonstration. The start and stop signals are presented at times $t = 0$ and $t = 80$**s**, respectively.

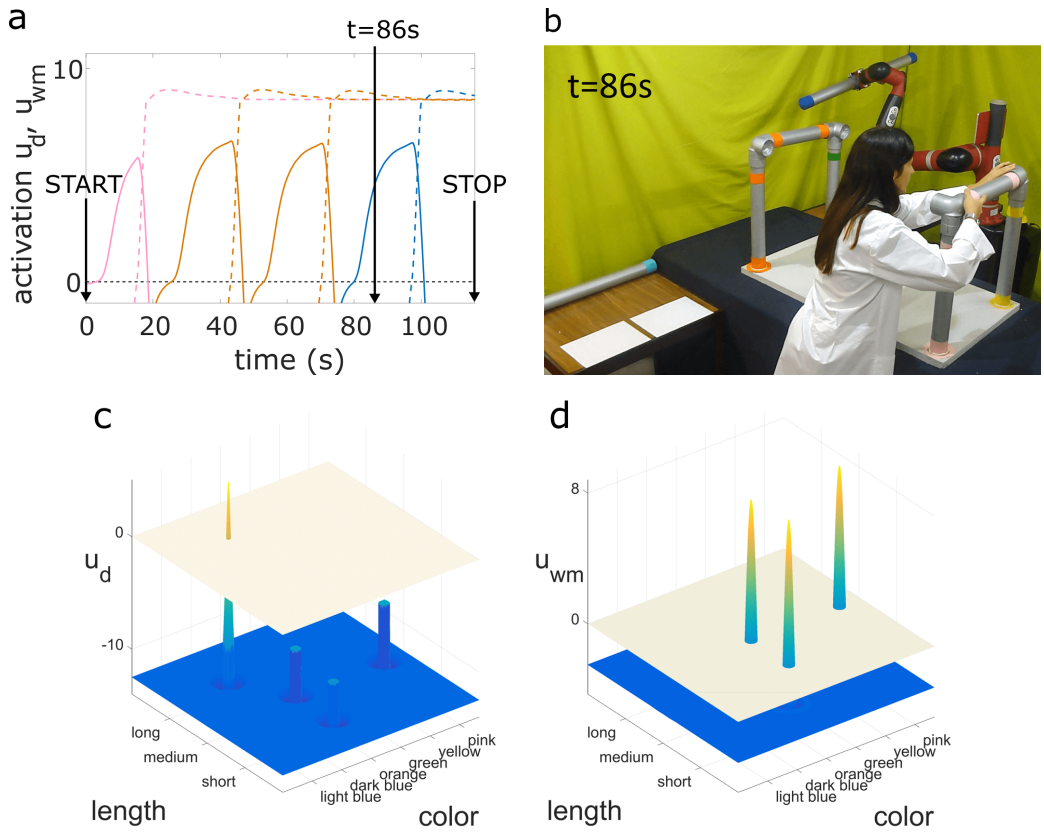

Figure 78: (**a**) Comparison of the temporal evolution of population activities in the decision field u_d (solid line) and the working memory field u_{wm} (dashed line). The start and stop signals are presented at $t = 0$ and $t = 110$**s**, respectively . (**b**) The worker is still mounting a pipe while Sawyer is already grasping the next one. (**c**) Bump formation in the decision field u_d, and (**d**) multi-bump pattern in the working memory field u_{wm} at time $t = 86$**s**.

During joint task execution together with the human operator, Sawyer takes the role of the giver. Figure 78a depicts the temporal evolution of suprathreshold activity of the subpopulations in the decision field u_d

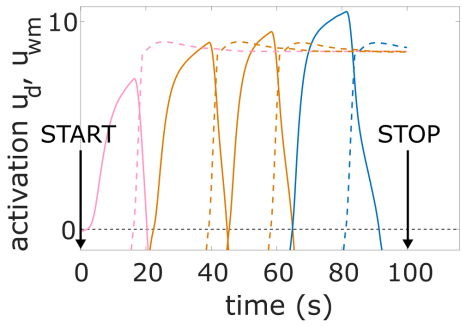

Figure 79: Comparison of temporal evolution of population activities in the decision field u_d (solid line) and the working memory field u_{wm} (dashed line) for a faster sequence planning and execution. The start and stop signals are presented at times $t = 0$ and $t = 100$**s**, respectively.

representing motor plans directed towards the different pipes (solid lines). The field dynamics activates the individual handovers in the correct serial order. The suprathreshold activity of each subpopulation decays back to resting state due to the inhibition from bumps evolving at corresponding sites in the working memory field u_{wm} (dashed lines). The video snapshot (Fig. 78b) taken at time $t = 86$**s** shows the worker mounting a pipe that she had picked from her workspace. By comparing the population activity in the decision field at the same time (Fig. 78c), it becomes clear that Sawyer already starts the handover of the dark-blue-long pipe that the worker has to assemble next. Note that the duration of the whole sequence during joint execution is significantly longer than during demonstration (compare Fig. 77) since the operator assembles additional pipes located within reach on her side.

As shown in Figure 79, the robot is able to accelerate the planning of the entire transfer sequence to adapt to an operator executing the assembly steps with higher speed. This acceleration can be achieved by applying an additional input to the decision field. It may for instance represent a request gesture signaling to the robot that the operator awaits the next pipe [49]. The additional input either increases the baseline activity h_{d_0} or the slope of the linear ramp-to-threshold dynamics (10.6). Since in modern assembly manufacturing the ordering of activities is often left to the discretion of the operator, the robot should also be able to adapt to changes in serial order of task execution [163]. The activation-based learning implemented in the DNF model ensures that a single task demonstration is sufficient to establish an activation gradient representing the new order. However, to memorize simultaneously the order preferences of different operators, activation gradients in separate memory fields have to be established (for a DNF representation of different serial orders in a single memory field see [144]). During joint task execution, the read-out of the correct memory representation can be ensured, in principle, by a multiplicative gating of the different memory inputs (defined by (10.5)) to the decision field u_d with a user-specific sensory signal. Only the

memory pattern which gets this additional support preshapes u_d and consequently affects sequence planning.

10.5 Conclusion

In this chapter, we have applied the two-field integrator model in DNF architecture that support natural and efficient human-robot cooperation. The test scenario is taken from modern manufacturing and assembly environment that is characterized by a high variability in the built process. To provide a productivity benefit, a robotic assistant should be able to efficiently acquire and adapt knowledge about the order of activities and workflow.

The presented computational principles and results may be used to address several key challenges that have been identified for close human-robot collaborative work in manufacturing environments [107, 151]. First, preferences about task completion are prone to change since the order of activities in many manual processes are left to the discretion of the human operators [163]. As already discussed before, the learning by demonstration paradigm can be in principle applied to quickly teach different serial orders represented by activation gradients in separate dynamic fields.

As shown in Figs. 76 and 78, the one-shot learning of serial order allows the robot to act in advance of the operator's need, rather than just reacting to a request. For efficient and successful joint action it is highly desirable that an assistant shows such a proactive attitude also when the operator makes an error [107]. To avoid time consuming disassembly steps, the robot should be able to detect and communicate errors before they manifest in the construction work (a capacity termed proactive resilience in engineered industrial systems [158]). In previous research, we have developed a control architecture for natural HRI based on the DNF framework. It implements a highly context-sensitive mapping of an observed action of the co-worker onto an adequate complementary robot behavior. This mapping takes into account different task-related and user-related factors including an error monitoring capacity [17, 18, 141]. Neural populations encode in their suprathreshold activity a mismatch between which assembly step the operator should execute (shared task knowledge) and the predicted assembly step inferred from the observed motor behavior. For the pipe assembly paradigm, assuming that the robot has learned the serial order of the entire assembly sequence, it may detect a serial order error at the moment when the operator grasps a specific pipe. An adequate complementary robot behavior would be to inform the operator verbally or with a communicative gesture about the error [19].

In future work, we plan to exploit the neural computations of the integrator model in an existing DNF-based architecture for fluent joint action in a shared task. The challenge will be to smoothly integrate a series of actions serving an operator like in the present joint assembly study with assembly work that the robot itself performs. Since a tight synchronization of activities between robot and operator is often required to achieve a shared goal [163], the robot should not only be able to adapt to changing preferences for workflow but also to flexibly time its goal-directed actions. We have recently applied the neural integrator model to measure and reproduce time intervals between sensory-motor events [172]. As a key processing mechanism to achieve adaptive motor timing, a bump reflecting measured duration in its amplitude affects either the resting state or the slope of the ramp-to-threshold dynamics in the decision field.

11 DNF model for value-based decision making[1]

11.1 Introduction

The second robotics experiment is a simulated material handling system in which a mobile robot transports parts or subassembly parts between workstations. Specifically, the robot has to search at two workbenches where a required part may appear with a certain probability in a fixed period of time. Humans and other animals show in a scenario with constant probabilities a choice behavior known as the matching strategy: the fraction of choices made to any option will match the fraction of total success (or reward) earned from that option [76, 104]. Using the neural integrator model to incorporate short-term memories of past choices and past successes in the decision process endows the robot with the matching behavior. Importantly, we show that the robot autonomously adapts its internal valuation of the competing alternatives and consequently its choice behavior to unsigned changes in the success probabilities [147]. The robot is thus better able to cope with specific challenges in more flexible and uncertain manufacturing systems.

11.2 Experimental setup

The experiment is inspired by challenges for material handling robots in more flexible and therefore less predictable manufacturing processes [31]. Such robots play a central role in industrial assembly lines by transporting parts or subassembly parts between workstations. Figure 80a shows a top view of a simulated environment in which a mobile robot equipped with a forklift has to pick up a bulky object positioned on a pallet to deliver it to an operator located in an uploading area. For future real-world tests, it is interesting to notice that the DNF approach to cognition is highly compatible with the attractor dynamics approach to autonomous navigation of mobile robots [20] (see the Discussion). Recently, the approach has been successfully tested in a factory environment cluttered with stationary and moving obstacles [108, 111].

[1] The content of this chapter is based on [174].

For the material handling task, the main challenge for the robot is to deal with an environment characterized by uncertainty. The searched object may arrive in a certain time interval ΔT with independent probabilities at two possible locations, A and B, which are hidden from the robot's camera view. To maximize the success rate of the object search over a longer time period, the robot has to adapt its choice behavior to the statistics of the environment.

We assume that during the duration T of the experiment, the robot is forced to make every ΔT time units a decision to search at A or B, and then deliver the object at the upload area, or, in case of no success, return directly to the park position. For the evaluation of the robot performance thus exist $N = T/\Delta T$ trials. For simplicity, we further assume the existence of an external computer clock to trigger the start of each decision process. Note that the neural integrator model (10.2) may be used as well to autonomously measure and reproduce time intervals [172]. We leave this interesting issue for future work (see the Discussion). Since the probabilities of finding the specific object at the two locations are independent, in each trial, both locations, only one of the locations or none of the locations guarantee success. Once the object has arrived at a particular location it stays there until the robot picks it up.

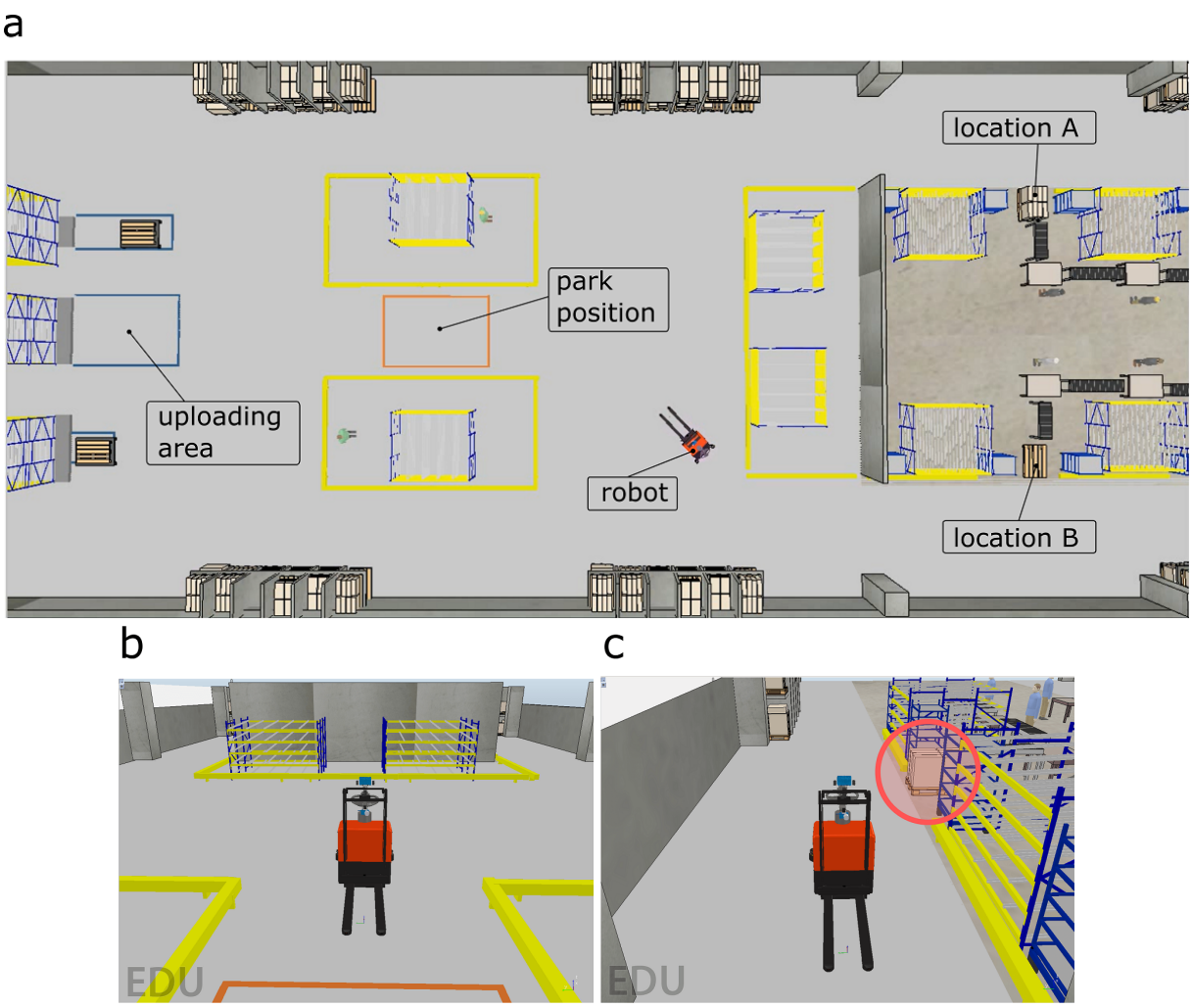

Figure 80: (**a**) Top-view of a simulated factory environment with a park position for the mobile robot, two target locations A and B, and an uploading area. (**b**) Robot at the moment of making a decision to search the object at location A (left side) or location B (right side). (**c**) Robot finds the object at location A (left) to pick it up and deliver it at the uploading area.

11.3 Model architecture

The DNF model guiding the robot's decisions is inspired by findings in neurophysiological and behavioral studies investigating choice behavior in conceptually similar tasks with humans and other animals [104, 147]. They suggest that it is necessary to integrate in the decision process both past choices and past successes in order to capture an optimal probabilistic strategy in stationary as well as dynamically changing environments.

Figure 81 depicts the model architecture with three coupled fields spanned over the behavioral dimension "movement direction". Bumps in the decision field u_d at locations encoding target A to the left or target B to the right of the start position drive the activation of two neural integrators (u_r, v_r) and (u_c, v_c). They

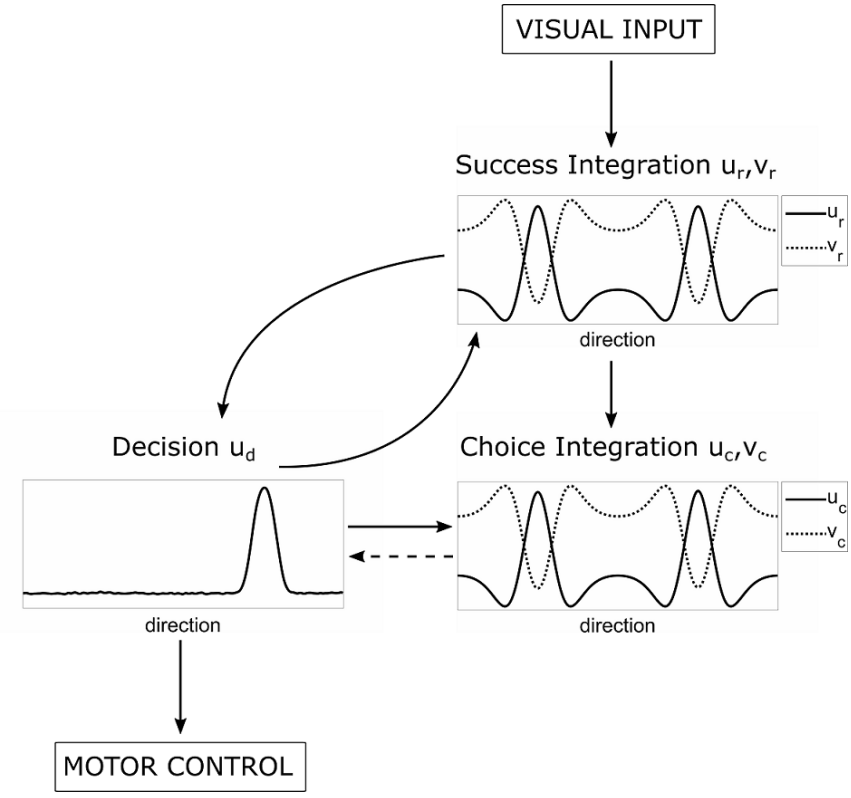

Figure 81: Model architecture consisting of a decision field u_d, and fields for choice and success integration, (u_c, v_c) and (u_r, v_r), respectively. Solid arrows indicate excitatory and dashed arrows inhibitory connections between fields.

represent, respectively, cumulative success and cumulative choice for each of the options. The input to the u_c-field is given by

$$I_c(x,t) = \int_\Omega w_{lat}(x-y) f(u_d(y,t) - \theta) \mathrm{d}y, \tag{11.1}$$

whereas the u_r-field receives the input

$$I_r(x,t) = K_r f(u_d(x,t) - \theta) R(x), \tag{11.2}$$

where $K_r > 0$ is a scaling factor. The integration of suprathreshold activation in u_d is gated by a function $R(x)$ which indicates whether the robot's camera has detected the color-coded object or not, that is, $R(x) = 1$ if the object is found and $R(x) = 0$ if not.

The decision field u_d receives in trial n the summed activation of the two success integration fields at the end of trial $n-1$, $u_{r_{n-1}} + v_{r_{n-1}}$, as excitatory input whereas the summed activation of the two choice integration fields, $u_{c_{n-1}} + v_{c_{n-1}}$, is taken as inhibitory input:

$$I_d(x,t) = \left(u_{r_{n-1}}(x) + v_{r_{n-1}}(x)\right) - c_d \left(u_{c_{n-1}}(x) + v_{c_{n-1}}(x)\right), \tag{11.3}$$

where $c_d > 0$ is a scaling parameter. The different input signs may be understood by the fact that the simple strategy to always choose the target with higher success probability will not maximize the overall success rate. Due to the persistence of the object at the target location, the likelihood to find the object at the less likely location increases with the time elapsed from the last choices. The robot should thus visit from time to time also this location. The net effect of the inputs to u_d at the beginning of each trial is a preshaping of the neural subpopulations encoding locations A and B. It sets on a trial-by-trial basis the initial condition for the bump formation which is initiated by the ramp-to-threshold dynamics (10.6). An open question is how many past trials should inform the current decision. The issue of the integration timescale is particularly relevant for environments in which the value (success frequency) of each option may change without warning [80]. Following the discussion in [147], we address this issue by resetting the activation pattern of the integrators to their initial values after a fixed number of $N_{re} = 8$ trials.

11.4 Results

In the first simulation experiment, we assume that the mobile robot knows the true success probability of each option either through learning in a stationary environment or by instruction. Under this condition, matching behavior is known to represent the optimal strategy for maximizing the overall success [104, 147]. The "matching law" states that an agent allocates choices in a proportion that matches the relative success experienced on these choices. For the present two-choice search task, this translates to

$$N_i/(N_A + N_B) = S_i/(S_A + S_B), \quad i = A, B, \tag{11.4}$$

where N_i represents the number of times location i has been chosen and S_i the number of times the robot has found the object at that location. The prior task knowledge is modeled as additional Gaussian inputs to the subpopulations representing directions A and B with strengths proportional to the success probabilities [50]:

$$I_{prob}(x) = A_{P_A} e^{\left(-(x-x_{P_A})^2/2\sigma_P^2\right)} + A_{P_B} e^{\left(-(x-x_{P_B})^2/2\sigma_P^2\right)}, \tag{11.5}$$

where $0 < A_{P_A} < 1$ and $0 < A_{P_B} < 1$.

The decision process in the first trial thus starts from a two-peak, bimodal resting state shown in Figure 82. Figure 83 illustrates the decision process in four successive trials in which the prior probabilities are 30% and 40% for target A and target B, respectively. The activity patterns in u_d at the start (top) and the end of each trial (middle) together with the pattern in u_c at the end of the trial (bottom) are shown. The decision

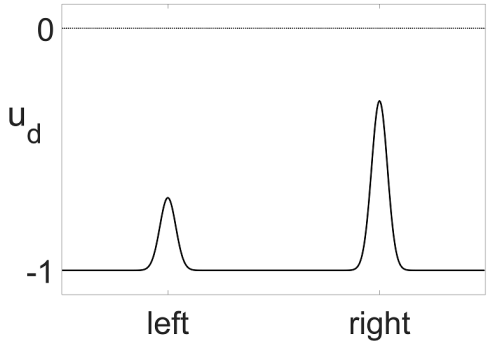

Figure 82: Initial state of the decision field u_d at the beginning of trial $n = 1$ which is shaped by the prior knowledge about the success probabilities for A and B given by (11.5) with $A_{P_A} = 0.3$, $A_{P_B} = 0.7$, $\sigma_P = 0.75$.

in the first trial reflects the prior information that the location B has higher success probability. In the second trial, the robot decides to go again to B despite the fact that the prior decision was unsuccessful and the inhibition from the bump in u_c has reduced the preshape at position B. The decision is again unsuccessful. In the third trial, the robot changes its decision and finds the object at A. The switch is due to the further increased inhibition from the pattern in u_c reflecting two B choices. In the fourth trial, the robot moves again to A due to the excitation from u_r, reflecting the success in the last trial (not shown), and the relatively smaller inhibition from u_c at A compared to B.

Trial no.	Available objects		Decision	Success
	Left	Right		
1	1	0	right	no
2	1	0	right	no
3	1	0	left	yes
4	0	0	left	no
5	0	1	right	yes
6	1	0	right	no
7	1	1	left	yes
8	0	1	right	yes

Table 3: Availability of objects in locations A and B, robot's decisions and decision outcomes in a series of 8 successive trials. The success probabilities for A and B are 30% and 40%, respectively.

Table 3 summarizes the results of eight successive trials with the choice pattern (B,B,A,A,B,B,A,B). It shows that in the fourth trial no object was available and in three trials with an object available at A the wrong decision was made. To systematically analyze the search efficiency of the robot and compare it with the efficiency of two alternative search strategies, we run blocks of $N = 1000$ trials with different probability ratios for locations A and B. Search efficiency is defined as the total success achieved divided by

Success probability (left/right)	Choice ratio (left/right)	Success ratio (left/right)	Search efficiency (DNF model)	Search efficiency (ML strategy)	Search efficiency (WSLS strategy)
30/70	24.0/76.0	23.5/76.5	76.5%	70.0%	64.7%
30/40	40.1/59.9	40.1/59.9	79.0%	57.1%	67.1%
60/70	43.2/56.8	42.4/57.6	65.9%	53.9%	55.4%
50/20	73.2/26.8	74.4/25.6	82.3%	71.4%	70.6%
30/30	49.7/50.3	49.8/50.2	81.0%	50.0%	69.7%

Table 4: The performance of the DNF model is compared with the performances of the ML and WSLS strategies in five blocks with different probability ratios for the two locations.

the number of available objects. The simple alternative strategies are (1) to go always to the location with higher success probability, which we call the "Most Likely" (ML) strategy, and (2) to stay at the option if successful and change the option if not, known in the literature as "Win-Stay-Lose-Switch" (WSLS) strategy. The results in Table 4 show that for all tested ratios, the DNF model outperforms the two alternative strategies. The difference in search efficiency is in particular evident for cases in which both targets have similar but relatively low success probabilities (e.g., 30/40). Moreover, the distribution of choices among the two alternatives generated by the DNF model closely matches the success ratio.

Block	Success probability (left/right)	Choice ratio (left/right)	Success ratio (left/right)	Search efficiency (DNF model)	Search efficiency (ML strategy)	Search efficiency (WSLS strategy)
1	30/40	47.0/53.0	41.7/58.3	85.7 %	57.1 %	71.4%
2	60/20	58.0/42.0	71.2/28.8	73.8 %	25.0 %	66.2%

Table 5: The performance of the DNF model is compared with the performances of the ML and WSLS strategies in a dynamic environment with two blocks with different probability ratios for the two locations. The change in the probabilities after $N = 100$ trials is not signaled to the robot. For the ML strategy, we assume that the robot still believes in the second block that location B is the more likely one.

In a second experiment, we tested the situation in which the robot searches the object at A and B without prior knowledge about the success probability at each location. In addition, the probabilities change after $N = 100$ trials without warning and the robot has to adjust the distribution of decisions among the alternatives to this new situation to guarantee a high search efficiency. The first decision process in u_d now starts from equally pre-activated populations representing the possible movement directions A and B (compare Fig. 82). Figure 84a shows the activity distribution in u_d at the beginning of trial 16 in a block

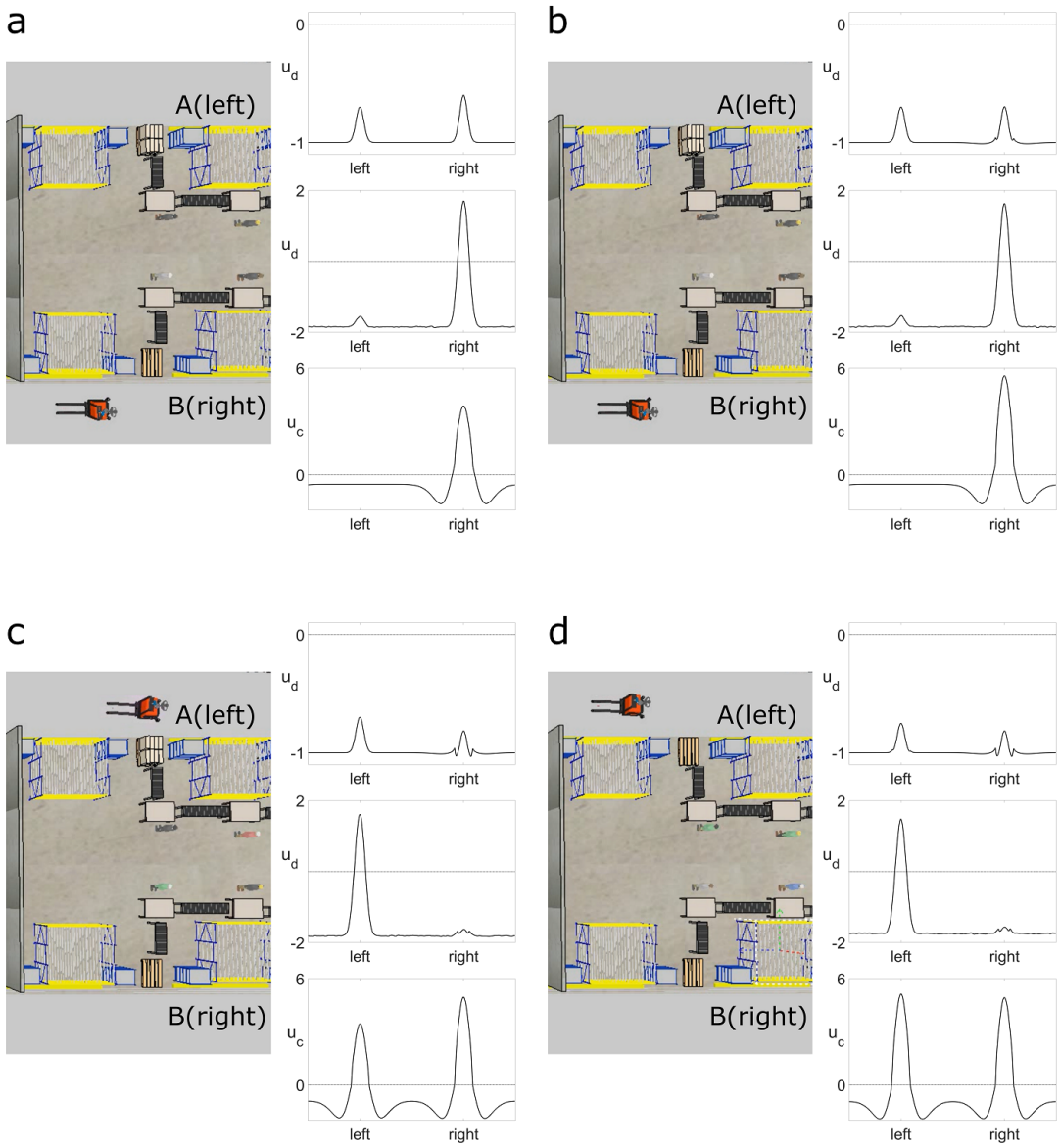

Figure 83: Snapshots of the simulator illustrating the robot's decisions in the first 4 trials of the experiment. For details see the text and Table 3.

in which the probabilities for A and B are 30% and 40%, respectively. The activity pattern is shaped by the summed activations of the choice and success integrators, $u_c + v_c$ (Fig. 84b) and $u_r + v_r$ (Fig. 84c), respectively. The preshape pattern predicts the decision to go to target B. Figure 84 (bottom row) depicts the same activation snapshots after trial 110 which is part of a block in which the success probabilities have changed (at trial 100) to 60% for A and 20% for B. Now the preshape pattern in u_d predicts location A as current choice. Figure 85 compares for both blocks of $N = 100$ trials the cumulative choices of target A and target B (blue curve) with the average ratio of success. Two features of the robot's behavior are notable. First, the robot appears to adjust quite quickly its decisions to the unsigned change in success

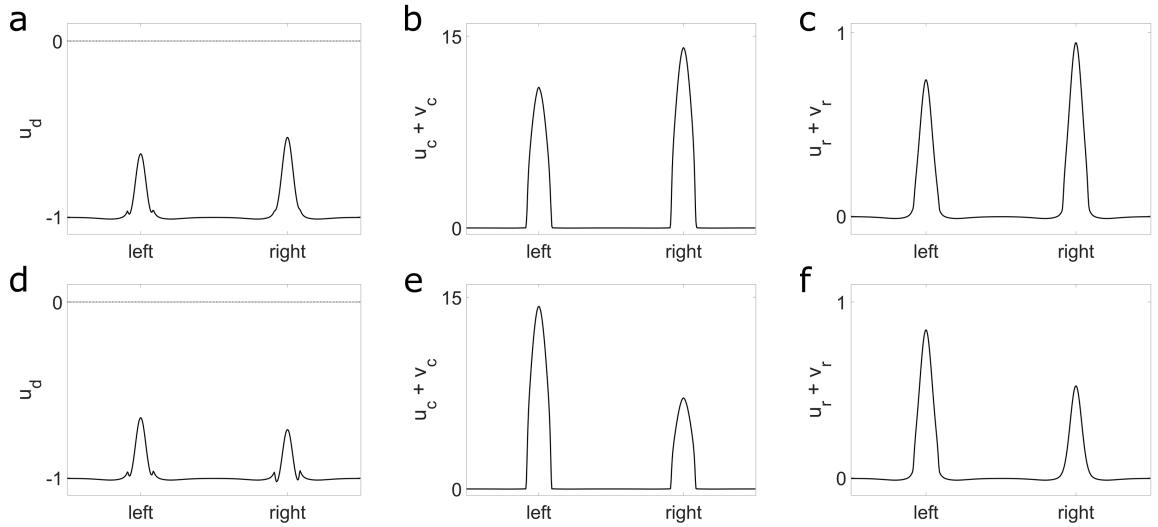

Figure 84: (**a**-**c**) First block of trials with 30% and 40% success probability for A and B, respectively. The resting state at the beginning of trial 16 is shown in the decision field u_d (**a**) which is shaped by the inputs from the choice integrator (**b**) and the success integrator (**c**). (**d**-**f**) Second block of trials with 60% and 20% success probability for A and B, respectively. The resting state at the beginning of trial 110 in shown in the decision field u_d (**d**) which is shaped by the inputs from the choice integrator (**e**) and the success integrator (**f**).

probabilities. Second, the robot chooses the location with lower probability more often than expected if it knew the true success probabilities, a well-known phenomenon described in the Cognitive Science literature as undermatching [80, 104]. Importantly, however, the robot shows a high search efficiency in both blocks with 85.7% and 73.8%, respectively. Again, the DNF model outperforms the two alternative strategies (compare Table 5).

In the present study, the two integrators were reset to their initial values every 8 trials. Intuitively it is clear that the integration time which maximizes the success rate for a given time period depends on the statistics of the environment. Under relatively stable conditions, it is better to take into account a large number of past choices and successes to estimate the current values of competing options. This is equivalent to introducing a constant prior belief in the model like shown in Figure 82. In nonstationary environments, however, the robot should weight recent events more heavily, as old ones may not be informative anymore for the current choice. The question how the neural integrators might autonomously adapt the integration time window to optimize search efficiency is a current research topic [80] but goes beyond the scope of this paper. It is interesting to notice however that the neural activations representing both options in (u_c, v_c) might be used to "count" the total number of past choices since the last reset. All one has to assume is that the reset mechanism is triggered when the total activation in the choice integration field reaches a pre-defined read-out threshold.

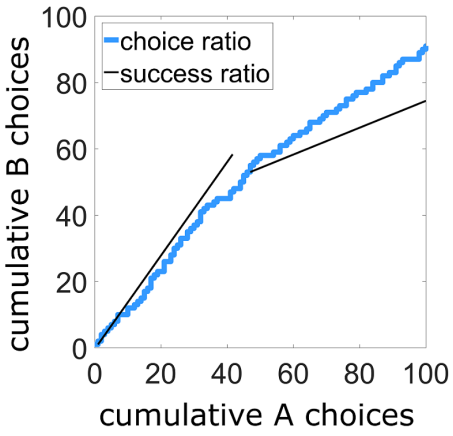

Figure 85: Dynamic matching behavior. The blue curve indicates the cumulative choices of target A and target B. The black lines represent the average ratio of success (B/A) within each of the two blocks of $N = 100$ trials: B/A $= 40/30$ in the 1st block and $20/60$ in the 2nd block. Search efficiency: 85.7% (1st block) and 73.8% (2nd block).

11.5 Conclusion

In this Chapter, we have used the two-field model (10.2) as a part of a control architecture of a mobile robot searching for an object at two different positions. Time-varying persistent activity of neuronal populations in the model represents gradual accumulation of evidence of past successes and choices that is used to guide robot's trial-by-trial decision process.

We tested our approach in two scenarios. In the first experiment we assumed that the robot knows the true probability of finding an object in each possible location. In the second scenario, the probabilities were not known a priori to the robot. We compared the efficiency of our DNF model with two alternative search strategies, namely "Most Likely" strategy and "Win-Stay-Lose-Switch" strategy. We demonstrated that our model outperforms both of them in both tested scenarios, for all tested probability ratios.

12 General discussion

12.1 Thesis summary

The goal of this thesis was to develop, rigorously analyze and apply a neural field model that provides a two-dimensional bump attractor, determined by a continuum of positions and amplitudes. The bump attractor network is able to self-sustain input-induced neural population activity at any level. This is achieved by combining a lateral-inhibition type network connectivity with local excitatory and inhibitory feedback mechanisms.

The proposed model is based on two coupled field equations of Amari type which allowed us to apply analytical and numerical tools that have been developed since Amari's seminal work. We analyzed and directly compared the conditions for the existence and stability of bump solutions of the Amari and the two-field model. The main conclusion is that in the absence of external input both models show the same qualitative behavior. Employing numerical continuation techniques allowed us to track bump solutions as model parameters are varied. For the case of spatially homogeneous initial conditions, the numerical results confirm the analytical findings about bump solutions. We then extended our numerical investigation of the two-field model to the case with spatially inhomogeneous initial conditions. Unlike the previous case, the neural network is able to stabilize bumps with a continuum of shapes depending on the initial condition. We also observed an additional branch of stable subthreshold bumps and branches of two- and three-bump solutions, which is not observed in the case of the Amari model.

Chapter 8 described the study of input-driven bump solutions of the two-field model which is guided by the new mathematical insights. With the goal to explain experimental findings in working memory tasks, we systematically compared the pattern formation process of the Amari and the two-field model when multiple inputs were applied sequentially or in parallel. Several distinct features of the new model were observed. First, two stable regions of excitation may exist at a distance where the bumps in the Amari model completely merge or drift apart. The two-field model shows a pattern of attraction of two nearby

bumps that is qualitativeley consistent with the behavior of biophysically more realistic bump attractor networks. Moreover, the lateral feedback excitation of the two-field model facilitates in general the formation of memory bumps. The two-field model thus predicts a higher working memory capacity than the Amari model. Second, the two-field model supports the existence of stable subthreshold activity patterns which might be linked to the notion of subconscious memory representations described in the experimental literature.

Unlike in bistable attractor models of Amari type, the baseline activity of the two-field neural integrator is not a stable state. A forgetting mechanism can thus not be implemented by simply applying a sufficiently strong inhibitory input that destabilizes existing bumps. For working memory applications, we have proposed a simple gating mechanism for the local feedback which restores the stable resting state of the Amari model without destroying the existence of subthreshold bump solutions.

Simulations of the stochastic version of the two-field model revealed that the noise-induced drift of a single bump decreases with increasing bump amplitude associated with stronger inputs. Larger bump amplitudes also greatly reduce the spatial interaction effect of nearby bumps representing similar memory items. These model predictions may guide future experimental and theoretical work which has not yet systematically investigated the impact of input features such as strength and duration on working memory precision.

The remaining part of the thesis was dedicated to the applications of the new model in the context of robotics research. Chapter 9 presented modeling results showing how the neural integrator can be used to first measure and subsequently reproduce time intervals. We discuss the results as an important step towards endowing autonomous robots with a sophisticated temporal cognition capacity. Chapters 10 and 11 were devoted to the application of the neural integrator to two real-world robotics tasks in a manufacturing environment. In the first experiment, the robot learned by observation the sequential order of object transfers between an assistant and an operator to subsequently substitute the assistant in the joint task. In the second experiment, the robot made a trial-by-trial decision to search for an object at locations where it may appear with some probability. The results show that the robot autonomously develops an efficient search strategy based on the accumulated evidence from previous trials.

12.2 Future work

The work presented in this thesis raised a number of interesting questions and possible directions for future research on the mathematical analysis, possible extensions and further applications of the two-field model.

Model analysis

The linear stability analysis of the two field model given in Chapter 6 was performed with initial condition of the model set to $u(x,0)+v(x,0)=K$. It would be interesting to extend the linear stability analysis presented in Chapter 6 to the case of inhomogeneous initial conditions $u(x,0)+v(x,0)=K(x)$ or the presence of an inhomogeneous external drive $I(x)$. We expect that the analytical results will be in line with the findings obtained with the numerical techniques in Chapter 7.

For the numerical analysis of bump solutions in Chapter 7, we employed the numerical continuation technique with one bifurcation parameter only to study the existence and stability of bumps solutions. It would be also interesting to perform a multi-parameter analysis to describe the exact regions for which localized solutions exist in terms of more than one model parameter, for example following lines presented in [54].

Model extensions

A number of natural extensions of the two-field model is possible. One direction is to consider a finite signal propagation speed in neural tissue. Neural fields with delays were recently discussed in relation to spiking neural networks. It was shown that the incorporation of delays leads to a larger range of possible spatiotemporal patterns that are not observed otherwise [132, 133]. In the neural field literature, two kinds of delays are typically introduced, constant delays and space dependent (propagation) delays [6, 153, 155]. In the simplest case of constant delays, the two field model becomes

$$\tau_u \frac{\partial u(\mathbf{x},t)}{\partial t} = -u(\mathbf{x},t)+v(\mathbf{x},t)+\int_\Omega w(\mathbf{x},\mathbf{x}')f(u(\mathbf{x}',(t-\delta))-\theta)\mathrm{d}\mathbf{x}'+I(\mathbf{x},t), \tag{12.1a}$$

$$\tau_v \frac{\partial v(\mathbf{x},t)}{\partial t} = -v(\mathbf{x},t)+u(\mathbf{x},t)-\int_\Omega w(\mathbf{x},\mathbf{x}')f(u(\mathbf{x}',(t-\delta))-\theta)\mathrm{d}\mathbf{x}', \tag{12.1b}$$

where the parameter δ is the transmission delay.

Unlike the Amari model, the two-field model is robust to changes in the tuning of the form of the nonlinearity or the connectivity since the same functions are used for the u-field and the v-field. An important consequence is that the assumption of a perfectly symmetric connectivity pattern in continuous bump attractor networks can be relaxed. Model simulations with a slightly asymmetric connectivity profile or a profile with random perturbations show that localized activity patterns with a biased or distorted shape are stabilized by the network dynamics. Mitigating the inherent structural instability of bump attractor models offers new perspective for applications of dynamic field theory that include for instance the learning of the connectivity pattern [60]. We will explore this line of research in future work.

Model applications

Since the first robotics applications of the two-field model showed promising results, we plan to further test the efficiency and robustness of the approach in challenging real-world experiments. Robotics research on an adaptive timing capacity without the need to refer to an external clock mechanism is still in its infancy. We therefore plan to integrate the two-field model in an existing DNF-based architecture for natural human-robot interaction in order to advance towards a tight spatio-temporal coordination of actions between robot and human.

The DNF model we presented in Chapter 11 was tested in a simulated factory environment. The simulation results demonstrated that the integrator model can be successfully used to accumulate the evidence form past choices and rewards which then guide the decision process. One of our future goals is the validation of this approach in a real-world industrial environment which are normally cluttered with dynamically changing obstacles. It's thus important that the robot takes online sensory information into account when deciding in which direction to move. We plan to address this challenge by integrating the neural field approach to cognitive robotics with the so-called attractor dynamics approach to path planning briefly discussed in section 11.5.

A Numerical simulations

In this appendix we discuss the methods used for numerical simulations presented in this thesis.

To find numerically approximate solutions of the neural field models we assume a finite domain L which we discretize over space by dividing it into N equal intervals. We then use the forward Euler method to solve the resulting system of ODEs [88].

To compute the spatial convolution of w and f formed by the integral

$$\int_{-L}^{L} w(\mathbf{x}, \mathbf{x}') f(u(\mathbf{x}', t) - \theta) \mathrm{d}\mathbf{x}' \tag{A.1}$$

we use the convolution theorem, stating that convolution in one domain equals point-wise multiplication in the other domain, which may be written as

$$\mathcal{F}\{f * g\} = \mathcal{F}\{f\} \cdot \mathcal{F}\{g\}. \tag{A.2}$$

By applying the inverse Fourier transform, $\mathcal{F}^{-1}$, we have

$$f * g = \mathcal{F}^{-1}\big\{\mathcal{F}\{f\} \cdot \mathcal{F}\{g\}\big\}. \tag{A.3}$$

The transform requires normalization by multiplying the result by a constant scaling factor, here the length of the domain $2L$ divided by the number of intervals N. We then have

$$f * g = \frac{L}{N} \cdot \mathcal{F}^{-1}\big\{\mathcal{F}\{f\} \cdot \mathcal{F}\{g\}\big\}. \tag{A.4}$$

The majority of numerical simulations presented in this thesis were done in MATLAB using a forward Euler method. To compute the spatial convolution we employed MATLAB's in-built functions `fft` and `ifft` to perform the Fourier transform and the inverse Fourier transform, respectively. An example of MATLAB code is given in Listing A.1.

```
%% Cleaning
```

```
clear; clc; close all

%% Spatial coordinates
L = 4*pi; N = 2^12; dx = 2*L/N; xDim = (-L+(0:N-1)*dx);

%% Temporal coordinates
dt = .01; tspan = 0:dt:50; M = numel(tspan);

%% Set up functions
kernel = @(x,A_ex,s_ex,A_in,s_in,g_i) ...
        A_ex* exp(-0.5 * (x).^2 / s_ex^2) - ...
        A_in * exp(-0.5 * (x).^2 / s_in^2) - g_i;
gauss = @(x,mu,sigma) exp(-0.5*(x-mu).^2/sigma^2);
sigmoid = @(x,beta,theta)  1./ (1 + exp(-beta*(x-theta)));

%% Paramaters
p(1) = 1000;    % mu
p(2) = 2;       % A_ex
p(3) = 1.25;    % s_ex
p(4) = 1;       % A_inh
p(5) = 2.5;     % s_inh
p(6) = 0.1;     % g_inh
p(7) = 0.5;     % theta
p(8) = 1;       % tau

%% Initial data
K = 0.0;
u_field = -p(7) * ones(1, N); v_field = K - u_field;

%% Connectivity function and its FFT
w = kernel(xDim,p(2),p(3),p(4),p(5),p(6));
```

```
wHat = fft(w);

%% Input
A_I = 1; sigma_I = 1;
Input = zeros(M, N);
Input_pattern = A_I * gauss(xDim, 0, sigma_I);
Input(1/dt:2/dt, :) = repmat(Input_pattern,1+(1/dt),1);

%% Main loop
for i = 1:M
f = sigmoid(u_field, p(1), p(7));
convolution = dx * ifftshift(real(ifft(fft(f) .* wHat)));
% 2-field model:
u_field = u_field + dt/p(8) * (-u_field + convolution + ...
          v_field + Input(i, :));
v_field = v_field + dt/p(8) * (-v_field - convolution + u_field);
end


%% Plot results
figure;
plot(xDim,u_field,'k','linewidth',3), hold on
plot(xDim,v_field,'--k','linewidth',3), hold on
plot(xDim,p(7)*ones(1,N),':k','linewidth',2);
xlabel('x'); ylabel('u(x), v(x)');
ax = gca; set(gca, 'FontSize', 20); set(gca, 'XLim', [-L L])
```

Listing A.1: Example of code written in MATLAB which can be used to reproduce Figure 47.

Numerical simulations of the model shown in Chapter 9 were done in Julia [15] using a forward Euler method. To compute the spatial convolution we used a fast Fourier transform (FFT), using Julia's package `FFTW` with functions `fft` and `ifft` to perform the Fourier transform and the inverse Fourier transform, respectively. An example of Julia code is given in Listing A.2.

```
# Load packages
using Plots, FFTW

# Set up functions
gauss(x,A,sigma) = A .* exp.(-0.5 .* (x).^2 ./ sigma^2)
wmex(x,A_e,A_i,s_e,s_i,g_inh) = gauss(x,A_e,s_e) .-
                                gauss(x,A_i,s_i) .- g_inh

function conv!(x,wHat)
    copy = fft(x)
    @. copy .= wHat .* copy
    ifft!(copy); @. x .= real(copy)
    x .= ifftshift(x)
end

function runNF()
    # Spatial coordinates
    L = 60; dx = 0.005; x = collect(-L/2:dx:L/2); N = length(x)
    # Temporal coordinates
    tmax = 3; dt = 0.001; steps = collect(0:dt:tmax)

    wHat = fft(wmex(x,3,1.5,1,3,0.5))  # FFT of w for convolution
    sample_intervals = collect(500:50:1000) # intervals to measure,
                                            # ranging from 500
                                            # to 1000 ms

    # Parameters
    A_input = 1.75; sigma_input = 2 # for gaussian input
    theta = 0.25 # firing threshold
    epsi = 0.01 # noise strength
    mu = 1000 # sigmoid steepness
```

```
    # Initialize fiedls
    u0 = 0.225 .* ones(length(x)); v0 = 0.5 .- copy(u0)
    u = copy(u0); v = copy(v0)
    max_u = zeros(length(steps),length(sample_intervals))
    u_save = zeros(length(x),length(sample_intervals))

    for sample in 1:length(sample_intervals)
        u = copy(u0); v = copy(v0)

        for i in 1:length(steps)
            # Apply inputs of different durations
            if 0.5/dt < i < (0.5/dt + sample_intervals[sample])
                input = gauss(x,A_input,sigma_input)
            else
                input = zeros(length(x))
            end
            # Update fields
            f = 1.0 ./ (1.0 .+ exp.(-mu .* (u .- theta)))
            conv = dx .* conv!(f,wHat)
            u .= u .+ dt .* (-u .+ v .+ conv .+ input
                .+ sqrt.(epsi) .*  randn(length(x)))
            v .= v .+ dt .* (-v .+ u .- conv)
            max_u[i,sample] = maximum(u); u_save[:,sample] = u
        end # end current sample
    end  # end sampling

    return x, steps, u, v, max_u, u_save
end

# Simulate the measurement epoch
```

```
@time x, t, u, v, max_u_final, u_final = runNF()

# Get bump amplitudes at the end of the measurement epoch
max_vals = max_u_final[end,:]

# Plot the results
h1 = plot(x,u_final, xlims = (-15,15), dpi = 300,
            xtickfont = font(12, "Arial"), ytickfont = font(12),
            xlabel = "x", ylabel = "u(x)", legend=:false)
display(h1)
```

Listing A.2: Example of code written in Julia v1.5.3 which can be used to reproduce Figure 66.

For performing numerical continuation in Chapter 7 we use the method described in [123] and adapted MATLAB code available in [8]. The main advantage of this method is that it can be applied directly to the full integral model. This is possible due to the usage of Newton-GMRES solvers combined with a fast Fourier transform (FFT) employed for computing the convolution term [123].

Numerical simulations of the stochastic models in Chapter 8 were done using an Euler-Maruyama method.

B Initial conditions and parameters used in Chapters 10 and 11

Initial conditions used in Chapter 10

For the model simulations, the initial conditions of the fields governed by the Amari dynamics, u_{per}, u_{on}, u_{wm} and u_d are defined by the inhibition parameter h. For the coupled two-field model the initial conditions are given by:

$$u_m(x, y, 0) = -1, \tag{B.1a}$$

$$v_m(x, y, 0) = -0.25 - u_m(x, y, 0). \tag{B.1b}$$

Initial conditions used in Chapter 11

The initial condition of the decision field at the start of simulation trial n is given by:

$$u_{d_n}(x, 0) = \begin{cases} I_{prob}(x) - h_{d_0} & \text{if } n = 1, \\ \left(u_{r_{n-1}}(x) + v_{r_{n-1}}(x)\right) & \\ - c_d \left(u_{c_{n-1}}(x) + v_{c_{n-1}}(x)\right) - h_{d_0}, & \text{otherwise.} \end{cases} \tag{B.2}$$

The initial condition for the choice integration layer (u_c, v_c) in the first trial and after each reset is given by

$$u_c(x, 0) = -0.5, \tag{B.3a}$$

$$v_c(x, 0) = -u_c(x, 0). \tag{B.3b}$$

The initial condition for the success integration layer (u_r, v_r) in the first trial and after each reset is given by

$$u_r(x, 0) = -0.5, \tag{B.4a}$$

$$v_r(x, 0) = I_{prob}(x) - u_r(x, 0). \tag{B.4b}$$

Model parameters used in Chapter 10

See Table 6.

Perception field u_{per}	
τ_{per}	3
w_{lat}	$A_{lat} = 6$, $\sigma_{lat} = 0.65$, $g_{lat} = 2$
I_t	$A_I = 6$, $\sigma_I = 0.75$, $g_I = 0$
h_{per}	1.5
Sequence onset field u_{on}	
τ_{on}	1
w_{mex}	$A_{ex} = 4$, $A_{in} = 2$, $\sigma_{ex} = 1.5$, $\sigma_{in} = 2.5$, $g_{mex} = 0.15$
I_{on}	$A_I = 1.25$, $\sigma_I = 1.5$, $g_I = 0$
h_{on}	0.5
Memory field u_m, v_m	
τ_m	3
w_{mex}	$A_{ex} = 6$, $A_{in} = 3.5$, $\sigma_{ex} = 1.5$, $\sigma_{in} = 2.25$, $g_{mex} = 0$
κ	0.04
Decision field u_d	
τ_d	2
w_{lat}	$A_{lat} = 5$, $\sigma_{lat} = 0.75$, $g_{lat} = 1.5$
h_d	$h_{d_0} = 13.5$, $\kappa = 0.0085$ (fast recall), $\kappa = 0.004$ (slower recall)
Working memory field u_{wm}	
τ_{wm}	2
w_{osc}	$A_{osc} = 2.4$, $b = 0.7$
h_{wm}	2.5

Table 6: Parameter values of the field equations used for sequence learning and planning.

Model parameters used in Chapter 11

See Table 7.

Decision field u_d	
τ_d	1
w_{lat}	$A_{lat} = 2$, $\sigma_{lat} = 0.75$, $g_{lat} = 1$
$\epsilon^{1/2}$	0.025
h_d	$h_{d_0} = 1$, $\tau_{h_d} = 7$
c_d	0.05
Choice integration field u_c, v_c	
τ_c	1
w_{mex}	$A_{ex} = 4$, $A_{in} = 2$, $\sigma_{ex} = 1.5$, $\sigma_{in} = 3$, $g_{mex} = 0.25$
Success integration field u_r, v_r	
τ_r	1
w_{mex}	$A_{ex} = 4$, $A_{in} = 2$, $\sigma_{ex} = 1.5$, $\sigma_{in} = 3$, $g_{mex} = 0.25$
K_r	$K_r = 0.02$ (static case), $K_r = 0.035$ (dynamic case)

Table 7: Parameter values of the field equations used for value-based decision making.

Numerical model simulations

Numerical simulations of the models used in Chapters 10 and 11 were done in MATLAB using a forward Euler method with parameters given in Tables 8 and 9, respectively.

Assembly task	
space	$L = 50$, $N = 1000$, $\mathrm{d}x = 2L/N = 0.1$
time	$\Delta T = 100$, $M = 10000$, $\mathrm{d}t = \Delta T/M = 0.01$

Table 8: Spatial and temporal discretisation of the model used in Chapter 10.

Value-based decision making	
space	$L = 20$, $N = 1000$, $\mathrm{d}x = 2L/N = 0.04$
time	$\Delta T = 10$, $M = 1000$, $\mathrm{d}t = \Delta T/M = 0.01$

Table 9: Spatial and temporal discretisation of the model used in Chapter 11.

Bibliography

[1] R. Almeida and A. Ledberg. “A biologically plausible model of time-scale invariant interval timing.” In: *Journal of computational neuroscience* 28.1 (Feb. 2010), pp. 155–175. issn: 1573-6873. doi: 10.1007/s10827-009-0197-8 (cit. on p. 25).

[2] R. Almeida, J. Barbosa, and A. Compte. “Neural circuit basis of visuo-spatial working memory precision: a computational and behavioral study”. In: *Journal of neurophysiology* 114.3 (2015), pp. 1806–1818 (cit. on pp. 94, 95).

[3] S.-I. Amari. “Dynamics of pattern formation in lateral-inhibition type neural fields”. In: *Biological Cybernetics* 27.2 (1977), pp. 77–87 (cit. on pp. 10–13, 17, 18, 28–30, 36, 38, 63, 75, 77, 84, 94, 104, 116, 122).

[4] S.-I. Amari. “Topographic organization of nerve fields”. In: *Bulletin of Mathematical Biology* 42.3 (1980), pp. 339–364 (cit. on p. 85).

[5] J. Appell and C.-J. Chen. “How to solve Hammerstein equations”. In: *The Journal of Integral Equations and Applications* 18.3 (2006), pp. 287–296 (cit. on p. 16).

[6] F. M. Atay and A. Hutt. “Stability and bifurcations in neural fields with finite propagation speed and general connectivity”. In: *SIAM Journal on Applied Mathematics* 65.2 (2004), pp. 644–666 (cit. on p. 142).

[7] B. B. Averbeck, M. V. Chafee, D. A. Crowe, and A. P. Georgopoulos. “Parallel processing of serial movements in prefrontal cortex”. In: *Proceedings of the National Academy of Sciences of the United States of America* 99.20 (Oct. 2002), pp. 13172–13177. issn: 0027-8424. doi: 10.1073/pnas.162485599 (cit. on p. 23).

[8] D. Avitabile. “Numerical computation of coherent structures in spatially-extended systems”. In: Second International Conference on Mathematical Neuroscience, Antibes Juan-les-Pins, 2016. 2016 (cit. on pp. 64, 65, 67, 149).

[9] D. Avitabile and H. Schmidt. “Snakes and ladders in an inhomogeneous neural field model”. In: *Physica D: Nonlinear Phenomena* 294 (2015), pp. 24–36. doi: 10.1016/j.physd.2014.11.007 (cit. on pp. 64, 77).

[10] F. A. Azevedo, L. R. Carvalho, L. T. Grinberg, J. M. Farfel, R. E. Ferretti, R. E. Leite, W. J. Filho, R. Lent, and S. Herculano-Houzel. “Equal numbers of neuronal and nonneuronal cells make the human brain an isometrically scaled-up primate brain”. In: *Journal of Comparative Neurology* 513.5 (2009), pp. 532–541 (cit. on p. 6).

[11] A. Baddeley. “Working memory: looking back and looking forward”. In: *Nature reviews neuroscience* 4.10 (2003), pp. 829–839 (cit. on p. 12).

[12] A. Bastian, A. Riehle, W. Erlhagen, and G. Schöner. “Prior information preshapes the population representation of movement direction in motor cortex”. In: *NeuroReport* 9.2 (1998), pp. 315–319 (cit. on pp. 17, 86).

[13] P. M. Bays and R. Taylor. “A neural model of retrospective attention in visual working memory”. In: *Cognitive Psychology* 100 (2018), pp. 43–52 (cit. on p. 91).

[14] R. L. Beurle. “Properties of a mass of cells capable of regenerating pulses”. In: *Philosophical Transactions of the Royal Society of London. Series B, Biological Sciences* (1956), pp. 55–94 (cit. on p. 7).

[15] J. Bezanson, A. Edelman, S. Karpinski, and V. B. Shah. “Julia: A fresh approach to numerical computing”. In: *SIAM review* 59.1 (2017), pp. 65–98 (cit. on pp. 110, 146).

[16] E. Bicho, W. Erlhagen, L. Louro, and E. C. e Silva. “Neuro-cognitive mechanisms of decision making in joint action: A human–robot interaction study”. In: *Human movement science* 30.5 (2011), pp. 846–868 (cit. on pp. 18, 19).

[17] E. Bicho, W. Erlhagen, L. Louro, E. Costa e Silva, R. Silva, and N. Hipolito. “A dynamic field approach to goal inference, error detection and anticipatory action selection in human-robot collaboration”. In: *New Frontiers in Human-Robot Interaction* (2011), pp. 135–164. doi: 10.1075/ais.2.10bic (cit. on p. 128).

[18] E. Bicho, W. Erlhagen, E. Sousa, L. Louro, N. Hipólito, E. Silva, R. Silva, F. Ferreira, T. Machado, M. Hulstijn, et al. "The power of prediction: robots that read intentions". In: *2012 IEEE/RSJ International Conference on Intelligent Robots and Systems*. IEEE. 2012, pp. 5458–5459. doi: 10.1109/IROS.2012.6386297 (cit. on p. 128).

[19] E. Bicho, L. Louro, and W. Erlhagen. "Integrating verbal and nonverbal communication in a dynamic neural field architecture for human-robot interaction". In: *Frontiers in neurorobotics* 4 (2010), p. 5. doi: 10.3389/fnbot.2010.00005 (cit. on pp. 109, 128).

[20] E. Bicho, P. Mallet, and G. Schöner. "Target representation on an autonomous vehicle with low-level sensors". In: *The International Journal of Robotics Research* 19.5 (2000), pp. 424–447. doi: 10.1177/02783640022066950 (cit. on pp. 12, 130).

[21] E. Bicho and G. Schöner. "The dynamic approach to autonomous robotics demonstrated on a low-level vehicle platform". In: *Robotics and autonomous systems* 21.1 (1997), pp. 23–35 (cit. on pp. 17, 18).

[22] R. Bogacz. "Optimal decision-making theories: linking neurobiology with behaviour". In: *Trends in cognitive sciences* 11.3 (2007), pp. 118–125 (cit. on p. 87).

[23] P. C. Bressloff, J. D. Cowan, M. Golubitsky, P. J. Thomas, and M. C. Wiener. "Geometric visual hallucinations, Euclidean symmetry and the functional architecture of striate cortex". In: *Philosophical Transactions of the Royal Society of London. Series B: Biological Sciences* 356.1407 (2001), pp. 299–330 (cit. on p. 12).

[24] P. C. Bressloff and S. Coombes. "Neural 'Bubble' Dynamics Revisited." In: *Cognitive Computation* 5.3 (2013), pp. 281–294 (cit. on pp. 15, 44).

[25] C. D. Brody, R. Romo, and A. Kepecs. "Basic mechanisms for graded persistent activity: discrete attractors, continuous attractors, and dynamic representations". In: *Current opinion in neurobiology* 13.2 (2003), pp. 204–211. doi: 10.1016/S0959-4388(03)00050-3 (cit. on pp. 13, 14).

[26] N. Brunel and M. C. Van Rossum. "Lapicque's 1907 paper: from frogs to integrate-and-fire". In: *Biological cybernetics* 97.5-6 (2007), pp. 337–339 (cit. on p. 6).

[27] N. Cain, A. K. Barreiro, M. Shadlen, and E. Shea-Brown. "Neural integrators for decision making: a favorable tradeoff between robustness and sensitivity". In: *Journal of neurophysiology* 109.10 (2013), pp. 2542–2559 (cit. on p. 102).

[28] M. Camperi and X.-J. Wang. “A model of visuospatial working memory in prefrontal cortex: recurrent network and cellular bistability”. In: *Journal of computational neuroscience* 5.4 (1998), pp. 383–405 (cit. on pp. 99, 103).

[29] M. Carandini and D. J. Heeger. “Normalization as a canonical neural computation”. In: *Nature Reviews Neuroscience* 13.1 (2012), pp. 51–62 (cit. on p. 86).

[30] S. Carroll, K. Josić, and Z. P. Kilpatrick. “Encoding certainty in bump attractors”. In: *Journal of Computational Neuroscience* (2013), pp. 1–20. doi: 10.1007/s10827-013-0486-0 (cit. on pp. 14, 98, 99).

[31] P. Choe, J. D. Tew, and S. Tong. “Effect of cognitive automation in a material handling system on manufacturing flexibility”. In: *International Journal of Production Economics* 170 (2015), pp. 891–899. doi: 10.1016/j.ijpe.2015.01.018 (cit. on p. 130).

[32] C. C. Chow and Y. Karimipanah. “Before and beyond the Wilson–Cowan equations”. In: *Journal of Neurophysiology* 123.5 (2020), pp. 1645–1656 (cit. on p. 10).

[33] A. Compte, N. Brunel, P. S. Goldman-Rakic, and X.-J. Wang. “Synaptic mechanisms and network dynamics underlying spatial working memory in a cortical network model”. In: *Cerebral cortex* 10.9 (2000), pp. 910–923 (cit. on p. 13).

[34] C. Constantinidis, M. N. Franowicz, and P. S. Goldman-Rakic. “The sensory nature of mnemonic representation in the primate prefrontal cortex”. In: *Nature neuroscience* 4.3 (2001), pp. 311–316 (cit. on p. 14).

[35] S. Coombes. “Waves, bumps, and patterns in neural field theories”. In: *Biological Cybernetics* 93.2 (2005), pp. 91–108. issn: 1432-0770. doi: 10.1007/s00422-005-0574-y (cit. on p. 77).

[36] S. Coombes and M. Owen. “Exotic dynamics in a firing rate model of neural tissue with threshold accommodation”. In: *AMS Contemporary Mathematics* 44 (2007), pp. 123–144 (cit. on p. 23).

[37] S. Coombes, G. J. Lord, and M. R. Owen. “Waves and bumps in neuronal networks with axo-dendritic synaptic interactions”. In: *Physica D: Nonlinear Phenomena* 178.3-4 (2003), pp. 219–241. doi: 10.1016/S0167-2789(03)00002-2 (cit. on pp. 63, 64).

[38] S. Coombes, H. Schmidt, and D. Avitabile. “Spots: Breathing, Drifting and Scattering in a Neural Field Model”. In: *Neural Fields*. Ed. by S. Coombes, P. beim Graben, R. Potthast, and J. Wright. Springer Berlin Heidelberg, 2014, pp. 187–211. isbn: 978-3-642-54592-4. doi: 10.1007/978-3-642-54593-1_7 (cit. on p. 64).

[39] S. Coombes, H. Schmidt, and I. Bojak. “Interface dynamics in planar neural field models”. In: *The Journal of Mathematical Neuroscience* 2.1 (2012), p. 9 (cit. on p. 39).

[40] A. Destexhe and T. J. Sejnowski. “The Wilson–Cowan model, 36 years later”. In: *Biological cybernetics* 101.1 (2009), pp. 1–2 (cit. on p. 10).

[41] A. Dhooge, W. Govaerts, and Y. A. Kuznetsov. “MATCONT: a MATLAB package for numerical bifurcation analysis of ODEs”. In: *ACM Transactions on Mathematical Software (TOMS)* 29.2 (2003), pp. 141–164. doi: 10.1145/980175.980184 (cit. on p. 63).

[42] E. J. Doedel, T. F. Fairgrieve, B. Sandstede, A. R. Champneys, Y. A. Kuznetsov, and X. Wang. “AUTO-07P: Continuation and bifurcation software for ordinary differential equations”. In: (2007). doi: 10.2172/919153 (cit. on p. 63).

[43] P. F. Dominey. “A shared system for learning serial and temporal structure of sensori-motor sequences? Evidence from simulation and human experiments”. In: *Cognitive Brain Research* 6.3 (1998), pp. 163–172. issn: 0926-6410. doi: http://dx.doi.org/10.1016/S0926-6410(97)00029-3 (cit. on p. 22).

[44] F. Edin, T. Klingberg, P. Johansson, F. McNab, J. Tegnér, and A. Compte. “Mechanism for top-down control of working memory capacity”. In: *Proceedings of the National Academy of Sciences* 106.16 (2009), pp. 6802–6807 (cit. on p. 105).

[45] A. Elvin, C. Laing, R. McLachlan, and M. Roberts. “Exploiting the Hamiltonian structure of a neural field model”. In: *Physica D: Nonlinear Phenomena* 239.9 (2010), pp. 537–546. doi: 10.1016/j.physd.2009.08.004 (cit. on p. 64).

[46] C. Engels and G. Schöner. “Dynamic fields endow behavior-based robots with representations”. In: *Robotics and autonomous systems* 14.1 (1995), pp. 55–77 (cit. on p. 18).

[47] W. Erlhagen, A. Bastian, D. Jancke, A. Riehle, and G. Schöner. “The distribution of neuronal population activation (DPA) as a tool to study interaction and integration in cortical representations”. In: *Journal of neuroscience methods* 94.1 (1999), pp. 53–66 (cit. on pp. 17, 94, 95).

[48] W. Erlhagen and E. Bicho. “The dynamic neural field approach to cognitive robotics”. In: *Journal of Neural Engineering* 3 (2006), pp. 36–54 (cit. on pp. 18, 116).

[49] W. Erlhagen and E. Bicho. “A dynamic field approach to natural and efficient human-robot collaboration.” In: *Neural Fields: Theory and Applications*. Ed. by S. Coombes, P. beim Graben, R. Pothast, and J. Weight. Springer Berlin Heidelberg, 2014, pp. 341–365. isbn: 978-3-540-23957-4. doi: 10.1007/978-3-540-30301-5_60 (cit. on pp. 18, 109, 117, 127).

[50] W. Erlhagen and G. Schöner. “Dynamic field theory of movement preparation.” In: *Psychological review* 109.3 (2002), p. 545. doi: 10.1037/0033-295X.109.3.545 (cit. on pp. 17, 134).

[51] B. Ermentrout. “Neural networks as spatio-temporal pattern-forming systems”. In: *Reports on progress in physics* 61.4 (1998), p. 353 (cit. on pp. 9–12, 15, 30).

[52] B. Ermentrout. *Simulating, analyzing, and animating dynamical systems: a guide to XPPAUT for researchers and students*. Vol. 14. SIAM, 2002. doi: 10.1137/1.9780898718195 (cit. on p. 64).

[53] G. B. Ermentrout and D. H. Terman. *Mathematical foundations of neuroscience*. Vol. 35. Springer Science & Business Media, 2010 (cit. on p. 10).

[54] G. Faye, J. Rankin, and P. Chossat. “Localized states in an unbounded neural field equation with smooth firing rate function: a multi-parameter analysis”. In: *Journal of mathematical biology* 66.6 (2013), pp. 1303–1338 (cit. on p. 142).

[55] F. Ferreira, W. Erlhagen, and E. Bicho. “Multi-bump solutions in a neural field model with external inputs”. In: *Physica D: Nonlinear Phenomena* 326 (2016), pp. 32–51 (cit. on pp. 27, 30, 63, 85).

[56] F. Ferreira, W. Erlhagen, and E. Bicho. “A dynamic field model of ordinal and timing properties of sequential events”. In: *International Conference on Artificial Neural Networks*. Springer. 2011, pp. 325–332 (cit. on p. 23).

[57] F. Ferreira, W. Erlhagen, E. Sousa, L. Louro, and E. Bicho. “Learning a musical sequence by observation: A robotics implementation of a dynamic neural field model”. In: *4th International Conference on Development and Learning and on Epigenetic Robotics*. IEEE. 2014, pp. 157–162 (cit. on pp. 23–25, 122).

[58] F. Ferreira, W. Wojtak, E. Sousa, L. Louro, E. Bicho, and W. Erlhagen. “Rapid learning of complex sequences with time constraints: A dynamic neural field model”. In: *IEEE Transactions on Cognitive and Developmental Systems* (2020). doi: 10.1109/TCDS.2020.2991789 (cit. on pp. 28, 91).

[59] R. FitzHugh. “Impulses and physiological states in theoretical models of nerve membrane”. In: *Biophysical journal* 1.6 (1961), p. 445 (cit. on p. 6).

[60] M. Fotouhi, M. Heidari, and M. Sharifitabar. “Continuous neural network with windowed Hebbian learning”. In: *Biological Cybernetics* 109.3 (2015), pp. 321–332 (cit. on p. 143).

[61] D. A. French. “Identification of a free energy functional in an integro-differential equation model for neuronal network activity”. In: *Applied mathematics letters* 17.9 (2004), pp. 1047–1051 (cit. on p. 39).

[62] S. Funahashi, C. J. Bruce, and P. S. Goldman-Rakic. “Mnemonic coding of visual space in the monkey’s dorsolateral prefrontal cortex”. In: *Journal of neurophysiology* 61.2 (1989), pp. 331–349 (cit. on pp. 10, 12, 13).

[63] J. M. Fuster and G. E. Alexander. “Neuron activity related to short-term memory”. In: *Science* 173.3997 (1971), pp. 652–654 (cit. on p. 13).

[64] C. R. Gallistel and J. Gibbon. “Time, Rate, and Conditioning”. In: *Psychological Review* 107.2 (2000), pp. 289–344 (cit. on p. 107).

[65] A. Gazzaley and A. C. Nobre. “Top-down modulation: bridging selective attention and working memory”. In: *Trends in cognitive sciences* 16.2 (2012), pp. 129–135 (cit. on p. 91).

[66] S. Glasauer, M. Huber, P. Basili, A. Knoll, and T. Brandt. “Interacting in time and space: Investigating human-human and human-robot joint action”. In: *19th International Symposium in Robot and Human Interactive Communication*. 2010, pp. 252–257 (cit. on p. 117).

[67] A. Gökçe, D. Avitabile, and S. Coombes. “The dynamics of neural fields on bounded domains: an interface approach for Dirichlet boundary conditions”. In: *The Journal of Mathematical Neuroscience* 7.1 (2017), p. 12 (cit. on p. 29).

[68] W. J. Govaerts. *Numerical methods for bifurcations of dynamical equilibria*. Vol. 66. SIAM, 2000 (cit. on p. 65).

[69] J. Griffith. “On the stability of brain-like structures”. In: *Biophysical journal* 3.4 (1963), pp. 299–308 (cit. on p. 8).

[70] S. Grossberg. “Behavioral contrast in short term memory: Serial binary memory models or parallel continuous memory models?” In: *Journal of Mathematical Psychology* 17.3 (1978), pp. 199–219. issn: 0022-2496. doi: http://dx.doi.org/10.1016/0022-2496(78)90016-0 (cit. on p. 22).

[71] Y. Guo and C. C. Chow. “Existence and stability of standing pulses in neural networks: I. Existence”. In: *SIAM Journal on Applied Dynamical Systems* 4.2 (2005), pp. 217–248. doi: 10.1137/040609471 (cit. on p. 64).

[72] A. Hammerstein. “Nichtlineare Integralgleichungen nebst Anwendungen”. In: *Acta mathematica* 54 (1930), pp. 117–176 (cit. on p. 16).

[73] D. Hansel and H. Sompolinsky. “Modeling feature selectivity in local cortical circuits”. In: *Methods in Neuronal Modeling, 2nd ed.* Ed. by C. Koch and I. Segev. MIT Press, Cambridge, MA, 1998 (cit. on pp. 12, 15).

[74] D. O. Hebb. *The organization of behavior: a neuropsychological theory*. J. Wiley; Chapman & Hall, 1949 (cit. on p. 13).

[75] R. N. Henson. “Short-term memory for serial order: The start-end model”. In: *Cognitive psychology* 36.2 (1998), pp. 73–137 (cit. on pp. 22, 23).

[76] R. J. Herrnstein. “Relative and absolute strength of response as a function of frequency of reinforcement”. In: *Journal of the experimental analysis of behavior* 4.3 (1961), pp. 267–272. doi: 10.1901/jeab.1961.4-267 (cit. on p. 130).

[77] A. L. Hodgkin and A. F. Huxley. “A quantitative description of membrane current and its application to conduction and excitation in nerve”. In: *The Journal of physiology* 117.4 (1952), p. 500 (cit. on p. 6).

[78] G. Houghton. “The problem of serial order: A neural network model of sequence learning and recall”. In: *Current research in natural language generation*. 1990, pp. 287–319 (cit. on p. 23).

[79] M. J. Hurlstone, G. J. Hitch, and A. D. Baddeley. “Memory for serial order across domains: An overview of the literature and directions for future research.” In: *Psychological bulletin* 140.2 (2014), p. 339 (cit. on p. 23).

[80] K. Iigaya, Y. Ahmadian, L. P. Sugrue, G. S. Corrado, Y. Loewenstein, W. T. Newsome, and S. Fusi. "Deviation from the matching law reflects an optimal strategy involving learning over multiple timescales". In: *Nature communications* 10.1 (2019), p. 1466. doi: 10.1038/s41467-019-09388-3 (cit. on pp. 134, 138).

[81] D. Jancke, W. Erlhagen, G. Schöner, and H. R. Dinse. "Shorter latencies for motion trajectories than for flashes in population responses of cat primary visual cortex". In: *The Journal of physiology* 556.3 (2004), pp. 971–982 (cit. on p. 17).

[82] B. H. Jansen and V. G. Rit. "Electroencephalogram and visual evoked potential generation in a mathematical model of coupled cortical columns". In: *Biological cybernetics* 73.4 (1995), pp. 357–366 (cit. on p. 7).

[83] M. Jazayeri and M. N. Shadlen. "A neural mechanism for sensing and reproducing a time interval". In: *Current Biology* 25.20 (2015), pp. 2599–2609 (cit. on pp. 108–112).

[84] J. S. Johnson, J. P. Spencer, S. J. Luck, and G. Schöner. "A dynamic neural field model of visual working memory and change detection". In: *Psychological science* 20.5 (2009), pp. 568–577 (cit. on pp. 85, 94).

[85] H. B. Keller. "Numerical Solution of Bifurcation and Nonlinear Eigenvalue Problems". In: *Applications of bifurcation theory* (1977), pp. 359–384 (cit. on p. 65).

[86] Z. P. Kilpatrick. "Wilson-Cowan model". In: *Encyclopedia of Computational Neuroscience*. Ed. by D. Jaeger and R. Jung. Springer New York, 2014 (cit. on p. 10).

[87] Z. P. Kilpatrick and B. Ermentrout. "Wandering bumps in stochastic neural fields". In: *SIAM Journal on Applied Dynamical Systems* 12.1 (2013), pp. 61–94 (cit. on p. 99).

[88] D. Kincaid, D. R. Kincaid, and E. W. Cheney. *Numerical analysis: mathematics of scientific computing*. Vol. 2. American Mathematical Soc., 2009 (cit. on p. 144).

[89] K. Kishimoto and S.-i. Amari. "Existence and stability of local excitations in homogeneous neural fields". In: *Journal of Mathematical Biology* 7.4 (1979), pp. 303–318 (cit. on p. 11).

[90] A. Koene, A. Remazeilles, M. Prada, A. Garzo, M. Puerto, S. Endo, and A. M. Wing. "Relative importance of spatial and temporal precision for user satisfaction in human-robot object handover interactions". In: *Third International Symposium on New Frontiers in Human-Robot Interaction*. 2014 (cit. on pp. 25, 117).

[91] K. Kopecz and G. Schöner. “Saccadic motor planning by integrating visual information and pre-information on neural dynamic fields”. In: *Biological cybernetics* 73.1 (1995), pp. 49–60 (cit. on p. 17).

[92] A. A. Koulakov, S. Raghavachari, A. Kepecs, and J. E. Lisman. “Model for a robust neural integrator”. In: *Nature neuroscience* 5.8 (2002), pp. 775–782 (cit. on pp. 14, 102).

[93] N. Krishnan, D. B. Poll, and Z. P. Kilpatrick. “Synaptic efficacy shapes resource limitations in working memory”. In: *Journal of computational neuroscience* 44.3 (2018), pp. 273–295 (cit. on pp. 94, 96).

[94] E. P. Krisner. “Periodic solutions of a one Dimensional Wilson-Cowan type model”. In: *Electronic Journal of Differential Equations* 102 (2007), pp. 1–22 (cit. on p. 12).

[95] S. Kubota and K. Aihara. “Analyzing global dynamics of a neural field model”. In: *Neural Processing Letters* 21.2 (2005), pp. 133–141 (cit. on pp. 36, 39).

[96] B.-C. Kuo, M. G. Stokes, and A. C. Nobre. “Attention modulates maintenance of representations in visual short-term memory”. In: *Journal of cognitive neuroscience* 24.1 (2012), pp. 51–60 (cit. on p. 14).

[97] C. R. Laing. “Numerical Bifurcation Theory for High-Dimensional Neural Models”. In: *The Journal of Mathematical Neuroscience* 4.1 (2014), p. 13. issn: 2190-8567. doi: 10.1186/2190-8567-4-13 (cit. on p. 63).

[98] C. R. Laing, W. C. Troy, B. Gutkin, and G. B. Ermentrout. “Multiple bumps in a neuronal model of working memory”. In: *SIAM Journal on Applied Mathematics* 63.1 (2002), pp. 62–97 (cit. on pp. 20, 27, 30, 63, 64, 77, 78).

[99] C. R. Laing. “PDE methods for two-dimensional neural fields”. In: *Neural Fields*. Springer, 2014, pp. 153–173. doi: 10.1007/978-3-642-54593-1_5 (cit. on pp. 64, 80).

[100] C. R. Laing and W. C. Troy. “PDE methods for nonlocal models”. In: *SIAM Journal on Applied Dynamical Systems* 2.3 (2003), pp. 487–516. doi: 10.1137/030600040 (cit. on pp. 64, 80).

[101] C. R. Laing and W. C. Troy. “Two-bump solutions of Amari-type models of neuronal pattern formation”. In: *Physica D: Nonlinear Phenomena* 178.3-4 (2003), pp. 190–218 (cit. on p. 85).

[102] L. Lapicque. “Recherches quantitatives sur l’excitation électrique des nerfs traitée comme une polarization”. In: *Journal de Physiologie et de Pathologie Générale* 9 (1907), pp. 620–635 (cit. on p. 6).

[103] P. E. Latham, B. Richmond, P. Nelson, and S. Nirenberg. “Intrinsic dynamics in neuronal networks. I. Theory”. In: *Journal of neurophysiology* 83.2 (2000), pp. 808–827 (cit. on p. 6).

[104] B. Lau and P. W. Glimcher. “Dynamic response-by-response models of matching behavior in rhesus monkeys”. In: *Journal of the experimental analysis of behavior* 84.3 (2005), pp. 555–579. doi: 10.1901/jeab.2005.110-04 (cit. on pp. 130, 132, 134, 138).

[105] S. Lim and M. S. Goldman. “Balanced cortical microcircuitry for maintaining information in working memory”. In: *Nature neuroscience* 16.9 (2013), p. 1306 (cit. on p. 109).

[106] P.-H. Lin and S. J. Luck. “The influence of similarity on visual working memory representations”. In: *Visual Cognition* 17.3 (2009), pp. 356–372 (cit. on pp. 94, 95).

[107] Y. Lin. “Toward Intelligent Human Machine Interactions”. In: *Mechanical Engineering* 139.06 (2017), S4–S8. doi: 10.1115/1.2017-Jun-4 (cit. on p. 128).

[108] L. Louro, T. Malheiro, P. Guimarães, T. Machado, S. Monteiro, S. Vaz Silva, W. Erlhagen, and E. Bicho. “Motion Control for Autonomous Tugger Vehicles in Dynamic Factory Floors Shared with Human Operators”. In: *IEEE 45th Annual Conference of Industrial Electronics Society (IECON’2019)*. 2019 (cit. on p. 130).

[109] W. J. Ma and M. Jazayeri. “Neural coding of uncertainty and probability”. In: *Annual review of neuroscience* 37 (2014), pp. 205–220 (cit. on p. 86).

[110] A. Machado, M. T. Malheiro, and W. Erlhagen. “Learning to time: A perspective”. In: *Journal of the experimental analysis of behavior* 92.3 (2009), pp. 423–458 (cit. on p. 107).

[111] T. Machado, T. Malheiro, S. Monteiro, W. Erlhagen, and E. Bicho. “Attractor dynamics approach to joint transportation by autonomous robots: theory, implementation and validation on the factory floor”. In: *Autonomous Robots* 43.3 (2019), pp. 589–610. doi: 10.1007/s10514-018-9729-2 (cit. on p. 130).

[112] C. K. Machens, R. Romo, and C. D. Brody. “Functional, but not anatomical, separation of “what” and “when” in prefrontal cortex”. In: *Journal of Neuroscience* 30.1 (2010), pp. 350–360 (cit. on p. 116).

[113] M. Maniadakis and P. Trahanias. “Temporal cognition: a key ingredient of intelligent systems”. In: *Frontiers in neurorobotics* 5 (2011), p. 2 (cit. on p. 117).

[114] N. Y. Masse, M. C. Rosen, and D. J. Freedman. “Reevaluating the Role of Persistent Neural Activity in Short-Term Memory”. In: *Trends in Cognitive Sciences* 24.3 (2020), pp. 242–258 (cit. on p. 92).

[115] G. Mongillo, O. Barak, and M. Tsodyks. “Synaptic theory of working memory”. In: *Science* 319.5869 (2008), pp. 1543–1546 (cit. on pp. 92, 105).

[116] C. Morris and H. Lecar. “Voltage oscillations in the barnacle giant muscle fiber”. In: *Biophysical journal* 35.1 (1981), pp. 193–213 (cit. on p. 6).

[117] J. Nagumo, S. Arimoto, and S. Yoshizawa. “An active pulse transmission line simulating nerve axon”. In: *Proceedings of the IRE* 50.10 (1962), pp. 2061–2070 (cit. on p. 6).

[118] M. R. Owen, C. R. Laing, and S. Coombes. “Bumps and rings in a two-dimensional neural field: splitting and rotational instabilities”. In: *New Journal of Physics* 9.10 (2007), p. 378 (cit. on pp. 36, 39).

[119] J. J. Paton and D. V. Buonomano. “The neural basis of timing: distributed mechanisms for diverse functions”. In: *Neuron* 98.4 (2018), pp. 687–705 (cit. on pp. 108, 116).

[120] D. J. Pinto, J. C. Brumberg, D. J. Simons, G. B. Ermentrout, and R. Traub. “A quantitative population model of whisker barrels: re-examining the Wilson-Cowan equations”. In: *Journal of computational neuroscience* 3.3 (1996), pp. 247–264 (cit. on pp. 9, 15).

[121] D. J. Pinto and G. B. Ermentrout. “Spatially structured activity in synaptically coupled neuronal networks: II. Lateral inhibition and standing pulses”. In: *SIAM Journal on Applied Mathematics* 62.1 (2001), pp. 226–243 (cit. on pp. 36, 40, 52).

[122] D. Purves, G. Augustine, D. Fitzpatrick, W. Hall, A. LaMantia, J. McNamara, and S. Williams. “Neuroscience. 3rd edition”. In: *Massachusetts: Sinauer Associates Inc Publishers* (2004) (cit. on pp. 5, 7).

[123] J. Rankin, D. Avitabile, J. Baladron, G. Faye, and D. J. Lloyd. “Continuation of localized coherent structures in nonlocal neural field equations”. In: *SIAM Journal on Scientific Computing* 36.1 (2014), B70–B93 (cit. on pp. 64, 66, 77, 83, 149).

[124] J. Rankin, É. Tlapale, R. Veltz, O. Faugeras, and P. Kornprobst. “Bifurcation analysis applied to a model of motion integration with a multistable stimulus”. In: *Journal of Computational Neuroscience* 34.1 (2013), pp. 103–124 (cit. on pp. 32, 64).

[125] E. D. Remington, S. W. Egger, D. Narain, J. Wang, and M. Jazayeri. “A dynamical systems perspective on flexible motor timing”. In: *Trends in cognitive sciences* 22.10 (2018), pp. 938–952. doi: 10.1016/j.tics.2018.07.010 (cit. on pp. 107, 109).

[126] J. Reutimann, V. Yakovlev, S. Fusi, and W. Senn. “Climbing Neuronal Activity as an Event-Based Cortical Representation of Time”. In: *Journal of Neuroscience* 24.13 (2004), pp. 3295–3303. issn: 0270-6474 (cit. on p. 109).

[127] B. J. Rhodes, D. Bullock, W. B. Verwey, B. B. Averbeck, and M. P. Page. “Learning and production of movement sequences: Behavioral, neurophysiological, and modeling perspectives”. In: *Human movement science* 23.5 (2004), pp. 699–746 (cit. on pp. 23, 91, 124).

[128] J. Rinzel. “Discussion: Electrical excitability of cells, theory and experiment: Review of the Hodgkin-Huxley foundation and an update”. In: *Bulletin of Mathematical Biology* 52.1-2 (1990), pp. 3–23 (cit. on p. 6).

[129] E. T. Rolls, L. Dempere-Marco, and G. Deco. “Holding multiple items in short term memory: a neural mechanism”. In: *PloS one* 8.4 (2013), e61078 (cit. on p. 85).

[130] R. Romo, C. D. Brody, A. Hernández, and L. Lemus. “Neuronal correlates of parametric working memory in the prefrontal cortex”. In: *Nature* 399.6735 (1999), pp. 470–473 (cit. on p. 13).

[131] N. S. Rose, J. J. LaRocque, A. C. Riggall, O. Gosseries, M. J. Starrett, E. E. Meyering, and B. R. Postle. “Reactivation of latent working memories with transcranial magnetic stimulation”. In: *Science* 354.6316 (2016), pp. 1136–1139 (cit. on p. 92).

[132] A. Roxin, N. Brunel, and D. Hansel. “Role of delays in shaping spatiotemporal dynamics of neuronal activity in large networks”. In: *Physical review letters* 94.23 (2005), p. 238103 (cit. on p. 142).

[133] A. Roxin and E. Montbrió. “How effective delays shape oscillatory dynamics in neuronal networks”. In: *Physica D: Nonlinear Phenomena* 240.3 (2011), pp. 323–345 (cit. on p. 142).

[134] Y. Sakai, H. Okamoto, and T. Fukai. “Computational algorithms and neuronal network models underlying decision processes”. In: *Neural Networks* 19.8 (2006), pp. 1091–1105. doi: 10.1016/j.neunet.2006.05.034 (cit. on p. 14).

[135] M. Sala, M. A. Heroux, D. M. Day, and J. M. Willenbring. “Trilinos Tutorial”. In: *Sandia National Laboratories, Tech. Rep. SAND2004-2189* (2004). doi: 10.2172/919153 (cit. on p. 63).

[136] S. Schneegans and P. M. Bays. “Restoration of fMRI decodability does not imply latent working memory states”. In: *Journal of Cognitive Neuroscience* 29.12 (2017), pp. 1977–1994 (cit. on pp. 92, 105).

[137] G. Schöner. “Dynamical systems approaches to cognition”. In: *Cambridge handbook of computational cognitive modeling* (2008), pp. 101–126 (cit. on p. 17).

[138] G. Schöner. *Dynamic thinking: A primer on dynamic field theory*. Oxford University Press, 2016 (cit. on pp. 17, 18, 109).

[139] G. Schöner, M. Dose, and C. Engels. “Dynamics of behavior: Theory and applications for autonomous robot architectures”. In: *Robotics and autonomous systems* 16.2-4 (1995), pp. 213–245 (cit. on pp. 17, 18).

[140] E. C. Silva, M. Costa, J. Araújo, D. Machado, L. Louro, W. Erlhagen, and E. Bicho. “Towards human-like bimanual movements in anthropomorphic robots: a nonlinear optimization approach”. In: *Applied Mathematics & Information Sciences An International Journal* (2015). doi: 10.12785/amis/090210 (cit. on p. 121).

[141] R. Silva, L. Louro, T. Malheiro, W. Erlhagen, and E. Bicho. “Combining intention and emotional state inference in a dynamic neural field architecture for human-robot joint action”. In: *Adaptive Behavior* 24.5 (2016), pp. 350–372. doi: 10.1177/1059712316665451 (cit. on p. 128).

[142] P. Simen, F. Balci, L. deSouza, J. D. Cohen, and P. Holmes. “A model of interval timing by neural integration”. In: *Journal of Neuroscience* 31.25 (2011), pp. 9238–9253 (cit. on p. 109).

[143] D. Soto, T. Mäntylä, and J. Silvanto. “Working memory without consciousness”. In: *Current Biology* 21.22 (2011), R912–R913 (cit. on p. 97).

[144] E. Sousa, W. Erlhagen, F. Ferreira, and E. Bicho. “Off-line simulation inspires insight: a neurodynamics approach to efficient robot task learning”. In: *Neural Networks* 72 (2015), pp. 123–139 (cit. on pp. 117, 127).

[145] A. S. Souza and K. Oberauer. “In search of the focus of attention in working memory: 13 years of the retro-cue effect”. In: *Attention, Perception, & Psychophysics* 78.7 (2016), pp. 1839–1860 (cit. on p. 91).

[146] T. C. Sprague, E. F. Ester, and J. T. Serences. “Restoring latent visual working memory representations in human cortex”. In: *Neuron* 91.3 (2016), pp. 694–707 (cit. on p. 92).

[147] L. P. Sugrue, G. S. Corrado, and W. T. Newsome. “Matching behavior and the representation of value in the parietal cortex”. In: *Science* 304.5678 (2004), pp. 1782–1787. doi: 10.1126/science.1094765 (cit. on pp. 130, 132, 134).

[148] D. W. Sutterer, J. J. Foster, K. C. Adam, E. K. Vogel, and E. Awh. “Item-specific delay activity demonstrates concurrent storage of multiple active neural representations in working memory”. In: *PLoS biology* 17.4 (2019), e3000239 (cit. on p. 92).

[149] J. G. Taylor. “Neural ‘bubble’ dynamics in two dimensions: foundations”. In: *Biological cybernetics* 80.6 (1999), pp. 393–409. doi: 10.1007/s004220050534 (cit. on pp. 15, 44).

[150] D. Trübutschek, S. Marti, A. Ojeda, J.-R. King, Y. Mi, M. Tsodyks, and S. Dehaene. “A theory of working memory without consciousness or sustained activity”. In: *Elife* 6 (2017), e23871 (cit. on pp. 92, 97).

[151] P. Tsarouchi, S. Makris, and G. Chryssolouris. “Human–robot interaction review and challenges on task planning and programming”. In: *International Journal of Computer Integrated Manufacturing* 29.8 (2016), pp. 916–931. doi: 10.1080/0951192X.2015.1130251 (cit. on p. 128).

[152] F. Ullén and S. L. Bengtsson. “Independent Processing of the Temporal and Ordinal Structure of Movement Sequences”. In: *Journal of Neurophysiology* 90.6 (2003), pp. 3725–3735. doi: 10.1152/jn.00458.2003 (cit. on p. 22).

[153] R. Veltz. “Interplay between synaptic delays and propagation delays in neural field equations”. In: *SIAM Journal on Applied Dynamical Systems* 12.3 (2013), pp. 1566–1612. doi: 10.1137/120889253 (cit. on pp. 64, 142).

[154] R. Veltz and O. Faugeras. “Local/global analysis of the stationary solutions of some neural field equations”. In: *SIAM Journal on Applied Dynamical Systems* 9.3 (2010), pp. 954–998. doi: 10.1137/090773611 (cit. on p. 64).

[155] N. A. Venkov, S. Coombes, and P. C. Matthews. “Dynamic instabilities in scalar neural field equations with space-dependent delays”. In: *Physica D: Nonlinear Phenomena* 232.1 (2007), pp. 1–15 (cit. on p. 142).

[156] C. R. Vokoun, X. Huang, M. B. Jackson, and M. A. Basso. “Response normalization in the superficial layers of the superior colliculus as a possible mechanism for saccadic averaging”. In: *Journal of Neuroscience* 34.23 (2014), pp. 7976–7987 (cit. on pp. 94, 105).

[157] J. Wang, D. Narain, E. A. Hosseini, and M. Jazayeri. “Flexible timing by temporal scaling of cortical responses”. In: *Nature neuroscience* 21.1 (2018), p. 102 (cit. on p. 117).

[158] J. Wang, R. Dou, R. R. Muddada, and W. Zhang. “Management of a holistic supply chain network for proactive resilience: Theory and case study”. In: *Computers & Industrial Engineering* 125 (2018), pp. 668–677. doi: 10.1016/j.cie.2017.12.021 (cit. on p. 128).

[159] X.-J. Wang, J. Tegnér, C. Constantinidis, and P. Goldman-Rakic. “Division of labor among distinct subtypes of inhibitory neurons in a cortical microcircuit of working memory”. In: *Proceedings of the National Academy of Sciences* 101.5 (2004), pp. 1368–1373 (cit. on p. 32).

[160] X.-J. Wang. “Synaptic reverberation underlying mnemonic persistent activity”. In: *Trends in neurosciences* 24.8 (2001), pp. 455–463 (cit. on p. 13).

[161] J. H. Wearden, R. Norton, S. Martin, and O. Montford-Bebb. “Internal clock processes and the filled-duration illusion”. In: *Journal of Experimental Psychology: Human Perception and Performance* 33.3 (2007), p. 716 (cit. on pp. 111, 116).

[162] Z. Wei, X.-J. Wang, and D.-H. Wang. “From distributed resources to limited slots in multiple-item working memory: a spiking network model with normalization”. In: *Journal of Neuroscience* 32.33 (2012), pp. 11228–11240 (cit. on pp. 84, 96, 105).

[163] R. Wilcox, S. Nikolaidis, and J. Shah. “Optimization of temporal dynamics for adaptive human-robot interaction in assembly manufacturing”. In: *Robotics* (2013), p. 441. doi: 10.15607/RSS.2012.VIII.056 (cit. on pp. 127–129).

[164] T. Wildegger, G. Humphreys, and A. C. Nobre. “Retrospective attention interacts with stimulus strength to shape working memory performance”. In: *PloS one* 11.10 (2016), e0164174 (cit. on pp. 14, 91).

[165] C. Wilimzig, S. Schneider, and G. Schöner. “The time course of saccadic decision making: Dynamic field theory”. In: *Neural Networks* 19.8 (2006), pp. 1059–1074 (cit. on p. 94).

[166] H. R. Wilson and J. D. Cowan. “Excitatory and inhibitory interactions in localized populations of model neurons”. In: *Biophysical journal* 12.1 (1972), pp. 1–24 (cit. on pp. 6, 8, 10, 17).

[167] H. R. Wilson and J. D. Cowan. “A mathematical theory of the functional dynamics of cortical and thalamic nervous tissue”. In: *Kybernetik* 13.2 (1973), pp. 55–80 (cit. on pp. 8, 10, 17).

[168] K. Wimmer, D. Q. Nykamp, C. Constantinidis, and A. Compte. “Bump attractor dynamics in prefrontal cortex explains behavioral precision in spatial working memory”. In: *Nature neuroscience* 17.3 (2014), pp. 431–439 (cit. on pp. 13, 14, 99).

[170] W. Wojtak, S. Coombes, E. Bicho, and W. Erlhagen. “Combining spatial and parametric working memory in a dynamic neural field model”. In: *Artificial Neural Networks and Machine Learning –- ICANN 2016, Lecture Notes in Computer Science*. Vol. 9886. Springer. 2016, pp. 411–418. doi: 10.1007/978-3-319-44778-0_48 (cit. on p. 109).

[171] W. Wojtak, F. Ferreira, W. Erlhagen, and E. Bicho. “Learning joint representations for order and timing of perceptual-motor sequences: a dynamic neural field approach”. In: *Neural Networks (IJCNN), 2015 International Joint Conference on*. IEEE. 2015, pp. 3082–3088 (cit. on pp. 24, 25, 117, 118).

[169] W. Wojtak, S. Coombes, D. Avitabile, E. Bicho, and W. Erlhagen. “A dynamic neural field model of continuous input integration”. In: *Biological Cybernetics* (2021), pp. 1–21 (cit. on p. 84).

[172] W. Wojtak, F. Ferreira, E. Bicho, and W. Erlhagen. “Neural Field Model for Measuring and Reproducing Time Intervals”. In: *Artificial Neural Networks and Machine Learning – ICANN 2019: Theoretical Neural Computation*. Ed. by I. V. Tetko, V. K□rková, P. Karpov, and F. Theis. Cham: Springer International Publishing, 2019, pp. 327–338. isbn: 978-3-030-30487-4. doi: 10.1007/978-3-030-30487-4_26 (cit. on pp. 86, 107, 129, 131).

[173] W. Wojtak, F. Ferreira, L. Louro, E. Bicho, and W. Erlhagen. “Towards temporal cognition for robots: A neurodynamics approach”. In: *2017 Joint IEEE International Conference on Development and Learning and Epigenetic Robotics (ICDL-EpiRob)*. IEEE. 2017, pp. 407–412 (cit. on pp. 25, 26).

[174] W. Wojtak, F. Ferreira, P. Vicente, L. Louro, E. Bicho, and W. Erlhagen. “A neural integrator model for planning and value-based decision making of a robotics assistant”. In: *Neural Computing and Applications* (2020), pp. 1–20 (cit. on pp. 120, 130).

[175] K. Zhang. “Representation of spatial orientation by the intrinsic dynamics of the head-direction cell ensemble: a theory”. In: *Journal of Neuroscience* 16.6 (1996), pp. 2112–2126 (cit. on pp. 12, 15).

[176] X. Zhou, F. Katsuki, X.-L. Qi, and C. Constantinidis. “Neurons with inverted tuning during the delay periods of working memory tasks in the dorsal prefrontal and posterior parietal cortex”. In: *Journal of Neurophysiology* 108.1 (2012), pp. 31–38 (cit. on p. 32).

[177] J. Zylberberg and B. W. Strowbridge. “Mechanisms of persistent activity in cortical circuits: possible neural substrates for working memory”. In: *Annual review of neuroscience* 40 (2017) (cit. on p. 13).